ABSTRACT

Title of Dissertation: COMBINATORIAL INVESTIGATION OF
FERROMAGNETIC SHAPE MEMORY ALLOYS

Olugbenga O. Famodu,
Doctor of Philosophy, 2005

Dissertation directed by: Associate Professor Ichiro Takeuchi
Department of Materials Science and Engineering
Center for Superconductivity Research

Combinatorial synthesis is research methodology which allows one to systemically study a large number of compositionally varying samples simultaneously. We apply this technique to the investigation of multifunctional materials. Different designs of combinatorial libraries and various characterization tools are implemented in order to rapidly map composition-structure-property relationships in a variety of materials systems.

In this thesis, I will discuss combinatorial investigation of various shape memory alloys. We have utilized the combinatorial magnetron co-sputtering deposition technique for fabricating composition spreads of ternary alloy systems containing ferromagnetic shape memory alloys (FSMAs) and thermoelastic shape memory alloys (SMAs).

Magnetic properties of the composition spreads were rapidly characterized using a room temperature scanning semiconducting quantum interference device (SQUID) microscope which provides mapping of the magnetic field emanating from different parts of the composition spreads. By applying the inversion technique to the mapping of the magnetic field distribution, we have mapped the magnetic phase diagram of the Ni-Mn-Ga

and Ni-Mn-Al systems whose Heusler compositions Ni_2MnGa and Ni_2MnAl are well known ferromagnetic shape memory alloys (FSMAs). In addition, a rapid visual inspection technique was developed for detection of reversible martensites using arrays of micromachined cantilevers. A large, previously unexplored compositional region of FSMAs outside the Heusler composition was found.

In search of novel FSMAs, we have also investigated a number of other ternary alloys systems. These systems included Ni-Mn-In, Gd-Ge-Si, Co-Mn-Ga, Ni-Fe-Al, and Co-Ni-Ga. A summary of the results from the investigation of these systems is presented. We have used the combinatorial technique to search for "ideal" SMAs with minimal hysteresis. For pursuing this, we had first set out to verify the geometric non-linear theory of martensites which predicts the conditions under which the "ideal" SMA can occur. This was facilitated by the composition spread investigation of the Ni-Ti-Cu system and the use of synchrotron x-ray microdiffraction. We found that one of the criteria prescribed by the theory for achieving minimal hysteresis is closely obeyed. We have demonstrated that we can indeed use the technique we have developed here together with the theory to explore SMAs with minimal hysteresis.

COMBINATORIAL INVESTIGATION OF FERROMAGNETIC
SHAPE MEMORY MATERIALS

by

Olugbenga O. Famodu

Dissertation submitted to the Faculty of the Graduate School of the
University of Maryland, College Park in partial fulfillment
of the requirements for the degree of
Doctor of Philosophy
2005

Advisory Committee:

        Associate Professor I. Takeuchi, Chairman/Advisor
        Associate Professor S. H. Ehrman
        Associate Professor I. K. Lloyd
        Professor G. W. Rubloff
        Associate Research Scientist P. M. Piccoli

DEDICATION

To my wife LaRonda, my son Ethan, my extended family, and all of the friends who
encouraged and supported me through this journey.

ACKNOWLEDGEMENTS

One of my favorite poems was written by Robert Frost, "The Road Not Taken." He wrote:

"Two roads diverged in a wood, and I-

I took the one less traveled by,

And that has made all the difference."

When I read this poem, it reminds me of my journey to this point and of the many diverging roads in life that I have traveled. And they have truly made all the difference. I cannot attempt to name all the people whom I have come across during this journey who have helped me in choosing the different paths that have gotten me to this point. I must apologize to all those whom I may unintentionally forget to mention here. I may have used the brain space for this dissertation work over the years. There are so many individuals who have helped me in a number of different ways. Each individual has touched me in his or her own special way, and made my journey unforgettable.

First, I would like to thank my advisor sensei Ichiro Takeuchi for the opportunity to develop, learn, and interact with many people in the scientific community. I have learned and acquired many personal and professional skills from him while working in his group. He has been a great advisor, mentor, and role model. I am grateful and honored to have had the opportunity to learn and work with him. Thank you for the financial support. Thank you for correcting my dissertation and the many practice talks for this work and other presentations.

I would also like to thank Dr. Otto Wilson, Jr., and Dr. Isabel K. Lloyd for encouraging, supporting, and mentoring me during this journey. Thank you both for believing in me and offering words of encouragement along the way. You both always made me feel welcomed and at home when I visited your offices. You kept me smiling even though it was difficult at times. Thank you for taking an interest in me and guiding me through this journey.

Thanks to my dissertation committee members Dr. Sheryl H. Ehrman, Dr. Isabel K. Lloyd, Dr. Gary W. Rubloff, and Dr. Philip M. Piccoli for taking time out of their busy schedules to serve on my committee and to read and provide constructive comments on my dissertation. I would also like to thank each one of you for your advice, teachings, support, hallway discussions, and encouragement. Each of you had a significant impact on me, and I am sincerely grateful for everything you have done for me.

I would like to thank all my group members who treated me with dignity and respect. Without the help and inspiration we provided each other, I probably would have gone insane. I thank my colleague, team mate, friend, and senior Dr. Kao-Shuo Chang for being the first to graduate in our group, teaching me discipline, and assisting me in a number of other ways. Thank you for being a great lab partner. Thank you for being a good and close friend and someone I can count on for the rest of my life. To my dear colleague and fond friend Dr. Maria A. Aronova, thank you for teaching me about SQUID and all the assistance on the magnetic measurements over the years. I enjoyed your company and friendship; you are like a sister to me. Thank you for the words of encouragement and support. Thanks for also being a great lab partner and friend. Dr. Makoto Murakami-san, thanks for being a good friend, team mate, and lab partner.

I would also like to thank the entire staff of the physics machine shop for their excellent workmanship on parts and the various things we came up with for my experiments. Thank you all for the rapid turnaround times on the target cutting and fabrication jobs. Thank you John Cataldi, Mark Vilas, Randy, and Ernie to name a few. Thank you for doing such a great job and making my experiments much easier. Thank you Russ Wood for the many discussions and education on drawings and specifications, this is a skill that will serve me well in the future.

I would like to thank everyone in the Center for Superconductivity Research. I would also like to thank the members of Dr. T. Venkatesan's group. Thank you Dr. Sanjay Shinde, Dr. Wei Yang, Dr. Tom Wu, Dr. Bin Ming, Dr. Eric Li, Dr. Supab Choopun, Dr. Z.-Y. Chen, Ram, Betsy Pugel, and Alvaro Godinez for making me feel welcomed in your labs, for having interesting conversations, and for teaching me many things about experiments. A special thanks to Betsy for the encouragement when things were not going well in the measurement lab. Thank you Dr. R. D. Vispute, Dr. R. P. Sharma, Dr. S. Ogale, Dr. Rao, and Dr. Shiva Hullavarad for your suggestions about my experiments and the discussions during my presentations at the group meetings. Thank you for the help with many measurements, supplies, discussions, and presentation feedback. Thanks to the office staff, Cleopatra White, Belta Pollard, Brian Barnaby, Grace Sewlall, Doug Benson, Brian Straughn, et al. Thanks to Dr. F.C. Wellstood, Dr. R. Green, Dr. T. Venkatesan, their post doctorial staff, and their students for their assistance.

Thanks to the shipping and receiving office personnel in the physics department Jesse Anderson, Robert Dahms, and Al Godinez for always being kind and patient with me.

always provided me with the best opportunity to succeed even when it was difficult. You taught me the value of character and honesty. You always supported and believed in me. I will always love you and will always do my best to make you both proud parents. Thanks to my one and only sister Mrs. Modupe Archer (nee Famodu) for your undying love and support throughout this journey. You have always been there for me when I needed you the most. You always had words of encouragement for me when I was down. You never doubted me and always prayed for me. Thank you for being the greatest sister an older brother could have ever asked for. I love you sis. Thanks to my brothers Olanrewaju and Olatunji Famodu for their love and support. I wish you both the best and love you guys. Thanks to my in-laws, Rev. and Mrs. Richard Chapple, Jr., and Richard Chapple III, for their unwavering love and support for me throughout this journey. Thanks to Aunt Donnie, Uncle Derrick, Aunt Rachel, Aunt Mae, Aunt Shelia, Uncle Fred, Uncle Kambra, and their families. Thank you all for welcoming me into your family and accepting mine. Thank you for the encouragement and support. I love you all.

And last, but not the least, I would like to thank my lovely wife LaRonda and adorable son Ethan for their undying love and support for me through it all. Thank you for bearing with me through the late nights and weekends at school. Thanks for being understanding and caring. Thank you, LaRonda, for giving us and caring for our wonderful son. Thank you for helping me balance the job of being a great father to Ethan with pursuing this goal. Thank you for supporting and encouraging me when things were tough. Thank you for always being there for whatever. It is often said that "behind every successful man is a great woman." But in your case, it should be said that "beside *this*

successful man stands a great, beautiful, and successful woman." I love you, and as Shige-san said, you have also earned a P.H.D. – Push Husband Degree!

TABLE OF CONTENTS

LIST OF TABLES

LIST OF FIGURES

Chapter 1

Introduction

Combinatorial synthesis is a research methodology which allows one to quickly investigate a large number of previously unexplored materials by fabricating arrays of compositionally varying samples. Within the last two decades, combinatorial chemistry and screening for new drugs and biomolecules has revolutionized the pharmaceutical and DNA-sequencing industries. This methodology can be used to address a wide range of issues at different levels in a wide range of topics from semiconductor manufacturing and smart thin film materials to catalytic powders and biomaterials.

Combinatorial synthesis techniques have been used to fabricate both bulk and thin film materials. However, the application of the combinatorial methodology to technologically relevant electronic materials is best implemented in the form of thin film libraries. A variety of fabrication techniques available in microelectronics can lend themselves to synthesis of thin film libraries. The biggest challenge in the combinatorial strategy is in implementing an effective tool for rapid characterization of large numbers of materials. To facilitate high-throughput screening of the combinatorial samples, parallel detection schemes and non-destructive scanning probe microscopes are used to identify compositional regions with enhanced physical properties. There are always long lists of topics in the field of inorganic functional materials which can be tackled with the combinatorial approach. There are a number of scanning probe microscopes that are ideal for scanning the libraries and mapping their composition, electric, magnetic, and

1

martensitic properties. They include the scanning superconducting quantum interference device (SQUID) microscope, scanning microwave, four point probe measurement device and scanning ferromagnetic resonance microscopes.

The focus of this thesis is on the application of the combinatorial research methodology to shape memory alloys. We have developed the combinatorial magnetron cosputtering thin film deposition system for synthesis of composition spreads for mapping compositional phase diagrams of a variety of metallic alloy systems. We have devised the scanning SQUID microscope for mapping of remanent magnetization of materials across composition spreads. Several different techniques were developed for rapidly detecting compositions which are reversible martensites. They include the use of micromachined cantilever arrays and the measurement of resistance as a function of temperature.

In Chapter 2, I introduce the basics of combinatorial synthesis. I discuss combinatorial thin film library fabrication by magnetron co-sputtering deposition. In particular, the basic design and operation of the magnetron cosputtering system we designed and built is described. I also briefly introduce the analysis and characterization tools that were used to characterize the composition spreads in this thesis.

In Chapter 3, I discuss combinatorial investigation of ferromagnetic shape memory alloys (FSMAs). I first introduce the mechanisms of SMAs and FSMAs and give some examples of applications of these materials. I show how we have mapped the ternary compositional phase diagram of different ternary alloy systems, and discuss the results of this investigation, where we extended the known FSMA regions to previously unexplored regions in certain alloy systems.

In particular, we mapped the functional phase diagram for the Ni-Mn-Ga and Ni-Mn-Al ternary alloy systems in search of FSMA compositions. A characterization technique that allows detection of martensitic transitions by visual inspection was combined with quantitative magnetization mapping using scanning SQUID microscopy.

An inversion technique was developed to perform quantitative mapping of magnetic properties. A clear relationship between magnetization and the martensitic transition temperature was observed in the Ni-Mn-Ga system, revealing a strong thermodynamical coupling between magnetism and martensitic instability across a large fraction of the phase diagram.

We also obtained room temperature remanent magnetization mapping in a variety of other ternary systems. We did not find reproducible evidence of martensites in many of these systems. This however does not rule out the possibilities that there are martensites in these systems. This we believe is due to the fact that our wafers are fabricated in a "pseudo-equilibrium" manner and many of the martensites are known to be metastable phases formed via quenching. We instead conclude that in these systems there are no stable martensitic phases which can be formed by equilibrium processes without quenching. We argue that martensites which are stable at room temperatures and can be formed without quenching are more suitable for applications. Our composition spread detection technique is ideal for detecting such martensites.

In Chapter 4, we have experimentally verified the geometric non-linear theory of martensite using the ternary composition spread approach. Here, we devised the thin film composition spread technique to rapidly map the lattice parameters and the thermal hysteresis of ternary alloy systems. Variable temperature x-ray microdiffraction and

synchrotron x-ray microdiffraction together with scanning four-point electrical resistivity measurements were used to map composition regions which exhibit structural phase transitions in the Ni-Ti-Cu alloy system. We have observed a clear relationship between the thermal hysteresis and the middle eigenvalue of the transformation stretch tensor for the first time. In addition, we have identified a new region of titanium-rich SMAs with potential for better control of SMA properties due to the presence of large amount of precipitates.

In Chapter 5, I summarize my thesis. Discussions of ongoing and future projects are given.

Chapter 2

Combinatorial Synthesis of Inorganic Thin Film Materials

In this chapter, basic elements of combinatorial thin film synthesis are introduced. I will discuss the fundamental design and operation of the combinatorial non-confocal magnetron co-sputtering deposition system which we built to fabricate natural composition ternary spread libraries. I will also introduce the analysis tools that were used to characterize the combinatorial samples.

2.1   Fundamentals of combinatorial synthesis

Throughout history, scientists and engineers have relied on trial-and-error processes for materials discovery. This process allows only a small number of materials to be examined in a given period of time. Combinatorial synthesis is a technique that allows one to quickly investigate a large number of previously unexplored materials compositions. Within the last two decades, combinatorial chemistry and screening for new drugs and biomolecules have revolutionized the pharmaceutical and DNA-sequencing industries [1]. Its application to inorganic solid-state materials was pioneered at Lawrence Berkeley National Laboratory (LBNL) [2], and the effectiveness of the approach has since been demonstrated in the discoveries of dielectric/ferroelectric materials [3, 4, 5, 6], ferromagnetic materials [7, 8], colossal magnetoresistive materials [9, 10], polymers [11, 12, 13], catalysts [14, 15], and luminescent materials [2, 5].

5

The combinatorial techniques can be used to address materials issues at different levels in a wide range of topics from semiconductor manufacturing and thin-film smart materials to catalytic powders and biomaterials. It is expected that the combinatorial approach to materials will lead to accelerated innovation in various industries broadly benefiting our society.

When surveying the history of materials science, one finds that most of the basic binary compounds have been explored, and most of their basic properties are known. However, as soon as one moves on to other multi-element compounds such as ternary or quaternary systems, one finds that a large fraction of all possible compounds (formed by combining different elements) remain unexplored. At the end of 1980s, J. C. Phillips estimated that there were about 24,000 known inorganic materials [16]. Out of these, 16,000 are binary compounds, and only 8,000 are ternary and other multi-element compounds. If one is simply to pick out any three or four elements from the periodic table to form different compounds (there are about 60 non-radioactive and non-gas elements), there are over 30,000 possible ternary compounds and 500,000 possible quaternary compounds. Clearly, an extremely large number of compounds are yet to be explored. Any effort to systematically explore them using the one-by-one traditional approach would take a prohibitively long time. Combinatorial synthesis offers a potential solution to this problem.

The general trend in materials discoveries is that new materials tend to have increasingly complicated structures, often consisting of a large number of elements. Looking at the development of materials, there is also a trend that compounds that are more complex tend to have physical properties that are more desirable. This is clearly

illustrated in the case of high-temperature superconductors, where the highest superconducting transition temperature is currently observed in the $HgBa_2Ca_2Cu_3O_{8+d}$ compound with a complicated layered structure. **Error! Reference source not found.** shows the critical temperature (T_c) of superconductors as a function of number of different elements required to form the compound. It suggests that T_c increases as the compounds become more and more complex.
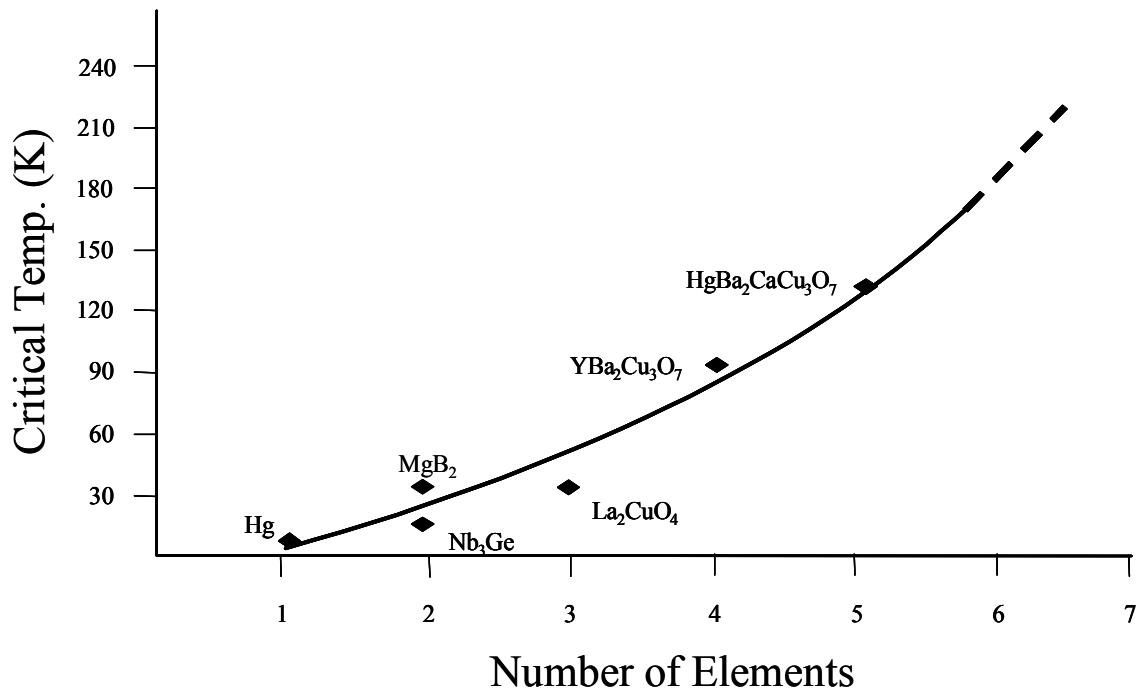
Figure 2-1: The correlation between materials complexity (reflected in the number of elements required to form the compounds) and a physical property (T_c) for superconductors.

The application of the combinatorial approach to technologically relevant electronic materials is best implemented in the form of thin-film libraries. Combinatorial thin-film libraries encompassing large compositional variations can be generated using different thin-film deposition techniques. Figure 2-2 shows the flow process of a representative combinatorial synthesis thin film experiment. In this scheme, a large

7

collection of compositionally varying samples is synthesized under the same conditions. In this scheme each composition is spatially separated from others by a grid formed by shadow masks. The samples are then processed and screened simultaneously. Different

Figure 2-2: The flow diagram of a representative combinatorial thin film experiment.

characterization tools are used depending on the desired application and physical properties of interest. Once compositions with enhanced physical properties are identified, they are analyzed individually in more details and subsequently, large scale synthesis is pursued. This strategy has the potential to unearth an abundance of useful materials in a single experiment. Materials scientists are increasingly taking advantage of

the efficiency of combinatorial synthesis and extending it to accelerate the discovery of complex compounds in a variety of areas.

In our group, we have developed several new combinatorial thin film deposition chambers. They include versatile pulsed-laser deposition systems with a modular combinatorial flange, a multi-gun ultra-high vacuum sputtering system, and a 12-source dual-gun electron beam evaporating system with the modular combinatorial flange.

natural composition spread   discrete library   composition spread layer-by-layer
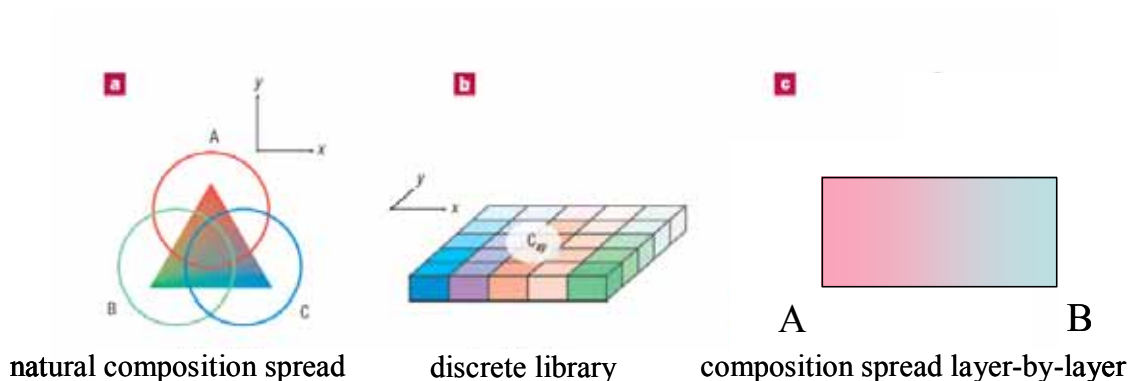
Figure 2-3: A schematic of three basic library designs used in our group. (a) Natural composition spread technique. Varying combinations of three different elements (A, B and C) are obtained at different positions on a wafer by co-deposition. The circles represent the general area under which each target material is deposited. (b) A discrete library. Each site has a different composition and can be addressed as C_{xy}. (c) Binary composition spread. The composition across the chip continuously changes from A to B.

We utilize several different kinds of library designs. Figure 2-3 (a) shows the natural composition spread typically made by co-deposition of 3 different elements (A, B, and C). The degree of intermixing of elements can vary depending on the deposition condition. This technique can be used to map different parts of ternary phase diagrams. This type of library design was employed for the search of new compositions of

ferromagnetic shape memory alloys (FSMA) and thermoelastic shape memory alloys [7], which are the main experiments discussed in this thesis. The discrete library is shown in Figure 2-2 and Figure 2-3 (b). Here, each site on the chip can have very different composition from its neighbors. Each site is spatially separated from other sites and can be addressed as C_{xy}. Each chip can contain up to thousands of different compositions. This type of library design has been used to investigate gas sensor materials [17]. The last type of combinatorial sample shown in Figure 2-3 (c), is the binary composition spread, where the composition across the chip continuously varies from pure A at one end of the chip to pure B at the other. This spread is typically fabricated using a layer-by-layer wedge deposition, which allows one to control the intermixing of the two materials A and B down at the nanometer level. Binary phase diagrams can be mapped on individual chips using this technique. This type of composition spread library has been used for the search of magnetoelectric materials.

Mapping compositional phase diagrams is of paramount importance in materials physics. For instance, establishing the doping phase diagram in cuprate superconductors and perovskite manganites has played a critical role in advancing the understanding of their physical properties [2, 18]. The continuous composition spread techniques (Figure 2-3 (a) and (c)) have proven to be a powerful means to quickly map previously unexplored regions of materials phase-space [7, 19, 20]. Such experiments can be used to elucidate the physics of various phenomena. In this thesis, I will show examples of experiments where we have used the composition spread techniques to get an insight into the relationship between magnetism and martensitic phase transformation in ferromagnetic shape memory alloys. We have also used it to investigate the relationship

10

between the lattice parameters and the martensitic transformation in thermoelastic shape memory alloys.

In combinatorial experimentation, the biggest challenges often lie in implementing an effective tool for rapid characterization. To facilitate high-throughput screening of combinatorial libraries and composition spreads for identifying compositional regions with enhanced physical properties, parallel detection schemes and non-destructive scanning probe microscopes are used. In our group, we have taken advantage of a number of recently invented scanning probe microscopes that are ideal for screening the combinatorial libraries and characterizing their electric and magnetic properties. They include the scanning superconducting quantum interference device (SQUID) microscope, and the scanning microwave microscope.

2.2 Combinatorial thin film library fabrication by magnetron co-sputtering deposition

There are two major methods to create large compositional variation in combinatorial libraries and composition spreads. They are (1) solution-based synthesis [21] and (2) solid-state thin films [22]. The basic premise of library fabrication is that compositional variation is achieved across a library through spatially selective materials deposition and synthesis. We have used magnetron co-sputtering deposition to make composition spread thin films. In this section, I discuss the basics of the sputtering process and then I will go on to discuss the application of sputtering for generation of composition spread thin films.

2.2.1 Fundamentals of sputter deposition

Bunsen and Grove were the first to observe sputtering in a gas discharge tube about 150 years ago. The cathode electrode material of the tube had been disintegrated by the discharge. The disintegration of the cathode material was caused by irradiation of the cathode surface by highly energetic ions. The removed particles were highly energetic atoms, called sputtered species, with energies ranging from 1 to 10 eV. This energy was higher than those of other deposition processes such as thermal evaporation and chemical decomposition. Despite the reaction of high energy ions, the sputtering process can achieve a deposition of a variety of materials without heating the source materials. This is a big advantage of the process.

Sputtering deposition is unique compared to other deposition processes in that it is a quenched or high–energy process. Thin films deposited by other processes such as thermal evaporation and chemical vapor deposition are formed under thermodynamically equilibrium conditions. In sputtering, highly energetic sputtered species are quenched on the surface of the substrate. Another advantage inherent in the sputtering process is the fact that the energetic sputtered particles lower the synthesis temperature of materials.

Sputtering has become a common manufacturing process for a variety of industries. In the semiconductor industry, it is used in the metallization process for the production of almost every integrated circuit. It is also used for exploratory research in the laboratory. Sputtering deposition is also present in many other niche areas. For example, it is used in the coating of mirror-like windows and reflective layers in many tall buildings [23]. The sputtering process is used to create narrow magnetic gap for videotape recording systems and for computer disk applications. Its precise, atomic scale achievability and controlled deposition is used in the development of multilayered heterostructured metal alloy systems including giant magnetoresistance (GMR) structures. It has also been used to achieve low-temperature synthesis of high-temperature materials such as SiC for commercial production to overcome issues of producing thermistors with high-accuracy [24]. Fabrication of high-efficiency thin film amorphous silicon solar cells benefits from the sputtering technology: it consumes much less energy than it takes to produce single crystal bulk Si solar cells [25].

The simple sputtering deposition process for materials production actually has a low level of efficiency. That is because the random bombardment of the sputtered target material by highly energized particles alone is inherently not very efficient because of

13

loss of momentum due to random collisions between the bombarding particles amongst themselves. Therefore, the sputtering process must be optimized for each material.

When a solid surface is bombarded with energetic particles such as accelerated ions, surface atoms of the solid surface are scattered backwards due to collisions between the surface atoms and the energetic particles as illustrated in Figure 2-4. This phenomenon is known as *back-sputtering* or simply *sputtering*. Figure 2-4(a) shows the overall process. The incident atom or ion generated by the discharge of the sputtering gas is highly energized and accelerated towards the surface of the target material (Figure 2-4(b)). Upon colliding with the target materials surface atoms, the ion or gas atoms impart their energy to the target material atoms which are scattered backwards towards the substrate (Figure 2-4(c)).
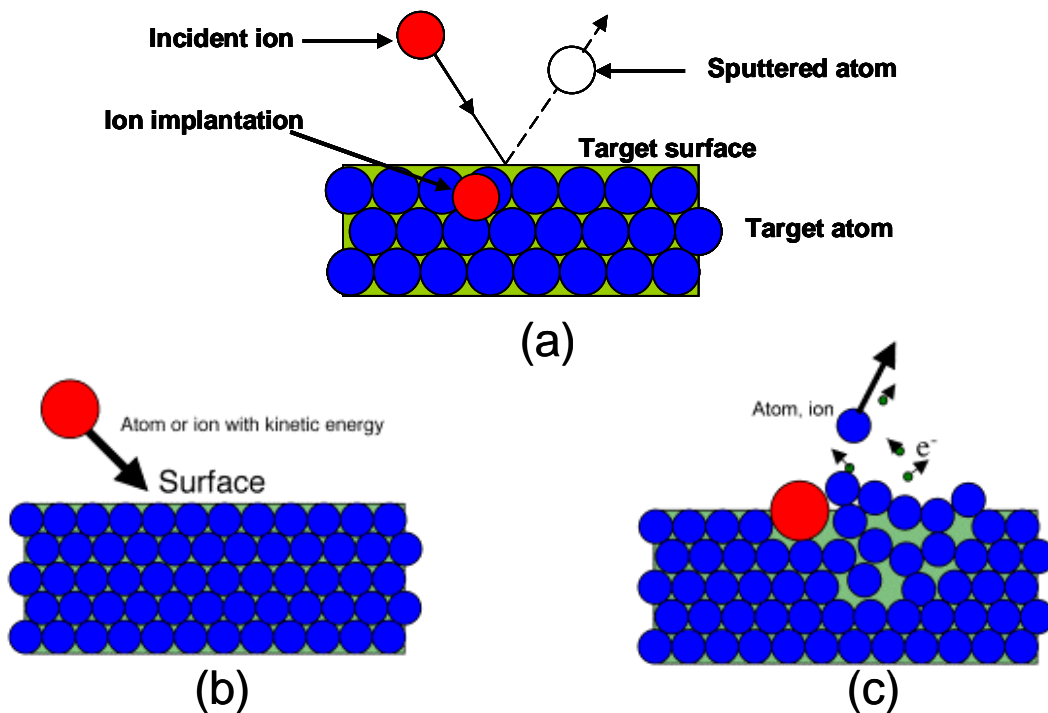
Figure 2-4: Physical sputtering processes. (a) and (b) Incident ion or atom from Ar gas is accelerated towards the target material surface and collides with surface atoms of the target embedding itself in the target material and (c) back scatters the target atoms towards the substrate.

In the case where a thin foil is bombarded with energetic particles, some of the scattered atoms transmit through the thin foil it self. This phenomenon is called *transmission* sputtering. The word "*spluttering*" is synonymous with "sputtering." *Cathode sputtering*, *cathode disintegration*, and *impact evaporation* are also used in the same sense. Several different types of sputtering systems are used for thin film deposition. They include direct-current (dc) diode, radiofrequency (rf) diode, magnetron, and ion-beam sputtering. McClanahan and Laegreid present an historical review of sputtering deposition [26]. Figure 2-5 shows the basic designs of dc and rf sputtering techniques.
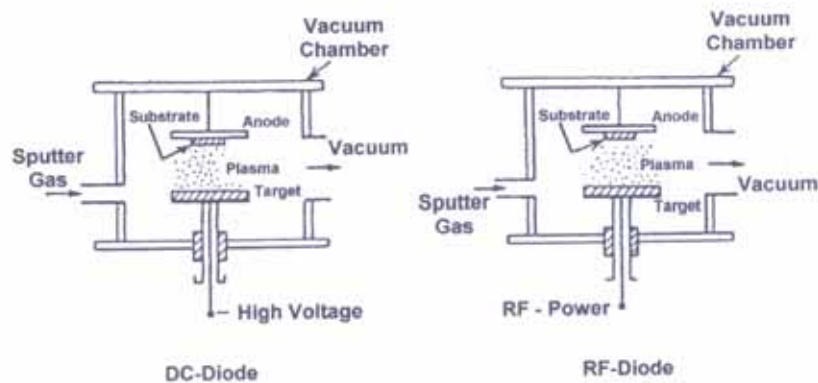
Figure 2-5: Basic design of sputtering deposition systems [23]

The simplest of the sputtering systems is the dc diode model. The dc sputtering system has a pair of planar electrodes. One of the electrodes is a cold cathode and the other is the anode. The planar surface of the cathode is covered with the source materials (or target material) to be deposited as a thin film on a substrate. The substrate is place on

the opposing surface of the anode. The sputtering chamber is then filled with a sputtering gas, typically high purity argon gas at a pressure of 5 Pa (4 x 10^{-2} torr). A glow discharge region is created and maintained by the application of a dc voltage between the two electrodes. Ar^+ ions generated in the glow discharge are accelerated towards the cathode electrode and sputter the source or target material onto the substrate on the anode, resulting in the deposition of thin films on the substrate. In dc sputtering systems the target materials must be composed of metal or conducting material since the glow discharge must be maintained between the metallic electrodes. If an insulating target material is to be sputtered in the dc sputtering system, the sputtering discharge glow cannot be sustained because of the immediate build up of surface charge of positive ions on the surface of the insulating target material. In order to sustain the glow discharge and sputter an insulating target material, an rf voltage must be supplied instead of a dc voltage. In the rf-sputtering system, thin films of insulating target materials can be sputtered directly from insulating targets.

A magnetron sputtering system superimposes a magnetic field on the cathode and glow discharge, which is parallel to the cathode surface. The electrons (Figure 2-6) in the glow discharge follow a cycloidal motion, and the center of the orbit drifts in the direction of **E x B** with a drift velocity of E/B, where **E** and **B** denote the electric field in the discharge and the superposed transverse magnetic field, respectively.
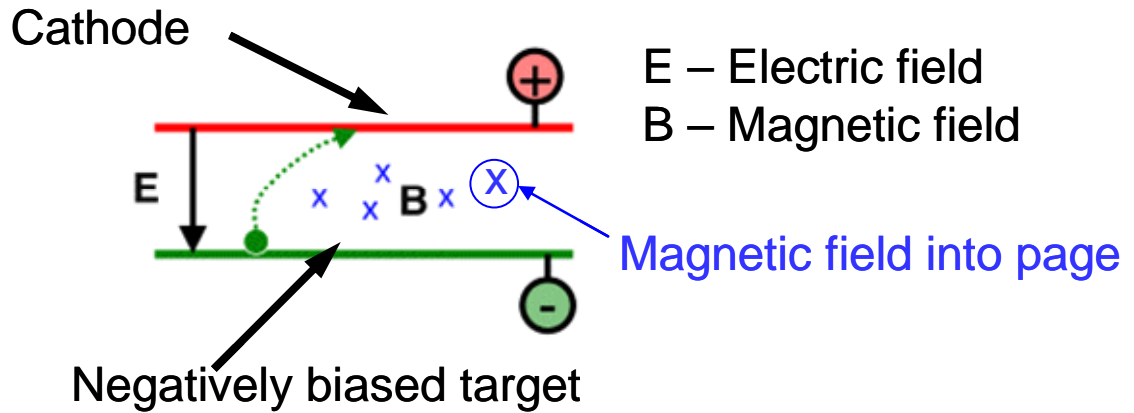
Figure 2-6: Schematic of electron drift in glow discharge in dc magnetron sputtering.

The drift paths for electrons form a closed loop due to the magnetic field. This entrapping of electrons increases the collision rate between the electrons and gas molecules. This allows the sputtering pressure to be as low as 10^{-5} torr. However, a typical sputtering pressure falls in the 10^{-2} to 10^{-3} torr range. The magnetic field simply increases the density of the plasma which in turn leads to the increase in the current density at the target material (cathode), which increases the sputtering rate of the target material on to the substrate. In addition, due to the low operating pressure of the system, the sputtered particles can travel through the discharge region without collisions, which also contributes to the high deposition rate of the target material.

Currently, the planar magnetron system is indispensable in the fabrication of semiconductor devices in industry. Historically, the first known magnetron sputtering device was proposed by Penning in 1935 [27]. A planar magnetron sputtering system prototype was later built by Wasa in 1967 [28]. A practical planar magnetron system was not built until 1974 by Chapin. Typical constructions of basic magnetron sputtering systems are shown in Figure 2-7.
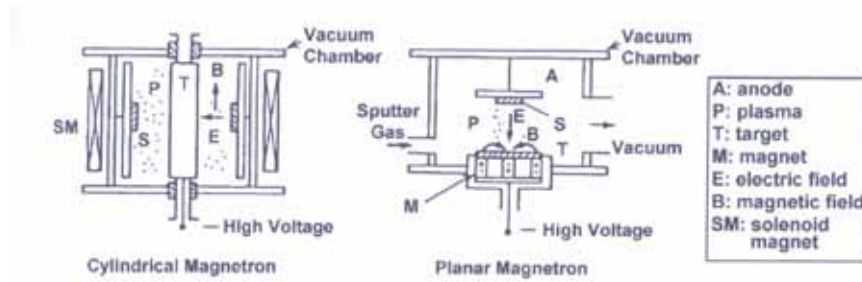
Figure 2-7: Basic design of magnetron sputtering deposition systems [24]

For the projects described in this thesis, we have chosen the magnetron sputtering deposition process. We have made thin films of ferromagnetic shape-memory alloys and thermoelastic shape memory alloys which consist of metal atoms. The increased deposition rate of magnetron sputtering makes it an ideal deposition technique for metal alloy films. The next section will discuss the combinatorial magnetron co-sputtering deposition system we designed and built for investigation of variety of metallic alloy systems.

2.2.2 Combinatorial magnetron sputtering deposition system

One of the challenges facing the combinatorial thin film synthesis is the lack of availability of ready made, off-the-shelf combinatorial thin film deposition systems and characterization tools. Often we are faced with adapting commercially available tools or designing and building new tools for this purpose. In this section, I will describe the features of the ultra-high vacuum (UHV) combinatorial magnetron co-sputtering deposition system we designed and built to synthesize natural composition spreads of ternary metallic alloy thin films. A picture of the deposition system is shown in Figure

2-8. I will highlight the features that distinguish this combinatorial co-sputtering deposition system from a commercially available co-sputtering system.

The combinatorial UHV magnetron co-sputtering deposition system is used to create composition spreads on 3-inch silicon wafers, created by natural mixing due to co-deposition. The system has a base pressure in the range of 10^{-9} torr. Depositions are typically performed at Ar pressures of 10^{-2} torr. The system consists of three 1.5-inch-diameter magnetron guns, placed parallel and adjacent to each other in a triangular configuration, Figure 2-9. Typical dc and rf power supplies range from 20 to 150 Watts for the magnetron guns. Each gun is housed in a 2-inch-long chimney, which helps to minimize the cross-contamination of the guns. Three different 1.5 in diameter targets can be sputtered simultaneously in the deposition system, and both dc and rf sputtering power supplies can be used. The system is fitted with an adjustable height substrate heater which is used to adjust the distance between the substrate and the guns. This distance is typically in the range of 12.5 to 18 cm. The adjustability of this distance is used to control the size of the composition region on the ternary phase diagram to be mapped. The temperature of the heater can also be adjusted (25 - 900 ^{o}C) as a major parameter of the processing conditions. The deposition system has a cryopump on the main chamber. A load-lock chamber is used to introduce the samples into the main chamber which minimizes the pump-down time between experiments. The load-lock chamber has a turbo vacuum pump with a scroll pump as a backing pump. Research grade Argon (99.9995 purity) gas is used as the sputtering gas.
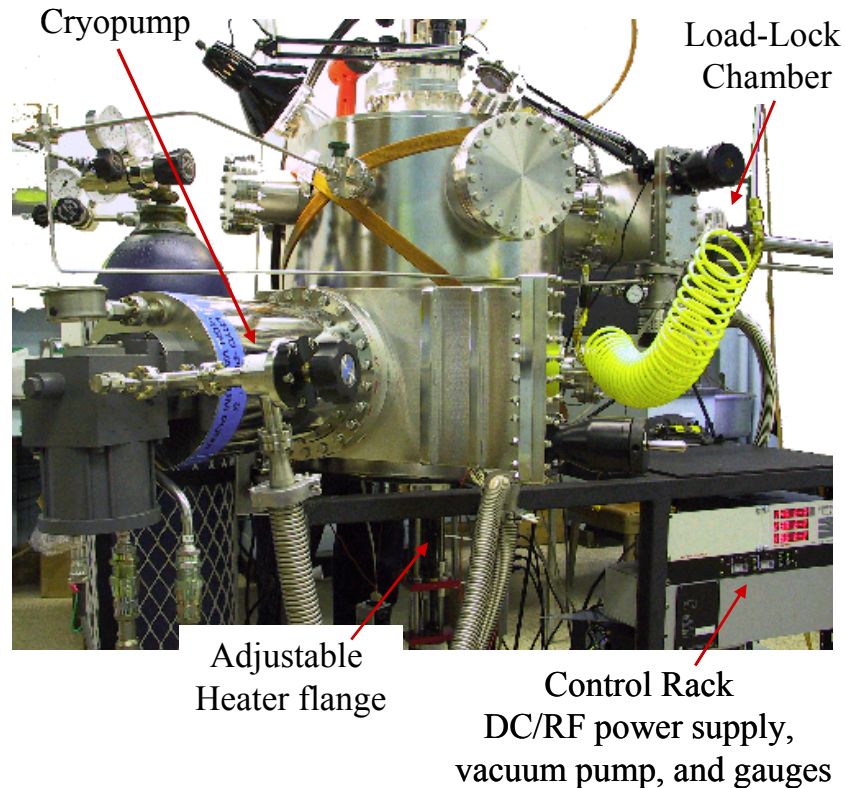
Figure 2-8: A picture of the UHV 3-gun co-sputtering thin film deposition system

A very distinctive feature in the design of our sputtering deposition system is the non-confocal parallel gun arrangement geometry. The typical multi-gun sputtering systems are confocal i.e. the guns are arranged to focus to a point so as to attain a uniform film thickness profile. A schematic deposition profile for co-sputtering materials A, B, and C using our non-confocal (i.e. guns are not focused to a point) gun arrangement is shown in Figure 2-9. A, B, and C are typically three different elemental metals. A natural overlapping deposition profile is created on the substrate, and as one moves away from directly beneath the center of each target, there is less material deposited, and a thickness gradient is formed from each sputtering gun. The region of overlapping target

materials results in a composition spread across the substrate. Co-sputtering guarantees intimate mixing of the 3 elements.
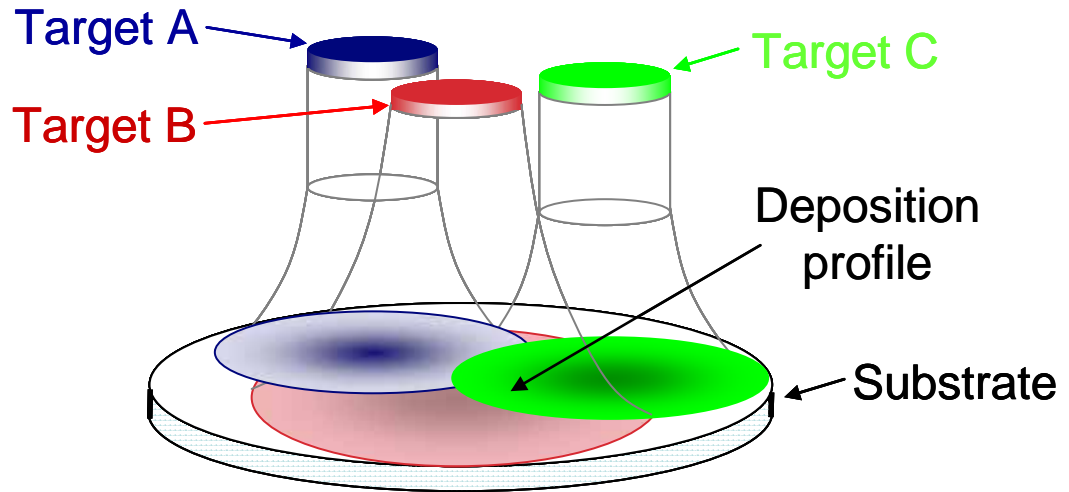
Figure 2-9: A schematic of the natural ternary deposition profile from the non-confocal gun geometry.

A typical deposition takes about 1.5 to 2 hrs to deposit films of ~ 0.5 μm in thickness. The argon sputtering gas pressure was maintained at 10^{-2} torr during the depositions by throttling the main valve to the cryopump. The reproducibility of the mapped composition region with nominally identical deposition conditions is very good in general, but there can be a small shift in mapped region from run to run. This can be attributed to slight variations in the power to the targets and the chamber pressure. For this reason, we directly measure the composition distribution of each spread using wavelength dispersion spectroscopy (WDS) in a scanning electron microscope. To facilitate indexing of mapped composition region on each wafer, we use a micro-machined silicon wafer grid as a physical mask to separate the continuous composition spread film into an array of 1.75 x 1.75 mm squares. The process for generating this

mask using the micromachining via wet etching is discussed in Appendix A. A typical 3-inch wafer has 535 or 635 squares depending on the spacing between squares. Figure 2-10, shows a typical composition spread wafer with 535 squares. The settings used for the WDS measurement are the thin film mode, with a current of 15 KeV, and the chamber pressure of 2 x 10^{-6} torr. A single WDS scan of the entire wafer mapping every square typically takes about 10 to 12 hrs.
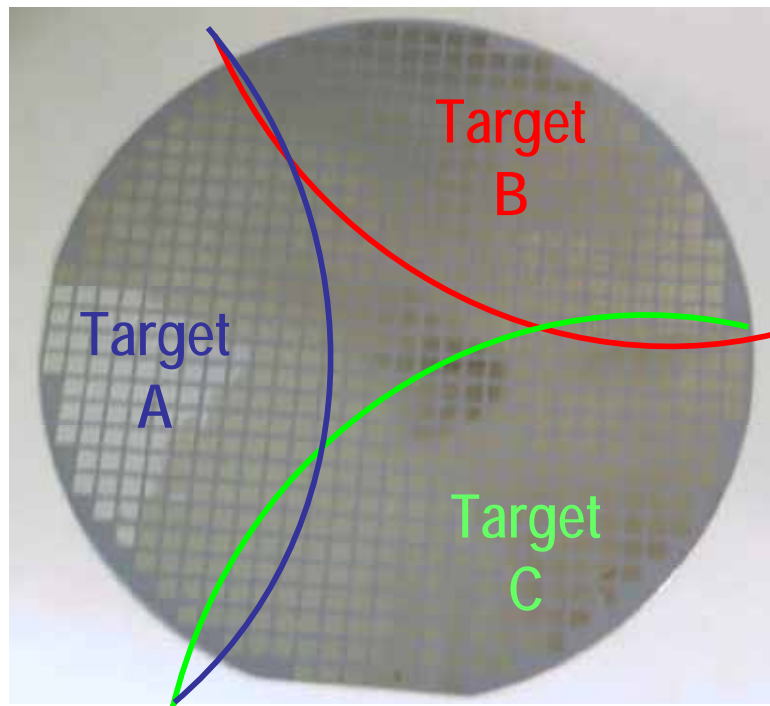
Figure 2-10: A picture of a composition spread wafer with 535 1.75 mm x 1.75 mm separated squares deposited using a micromachined silicon wafer grid mask. The colored lines roughly indicate the location of the targets over the wafer and the regions where respective material is deposited the most.

The parallel non-confocal gun arrangement in conjunction with the ability to adjust the distance between the guns and the substrate allows us to map nearly the entire ternary phase diagram consisting of elements A, B, and C. By decreasing the distance

between the guns and the substrate we can obtain a large composition variation in a single experiment. Increasing the distance between the guns and the substrate allows us to focus in on smaller range of composition regions of interest. This is illustrated in Figure 2-11.
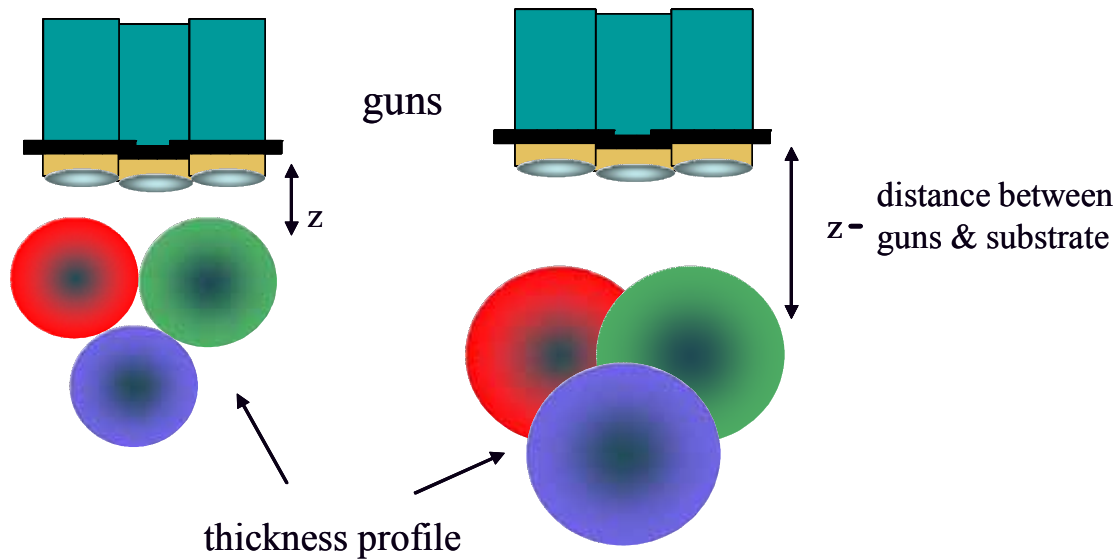
Figure 2-11: The nonconfocal configuration of the guns. The change in distance x varies the spread profile of the deposited materials.

The resulting phase diagrams are shown in Figure 2-12. The ability to cover different sized regions of a phase diagram is very useful in mapping phase diagrams and zooming into different regions of interest for focused investigation of composition-structure-property relationships.
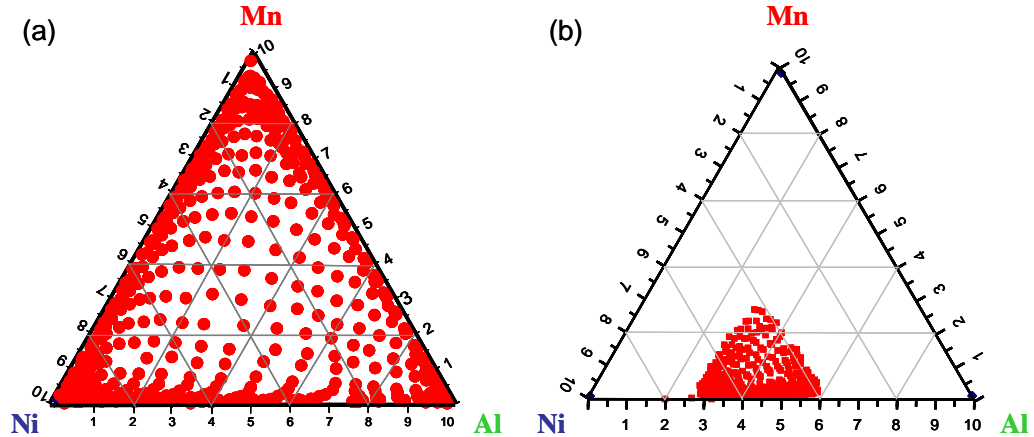
Figure 2-12: Different regions of a Ni-Mn-Al phase diagram are mapped by adjusting the distance between the sputtering targets and the substrate. (a) at short distance, and (b) at large distance. Each point on the phase diagram represents a composition created on a composition spread wafer. Each point is from a patterned square thin film region.

The composition spreads fabricated by the non-confocal parallel co-sputtering technique have the advantage of covering nearly the entire phase diagram in a single deposition as compared to other confocal three gun co-sputtering systems which cover very limited regions of the ternary phase diagram [29]. There is guaranteed intermixing of materials as they are being deposited. This in comparison to other methods such as the one where layer-by-layer wedge deposition of different materials is performed followed by an extensive heat treatment step in order to allow the materials to diffuse and mix [3,29]. However, there are some disadvantages to using this technique. They include, variations in thickness of the composition spread across the wafer and having to measure the composition of the composition spreads each time a sample is fabricated. As can be seen in Figure 2-11, distribution of composition on the spread wafer is not uniform.

Using co-deposition for generating thin film composition spreads is actually not a new idea. Pioneering work on making composition spreads was performed by Joseph J.

Hanak in the 1960's. Hanak adopted an existing rf cosputtering technique [30, 31] to synthesize binary and/or ternary solid alloy composition spreads. In one of his techniques, a single composite target is used instead of multiple, separately powered targets. Figure 2-13 shows schematic arrangements of the targets and substrates for co-sputtering composition spread films using composite targets for two- and three-component systems, respectively.
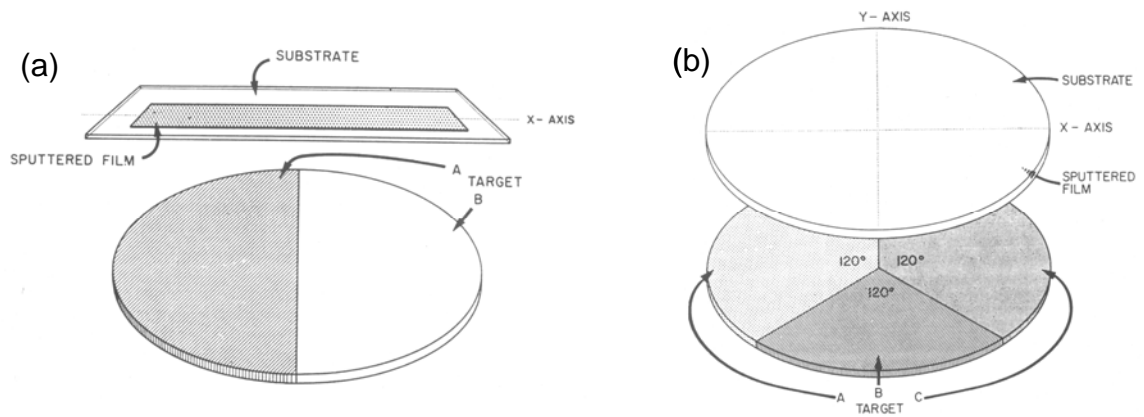
Figure 2-13: Schematic for cosputtering to create composition spreads (a) two- and (b) three-component systems using a composite target [32].

One drawback of this technique is that one needs to make the special composite targets. In addition, cross contamination and diffusion of the component materials during sputtering are of concern.

Hanak and his colleagues at RCA used the cosputtering techniques to systematically study a number of different materials such as cermets [33], granular and compound superconductors [31,32], electroluminescence materials [34], and photovoltaics [35,36]. One such early experiment was the systematic study of the

electrical and magnetic properties of a cosputtered Ni-Fe-SiO$_2$ cermet system as a function of composition, including resistivity, and permeability by Gittleman et al. [37]. In this experiment, the targets consisted of three disk segments of Ni, Fe, and SiO^2 placed on the disk target electrode. They found that the material (Ni$_{0.7}$Fe$_{0.3}$)$_{0.55}$(SiO$_2$)$_{0.45}$ (by volume) had a particularly prominent permeability peak of $\mu \approx 170$. A magnetic recording head was used to measure the permeability. The results from this experiment taken from Ref [37] are shown in Figure 2-14(a).
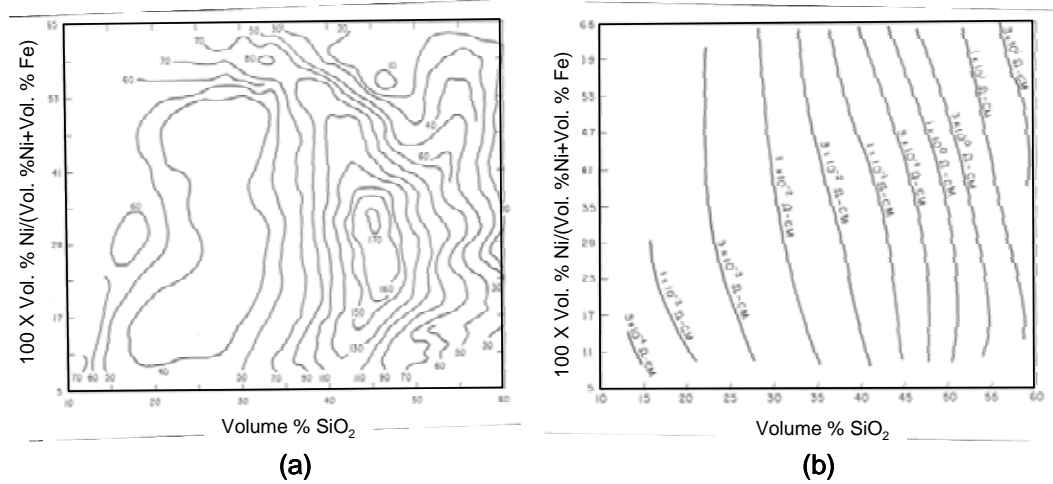
Figure 2-14: Contours of (a) initial permeability and (b) electrical resistivity as a function of composition for the ternary (Ni$_y$Fe$_{1-y}$)$_{1-x}$(SiO$_2$)$_x$ system studied by a composition spread [37].

A rather high electrical resistivity of 10^{-1} ohm-cm, shown in Figure 2-14(b), was observed at this composition. The goal of this experiment was to find cermets for an improved intensity-correction filter cathode ray tube (CRT).

Continuous composition spreads have also been achieved by using a three-gun system with an off-axis configuration. Figure 2-15 is a schematic of a three gun system

that was used to deposit oxides by van Dover et al [38]. In this system, the guns are oriented 90° to the normal of the substrate.
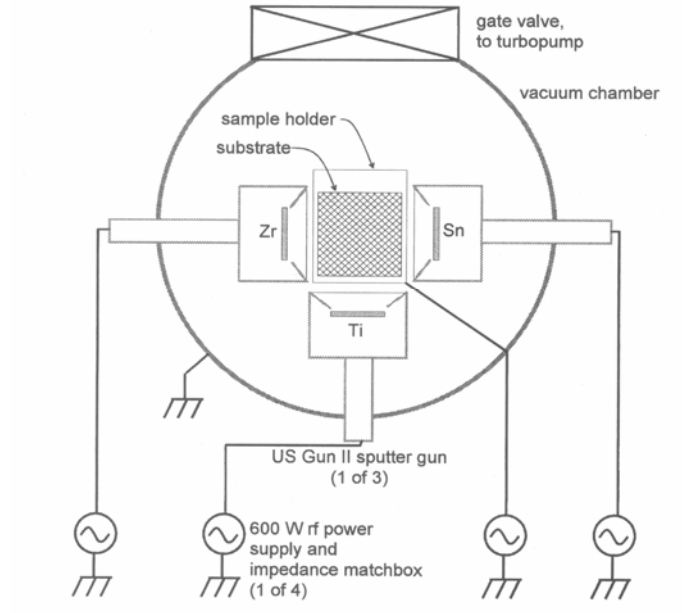
Figure 2-15: Schematic of a 90° off-axis three-gun deposition system [38].

van Dover et al used the off-axis three-gun deposition system to deposit composition spread films of amorphous dielectric materials in search of materials that combined both a high dielectric constant and a high breakdown field for an application in embedded dynamic random-access memory devices (DRAM). They found that the Zr-Ti-Sn oxide system was particularly promising. Figure 2-16 shows the experimentally obtained raw capacitance and breakdown voltages, displayed as a function of position on the substrate where the ternary composition spread was deposited.
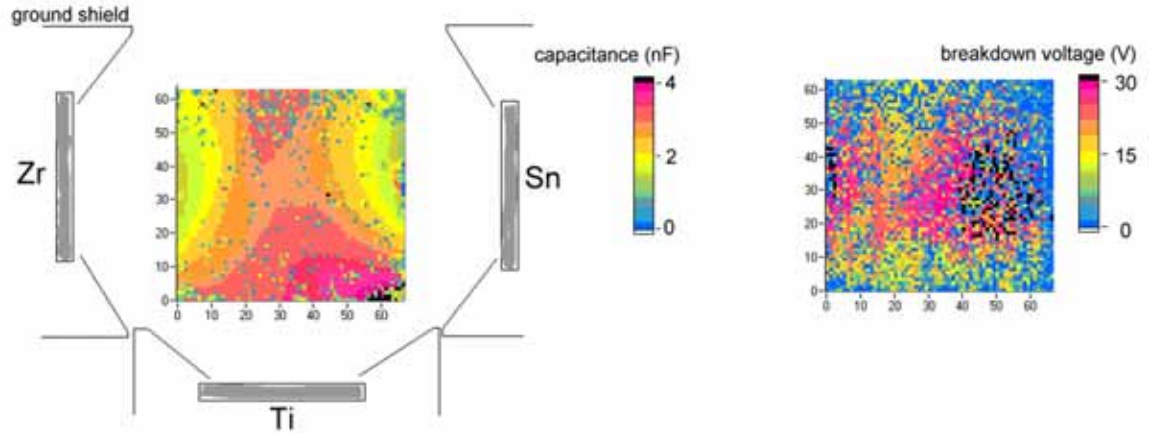
Figure 2-16: Raw capacitance and breakdown voltage for Zr-Sn-Ti-O film, plotted as a function of position on a rectangular substrate. The position of the sputter guns during deposition is shown schematically with respect to the capacitance data. The vertical and horizintal scales are in millimeters. [38]
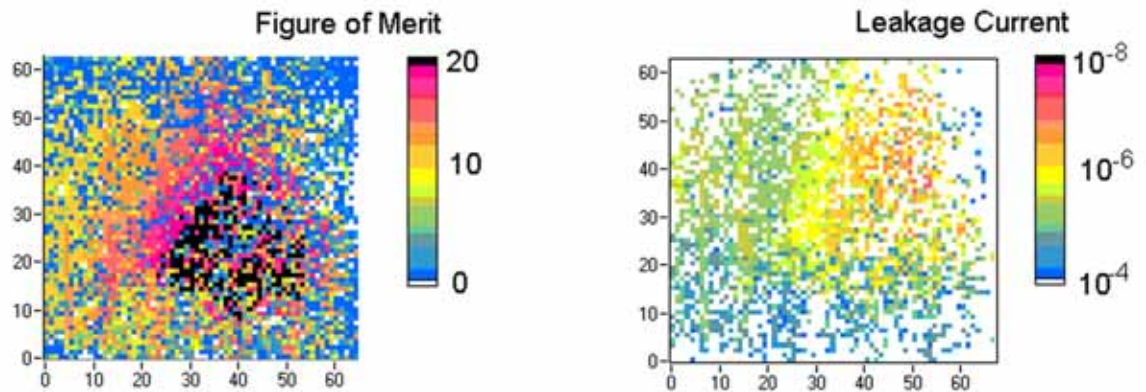
Figure 2-17: Figure of merit (defined as FOM= $\varepsilon_r\varepsilon_o E_{br} = CV_{br}/A$, measured in $\mu C/cm^2$) and leakage currents (measured at a stored charge of 7 $\mu C/cm^2$, current density measured in amps/m^2) as a function of position on substrate, for the same sample as in Figure 2-14 [38]. C, ε_r, ε_o, E_{br}, V_{br}, and A are capacitance, relative permittivity of the material, permittivity of free space, breakdown field, breakdown voltage, and area of the test capacitor, respectively.

The capacitance, C and breakdown voltage, V_{br} were multiplied point by point to obtain

the figure of merit (FOM), and the leakage current at a fixed stored charge, Q, was

evaluated from I-V curve data and plotted on a logarithmic scale (Figure 2-17).

28

Combining the information about the composition distribution on the film and the corresponding FOM and leakage current, they mapped this information onto a ternary phase diagram, as shown in Figure 2-17.
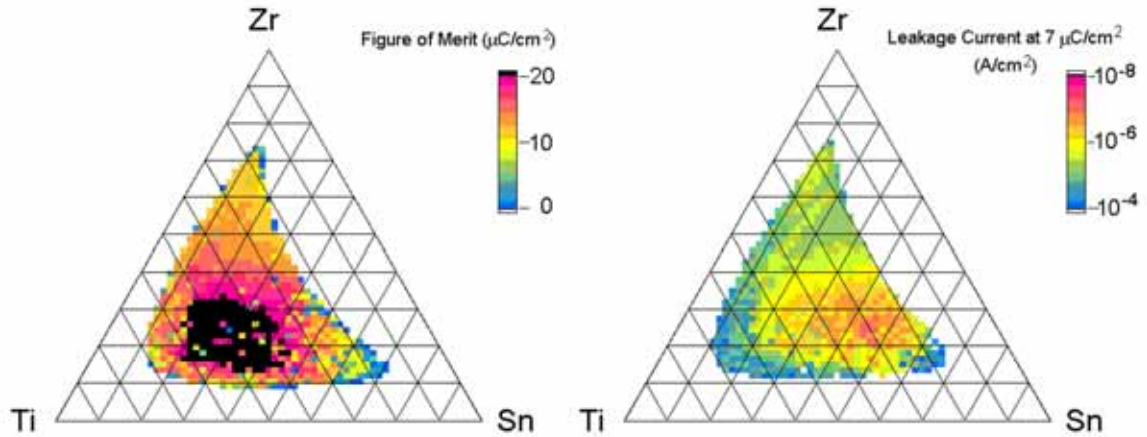
Figure 2-18: Figure of merit and leakage current data from Figure 2-17, mapped on ternary composition phase diagrams [42].

It is interesting to note that prior to this study, crystalline $Zr_{1-x}Sn_xTiO_4$ [39, 40] was known to display good dielectric properties, including its near-zero temperature coefficient of the dielectric constant. However, van Dover et al found that in their Zr-Ti-Sn-O films, neither the high-FOM region nor the low-leakage region corresponded to the composition area occupied by the crystalline dielectric. With a modest amount of optimization, dielectric films with FOM of 25 $\mu C/cm^2$ were obtained which is higher than that of SiO_2 (FOM typically 3.5) which is currently being used in DRAMs.

29

2.3   Screening of combinatorial samples

After the combinatorial composition spreads are made, properties of the thin film materials on the composition spread need to be rapidly and accurately measured. In any type of combinatorial investigation, having the appropriate characterization tool is critical. Without a suitable high-speed screening technique, high throughput synthesis serves little purpose. In advanced functional materials, the required performance can be very application-specific. This often translates into having to design, develop and tailor screening techniques that are specialized for individual applications. For instance, capacitor dielectrics in memory devices and tunable microwave devices using the same class of ferroelectric materials have entirely different sets of performance requirements, necessitating two different screening techniques.

The diverse spectrum of functionalities in materials (ranging from optical nonlinearity to piezoelectricity and magnetoresistance) represents a tremendous challenge in high-throughput screening, often requiring new measurement instruments to be developed. This is in contrast to combinatorial chemistry in life sciences, where the luminescent tagging technique is applicable in a wide range of studies. In many ways, the availability of characterization tools defines the scope of one's combinatorial materials research.

Scanning probe microscopes are often used for rapid characterization of thin film materials. The ability of the scanning probe microscopes to provide non-destructive, spatially resolved mapping makes them the ideal screening tools for a variety of physical properties. For instance, scanning SQUID microscopes have proved essential for investigation of magnetic materials [7, 22]. Microwave microscopes were born out of the

30

need to carry out non-contact electrical impedance measurements, and they are used for quantitative mapping of dielectric or ferroelectric materials libraries as well as resistance or conductance in thin-film libraries and spreads [3, 4]. Rapid characterization of optical properties (luminescence, transmission and so on) is relatively straightforward because the necessary components for building the measurement setups are mostly commercially available. On the other hand, there are physical parameters that are more difficult to extract accurately from small volumes of thin-film samples on the composition spread, such as thermal conductivity and elastic constants.

Aside from scanning probe techniques, methods that allow screening or detection by visual inspection represent some of the most desirable and elegant embodiments of the combinatorial strategy. Investigation of luminescent materials has yielded some striking examples [5], where 'one look' can often convey all the information one initially needs about the distribution of emission profiles.

An important new direction in rapid characterization techniques is the incorporation of microelectromechanical systems (MEMS). Arrays of MEMS devices have a natural configuration that enables high-throughput evaluation of materials' performance. For example, arrays of micro-hotplates have been successfully used for developing libraries of inorganic films for gas sensors with individually addressable sensor elements [41, 42]. We have demonstrated the utility of arrays of micromachined silicon cantilevers to fabricate 'self-reporting' libraries allowing rapid identification of martensitic transformation of shape-memory alloys by visual inspection [7]. This will be described in Chapter 3 of this thesis.

Obtaining accurate mapping of composition and phase distribution is essential for constructing the relationship between composition, structure and properties of materials. It is easy to overlook the importance of materials diagnostics in this field. Even when the composition distribution is clearly laid out in the design of a composition spread, the original compositional variation may shift or change during the processing, depending on the synthesis procedure of samples. Thus, it is important to determine the composition distribution of libraries and composition spreads using techniques such as wavelength dispersive spectroscopy (WDS).

For the experiments described in this thesis, the relevant properties to be mapped include the deposited thin film thickness, composition at each point on the substrate, and the corresponding magnetic and structural properties at each point. We used a Dektak II profilometer to measure the thickness of our thin films across the wafer. (This was not measured in a high throughput way.) We used WDS to obtain compositions at each point on the composition spread and used the data to map the points on ternary phase diagrams. For the magnetic property measurements, a room temperature scanning superconducting quantum interference device (SQUID) microscope was used to measure the magnetic field emanating from the samples. We performed quantitative calculation of magnetization of materials from these data for composition spreads of ferromagnetic shape memory alloys. For general microstructure and phase determination, we performed structural analysis of each discrete composition spread using a scanning x-ray microdiffractometer. For detailed phase characterization of shape-memory alloys we used x-ray microdiffraction at a synchrotron source. This is described in Chapter 3. In order to rapidly characterize the shape-memory properties of the thin films on

composition spread, we successfully designed and developed a rapid visual inspection technique to quantitatively detect reversible martensitic transformations using micromachined arrays of cantilevers.

We have also investigated the use of other rapid characterization techniques for the quantitative mapping of the phase transition behavior and mechanical properties of the films in a number of different alloy libraries. These techniques include the use of four point probe resistance measurements to quantitatively determine the martensitic and austenitic transition temperatures and the use of nanoindentation to measure the mechanical properties of the films such as hardness and modulus. I will describe how we use these techniques to analyze the properties of interest in details in this thesis.

Chapter 3

Combinatorial Investigation of Ferromagnetic Shape Memory Alloys

This chapter will discuss the combinatorial investigation of ferromagnetic shape memory alloys (FSMA). The chapter will provide a brief introduction to FSMAs and their applications. I will then discuss the high-throughput synthesis and characterization techniques that we used to investigate these alloys with focus on a particular system, Ni-Mn-Ga. We have mapped ternary compositional phase diagram of the Ni-Mn-Ga system. I will discuss the results of this investigation, where we extended the known FSMA regions to previously unexplored regions and explored the physics of the phenomenon. Magnetic properties were mapped by applying the inversion technique on the magnetic field data of the entire composition spread, obtained from the scanning SQUID microscope. The shape-memory property was qualitatively measured by a high throughput method that we have developed especially for combinatorial investigation.

3.1   Introduction to FSMA

Smart materials are a class of materials that function as both sensors and actuators [1]. They respond to external fields, such as stress, electric and magnetic fields and display field induced strain. Piezoelectric materials, magnetostrictive materials and shape memory alloys (SMA) are examples of smart materials. When stress is applied to a piezoelectric material, there is a change in the electric polarization, and a voltage is induced. When the electric field is applied to a piezoelectric material, there is a change in polarization and strain is induced. Magnetostrictive materials behave similarly to the piezoelectric, except it is the magnetic field that induces strain. Shape memory alloys (SMA) are sensitive to temperature and stress instead of electric or magnetic field. Changes in temperature and stress will induce strain or volume change in shape memory alloys.

Ferromagnetic shape memory alloys (FSMAs) have two properties that coexist together which distinguish them from other smart materials. They are ferromagnetism and shape memory alloys. FSMAs are ferromagnetic materials that undergo reversible martensitic transformation. A strong magnetoelastic coupling in FSMAs results in enormous magnetic field induced strain. Strains as large as 9.5 % have been reported for applied field of less than 1T [2].

Figure 3-1 shows the history of discovery of magnetostrictive materials. One can see that recently discovered FSMA have magnetic field induced strains two orders of magnitude higher than the giant magnetostrictive material, terfenol.

35
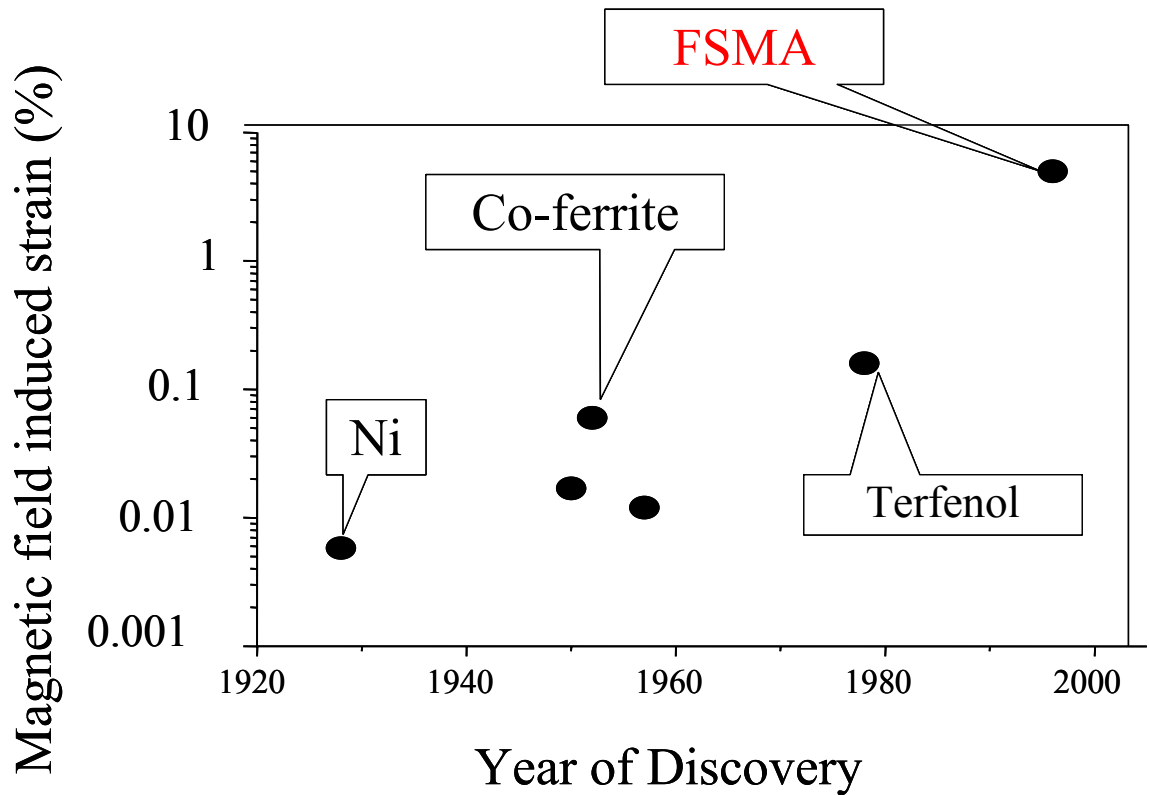
Figure 3-1: History of discovery of magnetostrictive materials.

In the next section, I briefly discuss the mechanism of field induced strain in FSMAs. We used the combinatorial method to explore FSMAs in order to find new compositions of FSMAs and understand their composition-property relationship in the ternary phase diagram.

3.1.1 Mechanism of shape memory and FSM effects

In order to begin the discussion of how FSMAs function, we must first introduce and discuss the SMA effect. The SMA effect is pictorially shown in Figure 3-2.
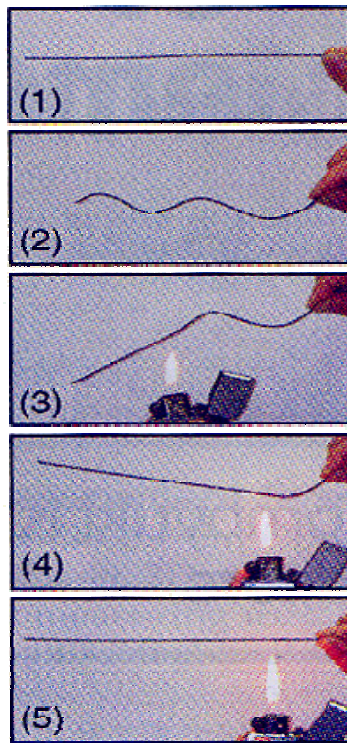
Figure 3-2 NiTi wire exhibiting the shape memory effect. [3]

Nitinol, NiTi, is a well-known SMA that has up to 8% induced strain when heated. Figure 3-2 [3] shows the step-by-step change in the wire after it is bent. First a straight NiTi wire (1) is bent to a different shape (2). Then as it is heated (3, 4) it straightens out (5) "remembering its original shape" in (1).

To explain the mechanism of the shape memory effect, we must consider a change in the crystal structure of the material. An example is a transformation from a cubic structure (which is the parent, high temperature phase) to a tetragonal, low temperature phase. Figure 3-3 illustrates the transformation and its effect. For clarity, we must first define the two phases (Figure 3-3 (a)). The first phase is a cubic phase that
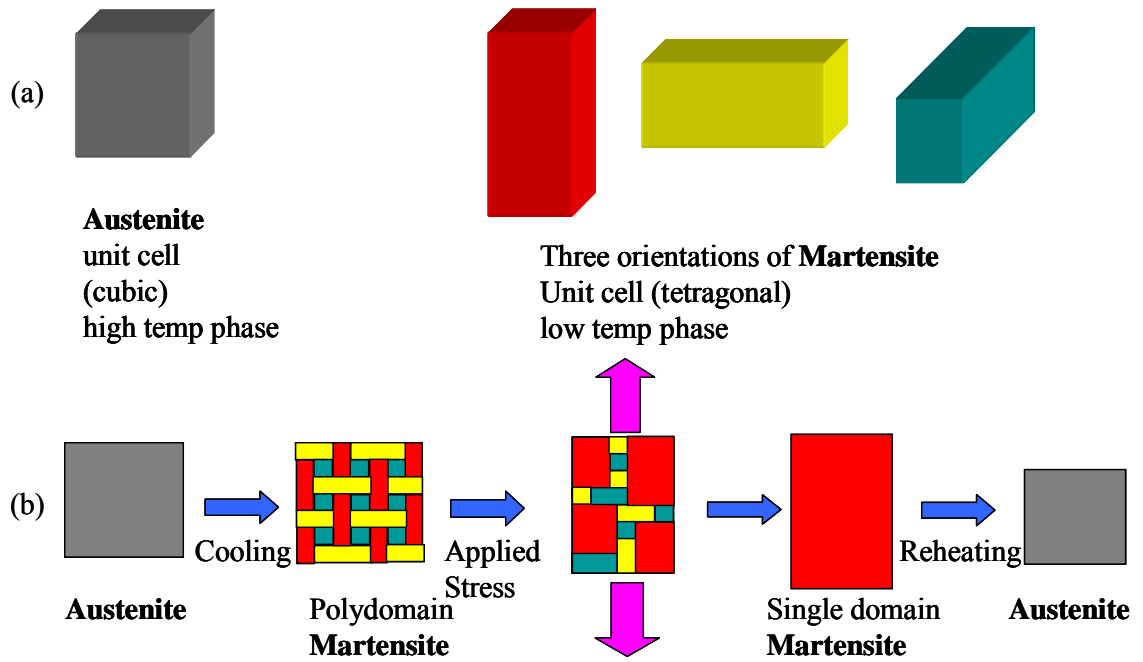
Figure 3-3: An example of a transformation of a cubic structure to a tetragonal case: (a) structure of high temperature and low temperature phases, (b) shape memory effect involving the structural transition.

is called an austenite. It is the high temperature and high symmetry phase. The second phase is a tetragonal phase and is called a martensite. It is the low temperature and lower symmetry phase and has three orientations or variants (domains) relative to the austenite phase, as shown in Figure 3-3 (a).

Several transition temperatures are associated with this phase transformation. When an austenite is cooled to the temperature M_s, the martensitic phase starts to form. It then continues to form until the temperature reaches M_f or the martensite-finish temperature. In the martensitic phase, three different orientations are possible, shown as red, yellow and blue in the figure. The two neighboring variants are twin-related to each other and may contribute to deformation if the interface is mobile under stress. Thus, when stress is applied to the polydomain martensite (Figure 3-3 (b)), deformation

38

proceeds by twin boundary movement, and a single-domain martensite is formed. When this single-variant martensite is heated, an austenite phase starts to form at the temperature A_s. The transition is completed at the temperature A_f. Above A_f, the martensite variants have all transformed back to the single parent (cubic) phase. This transformation is crystallographically reversible.

Now, let us look back at Figure 3-2, which shows the SMA effect in a NiTi wire. The wire is straight in the initial martensite phase (Figure 3-2 (1)). It was made straight at temperature above A_f in the austenite phase. The wire is then deformed in the martensitic state (see Figure 3-2 (2)). Room temperature is below M_f. Then as the wire is heated, it reverts back to its original shape as shown in Figure 3-2 (3-5) at a temperature above A_f.

We can now look at the mechanism of magnetic field induced strain in FSMAs. The difference between FSMAs and SMAs is that in FSMAs, ferromagnetism is coupled to the SMA effect. Figure 3-4 shows a similar schematic as in Figure 3-3 (b) for the transformation of a cubic phase to a tetragonal phase. The key here is that the magnetic domains are coincident with the martensitic variants. Thus, instead of using an applied stress to deform the martensites, a magnetic field, B, can be used to drive the twin boundary motion. The FSMA is an SMA and thus goes through the same reversible crystallographic transformation as discussed above in the shape memory alloy.
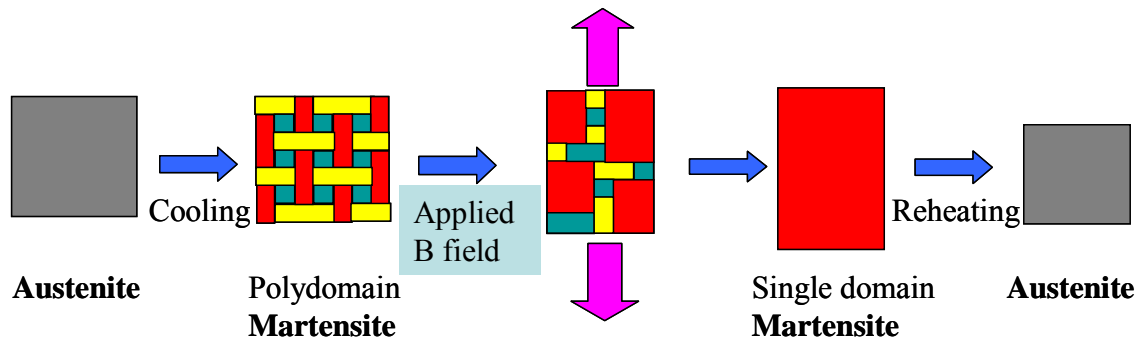
Figure 3-4: Schematic of FSMA effect for a transformation of cubic structure to tetragonal

An ideal FSMA possesses both a high room-temperature magnetization, which results in high magnetostatic energy (so that it is not necessary to apply a large B field to rotate the domain and induce strain) and a high martensitic transition temperature so that the martensite material is stable at room temperature.

3.1.2 Applications of SMA and FSMA materials

SMAs are commonly used already. The first successful application of SMAs was made by Raychem Corp. for fasteners and tube couplings [4]. These couplings are also used for the hydraulic systems of jet fighters. SMAs are used in heat engines, where thermal energy is converted to mechanical work. This is an example of environmentally-oriented applications. Various thermal actuators and thermostatic mixing valves [5] also use SMAs. Furthermore, in biomedical fields, they are used as minimally invasive devices [6] and surgical anchors [7], since the temperature of the human body is enough to induce transformation and leads to actuation. FSMAs are not used in practical applications yet. But there has been significant progress in materials development in the FSMA field, and their application in sensors and actuators are being pursued by many

groups around the world [8]. In some applications, not only bulk FSMAs but also thin film FSMAs are important. Examples of FSMAs include MEMS actuators. In our group, we focused on the thin films of FSMAs. In the next sections, I describe how we fabricate and characterize our composition spreads of FMSA thin films.

3.2   Fabrication of FSMA thin film composition spreads

So far, I have given a general description of FSMAs, and their properties. From here on, I will primarily focus on the Ni-Mn-Ga ternary alloy system. We have started with this system because there is a well-known composition of Ni_2MnGa, which is an FSMA. Prior to our investigation, there were limited studies of other Ni-Mn-Ga compositions. Thus, the purpose of our study was two fold: 1) to see if there are other compositions which are FSMAs in this ternary system; 2) to map the composition-property (magnetic and martensitic) relationship in this system in order to better understand the co-occurrence of ferromagnetism, and the shape memory effect. We note that our phase-diagram mapping experiments are performed entirely with thin film samples. It is well known that thin films and bulk samples can in general exhibit different properties. In particular, thin film FSMAs can display significantly reduced strain because of the clamping effect of the substrate. On the other hand, there have also been reports that thin films of FSMAs show similar magnetic properties (such as saturation magnetization) as bulk samples [9]. It has also been reported that martensitic transitions in thin film FSMAs occurs at roughly the same temperature as the transition temperature range in bulk samples [10]. Thus, we believe it is justified to use thin film samples to obtain the correct trend in the composition-property relationship in general.

41

Composition spreads were deposited using the ultra-high-vacuum magnetron co-sputtering system discussed in Chapter 2. We have confirmed that, by adjusting the power applied to each gun and the distance between the guns and the substrate (typically 15.5 cm), a large region of the ternary phase diagram can be mapped out. The three targets used in this experiment were Ni, Mn and Ni_2Ga_3, and both DC and RF sputtering were used. The Ni_2Ga_3 target was used because Ga is liquid at room temperature, and the Ni_2Ga_3 was the target material available with the largest amount of Ga in a solid. This target was made by the arc-melting method at Ames National Laboratory.

We used 3-inch diameter, Boron (p-type) doped Silicon (Si) substrate wafers that were (100) oriented. Depending on the property of interest, either a micromachined cantilever array substrate or a micromachined physical shadow mask substrate is used to deposit the composition spread thin film as discussed in Chapter 2. One of the wafers deposited through the physical shadow mask is shown in Figure 3-5. The regions of directly under 3 sputtering guns are marked.

Two deposition conditions were used to deposit thin film libraries that produced similar results. In the first, we deposited the composition spread thin film of the ternary alloy at room temperature for roughly 1.5 hr followed by annealing the wafer in situ at 550 °C for 2 hours in vacuum. For the second condition, we directly deposited the thin film on a wafer heated to 500 °C for 1.5 hr and allowed the substrate to cool down to room temperature by natural convection on the substrate heater. The typical gun power was 50–100 watts, and the composition spread thin film thicknesses were in the range of 500 nm to 1 μm.

42
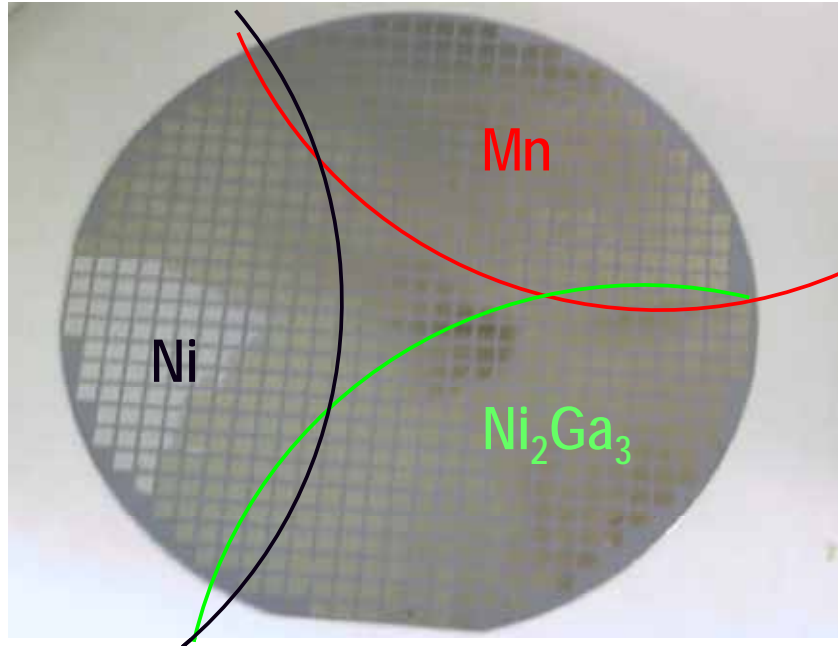
Figure 3-5 An example of FSMA composition spread made with three targets: Ni, Mn, Ni_2Ga_3 on a Si substrate of thickness 5000 Å, in situ deposited with a physical mask and annealed at a temp 500 ^{o}C. The colored lines roughly indicate the location of the targets over the wafer and the regions where respective material is deposited the most.

The films were fiber-textured with predominantly (110) orientation normal to the substrate (as revealed by x-ray diffraction). After fabricating the libraries, we characterized them for their ferromagnetic and SMA properties.

3.3 Characterization of FSMA composition spreads

The FSMA effect occurs in materials that are simultaneously ferromagnetic and reversible martensites, which make them shape-memory alloys. This defines our strategy for high-throughput screening: search for compositions that show both properties. First, we measure the composition of each square of our shadow mask patterned spreads. For ferromagnetic properties, we used the scanning SQUID microscope. For detecting reversible martensites, we made micromachined cantilever libraries. We used scanning x-ray diffraction to track the structure change as the composition changed in some regions of the spread. These characterization techniques are discussed in the next section.

3.3.1 Composition verification

To accurately map the exact composition distribution of the combinatorial samples, a scanning electron microprobe (JEOL 8900 R superprobe) was used for quantitative compositional analysis of samples using energy dispersive spectroscopy (EDS) and wavelength dispersive spectroscopy (WDS). We use the WDS analysis primarily to obtain the quantitative compositional value of each position of the spread on the substrate. WDS is a widely used microprobe technique for obtaining composition distribution information. The principle of this technique is that when an electron beam strikes the sample, x-rays emitted will have different wavelengths depending on the element present. By detecting characteristic wavelengths of different elements, quantitative identifications of elements can be performed. An illustration of the use of WDS to map regions of a ternary system is shown in Figure 3-6. Here, A, B, and C are

three elements. Each point on the composition spread A-B-C has a different atomic percentage of each element. The composition data for each point scanned by the probe is then converted to a position on a ternary A-B-C phase diagram. Phase diagram plots allow us to visualize the data for hundreds of compositions and their corresponding characteristic properties such as the values of magnetization and martensitic transformation temperature.

A-B-C composition spread

A-B-C ternary phase diagram
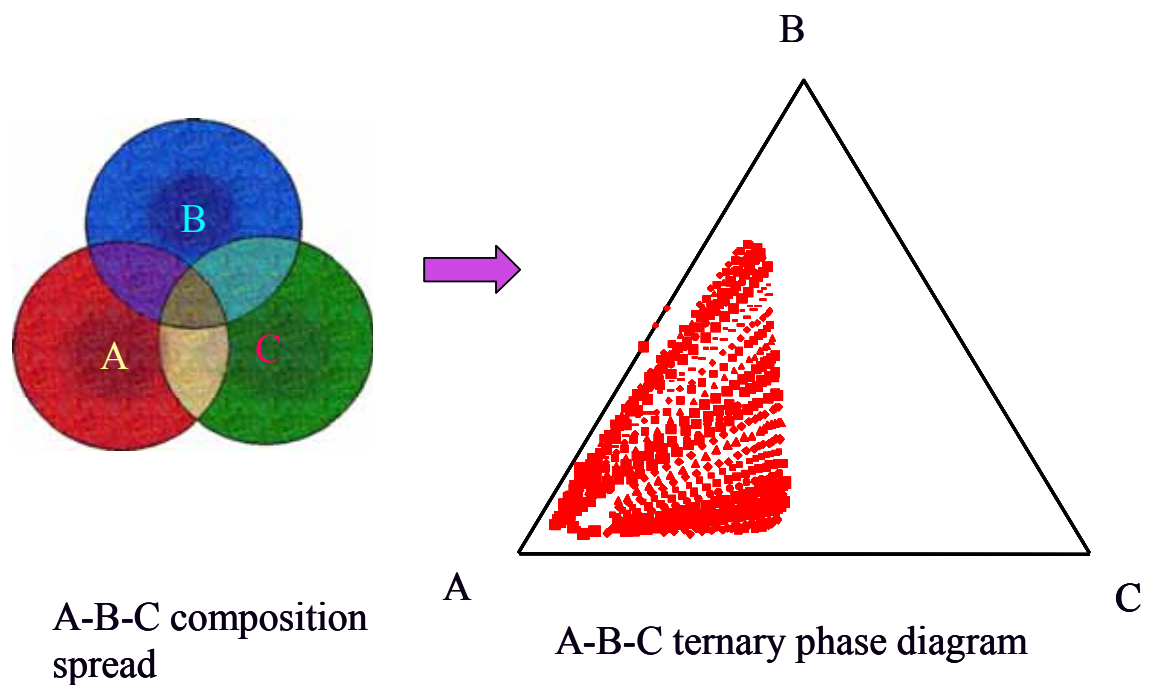
Figure 3-6: An illustration of how we convert compositions $A_xB_yC_z$ from a spread to compositions on a ternary A-B-C phase diagram using WDS.

3.3.2 Magnetic properties of FMSA spreads by scanning SQUID

For the rapid characterization of the magnetic properties, we used a room temperature scanning SQUID microscope, as mentioned in the previous chapter. After

the fabrication of the thin film composition spread, the sample is magnetized in-plane uniformly with a 1 T permanent magnet. We have found that our textured films always have the in-plane direction as the easy axis due to the shape anisotropy of the film. We used a vibrating sample magnetometer (VSM) and a standard SQUID magnetometer to confirm that the easy axis of the films is in-plane. Figure 3-7 shows a magnetic field image of a thin film spread wafer taken by the room temperature scanning SQUID microscope covering a large fraction of the Ni-Mn-Ga ternary system. This wafer was scanned at z =300 μm, which is the distance from the film to the SQUID, with a step size of 300 μm in the x and y directions.
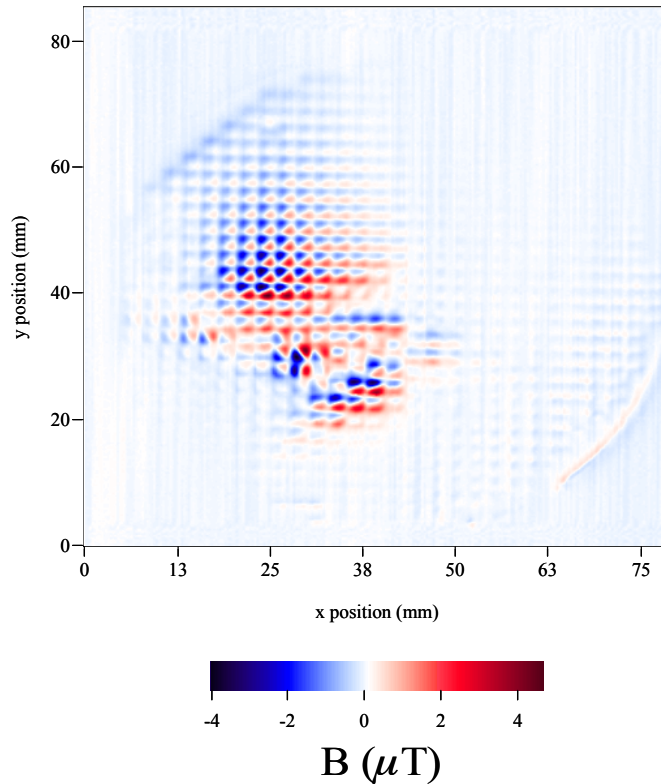
Figure 3-7: A scanning SQUID image of Ni-Mn-Ga combinatorial library wafer.

Variation in the strength of the magnetic field as a function of composition is evident. An inversion technique is used on the entire spread to calculate remanent magnetization from the magnetic field distribution data. Using optimized parameters, the magnetic pole density (ρ_m) is calculated using Transform™ software. From the ρ_m, the remanent in-plane magnetization for each square is calculated by integration, since each square is a dipole [11]. The plot of ρ_m of the entire data and the most magnetic regions can be seen in Figure 3-8.
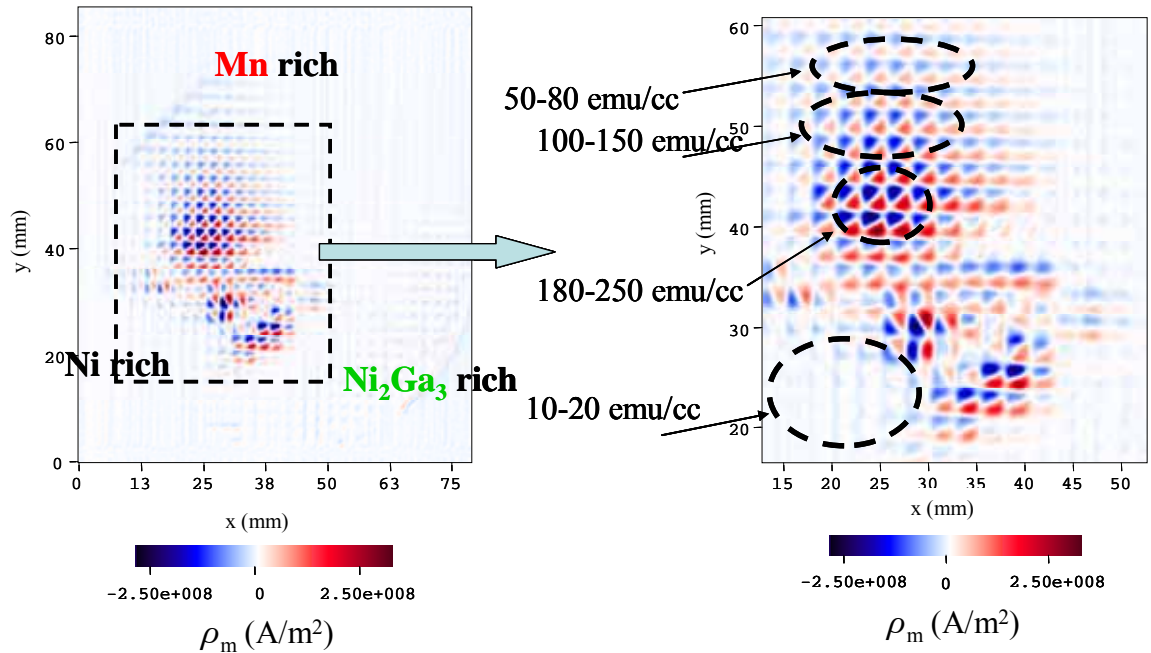
Figure 3-8: Two dimensional image of ρ_m for the same wafer as in Figure 3-7, denoting the most magnetic regions on the wafer.

A program was developed using software (Matlab™) that automates the integration process and that calculates the magnetization for each dipole (i.e. each square patterned film structure). The software takes the data for ρ_m and plots it in two dimensions (as in the software Transform, as shown in Figure 3-8). After entering the

47

parameters for the length and the width of a single square, a grid of many squares is overlaid on the sample. The grid is carefully matched to the physical grid of the sample as seen in Figure 3-5. If there is a tilt in the scan or in the pattern, the wafer data must be divided into several parts and integrated individually. It is very important that the integration area for each square is as accurate as possible. If this is not the case, there will be an error in the final quantitative remanent magnetization value M.

The space between the squares must be large enough for ρ_m to decay; and we have adjusted the size of the squares and the space between the squares as we learned about the effect of these parameters on the result of the room temperature SQUID scans and calculations. For the spread shown above, the size of each square is 1.75mm x 1.75 mm (Figure 3-9), and the spacing between each square is 0.5 mm. The size of the square and the spacing defined the integration area. Each area of integration is 1.75~2 mm by 1.75~2 mm. In this way, all the data for each square is included in the integration area.
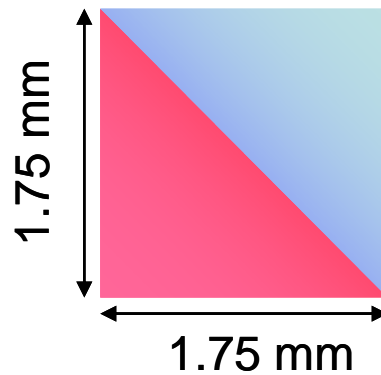
Figure 3-9: The schematic of a patterned square in a composition spread. Each square is 1.75 mm x 1.75 mm. The spacing between the squares is 0.5 mm. This square is diagonally magnetized.

The grid sets up an integration area for each square in the entire spread wafer. Then the program calculates M for each square, by integrating ρ_m. The result is given in

the form of a matrix: *x, y* and *M* for each square. Figure 3-10 shows the plot of this matrix in Matlab™. In Figure 3-10, the colors denote the value of *M* calculated from the magnetic field data. *x* and *y* are the positions of the center of each square on the wafer. The details of the calculations and the programming code used in the computation of the magnetization is presented in the dissertation work of M. A. Aronova[11]. The orientation of the wafer is the same as shown in Figure 3-8.
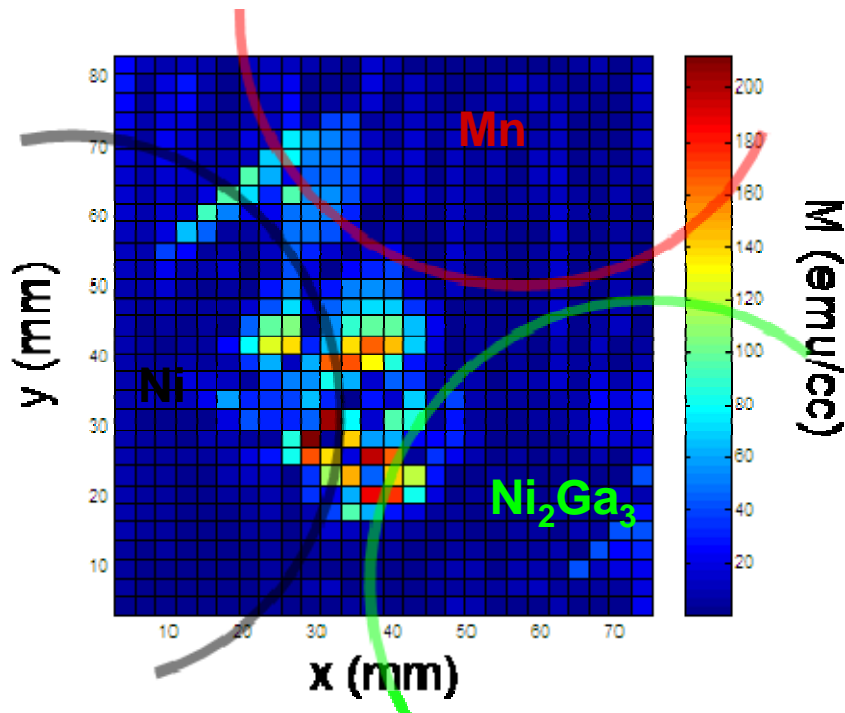
Figure 3-10: Distribution of M as a function of position on a spread.

This result is combined with the composition mapping from WDS analysis of the spread to construct a phase diagram of the remanent magnetization as a function of composition (Figure 3-11). Remanent magnetization is one measure of the strength of magnetism, and thus, we call this a magnetic phase diagram. In this figure, the blue line

is the outline marking the compositional region mapped on this particular composition spread.
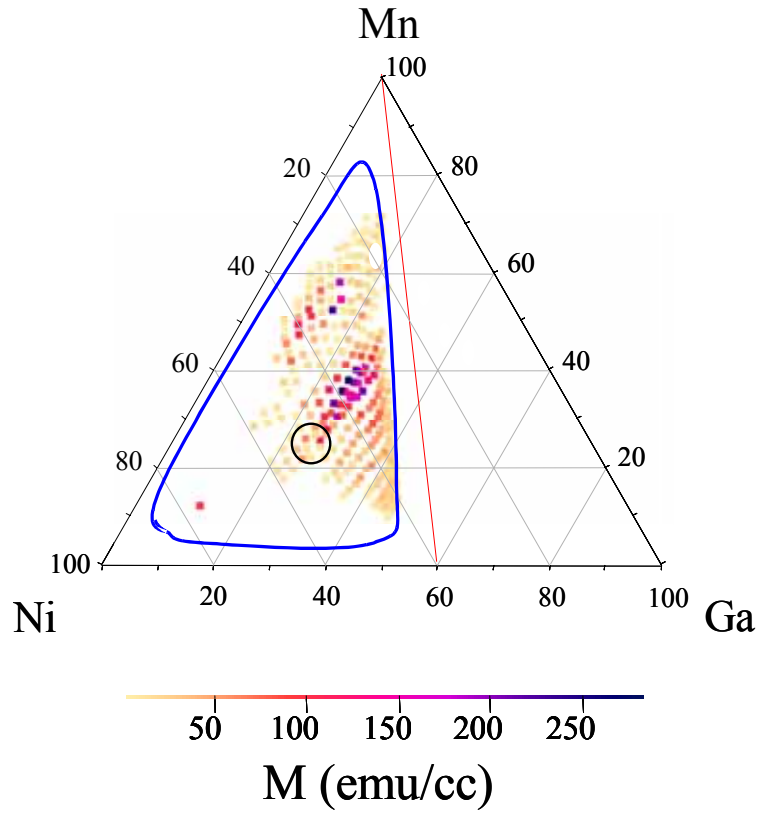
Figure 3-11: Room temperature magnetic phase diagram of Ni-Mn-Ga. The region inside the blue curve is the compositional region mapped on the spread wafer. The composition where the orange line meets the Ni-Ga line is Ni_2Ga_3, which is one of the target compositions we used. The circle inside the diagram marks the compositions near the Ni_2MnGa Heusler composition.

3.3.3 Cantilever libraries for SMAs

Properties of thin-film SMAs can be studied by depositing them on micromachined Si cantilevers [9]. By monitoring the reversible thermally induced actuation of such SMA film/Si cantilever bimorphs, martensitic transformation temperatures can be detected [9]. For individual cantilevers, actuation is typically measured using a capacitance formed between the end of the cantilever and a separate electrode. To map the regions of SMAs and their transition temperatures for the entire spread, we have micromachined arrays of cantilevers, and deposited the composition spreads directly on the array wafers. Each cantilever is 8.5 mm long, 2 mm wide and 60 μm -100 μm thick, and one wafer has 90-100 cantilevers on it. To study thermally induced actuation of the entire cantilever array simultaneously by visual inspection, we have developed a method that works on the simple principle that individual cantilevers with metallic films deposited on them behave as concave mirrors. During a transition, stress-induced actuation of a cantilever results in a sudden change in the radius of curvature of the 'mirror', and an image reflected off the cantilevers responds very sensitively as the concavity of the mirrors change. By monitoring the change in the image as a function of temperature, we can readily discern composition regions undergoing a transition. In this manner, a cantilever array serves as a 'self-reporting' combinatorial library for detection of structural phase transitions. Figure 3-12 (a) is a photograph of a spread deposited on a cantilever array that is reflecting an image (a series
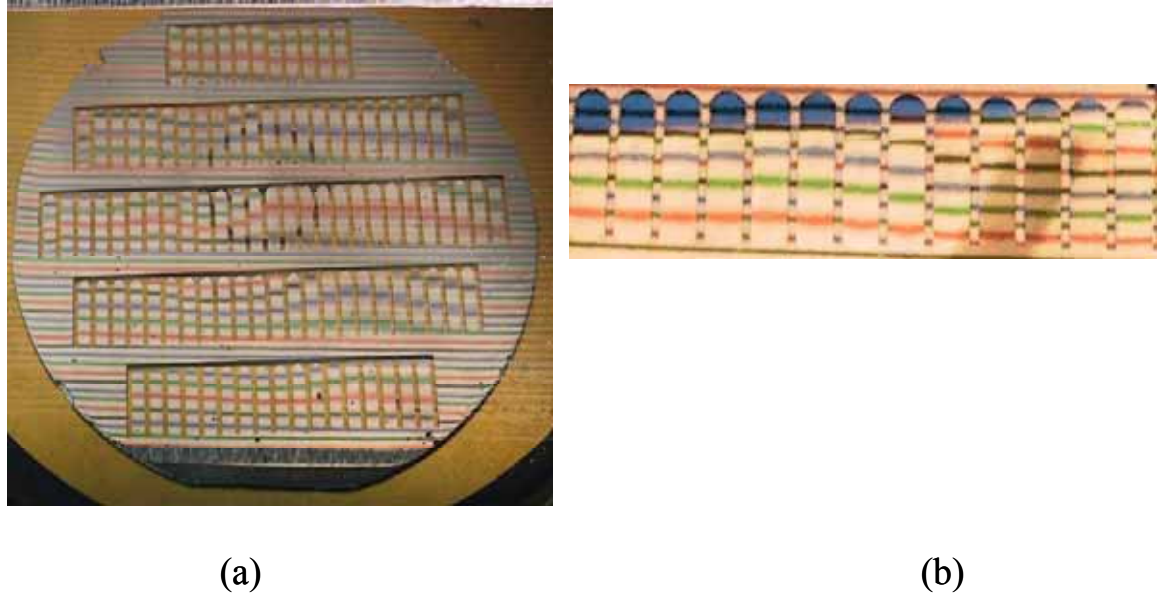
Figure 3-12: (a) A photograph of Ni-Mn-Ni$_2$Ga$_3$ spread deposited on a cantilever library taken during the temperature-dependent measurement. The lines are a reflection of an image with colored lines held over the wafer. The shifts in the positions of the lines as a function of temperature are used to detect small changes in the local curvature of the cantilever. (b) Zoomed up view of a row of cantilevers that showed martensitic transitions.

of colored lines). The measurement consists of recording the image projected on cantilever arrays as the temperature is varied. Figure 3-12 (b) shows a row of cantilevers. All transitions observed here were found to be reversible. From the cantilevers displaying transitions, another phase diagram is constructed (Figure 3-13), which shows the composition regions that undergo a martensitic transition and the corresponding transition temperature. Because of the finite size of individual cantilevers, there is compositional variation on each cantilever. A typical thermal hysteresis width is about 50 K, and this is partly attributed to the compositional variation within each cantilever. WDS was done at three positions along the length of each cantilever. For mapping, we have labeled these three compositions
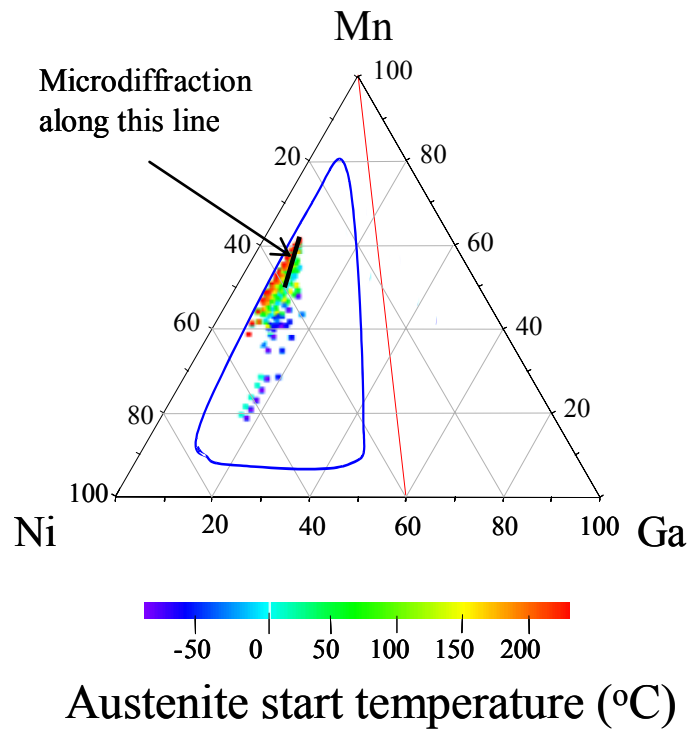
Figure 3-13: Mapping of compositional regions on the phase diagram that displayed martensitic transformation. The composition where the orange line meets the Ni-Ga line is Ni_2Ga_3.

with one transition temperature observed for the cantilever. A large region previously unexplored was found to be SMAs.

Because of the layout of the cantilever libraries, there are regions of the spread not covered by active areas on cantilevers. We therefore sometimes compiled data from several spread libraries deposited at slightly different relative orientation of the sputtering guns with respect to the cantilever spread libraries in order to obtain more points on the phase diagram.

3.3.4 X-ray analysis

An X-ray diffractometer is used to characterize the structure of materials. Using Bragg's law $n\lambda = 2d\sin\theta$, where n is an integer, λ the wavelength of the incident beam, d the spacing between two atomic planes, and 2θ the reflection angle, one can calculate the spacing d or the lattice constant of the material. X-ray diffraction patterns are obtained as a result of atoms scattering from different planes thus revealing the atomic arrangement of a material. Figure 3-14 shows the scanning X-ray microdiffractometer, D8 DISCOVER with GADDS by Bruker-AXS, equipped with a two-dimensional (2-D) area detector (diameter: 11.5 cm) and an x-y-z stage for combinatorial mapping of out-of-plane lattice constant.
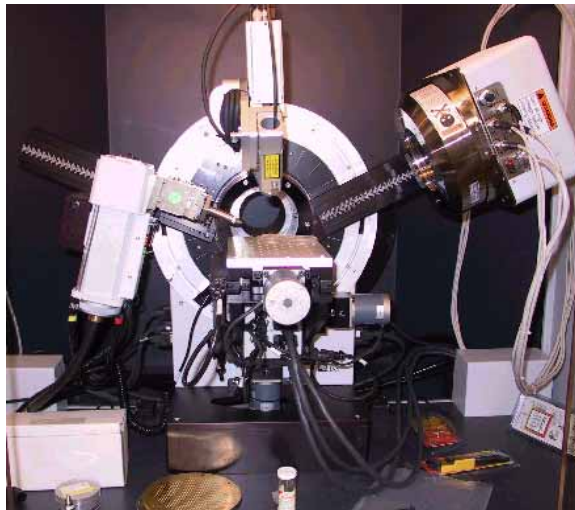
Figure 3-14: A photograph of the scanning x-ray microdiffractometer.

A schematic drawing of the diffraction geometry in the 2-D area detector is shown in Figure 3-15. When one uses the traditional point detector, only the diffracted beam in the detection plane can be detected, and the plane along z-direction cannot be measured. In

contrast, the area detector can pick up x-ray signals ranging along the z-direction. As a result, χ information is also obtained. The range of 2θ depends on the distance between the detector and the sample. By integrating intensities in the χ plane, a spectrum that resembles a regular θ - 2θ diffraction pattern can be obtained. The x-ray beam size can be adjusted, and it is in the range of 50 μm to 500 μm. The beam size used for individual spots of discrete libraries was 500 μm. The microdiffractometer is fully automated and controlled by a computer. Scanning across a combinatorial sample is relatively easy and efficient.
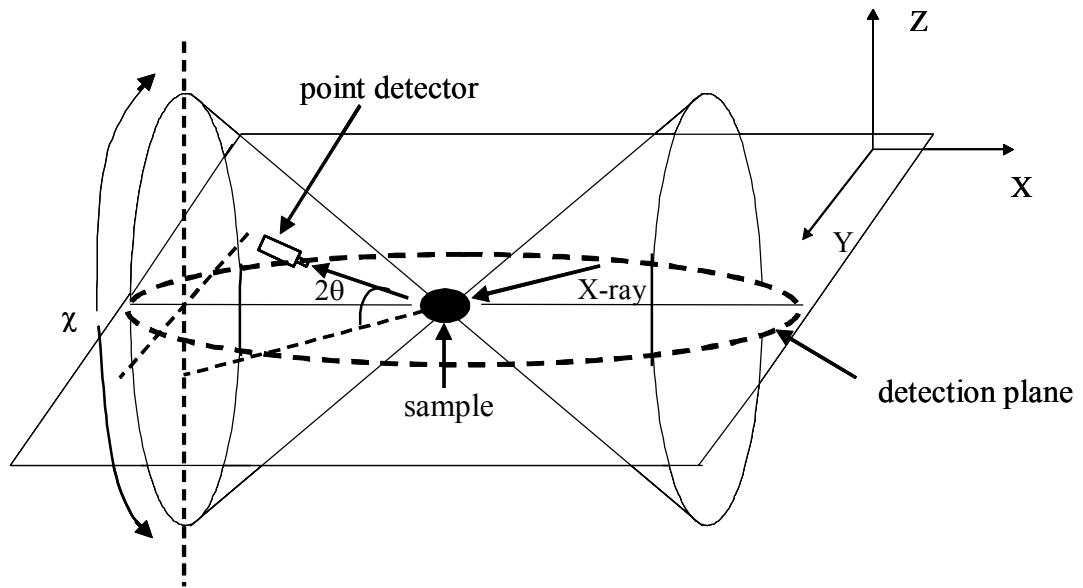
Figure 3-15: A schematic drawing of diffraction geometry when using a 2-D area detector. A range of 2θ and χ are detected simultaneously.

3.3.5 Mapping of mechanical properties of thin films by nanoindentation

In keeping with the paradigm of combinatorial high throughput synthesis and rapid characterization, we have explored the use of nanoindentation as a rapid characterization tool for the measurement of mechanical properties of our thin films. This work has been a collaborative effort with Dr. Oden Warren [12] of Hysitron Incorporated. Mechanical properties are important physical properties for several materials classes currently under investigation using the combinatorial approach [13]. We fabricate the SMA thin film libraries and nanoindentation is used to measure mechanical properties. The idea is to see if we can use this rapid characterization technique to study and map martensites on the composition spread.

Nanoindentation [14] refers to depth-sensing indentation testing in the submicrometer range and has been made possible by the development of 1) machines that can make such tiny indentations while recording load and displacement with very high accuracy and precision, and 2) analysis models by which the load displacement data can be interpreted to obtain hardness, modulus, and other mechanical properties. Nanoindentation has been used to measure mechanical properties of thin films such as the mechanical toughness, hardness, elastic modulus and Young's modulus. A TriboIndenter® nanomechanical test instrument (Hysitron, Inc., Minneapolis, MN) equipped with a three plate capacitive force-displacement transducer and a Berkovich diamond indenter was used to perform nanoindentation force-displacement curves. The Oliver-Pharr method of analysis [15] was used to determine the hardness, H, of the thin film samples as well as the reduced modulus, E_r, of the contact:

$$E_r = \left[\frac{(1-\upsilon_i^2)}{E_i} + \frac{(1-\upsilon_s^2)}{E_s} \right]^{-1} \qquad \text{(Eq. 1)}$$

where E represents elastic or Young's modulus, υ indicates Poisson ratio, and subscripts

i and s denote indenter and sample, respectively. Figure 3-16 is a schematic

representation of a typical triboindenter setup.
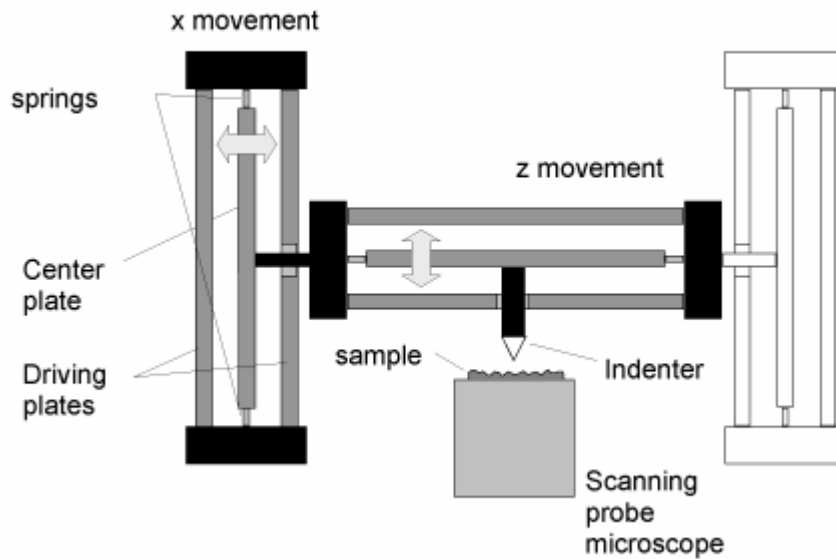
Figure 3-16: A schematic illustration of a triboindentor.

An indenter tip with a known geometry is driven into a specific site of the material to be

tested by applying an increased normal load. When reaching a preset maximum value, the

normal load is reduced until partial or complete relaxation. This procedure is performed

repetitively; at each stage of the experiment the position of the indenter relative to the

sample surface is precisely monitored with a differential capacitive sensor. For each

loading/unloading cycle, the applied load value is plotted with respect to the

corresponding position of the indenter. The resulting load/displacement curves provide

data specific to the mechanical nature of the material under examination. Established models, such as the Oliver-Pharr [15], are used to calculate quantitative hardness and modulus values from such data. Figure 3-17 is an example of the indentation hardness result from a nanoindentation measurement of a Ni-Mn-Al composition spread wafer.
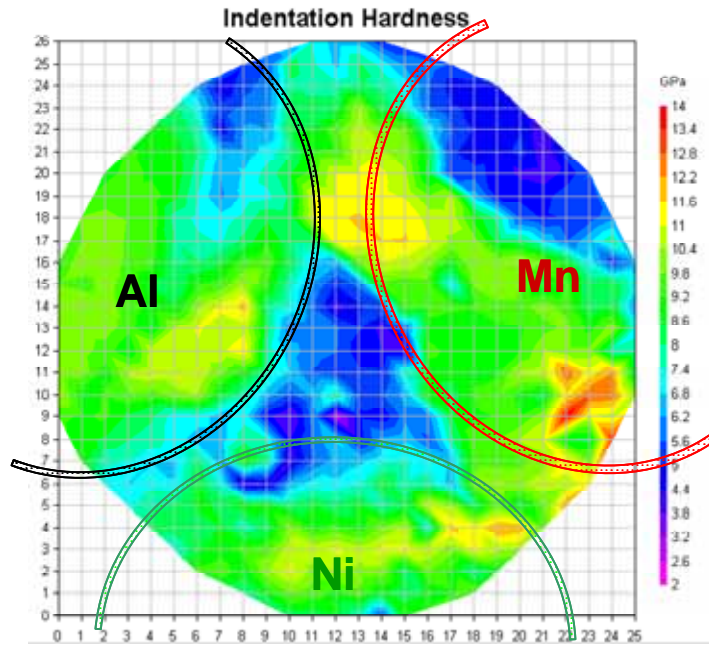
Figure 3-17: Indentation hardness result from a Ni-Mn-Al spread wafer.

The modulus of the thin film spread was also measured and the result is shown in Figure 3-18. The data is then used to map the properties on a phase diagram. Using the composition analysis data and the corresponding position on the thin film spread, we can map the hardness and modulus data on a phase diagram. An example of the results from the compilation of these data is shown in Figure 3-19.

We have shown that nanoindentation can be used to obtain the hardness and modulus of our composition spreads and are exploring it as a tool to identify martensites using the load-displacement curves. Because this is a relatively new approach, we have

only applied this technique to the Ni-Mn-Al system. The summary of the results are discussed in the Ni-Mn-Al section.
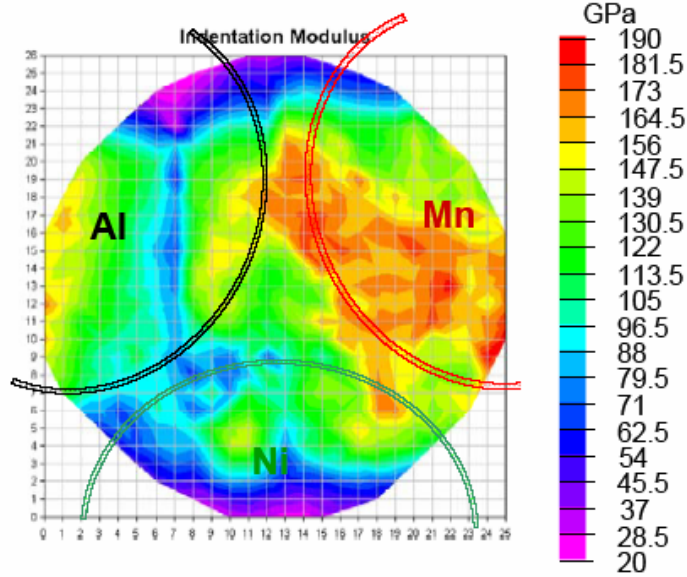
Figure 3-18: Indentation Modulus result from a Ni-Mn-Al spread.
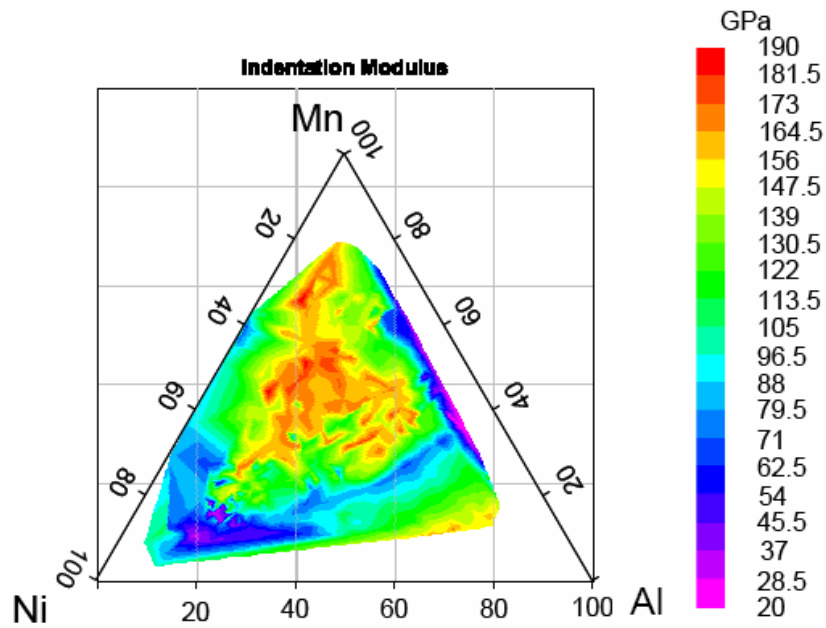
Figure 3-19: Phase diagram mapping of nanoindentation measurement of Modulus.

3.4 Mapping of functional phase diagrams

In this section, I will discuss the results of functional phase diagram mapping of various ternary alloy systems. The results will be summarized using phase diagrams.

3.4.1 Ni-Mn-Ga ternary system

Figure 3-11 shows the mapping of remanent magnetization from one Ni-Mn-Ga wafer. It is clear that the most strongly magnetic region stretches from near the middle of the phase diagram towards slightly Ni-rich composition. The black circle indicates the region surrounding the well known Heusler composition, Ni_2MnGa, which has been extensively studied [16, 17, 18, 19] and which lies near one end of this highly magnetic region. As one moves away from this region, the magnetization becomes smaller. Nickel is strongly magnetic, but its moment decreases rapidly as it is diluted with other elements, and in the Ni-rich region covered in this spread, the composition is already only weakly magnetic. On the other hand, manganese is antiferromagnetic, and this is not detectable by SQUID.

The peak in magnetization is observed near the center of the phase diagram around the half-Heusler composition, NiMnGa. Several composition spreads fabricated under slightly different conditions (i.e. annealing temperatures) were all found to result in the similar phase diagram trend. The values of magnetization extracted here are consistent with those of remanent magnetization obtained by a VSM on separate individual composition samples measured at room temperature. Ferromagnetic resonance measurements of the individual samples showed a very narrow line width (as low as 70

Oe) as well as well-defined spin resonance waves, indicating that the films are generally of very high quality and magnetically very homogeneous [20].

Mapping of regions that exhibit reversible martensitic transitions are mapped on Figure 3-13. This plot was made by compiling data from several wafers made at the same conditions, but with the wafers placed on the heater during the deposition at different angles relative to the gun geometry. A clear trend emerges, and the general region that undergoes martensitic transitions can be easily seen from the phase diagram. The exact martensitic transition temperatures are known to depend on many factors such as atomic ordering, microstructure and the residual stress [10, 21, 22]. Reported values of the martensitic transition temperature of nominally Ni_2MnGa samples vary widely, and in one study [18] it was found to range from 113 K to 298 K. Naturally, we expect to have regions that undergo transitions at temperatures out of the range of our measurements (150–570 K), and we believe this is the reason we do not see Ni_2MnGa transforming in our measurement range in this particular experiment.

Rather than focusing on the exact transition temperature, we discuss the trend as a function of compositional variation. There are reversible martensites in large compositional regions previously not reported. This region stretches from near Ni_2MnGa to Ga-deficient, Mn-rich regions. The transition temperature increases as the molecular percentage of Ga is decreased. A typical composition here is $Ni_{43}Mn_{47}Ga_{10}$, whose martensite start temperature was found to be 400 K. In much of the newly discovered region, the martensitic transformation temperature is near room temperature or above, which is desirable for practical applications.

Scanning X-ray microbeam diffraction of the spread indicates that most of the composition regions mapped on our composition spreads have the diffraction pattern consistent with the L21 structure, (Figure 3-20) [23], of the Heusler composition or a tetragonally distorted $L2_1$ structure (for the martensite). Figure 3-21shows a scanning
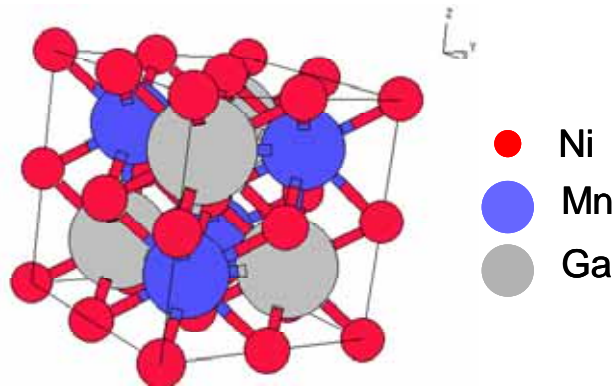
Figure 3-20: A unit cell of $L2_1$ structure of an austenite. [23]

diffractogram taken at room temperature along the black line region in Figure 3-13. In this region, the composition goes from the mixed phase displaying three peaks (two from the martensite and one from the austenite) to a region where it is mostly austenite. This verifies that the new region we found is indeed martensites.
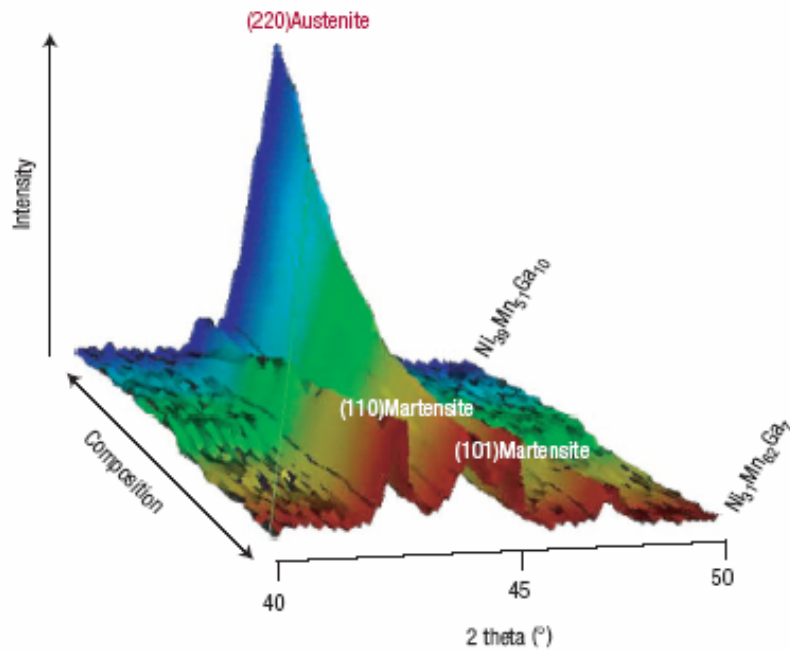
Figure 3-21: Scanning X-ray microdiffractogram taken at room temperature along a compositional region marked by the solid black line in Figure 3-13. There are three peaks, two are from a martensite and the middle one is from an austenite.

Figure 3-22 summarizes the magnetic and the martensite phase diagrams deduced from the obtained data for the Ni-Mn-Ga ternary system. To date the overwhelming majority of reported work had focused on regions inside the blue circle whose composition is close to the Heusler alloy. It is evident that there is a large region well outside the near- Heusler composition that contains ferromagnetic, reversible martensites. It has been shown [24, 25] that this class of material displays martensitic instability for stoichiometries where the average number of electrons per atom is ~7.4. Here the total number of s, p and d electrons of incomplete subshells is counted and divided by the number of elements. The green hatched area in Figure 3-22 covers the region where the average number of electrons per atom is 7.3–7.8. There is a large overlap between this

63

region and the observed reversible martensite region. Because the electron/atom ratio rule is expected to apply strictly in the $L2_1$ structure, the overlap is perhaps an indication that the structure in the region is indeed $L2_1$ or one close to it.
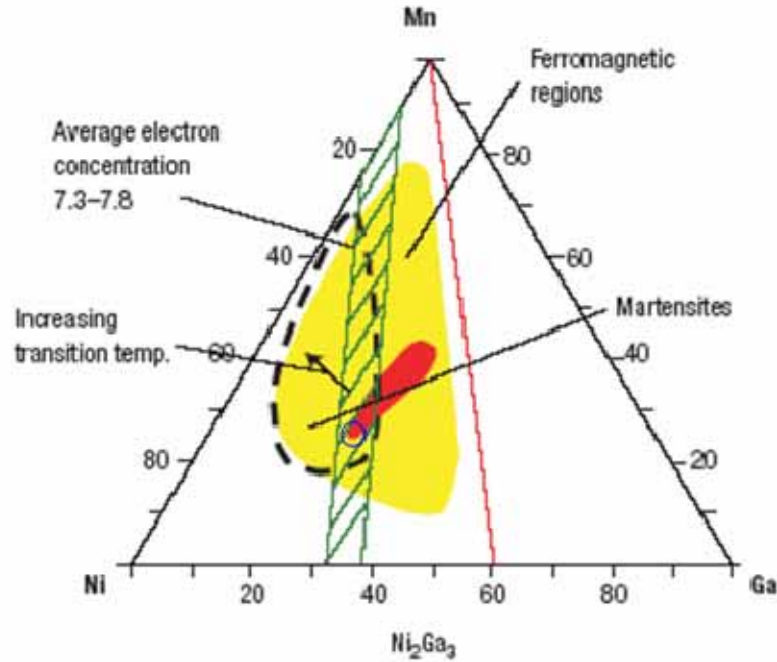
Figure 3-22: Functional phase diagram deduced from the present experiment. The hatched region has compositions with average electron/atom ratio 7.3–7.8. The dotted line surrounds the region of reversible martensites. In the ferromagnetic region, the red area has the highest magnetization.

The closer the composition is to the $Ni_{1-x}Mn_x$ line of the phase diagram, the lower the magnetization becomes. A separately prepared $Ni_{1-x}Mn_x$ spread did not show any indication of reversible martensites. $Ni_{1-x}Mn_x$ is known to be ferromagnetic for x < 0.25–0.4 and antiferromagnetic for greater x, and the actual value of x where the transition takes place is dependent on atomic ordering [26, 27]. Martensitic instabilities are often associated with magnetic transitions [28]. We speculate that it is the ferromagnetic–antiferromagnetic transition or competition in $Ni_{1-x}Mn_x$ that is serving as the precursor to

the martensites in the Ni–Mn–Ga system. The martensitic instability is perhaps set off by introduction of a small Ga concentration. The robustness of the martensite associated with the L2$_1$ phase may be reflecting the large solid-solution region in the Ni$_{1-x}$Mn$_x$ phase diagram near the Ni end.

The room-temperature magnetization is plotted against the martensitic start temperature in Figure 3-23 for the compositions studied here. There is a clear relationship between the two parameters: the higher the magnetization, the lower the transformation temperature. We have confirmed that, for different samples, the magnetization at room temperature is roughly proportional to the Curie temperature. For this, we measured individual cantilevers using a vibrating sample magnetometer. The plot points to a strong thermodynamic magneto-structural coupling in this system. Such a coupling has previously been observed in a limited range of composition near Ni$_2$MnGa (inside the circle in Figure 3-11) [19], and a Ginzburg–Landau model has been used to explain the influence of the magnetic order on the martensitic transition [19, 29]. Our experiment shows that the same coupling behavior holds for a much wider compositional range. A phenomenological interpretation of this is that magnetism tends to stabilize the austenite structure of the alloy, and this necessarily lowers the structural transformation temperature. It is interesting that a first-principles calculation has suggested [30] that a cubic to tetragonal change would actually result in a slight increase in the total magnetic moment in Ni$_2$MnGa. The seeming discrepancy may indicate the importance of a magneto-elastic coupling term in the free energy, which gives rise to the observed trend.
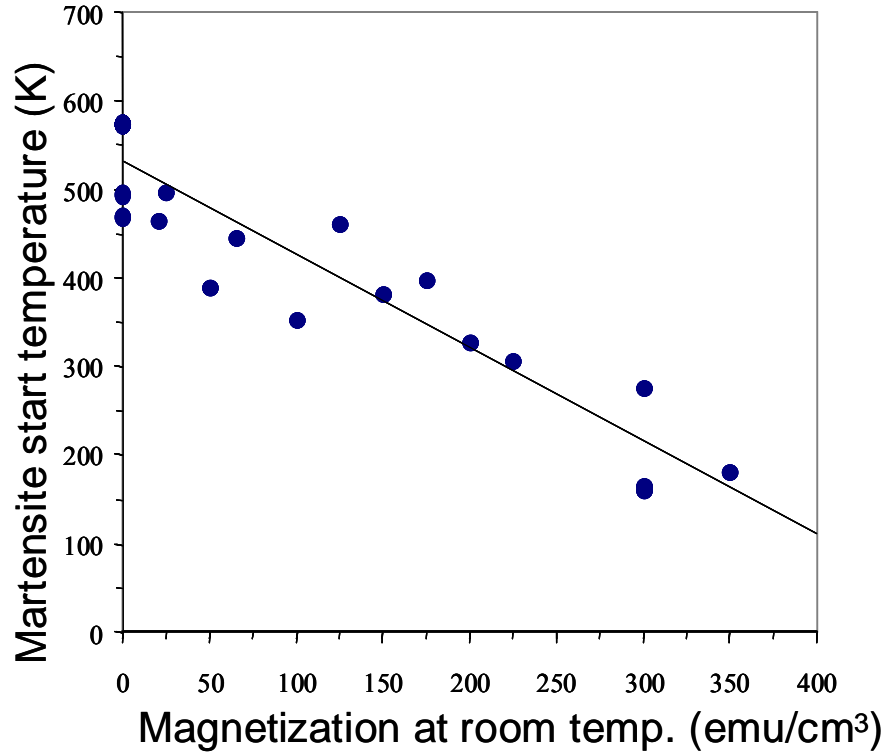
Figure 3-23: Martensitic start temperature against room temperature saturation magnetization for data points mapped in Figure 3-13. For this magnetization, cantilevers were measured individually using a vibrating sample magnetometer. The line is a linear fit to the data. [44]

For applications, the goal when searching for new FSMAs is to find compositions with (1) high Curie temperature, and thus increased room-temperature magnetization, which in turn results in increased magnetostatic energy necessary for rotating the magneto-elastic domains, and (2) high martensitic transition temperatures. Our results clearly indicate an intrinsic trade-off between the two in a given system. Also, within a given ternary system, the Heusler composition does not necessarily provide the optimized functionality. This may also be the case for other properties such as complete spin polarization, which has been predicted in some Heusler compounds but not yet

unambiguously established [31]. Perhaps exploration is warranted outside the Heusler composition in the ternary phase diagram for high spin polarization.

Figure 3-24 shows the isothermal ternary phase diagram for the Ni-Mn-Ga system at 800 °C previously published by C. Wedel and K. Itagaki [32]. In comparism to our functional room temperature phase diagram (Figure 3-22) there are some similarities. The beta phase in Figure 3-24, which is at 800 °C corresponds almost exactly to the regions where we observed increasing martensitic phase transitions in our functional room temperature phase diagram. Thus, this indicates that the beta phase mapped here is perhaps what transforms to martensites at lower temperatures.
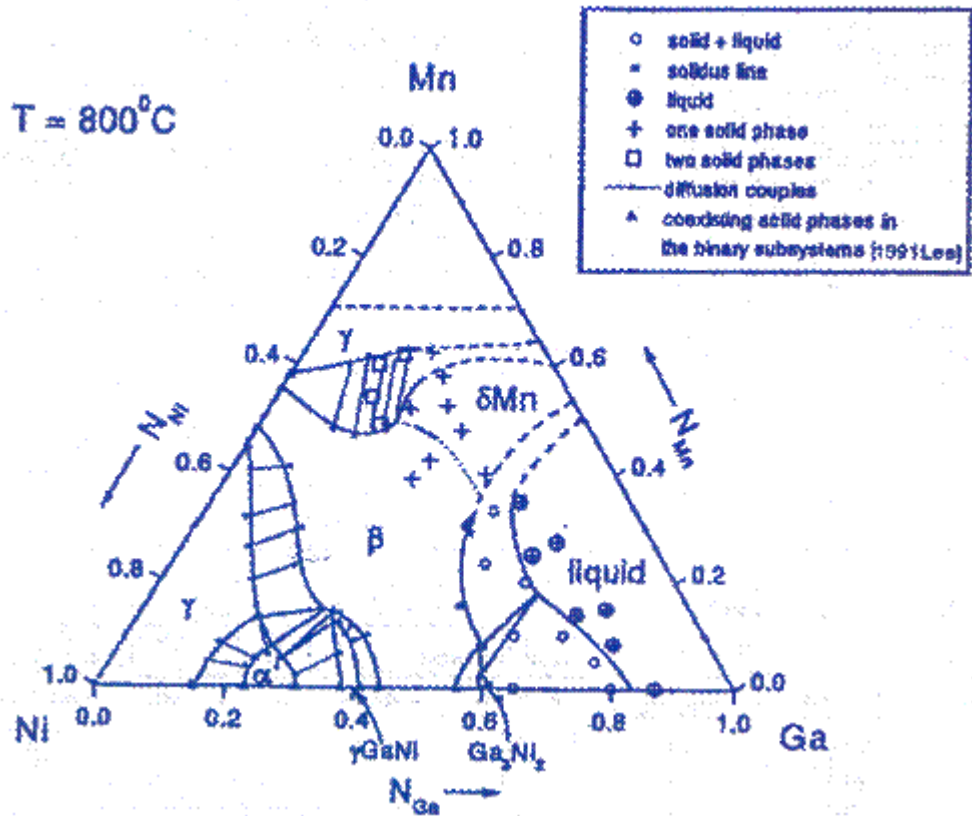
Figure 3-24: Isothermal section of the ternary Ni-Mn-Ga phase diagram at 80 °C for alloys with Mn content below 70 at. % [32].

3.4.2 Ni-Mn-Al ternary system

Research in the FSMA field has been largely focused on Fe-Pd and Ni_2MnGa due to the large strains induced in these systems by an external magnetic field [33, 34, 35]. Other alloy systems such as Co_2NiGa and Co_2NiAl have also been shown to be FMSAs [36, 37]. Partly due to the brittleness of these known materials, there is a continuing interest in finding other FMSAs [38, 39]. The Ni-Mn-Al alloy system is considered to be a good candidate because it does not contain Ga and the alloys are less brittle than Ni-Mn-Ga [38, 40, 41]. Thus, we have mapped the physical properties of the Ni-Mn-Al ternary system with respect to ferromagnetism and martensitic transitions using the composition spread technique.

The three targets used in this experiment were Ni, Mn and Al. The composition spread wafers were deposited at room temperature followed by an in-situ annealing in vacuum at temperatures in the range of 575-700 ^{o}C for 2 h. Figure 3-25(a) is a magnetic field image of a region from a Ni-Mn-Al spread wafer obtained with the scanning SQUID microscope. This spread was annealed at 700 ^{o}C for 2 h. In this ternary system, we have consistently observed two distinct compositional regions, which showed ferromagnetism at room temperature. The values of remanent magnetization extracted here are consistent with those obtained by a VSM on separate individual composition samples measured at room temperature. Figure 3-25(b) shows the magnetic phase diagram.
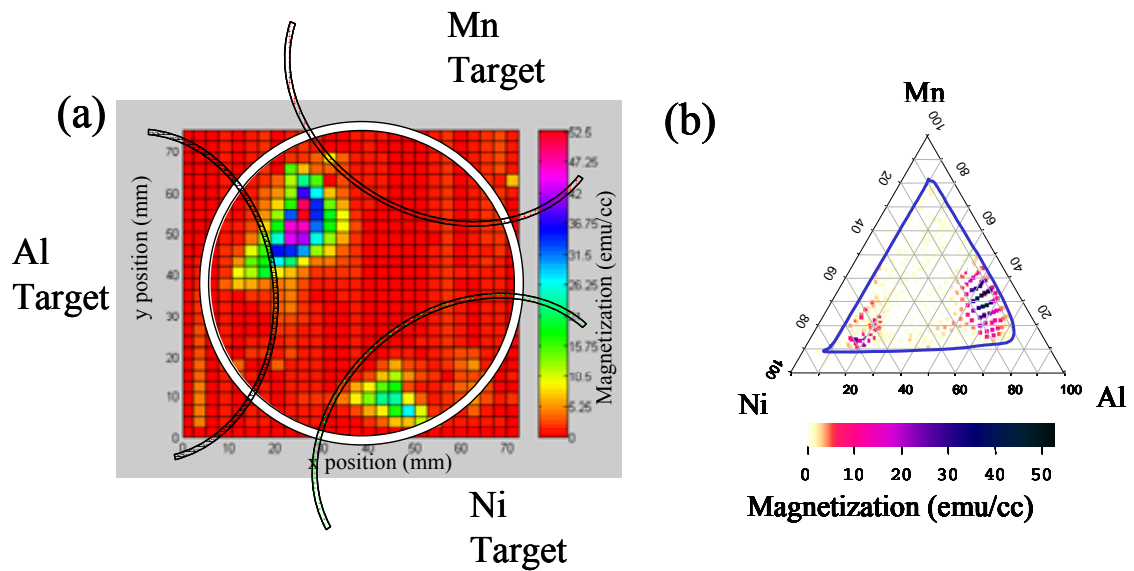
Figure 3-25: Scanning SQUID microscope mapping of magnetic properties at room temperature. a) Scanning SQUID image of a N-Mn-Al spread wafer. The separation between the SQUID and the sample is about 0.3 mm. The circle is the outline of the wafer. This wafer was annealed at 700°C. (b) Room-temperature magnetic phase diagram of Ni-Mn-Al deduced from (a). The region inside the curve is the compositional region mapped on the spread wafer.
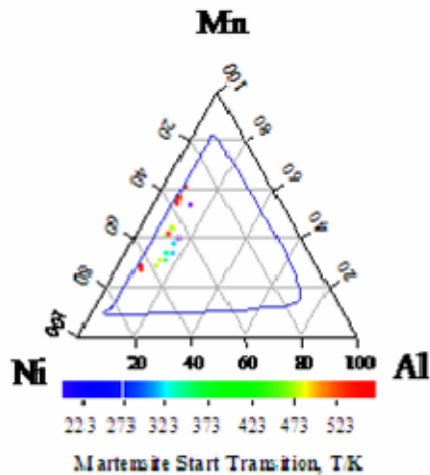
Figure 3-26: Mapping of the compositional regions on the Ni-Mn-Al phase diagram that displayed martensitic transformation on one wafer, which was annealed at 580°C. Martensite start temperature is plotted. The region inside the curve is the compositional region mapped on the spread wafer.

Figure 3-26 shows the composition regions that undergo martensitic transitions, and the corresponding transition temperatures. In Figure 3-26, we plot results from one composition spread wafer. This spread was annealed at 580°C for 2 h. The general region that undergoes martensitic transitions can be easily seen from the phase diagram. The exact martensitic transition temperatures are known to depend on many factors such as atomic ordering, microstructure and the residual stress in the film [10, 21, 22]. Reported values of the martensitic transition temperatures of Ni-Mn-Al samples in the literature also vary widely, depending on the composition and processing conditions. For this reason, we focus again on the trend of the martensitic transition temperature as a function of compositional variation, rather than on the exact transition temperatures.

There have been a number of reports on the investigation of properties of different regions of the Ni-Mn-Al ternary system over the years. Most of the work has been on bulk alloy samples. Recently, there have also been reports on Ni-Mn-Al thin films [33, 42]. There are some discrepancies in the reported magnetic properties of Ni-Mn-Al alloys. This appears to originate from the sensitivity of the properties on thermal treatment, which varies among different work [43]. Different thermal treatments naturally affect the degree of crystallization as well as the degree of disorder in samples.
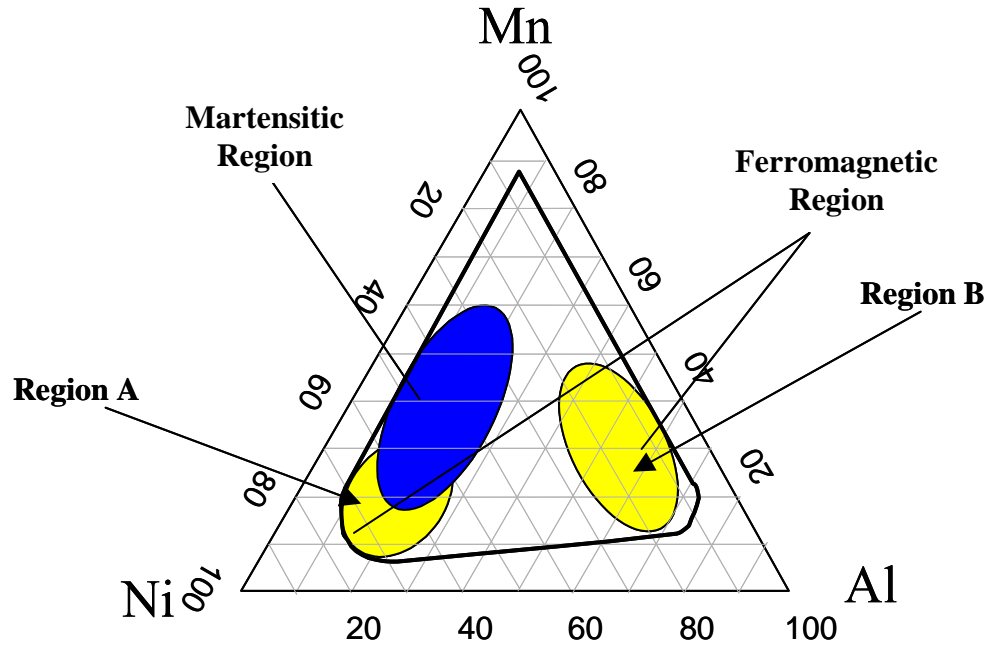
Figure 3-27: Trends observed in the spread pictured in Figure 3-25(b) and the cantilever spread array in Figure 3-26 are summarized. Ferromagnetism was observed in two regions. Martensites are observed in a compositional region similar to the region in the Ni-Mn-Ga system.

Figure 3-27 summarizes our findings in the present experiment on the Ni-Mn-Al system. There are two compositional regions that display ferromagnetism in this ternary system as can be seen in Figure 3-25(b). In Region A, the composition range encompasses Ni (50-90 at. %), Mn (10-40 at. %), and Al (8-23 at. %) and in Region B the composition range covers Ni (9-25 at. %), Mn (15-50 at. %), and Al (40-70 at. %). In Region A, the magnitude of Ms becomes stronger as one goes towards higher Ni contents. The maximum remanent magnetization found here in Region A was in the range of roughly 40 emu/cc for a nominal composition of $Ni_{76}Mn_{17}Al_7$.

It is well-known that order-disorder plays an important role in determining ferromagnetic and antiferromagnetic (AFM) properties of materials as has been reported

in previous work [26, 44, 45, 46]. It is known that the nominal Ni_2MnAl composition can display ferromagnetism or antiferromagnetism depending on processing conditions, and in turn on the degree of order/disorder [42, 45, 47]. We believe that this is the main reason that nominal Ni_2MnAl does not appear to be ferromagnetic in our phase diagram. We are currently investigating the details of the effect of order/disorder by fabricating spreads with different cooling procedures so that different degrees of disorder will occur in our films.

In addition, many different composition regions exist in the sputtered film, which could have different phases and crystal structures. Hence, it can be considered that the atomic order parameter after heat-treatment is different for each region and as a result, the magnetic properties are not the same for each region. This may be one possible explanation for our observation in Figure 3-25. Since we did not observe any metastable quenched phases in the film we assume we have close to equilibrium and therefore Figure 3-27 is plotted on this basis.

We find that the compositional trend of martensites here appears to be very similar to what we found in the Ni-Mn-Ga system. This region stretches from the Heusler composition of Ni_2MnAl to the Al-deficient region (Figure 3-27). As one moves towards the more Al-deficient region, the martensite transition temperature increases (Figure 3-26). This region appears to correspond exactly with the region where the β/B2 parent phase has been reported [39, 40, 43, 46]. An x-ray microbeam diffraction scan of the entire spread library indicates that most of the regions have diffractions consistent with the $L2_1$ or the B2 phase. This is in agreement with other published work [38-40, 42, 48, 49, 50, 51].

Previously, Kainuma, *et. al.* [39, 48] also mapped the martensites in this region using individual bulk samples and reported a trend that was similar to the phase diagram reported in Ni-Mn-Ga. This phase diagram is shown in Figure 3-28. Comparing to our results, again it appears that part of the high temperature beta phase is what is responsible for reversible martensites at lower temperatures.
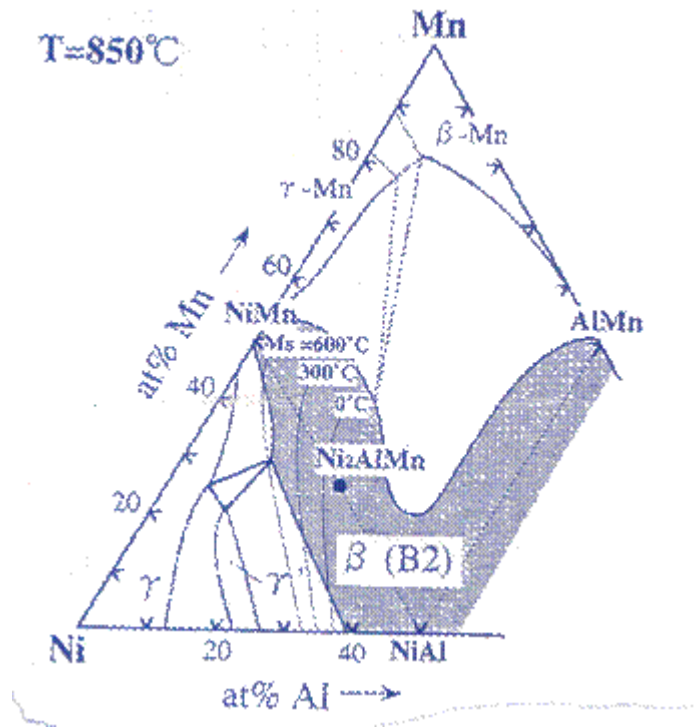
Figure 3-28: Isothermal section of the ternary Ni-Mn-Al phase diagram at 850 ^{o}C for alloys with Ga content below 60 at. % [39].

The finding here seems to indicate the presence of FMSAs in the Al-deficient Ni-rich region of the phase diagram where there is an overlap of compositions displaying martensites and remanent magnetization. In order to confirm our findings from composition spreads, a bulk sample was made with a nominal composition of $Ni_{52.5}Mn_{30.9}Al_{16.5}$, which is in our overlapping region. An ingot of $Ni_{52.5}Mn_{30.9}Al_{16.6}$ alloy was prepared from manganese, nickel and aluminum by using an arc-melting method in

an argon atmosphere. A composition of the alloy was determined by electron microprobe. The bulk sample was annealed for 1 hr at 500 $^{\circ}$C and then quenched in water. Figure 3-29 shows the room temperature x-ray diffraction of the bulk sample after it was anneal at 500 $^{\circ}$C. After the anneal, the (220) peak has split into two peaks indicating that the alloy is indeed a martensite. This sample was however found to be

$$Ni_{52.5}Mn_{31}Al_{16.5}$$
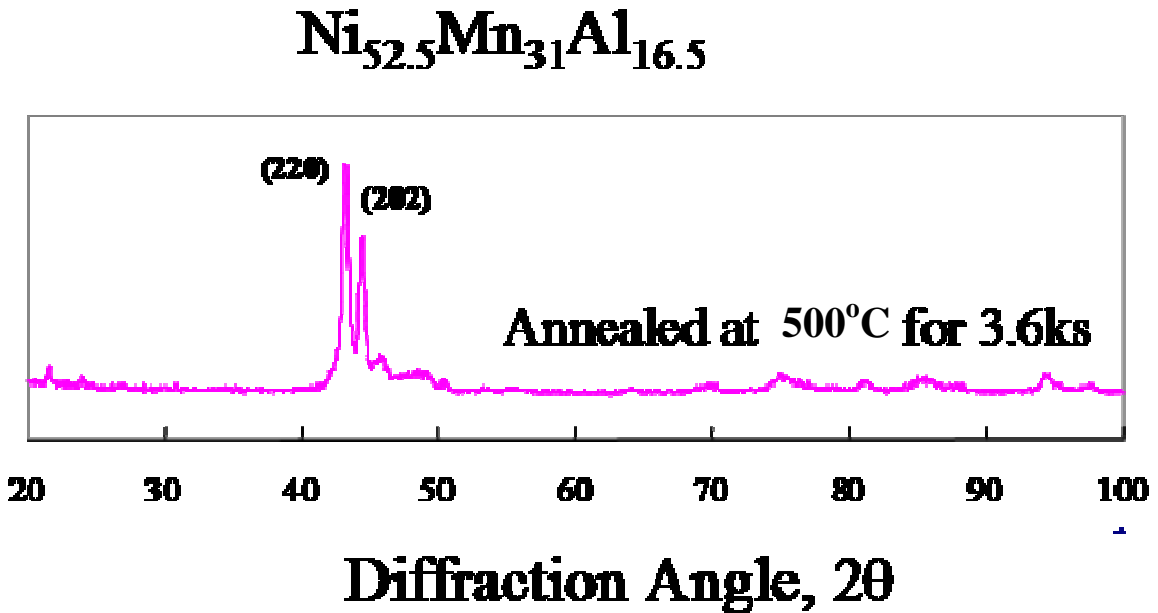
Figure 3-29: X-Ray diffraction taken at room temperature of a bulk sample after it is annealed at 500 $^{\circ}$C for 1h.

mostly paramagnetic down to -269 $^{\circ}$C. We again attribute the difference in magnetic properties to different degrees of disorder in the bulk sample and our thin film spread. Analysis of the XRD result for the bulk sample also showed that the sample was polycrystalline and orthorhombic. An optical microscope study of a bulk sample has revealed plate like features consistent with the presence of martensites.

Figure 3-30 is a mapping of the Young's Modulus obtained by nanoindentation of a Ni-Mn-Al spread wafer. Here, nanoindentation is being explored as a high-throughput

technique for screening thin film composition spreads with regard to their mechanical properties [52]. Indicated in the figure are the regions of compliance introduced into the wafer by the tool. Figure 3-31 is the corresponding indentation modulus phase diagram showing the % deviation from the rule-of-mixture, which is calculated by adding up the modulus obtained from 3 pure elements in fractional percentage amount. The blue region near the Ni-Mn binary line shows strong deviations from the rule-of-
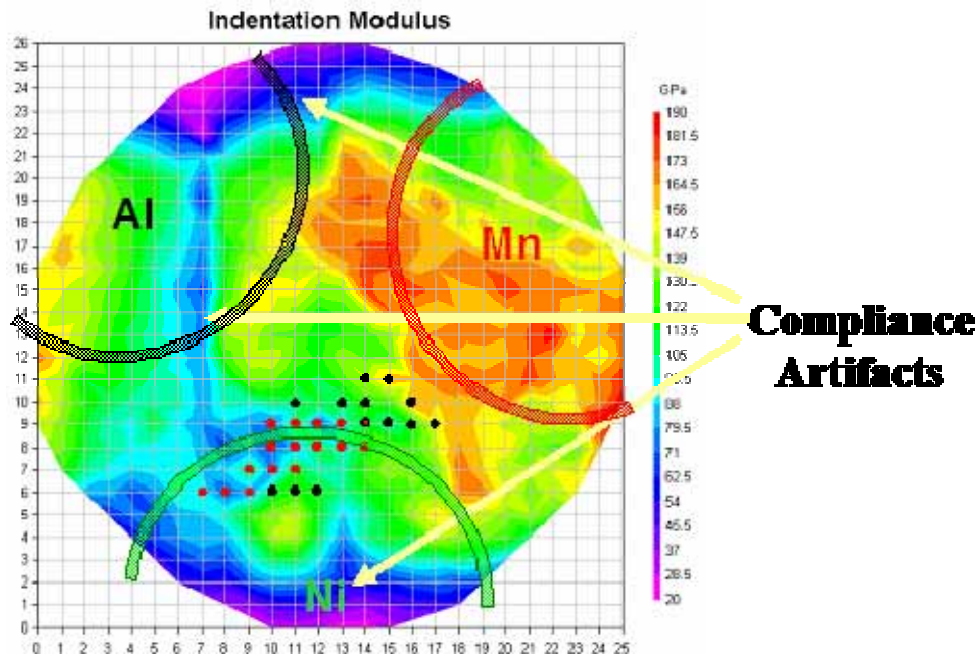
Figure 3-30: Mapping of Modulus from nanoindentation of a Ni-Mn-Al wafer. Regions of compliance artifacts are indicated. Approximate regions where high concentration from each target is obtained are indicated. The red dots are compositions showing the presence of at least two material phases as judged by optical microscopy. The black dots are compositions closest to the Heusler composition.
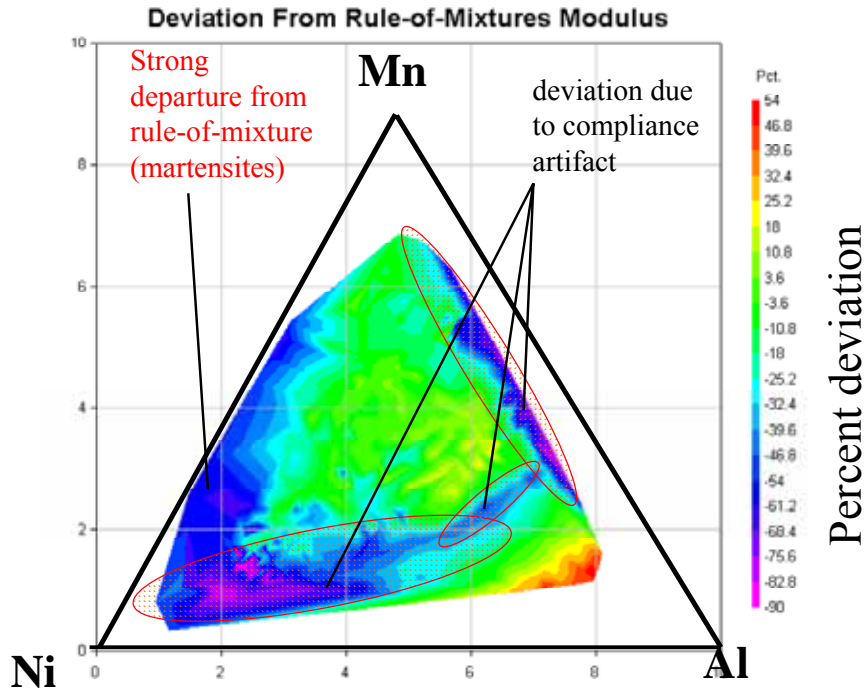
Figure 3-31: Phase diagram mapping of deviation from rule-of-mixture. The regions of the wafer with compliance artifacts are indicated. A region that shows large deviation from rule-of mixture is indicated. The compliance artifact is believed to arise from regions near the edges of the wafer.

mixtures which we believe is an indication of martensites. Indeed, this region is consistent with the region we found to be martensites (Figure 3-27).

We have found a large, previously unknown, area of the ternary phase diagram (Region B in Figure 3-27) that displays marked ferromagnetism. This region contains compositions with remnant magnetizations up to 50 emu/cc. A qualitative maximum of remnant magnetization 53 emu/cc is reached at $Ni_{14}Mn_{32}Al_{54}$ on the spread. This was confirmed by measuring a single square sample of the thin film cut from the spread with a VSM.

Near Region B, MnAl is known to have a metastable bct τ-phase, which displays hard ferromagnetic properties. This phase has been synthesized in bulk as well as in thin

films [51,53,54]. In sputtered films, it was found that upon substituting Ni ions into MnAl, the lattice forms a more stable cubic κ-phase, which has a CsCl type structure [54]. It has been reported that the magnetic properties of the κ-phase varies as the Ni concentration is increased.

We have discovered a much larger area with remnant magnetization that had been previously unexplored. The qualitative trend of magnetization we observe for iso-aluminum samples in our spreads, which include the region in which the κ-phase was reported, is very similar to the reported trend, and there is a rather broad maximum of remnant magnetization being observed for intermediate dopings of Ni. The values of magnetization we observe in this region are of the same order as those in the previous reports [53, 54].

XRD data of our spread wafers show that in this compositional region the value of the lattice constant is higher than in any other region of the ternary phase diagram. This may explain the occurrence of ferromagnetism: it is consistent with the picture that as the distance between Mn ions is increased, coupling shifts from anti-ferromagnetic to ferromagnetic [45].

3.4.3 Other ternary systems

In the process of quickly surveying the vast compositional landscape of ternary Heusler alloys and related compounds consisting of different elements in search of FMSAs, we have investigated a number of different ternary alloy systems. This section lists and briefly discusses the results of the other ternary alloys we have investigated.

3.4.3.1 Co-Mn-Ga

Figure 3-32, shows the magnetic ternary phase diagram of the Co-Mn-Ga system at room temperature. Targets of Co, Mn, and Co_2Ga_3 alloy were used to deposit the thin film composition spread. Synthesis conditions were similar to those used for the Ni-Mn-Ga thin film composition spread. Again, since pure Ga is difficult to handle at room temperature, it was alloyed in the highest concentration possible with Co to obtain a target compound. Thus the right side of the phase diagram was not mapped.

The room-temperature magnetic phase diagram of the Co-Mn-Ga (Figure 3-32) system is qualitatively very different from the Ni-Mn-Ga (Figure 3-11) system. The regions with the highest magnetization are associated with high concentrations of Co in the Co-Mn-Ga system. Apparently, the magnetic moment of Co is not affected by "mixing" it with other atoms, unlike Ni whose magnetic moment falls off very rapidly with slight impurity atom concentrations. We observed no martensitic transformation for the spread using our cantilever array technique.
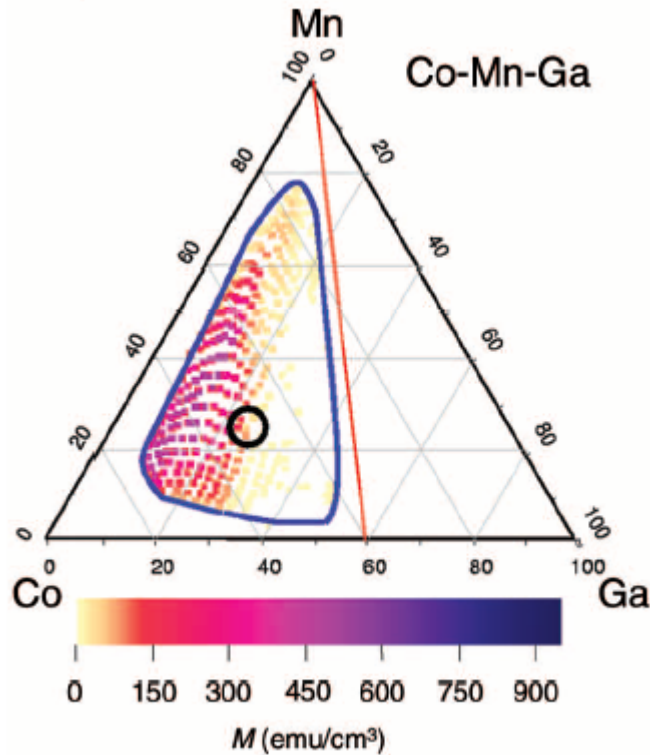
Figure 3-32: Map of the room-temperature remanent magnetization of Co-Mn-Ga system. Regions inside the blue curve are the composition regions mapped on the spread wafer. The composition where the red line meets the Co-Ga line is Co_2Ga_3, which is one of the three target compositions used in the experiment. The black circle marks the composition near the Heusler composition in the system.

3.4.3.2 Co-Ni-Ga

Figure 3-33, shows the magnetic ternary phase diagram of the Co-Ni-Ga system at room temperature. Targets of Co, Ni, and Co_2Ga_3 alloy were used to deposit the thin film composition spread. Synthesis conditions were similar to that used for the Ni-Mn-Ga system.

Much like in the Co-Mn-Ga system, the regions with the highest magnetization are associated with high concentrations of Co in the Co-Ni-Ga system. Although Co_2NiGa has been reported to show FMSA behavior [33], we observed no martensitic

transformation for the spread. It is known that martensites in Co_2NiGa are unstable phases formed by quenching. Because we do not quench our samples, we do not expect to see martensites that result from quenching. Thus, it is perhaps not unreasonable to state that in general our technique for the most part is sensitive to detecting thermodynamically stable martensites only.
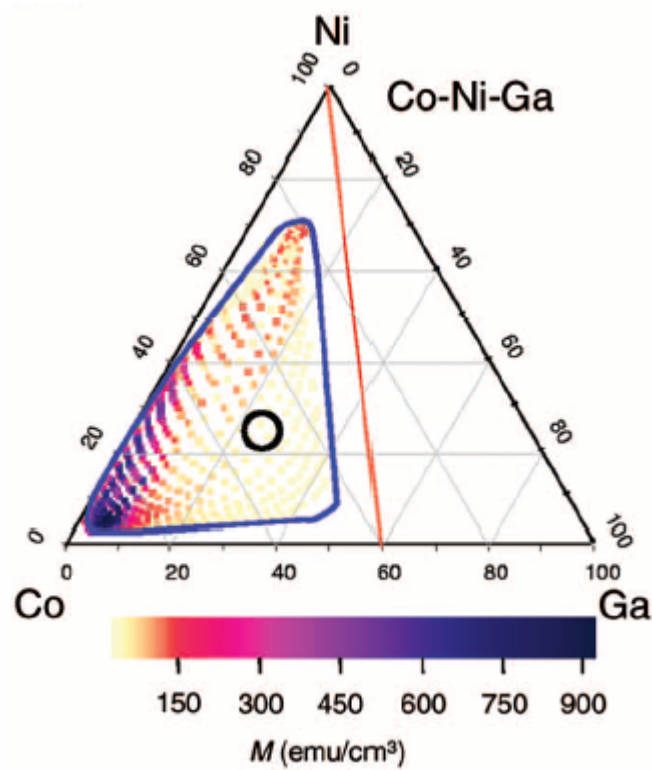
Figure 3-33: Mapping of the room-temperature remanent magnetization of Co-Ni-Ga system. Regions inside the blue curve are the composition regions mapped on the spread wafer. The composition where the red line meets the Co-Ga line is Co_2Ga_3, which is one of the three target compositions used in the experiment. The black circle marks the composition near the Heusler composition in the system.

3.4.3.3 Ni-Fe-Al

Figure 3-34, shows the magnetic ternary phase diagram of the Ni-Fe-Al system at room temperature. Targets of Ni, Fe, and Al were used to deposit the thin film composition spread. The strongly magnetic region of the phase diagram was observed to occur near the Fe rich region (Figure 3-34(a)).
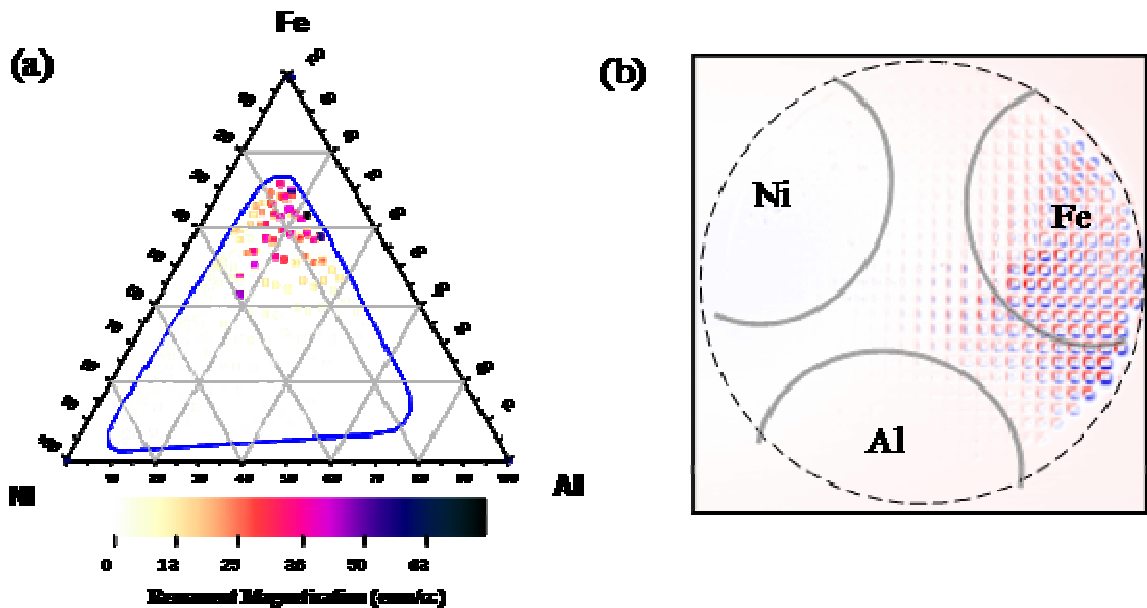
Figure 3-34: Map of the room-temperature remanent magnetization of Ni-Fe-Al system. (a) Magnetic phase diagram of Ni-Fe-Al system. Regions inside the blue curve are the composition regions mapped on the spread wafer. (b) Scanning SQUID image of a N-Fe-Al spread wafer. The black-dashed circle marks the boundary of the wafer.

Synthesis conditions were similar to those of the Ni-Mn-Ga and Ni-Mn-Al systems.

We did not observe any martensitic transformation in this composition spread reproducibly. We did make one sample that showed a small region of martensitic transformation as detected by the cantilever array visual inspection method. But we were

unable to reproduce the results in subsequent samples and measurements on the same sample. We believe that the phase that showed the martensitic transformation was an unstable phase. The result from this one spread sample is summarized in Figure 3-35 below.
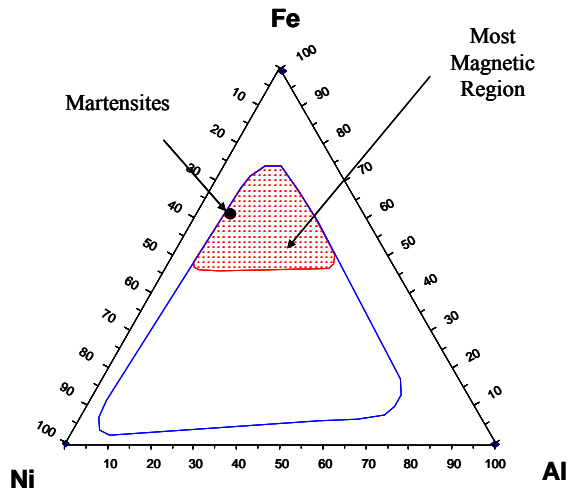
Figure 3-35: Summary of results from a composition spread that showed martensitic transformation. The magnetic region is indicated in red and the martensitic region in the black dot.

3.4.3.4 Ni-Mn-In

Figure 3-36, shows the scanning SQUID image results from a scan of Ni-Mn-In system at room temperature. Targets of Ni, Mn, and In were used to deposit the thin film composition spread. Synthesis conditions were similar to that used for the Ni-Mn-Al system. The strongly magnetic region of the phase diagram was observed to occur near the Ni rich region (Figure 3-36(a)). However, in a few samples there was a region in the middle of the samples that showed magnetic properties (Figure 3-36(b)).
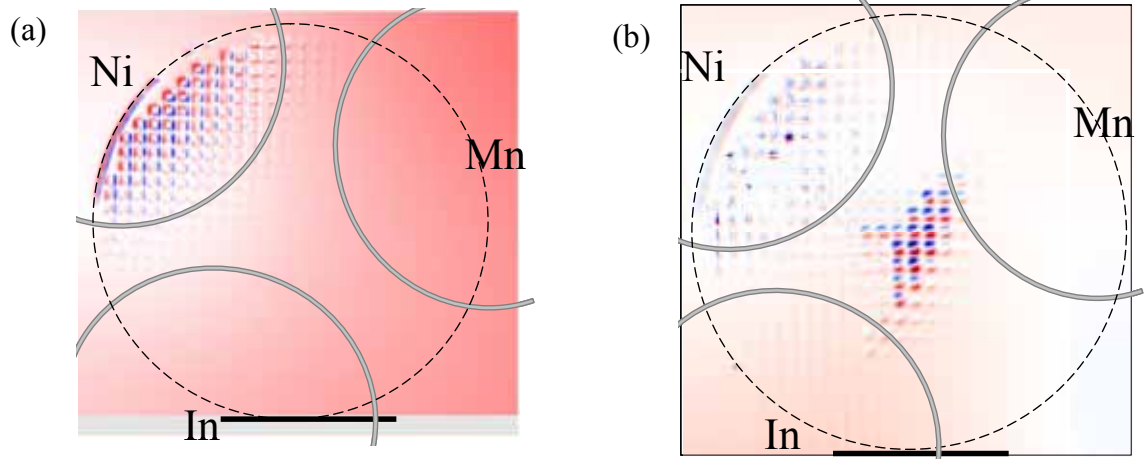
Figure 3-36: Scanning SQUID image results of composition spread scans of two spreads . (a) Shows only the Ni rich region of the spread to be magnetic (b) Shows regions other than the Ni rich with magnetic properties.

3.4.3.5 Gd-Ge-Si

It was reported that some compositions in the Gd-Ge-Si system may be FSMAs [55]. It is known that there are thermomagnetic materials in this ternary system. Thus, we decided to take a quick look at this system.

Targets of Si backed with copper, Ge, and Gd were used to deposit the thin film composition spread. Synthesis conditions were similar to that used for the Ni-Mn-Al system. Figure 3-37, shows the scanning SQUID image results of a scan of the Gd-Ge-Si system at room temperature.   The scan showed that the composition spread was not magnetic at room temperature. This is consistent with the fact that the T_c for Gd is close to room temperature. Therefore no further work was done on this system. It would be interesting to pursue this system using low temperature magnetic measurements as well as martensite detection measurements in the future.
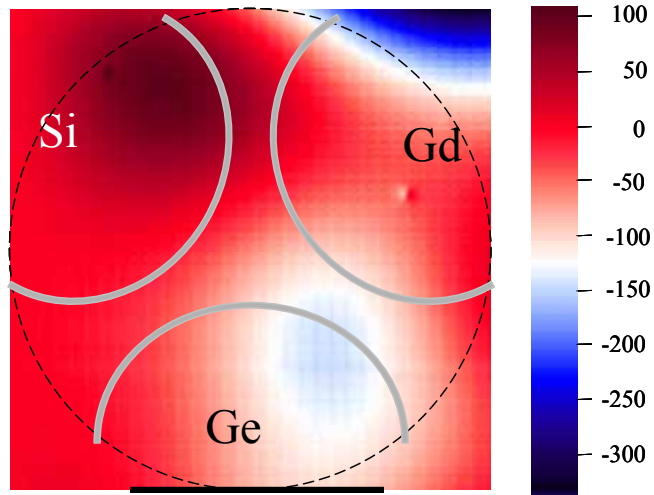
Figure 3-37: Scanning SQUID image of a Gd-Ge-Si spread wafer. The black-dashed circle marks the boundary of the wafer. Small changes in contrast observed here are due to background.

3.5 Conclusions

Using thin-film composition spreads, we have mapped the functional phase diagram of a number of ternary alloy systems in search of FSMA compositions. A characterization technique that allows detection of martensitic transitions by visual inspection was combined with quantitative magnetization mapping using scanning SQUID microscopy.

We found in both the Ni-Mn-Ga and Ni-Mn-Al systems that there are large, previously unexplored regions outside the Heusler composition which contain reversible martensites that are also ferromagnetic. A clear relationship between magnetization and the martensitic transition temperature was observed in the Ni-Mn-Ga system, revealing a strong thermodynamical coupling between magnetism and martensitic instability across a large fraction of the phase diagram.

We have also obtained room temperature remanent magnetization mapping for Co-Mn-Ga, Ni-Co-Ga, Ni-Fe-Al, Ni-Mn-In, and Gd-Ge-Si systems. We did not find reproducible evidence of martensites in many of these other systems. This however does not rule out the possibilities that there are martensites in these systems. This is because we make our wafers in a "pseudo-equilibrium" manner and many of the martensites are known to be metastable phases formed via quenching. We could instead conclude that in these systems there are no stable martensitic phases which can be formed by equilibrium processes without quenching. One can perhaps argue that martensites which are stable at room temperatures and can be formed without quenching are more suitable for applications. Our composition spread detection technique is ideal for such martensites.

Our work also reinforces the importance of systematically exploring structural transitions in looking for novel ferroic materials as well as understanding their physical origin. Guided by techniques such as the ones described here, it would also be possible to make a systematic search and survey of functional correlations of other multiferroic materials.

Chapter 4

Combinatorial Search for "Ideal" Thermoelastic Shape Memory Alloys

In this chapter, we describe an experiment where we used combinatorial synthesis to search for "*ideal*" thermoelastic shape-memory alloys. First I will define what we mean by an "ideal" thermoelastic shape memory alloy. I will discuss the motivation for this work and briefly discuss the geometric non-linear theory of martensite which was used as a guide in the search. The theory provides a phenomenological model of the martensitic transformation that occurs in shape memory alloys. The theory relates the thermal hysteresis of a martensitic transformation to the lattice parameters of the alloy.

The experiment we have performed was aimed at verifying the geometric non-linear theory. In order to test the relationship between the hysteresis and lattice parameters predicted by the theory, a large number of different compositions need to be studied. This was facilitated by the composition spread approach. I will discuss different approaches we used to systematically study the martensitic transformation in the thin film alloys. We found that one of the criteria prescribed by the theory for achieving minimal hysteresis is closely obeyed. Although, we did not find any "ideal" thermoelastic shape memory alloys within the composition region we studied in the Ni-Ti-Cu phase diagram. We have demonstrated that we can use the technique we have developed here together with the criterion we verified to explore in other systems.

4.1 Introduction

Structural phase transitions in crystalline materials are often accompanied by spectacular macroscopic effects such as the onset of ferroelectricity and ferroelasticity. One measure of efficacy of a structural transition is its reversibility, which has profound technological implications in a wide range of applications from fatigue life in SMAs to magnetism in multiferroic oxides. Recently, there has been significant development in the field of martensitic phase transition [1, 2]. At the center of the development is the geometric nonlinear theory of martensite universally applicable to all structural transitions [3]. The theory predicts the reversibility of the transition as manifested in the hysteresis behavior based solely on crystal symmetry and geometric compatibilities. It can be used to explain the fundamental cause of large transformation hysteresis commonly exhibited by thermoelastic shape memory alloys (SMAs). In particular, the theory prescribes a set of constraints on the lattice parameters in order for a SMA to exhibit extremely low thermal/stress hysteresis. We thus define, the "ideal" SMA to be the one with minimal hysteresis width. This is directly related to a change in lattice parameter of the material. While the theory can be used as a general guideline for identifying SMAs with minimal hysteresis, it is not practical to use conventional bulk methods to systematically search for such alloys because of the limited throughput.

In this chapter, I will discuss the experimental verification of the geometric non-linear theory of martensite using the combinatorial high-throughput approach. We have devised the thin film composition spread technique to rapidly map the lattice parameters

and the thermal hysteresis of ternary alloy systems. Variable temperature x-ray microdiffraction and synchrotron x-ray microdiffraction together with scanning four-point electrical resistivity measurements were used to map composition regions which exhibit structural phase transitions in the Ni-Ti-Cu system. We have observed a clear relationship between the thermal hysteresis and the middle eigenvalue of the transformation stretch tensor for the first time. In addition, we have identified a new region of titanium-rich SMAs with potential for better control of SMA properties due to the presence of large amount of precipitates.

4.2   Shape memory alloys (SMAs) revisited

As discussed in Chapter 3, SMAs have already found a number of uses in different applications.   SMAs derive their functionalities as sensors, actuators, and mechanical dampers from the properties of martensites and their reversible transformation. One application of special interest is the medical stent device used to prop and hold open a narrowed or blocked artery caused by the accumulation of fat and cholesterol. Currently, most stents are made of stainless steel which is sufficient for the relatively still cardiovascular arteries. However, they are not suitable for peripheral arteries which frequently involve large bending motion because the implanted steel stent would experience permanent deformations leading to fracture (Figure 4-1).
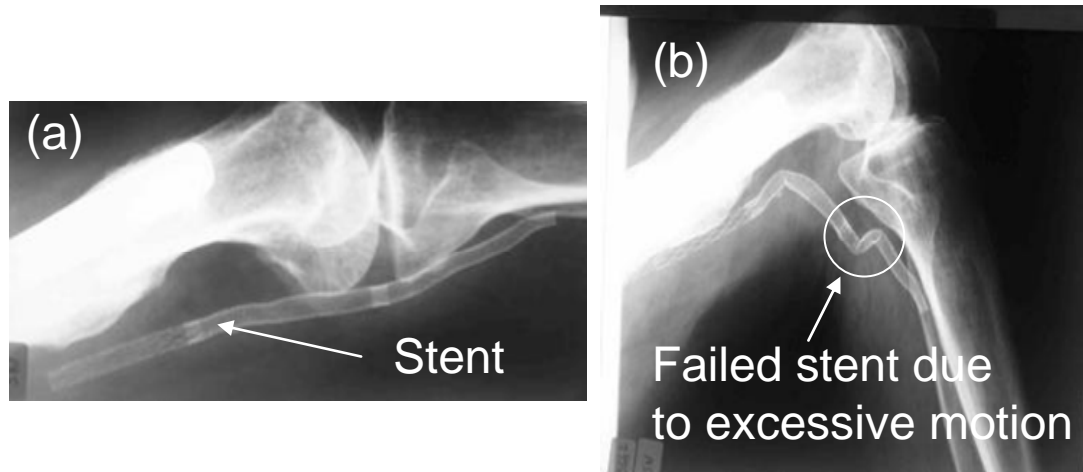
Figure 4-1: x-ray pictures showing a (a) stent crossing a movable joint in a human leg. (b) Fatigued stent in bent joint

 SMA stents, on the other hand, have already enjoyed widespread use due to their ability to recover the original shape. However, SMA stents are known to suffer from fatigue because of the existence of tensile residual stress in a corrosive environment. The large temperature/stress hysteresis, the narrow temperature range, as well as the undesirable fatigue life have hindered further incorporation of SMAs into applications despite their vast potential. Therefore, it is of paramount importance to improve and stabilize the shape memory effect in known materials and develop new materials. Among many theories and hypotheses, the geometric nonlinear theory of martensite by Ball and James [3], represents the most comprehensive theory that can guide the development of superior SMAs.

Figure 4-2 [4] illustrates the mechanism of the shape-memory effect, which was discussed in Chapter 3. Thermally induced reversible phase transformation process is shown by the solid path. All SMAs are thus thermoelastic shape memory alloys. In addition to this process, the phase transformation can also be induced by stress

loading/unloading as indicated by the dashed-line path. Our experiment has focused on the thermally driven actuation of this reversible phase transformation.
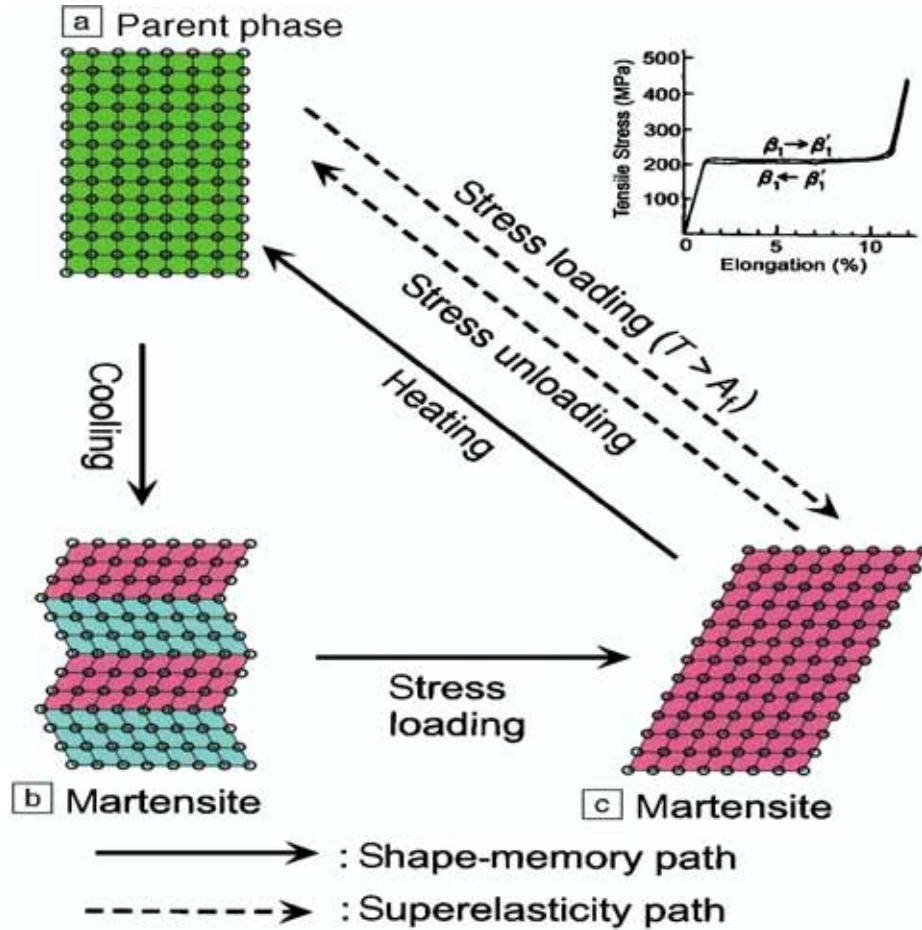
Figure 4-2: Shape-memory mechanism. [4]

4.3 The geometric non-linear theory

A martensite phase transformation is diffusionless and involves crystallographic shearing deformation. It reduces the symmetry of the parent phase (austenite) and results in formation of crystallographic domains with several possible geometric arrangements. These possible domains are referred to as martensitic variants. The variants can be

described by the transformation stretch tensor. There are several ways to transform from the parent austenite phase to the product martensite phase. Each way can be described by a 3 x 3 symmetric matrix, denoted by U_i, i = 1, ... , N. Thus, the matrices are also called variants.
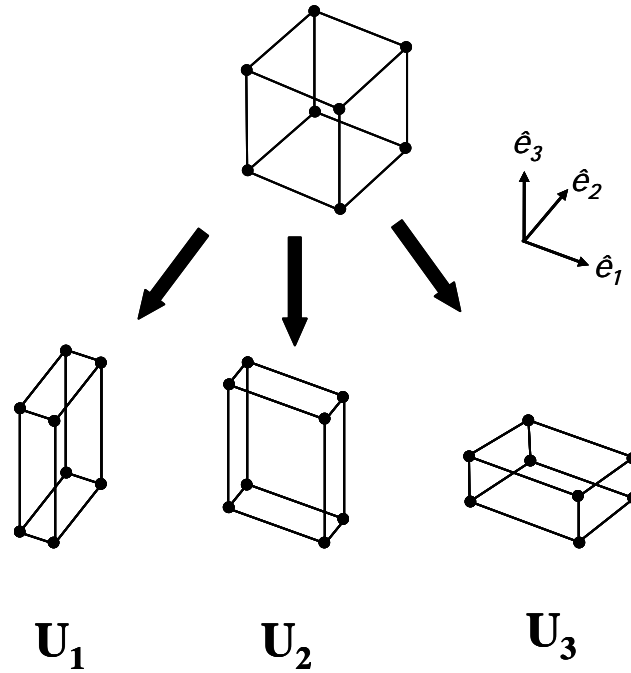
Figure 4-3: Cubic to tetragonal transition has 3 variants, U_1, U_2, and U3.

The simplest case is the cubic to tetragonal transformation. There are only three possible martensitic variants U_1, U_2, and U_3. The variants are given as follows:

$$U_1 = \begin{pmatrix} \beta & & \\ & \alpha & \\ & & \alpha \end{pmatrix} \quad U_2 = \begin{pmatrix} \alpha & & \\ & \beta & \\ & & \alpha \end{pmatrix} \quad U_3 = \begin{pmatrix} \alpha & & \\ & \alpha & \\ & & \beta \end{pmatrix}$$

where $\beta = c/a_0$, $\alpha = a/a_0$, and c, a are the lattice parameters for the tetragonal phase and, a_0 is the lattice parameter of the cubic phase. The exact form of the variants can be derived

92

if lattice parameters of both the austenite and the martensite phases are known. A more complex example is the cubic to orthorhombic transformation for which there are six martensitic variants. In the case of transforming through face-diagonal stretch, the exact forms of these variants are:

$$U_1 = \begin{pmatrix} \beta & 0 & 0 \\ 0 & \dfrac{\alpha+\gamma}{2} & \dfrac{\alpha-\gamma}{2} \\ 0 & \dfrac{\alpha-\gamma}{2} & \dfrac{\alpha+\gamma}{2} \end{pmatrix}, \quad U_2 = \begin{pmatrix} \dfrac{\alpha+\gamma}{2} & 0 & \dfrac{\alpha-\gamma}{2} \\ 0 & \beta & 0 \\ \dfrac{\alpha-\gamma}{2} & 0 & \dfrac{\alpha+\gamma}{2} \end{pmatrix}, \quad U_3 = \begin{pmatrix} \dfrac{\alpha+\gamma}{2} & \dfrac{\alpha-\gamma}{2} & 0 \\ \dfrac{\alpha-\gamma}{2} & \dfrac{\alpha+\gamma}{2} & 0 \\ 0 & 0 & \beta \end{pmatrix},$$

$$U_4 = \begin{pmatrix} \beta & 0 & 0 \\ 0 & \dfrac{\alpha+\gamma}{2} & \dfrac{\gamma-\alpha}{2} \\ 0 & \dfrac{\gamma-\alpha}{2} & \dfrac{\alpha+\gamma}{2} \end{pmatrix}, \quad U_5 = \begin{pmatrix} \dfrac{\alpha+\gamma}{2} & 0 & \dfrac{\gamma-\alpha}{2} \\ 0 & \beta & 0 \\ \dfrac{\gamma-\alpha}{2} & 0 & \dfrac{\alpha+\gamma}{2} \end{pmatrix}, \quad U_6 = \begin{pmatrix} \dfrac{\alpha+\gamma}{2} & \dfrac{\gamma-\alpha}{2} & 0 \\ \dfrac{\gamma-\alpha}{2} & \dfrac{\alpha+\gamma}{2} & 0 \\ 0 & 0 & \beta \end{pmatrix}. \quad \textbf{(1)}$$

where α, β, γ are proportional to a/a_0, b/a_0, c/a_0, , and a, b, c, and a_0 are the lattice parameters of the orthorhombic and cubic lattice, respectively.

The geometric nonlinear theory of martensite explains why martensites form microstructure and describes how this microstructure and the shape memory effect are tied to the crystalline symmetry and the lattice parameters. It shows that the microstructure arises as a consequence of energy minimization [1, 3]. In addition, it predicts various aspects of the microstructure, and consequently the macroscopic properties. The theory predicts that for a SMA to exhibit extremely low hysteresis, certain geometric compatibility has to be satisfied. Specifically, the lattice parameters of the parent and product phases must satisfy at least two conditions.

The first condition an ideal SMA must satisfy is that the determinant of the transformation matrix **U** must equal 1,

$$\det(U) = 1$$

where **U** is the stretch tensor of the martensitic variant. The determinant of the stretch tensor represents the volume change due to the transformation. The determinant of this stress tensor being equal to one signifies that the material is subject to zero volume change and allows the material to transform without introducing extra bulk energy, thus, potentially transforming with small hysteresis. In addition, the zero volume change results in the minimal residual stress, thus significantly improving the fatigue life.

The second condition an ideal SMA must satisfy is that the middle eigenvalue of the transformation stretch tensor, λ_2, must also equal one:

$$\lambda_2 = 1,$$

The significance of this second condition is that the austenite can be directly compatible with a single variant martensite. During the phase transformation, martensitic variants and the austenite all have the same free energy in the absence of biasing stress, and thus they can often coexist and form complex microstructures. A commonly observed microstructural feature for materials undergoing a martensite phase transformation is a fine band texture that consists of alternating layers of two martensitic variants meeting a homogeneous region of austenite, as illustrated in Figure 4-4 [5]. In the figure, there exists a transition layer between the twin martensite and the austenite. As the twin bands approach the austenite region, they branch into finer bands. This branching is the result of the energy minimization, a process to balance the bulk energy stored in the transition layer and the interface energy which is proportional to the surface area of the twins. By branching, the transition layer can become thinner, which reduces the bulk energy. At

the same time, the branching increases the surface area, consequently increasing the interfacial energy.
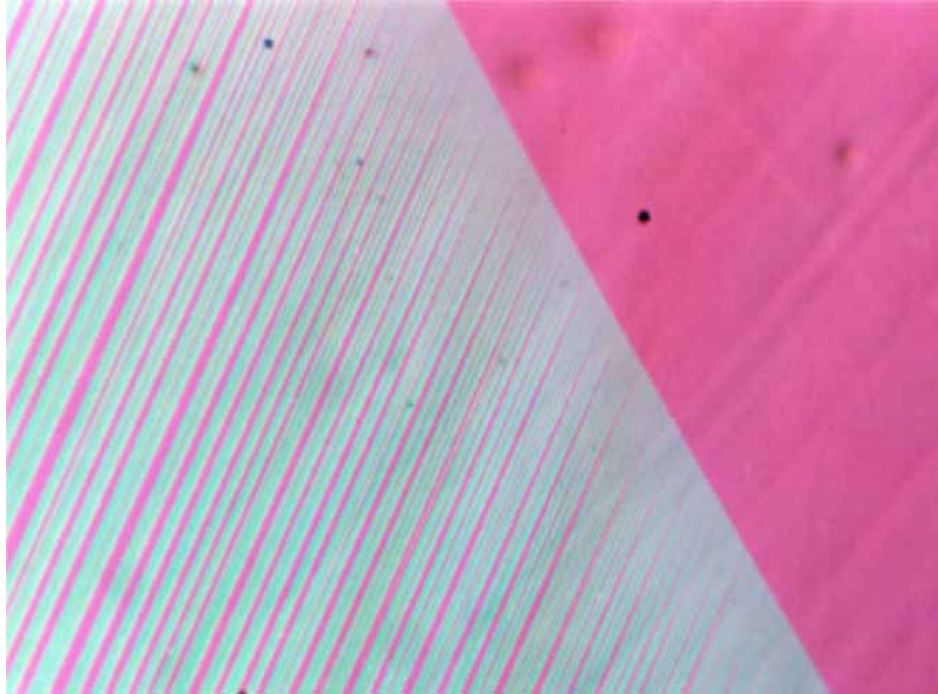
Figure 4-4: Microstructure of twin martensite meeting a homogeneous region of austenite. Courtesy of C. Chu [5].

Fundamentally, branching along with twinning is a mechanism for materials to self-accommodate the incompatibility between austenite and martensite. It is this self-accommodation mechanism that gives rise to most of the thermal or mechanical hysteresis, because time and energy are required to complete the process and to reach a local stable condition. Satisfying the second constraint will not prevent martensite from twinning, but it will bypass the self-accommodation process, i.e., twin branching.

Another possible microstructure that would minimize the hysteresis is one where the whole martensitic region consists of a single variant, which meets the austenite phase,

instead of multiple competing variants. The occurrence of this possibility is rare and requires exact crystallographic matching of the austenite and the martensite along certain directions. Such a case may exist if and only if the middle eigenvalue of the transformation stretch tensor is equal to one. The closer the middle eigenvalue is to one, the more compatible the austenite and the martensite interface are, and thus the smaller the hysteresis.

Evidence supporting the validity of these two constraints can be found in some existing SMAs. Though none of the known SMAs satisfies the two constraints exactly, some come quite close. For example, $Ni_{40.5}Ti_{49.5}Cu_{10}$ (Table 4-1) alloy has $\lambda_2 = 0.9986$ and det (U) = 1.0002. Its hysteresis is about 100 MPa and 20 °C, in terms of stress and temperature, respectively. These values are among the smallest reported to date [6, 7].

Alloys in red have unusually low hysteresis.

Alloy	Eigenvalues of U_1	Determinant of U_1
$Ni_{50}Ti_{50}$	(1.10655, 0.96627, 0.932076)	0.9966
$Ni_{40.5}Ti_{49.5}Cu_{10.0}$	(1.0534, 0.9986, 0.9508)	1.0002
$Cu_{69}Al_{27.5}Ni_{3.5}$ (orthorhombic)	(1.0618, 1.023, 0.9178)	0.9969
$Cu_{69}Al_{27.5}Ni_{3.5}$ (monoclinic)	(1.1067, 0.9959, 0.9127)	1.006
$Cu_{68}Zn_{15}Al_{17}$	(1.0944, 1.0026, 0.9093)	0.9977

Table 4-1: List of SMAs with low hysteresis

Lattice parameters are the only factors that enter into determining λ_2 and det(U). Because lattice parameters can be tuned by composition, the search of superior SMAs is then reduced to mapping the lattice parameters versus compositions for a variety of alloy

systems. This calls for a high-throughput method that can rapidly synthesize and characterize a large number of different compositions. Our combinatorial methods of synthesizing and rapidly characterizing composition spreads provide an elegant solution to the task of tracking the lattice parameter change across compositional phase diagrams. The key for this experiment is the accurate measurement of the lattice parameters to about four or five decimal places.

4.4   Fabrication of SMA composition spreads

Thin film composition spreads of the Ni-Ti-Cu ternary alloy system were prepared using the combinatorial co-sputtering system on 3 different substrate materials. The Ni-Ti-Cu system was selected for this initial investigation because this system was known to contain some compositions whose lattice parameters almost satisfy the conditions prescribed by the theory (Table 4-1). Composition spreads of the Ni-Ti-Cu ternary alloy system were deposited on 1) 2 x 1.5 inch glass substrates, 2) 3 inch silicon wafers, and 3) 3 inch Si/SiO$_2$ substrates (silicon wafer with 400±20 nm wet oxidation layer). We found that the best quality films were obtained by depositing the composition spread on the Si/SiO$_2$ substrate. Composition spread films with thicknesses 0.5~0.75 μm were deposited at room temperature followed by extensive annealing. By adjusting the power applied to each gun and the distance between the guns and the substrate, different regions of the ternary phase diagram can be mapped out as discussed previously. Some of the spreads were deposited through a metal mask with ~ 800 square holes (each 1.5 x 1.5 mm^2) in order to produce a gridded array of separate composition spread squares. WDS was used to map the compositions of every square on the spread.

It is well known that shape memory properties of the Ni-Ti-Cu films are dependent on the sputtering and post-annealing conditions [8, 9, 10, 11]. In order to quickly identify the optimum processing condition, a number of composition spreads were deposited on arrays of micromachined cantilevers [12]. The cantilever composition spread technique has been used earlier to detect occurrence of martensitic transitions in different composition regions by monitoring the deflection of the cantilevers as a function of temperature [11]. After a number of trials, we found that the films deposited at room temperature followed by annealing in vacuum at 550 °C for 2 hours followed by a high temperature annealing at 750 °C for 30 minutes displayed the optimum crystallinity exhibiting large composition region which transform martensitically (Figure 4-5). Thus, this schedule was adopted for preparing all the subsequent composition spread samples.
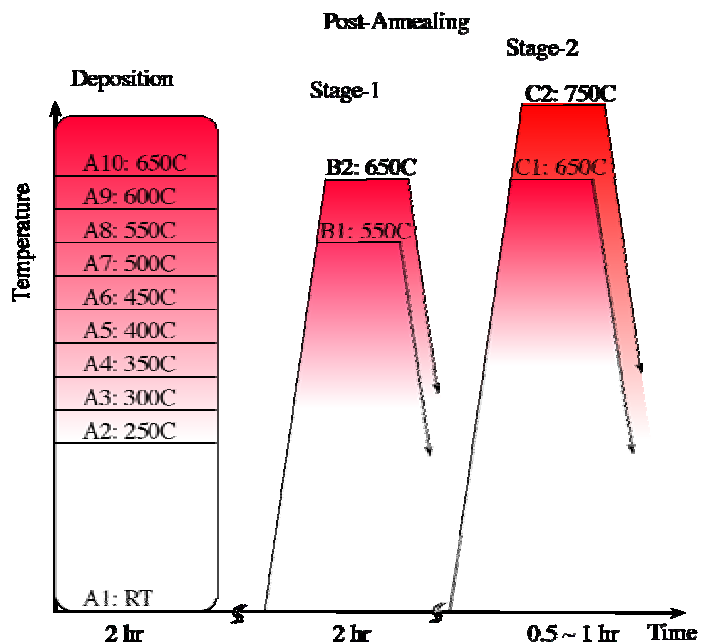
Figure 4-5: Summary of processing schedules of different composition spreads that were fabricated and treated to optimize the SMA property of the spread. Deposition temperatures, A, post-annealing temperatures, B, and high temperature treatment temperatures, C, of composition spreads for property optimization.

98

Figure 4-6 shows the regions of the Ni-Ti-Cu phase diagram that we mapped for the experiment. Even though we can map a much larger region of the ternary phase diagram for the Ni-Ti-Cu alloy system, we focused our investigation on the region that was most promising from the point of view of martensitic transformation.
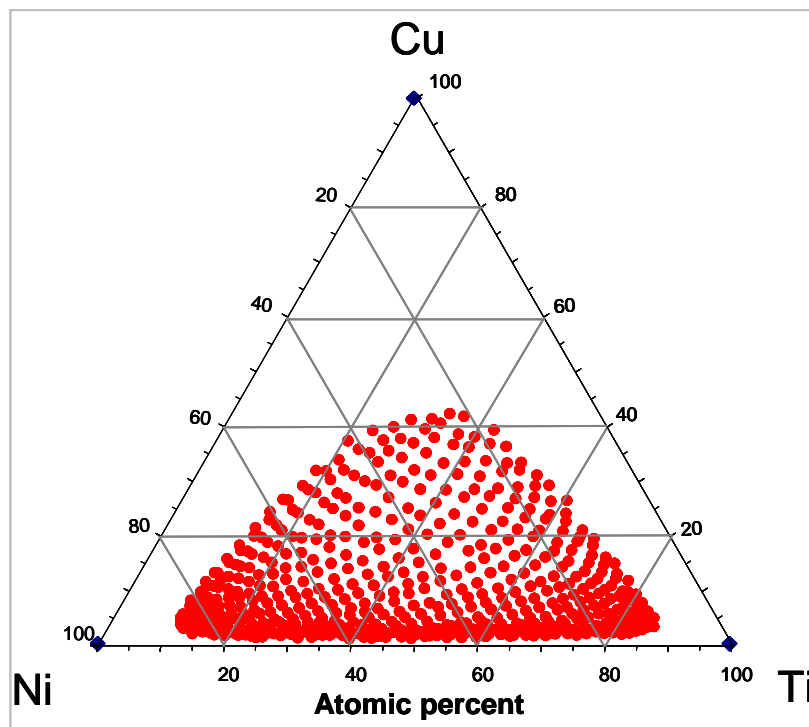
Figure 4-6: Mapped region of interest on the ternary phase diagram for the Ni-Ti-Cu alloy system.

4.5   Removing mechanical constraint from thin films

Initially, we were concerned about the mechanical constraint effect the substrate poses on the properties of SMA films. For instance, one would expect that the lattice parameters and the transformation behavior of the films are affected by the presence of

the substrate. To this end, we attempted to free parts of the deposited films from the substrate to create a library of partially free standing thin film bridges. The schematic of this approach is shown in Figure 4-7.

To accomplish this, first we need to make an array of thinned Si bridges. A layer (~ 3 µm) of positive photoresist (PR) is spun at 3000 RPM and hard baked onto the front and back sides of a 350-400 µm thick three-inch silicon wafer with 2 µm of silicon dioxide (SiO$_2$) coating on both sides. A photolithography mask pattern is used to transfer the desired patterns onto the front and back side of the wafer by exposing the mask under a UV-400 light source.
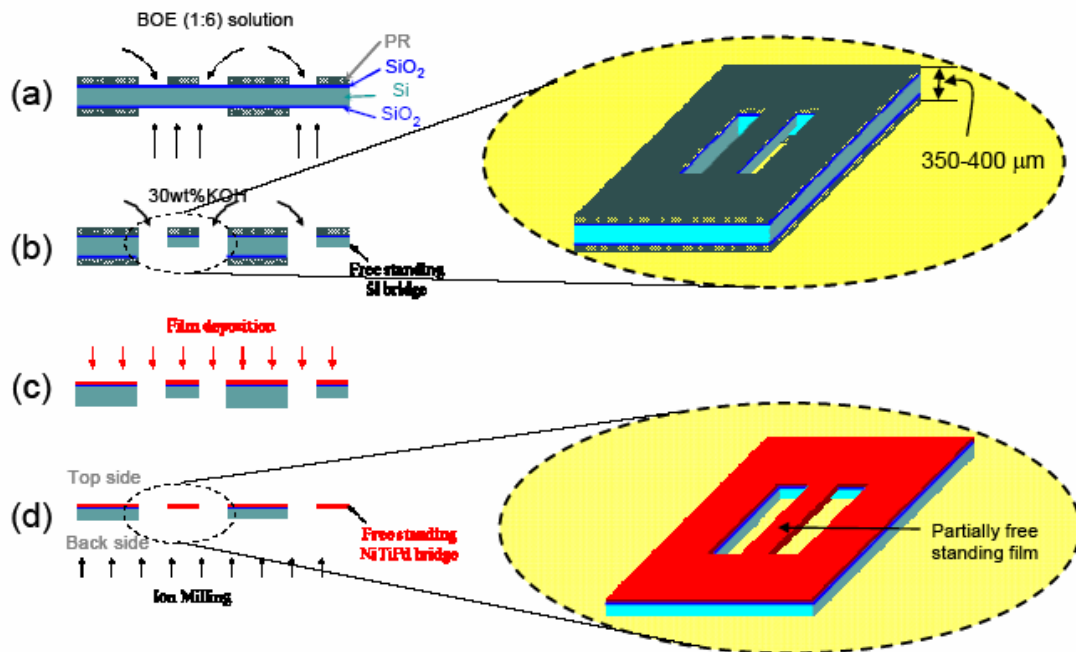
Figure 4-7: Step-by-step schematic of the micromachining process for creating partially free standing film. (a) Buffered oxide etch (BOE) etching, (b) KOH etching of Si, (c) composition spread deposition on arrays, and (d) ion milling back side to create the partial free standing film.

Using a developing solution, AZ 400K or CD-30, the exposed regions of the PR will dissolve and be removed from the surface of the wafer leaving behind the desired pattern as seen in Figure 4-7(a). The patterned PR wafer is then dipped in a buffered oxide etchant, BOE (mixture of hydrogen fluoride and ammonium fluoride (1:6)) to remove the SiO_2 layer. The PR is then removed using acetone, methanol and de-ionized water, and the silicon dioxide now serves as the mask. This step is immediately followed by anisotropic silicon etching in a 30% (by volume) potassium hydroxide (KOH) solution until the pattern etches through the wafer as in Figure 4-7(b). Additional time is allowed for the silicon bridge to reach the desired thickness, typically about ~ 70-100 μm. The wafer is cleaned and the composition spread is deposited on the micromachined free standing bridge array as shown in Figure 4-7(c). After deposition of the spread, the back-side of the wafer can then be etched to remove the remaining Si/SiO_2, as shown in Figure 4-7(d), to obtain the partially free standing films. The "bridge" films are only partially free standing in the sense that the edges of the bridges are still clamped by the film on the substrate.

There were two ways to accomplishing the micromachining of the free standing thin film bridge array on the wafers. One approach is to use a wet etching technique to pattern the substrate prior to film deposition followed by ion milling the rest of the substrate after films are deposited to obtain a free standing library of films. The second is using wet etching for both steps. However, since access to an ion mill was not available, the second approach was adopted. This process proved to be difficult and not very

successful.   Figure 4-8 is a picture of a micromachined array of partially free standing structures.
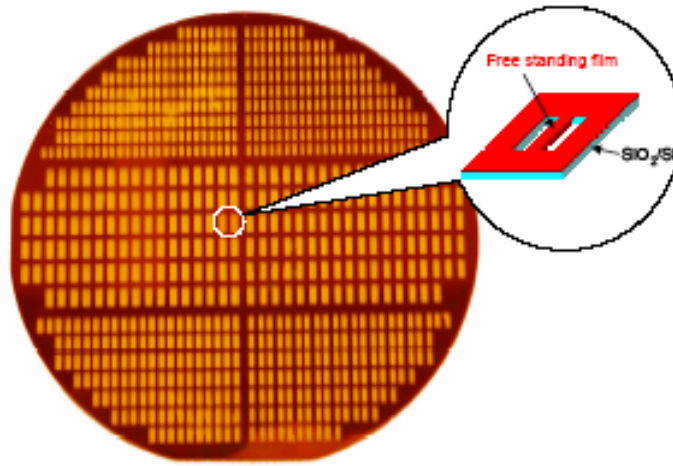
Figure 4-8: A micromachined free-standing SiO_2 coated Si wafer array.

The main problem with this approach was that the etchant attacked the deposited film in addition to removing the substrate from the film.   In addition, over-etching occurred leading to the dimensions of the free standing films to vary very drastically across the wafer array.   This added an additional variable to the library which would have to be taken into consideration during characterization.

We took an alternative approach to reducing the effect of the mechanical constraint from the substrate. The idea is to transfer the deposited film onto a polymer matrix which has substantially less constraint. The constraint is expected to scale with the Young's modulus. The Young's modulus of the different constraining materials in contact with the composition spread squares are listed in Table 4-2 below.

	(100) Si	SiO$_2$	M-Bond 43B
Young's modulus	125 to 130 (GPa)	66 (GPa)	3 (GPa)

Table 4-2: Young's modulus of the different constraining substrate materials that are in contact with the composition spread.

We prepared several composition spreads where films are lifted and transferred from the original Si/SiO$_2$ substrate and embedded into a soft polymer matrix.
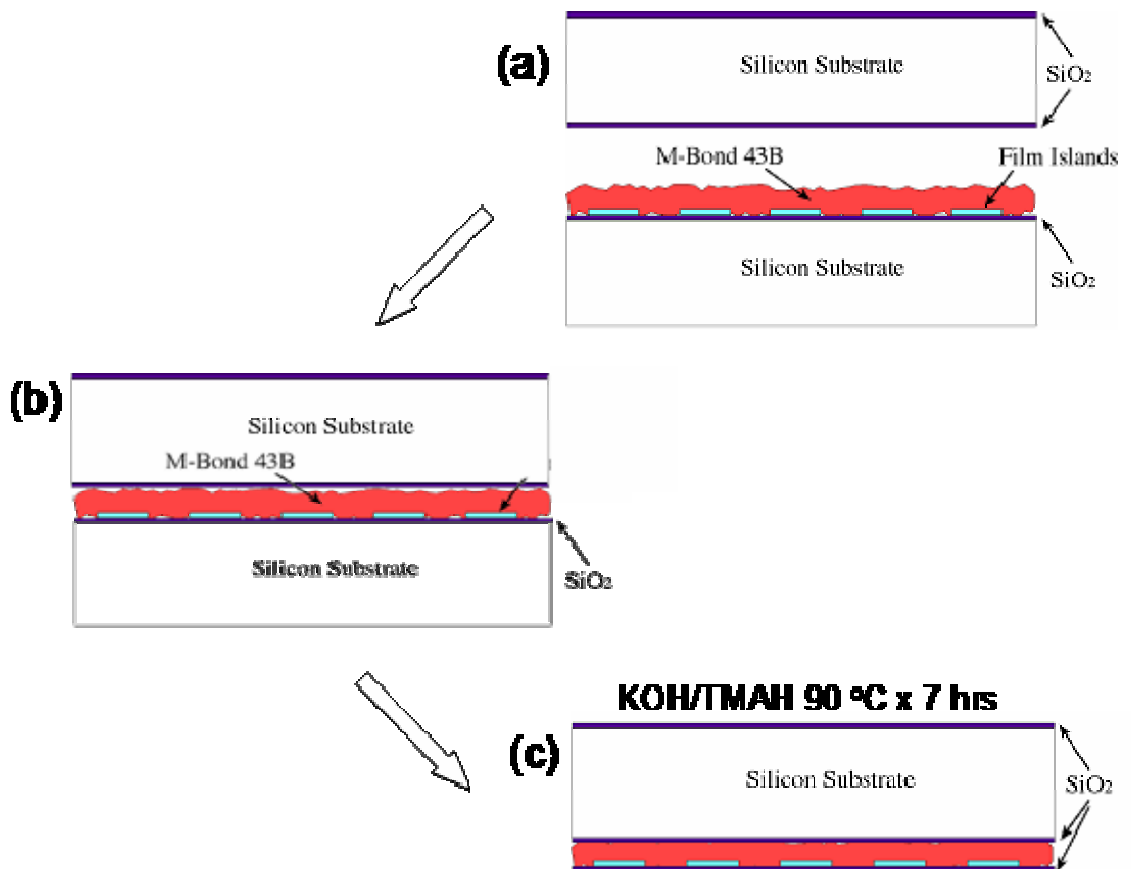
Figure 4-9: Scheme of transferring a film onto a polymer matrix. (a) Polymer is applied onto spread wafer, and another silicon wafer is placed on top. (a) Wafers are clamped and polymer is cured, (b) and the original spread Si wafer is etched away from the back to leave the embedded film.

103

This process is shown in Figure 4-9. The polymer matrix material that we adopted was M-Bond 43B (Bisphenol-A epoxy resin). A composition spread of the Ni-Ti-Cu ternary alloy system was deposited on a SiO_2/Si substrate. The spread was covered with the polymer (M-Bond 43B) and another plain wafer so that the spread and polymer are sandwiched between the two wafers (Figure 4-9(a)). The two wafers are clamped (Figure 4-9(b)), and the M-bond is allowed to cure in an oven at 175 ^{o}C for 2 hrs. The SiO_2 on the back side of the original composition spread wafer is etched away in BOE. The exposed silicon is then etched away using a 30 wt% KOH or 20 wt% tetramethyl ammonium hydroxide (TMAH) solutions (Figure 4-9(c)). We observed that the KOH etching was too aggressive and attacked the deposited composition spread whereas the TMAH solution was less aggressive and ideal for our etching process.

To our surprise, films on the polymer matrix did not exhibit significant departure in structural properties (as determined by x-ray diffraction) from films on regular Si/SiO_2 substrates. This may be understood in view of the fact that the residual stress that is expected to cause lattice distortion may very well be relaxed by the post-deposition heat treatment. In light of this finding, all the results described in this chapter were taken from composition spreads on their original Si/SiO_2 substrates.

4.6   Screening of SMA composition spreads

After the SMA composition spreads are made, properties of materials on the composition spread need to be measured. In particular, in order to verify the non-linear geometric theory, we need to be able to measure the composition hysteresis, and the lattice parameters at each point. Prior to this project, we had extensively used arrays of micromachined cantilevers for detection of martensites. For the experiment described in this chapter, the thermal transformation hysteresis was measured for each point on the wafer using the principle that SMA films exhibit abrupt changes in their electrical resistivity due to phase transformations [13]. Electrical resistance, R of the library was mapped by scanning the entire library with a four point probe at a constant temperature (Figure 4-10). This measurement was carried out by A. Ludwig at the Caesar Research Center, Germany. This technique has the advantage over cantilever technique that the measurements are more spatially localized on the wafer.
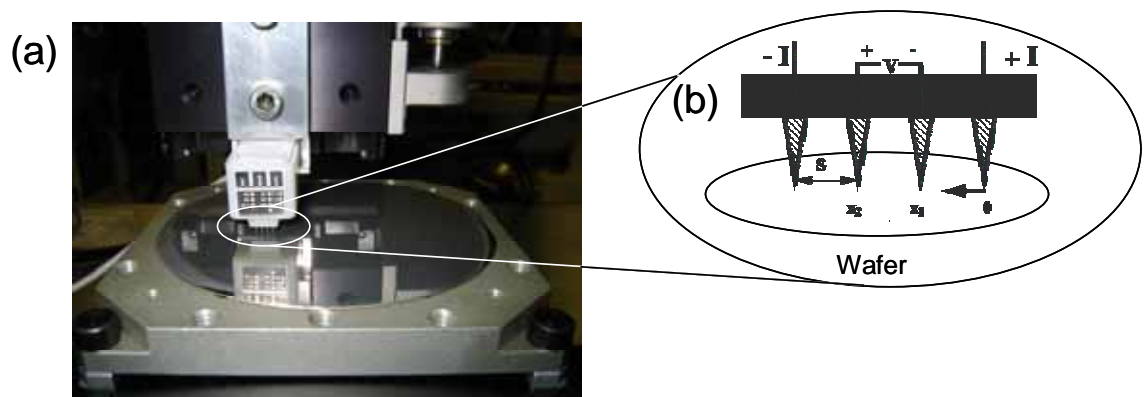
Figure 4-10: (a) A picture of a typical four point probe measurement system (b) Schematic of probe head: Current is fed in and out through the outer probes while the voltage drop across the film is measured by the two inner probes x_1 and x_2.

The mapping was then repeated at different temperatures from -20 to 100 °C, then back to -20 °C with a 2 °C increment. Following the measurement, R(T) curves (electrical resistance versus temperature) of each composition was plotted, and the transformation temperatures were then determined from the R(T) curves. Figure 4-8 shows a typical heating and cooling R(T) curves of the selected spots with and without transformations on a library. It also depicts the rule of determining the transformation temperature and hysteresis. We determine the temperature at which the slope of the R(T) curve starts to display significant departure from linearly and/or monotonically changing R(T) regions as the location of transformation. We have defined the hysteresis as the difference in this temperature observed between R(T) taken during a warm-up process and that taken during cool-down process. While significantly more time-consuming compared to the cantilever library technique [11], this technique represents a significant improvement in providing accurate and quantitative information regarding transformations across libraries and composition spreads.

The high-throughput structural characterization is the other important feature of this study. Characterization of the crystal structure was carried out using x-ray microdiffractometer with a synchrotron source located at the beam line 2-BM (bending magnet) at the Advanced Photon Source (APS), Argonne National Laboratory. Because of the brilliance of the x-ray source at APS, it only requires 3 minutes per spot to obtain enough diffraction data for complete lattice parameter analysis from a textured thin film sample. In comparison, such an analysis with our in-house x-ray diffractometer would require approximately 3 hours per spot. (This would translate to over 2400 hours if we had to perform the measurement using the in-house diffractometer.) Synchrotron
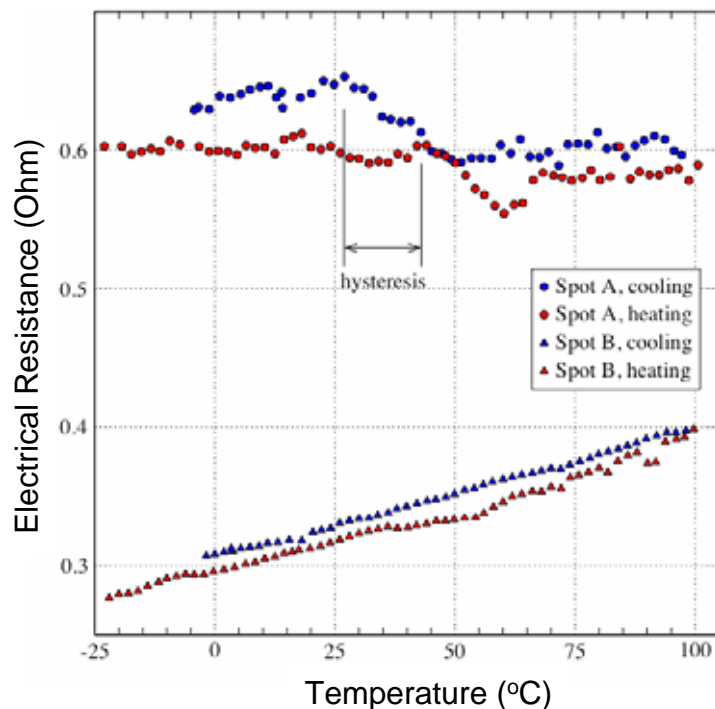
Figure 4-11 : Temperature dependence of the electrical resistance. Composition of spot A is $Ni_{25.7}Ti_{72.6}Cu_{1.7}$, and spot B is $Ni_{78.4}Ti_{13.1}Cu_{8.5}$.

diffraction experiment was assisted by Yong Chu at the Advanced Photon Source, Argonne National Laboratory, Argonne, Illinois.

In this study, the beam size was focused to 0.1 x 0.1 μm^2, and the photon energy was set to 15 keV. A CCD camera was positioned at $2\theta = 34°$ and 65 mm from the sample. The camera took images at 3 different θ angles, 10°, 12°, 14°, and at 2 different temperatures, 135 °C and 0 °C. The exposure time of each image was 3 minutes. An algorithm was developed to convert the images to diffraction patterns. It was calibrated using a NIST prepared CeO_2 standard and verified using silicon powder. Example images and integrated diffraction patterns are shown in Figure 4-9. Difference in the spectra at

the two temperatures indicates that a martensitic transformation takes place for this composition.
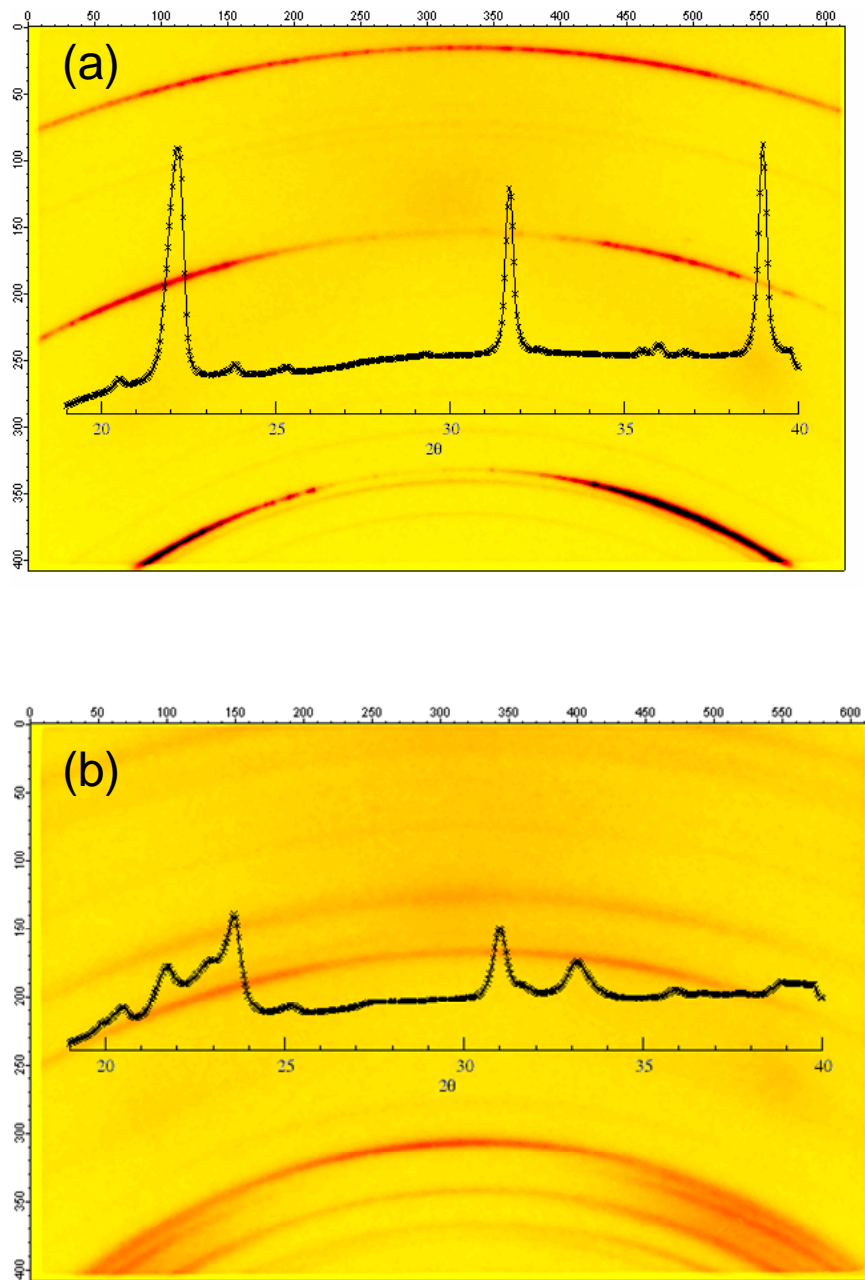
Figure 4-12: X-ray diffraction images and integrated patterns of the spot with composition $Ni_{35.4}Ti_{62.9}Cu_{1.7}$. The images were taken at (a) 135 °C and (b) 0 °C, respectively.

Lattice parameters were extracted from these diffraction patterns, and then they were used to calculate the transformation stretch tensors and the determinant det(**U**) and the middle eigenvalue λ_2. The lattice parameters were obtained by performing a structural refinement on the x-ray diffraction patterns for each square on the spread using a program called CMPR [14] refinement.

4.7   Results and discussion

Figure 4-13 shows the transforming regions and the thermal hysteresis as deduced from the R(T) measurements. The measurements produced about two thousand R(T) curves, examples of which are shown in Figure 4-11. While some curves clearly showed reversible transformations, others were less obvious. In Figure 4-13, only the regions with unambiguously discernible transformations behavior are shown. It is known that alloys that exhibit shape memory effect in the Ni-Ti-Cu alloy system are near Ti 50 at.% with Cu varying from 0 to 20 at.% as shown by the strip enclosed by the white dotted lines. However, the exact boundary of the shape memory regions on the Ni-Ti-Cu phase diagram is not known. Although this study was not designed to answer this question, it is able to provide an answer. We see that the transforming region is already significantly extended from the strip near the Ti 50 at.% line.

One striking result clearly present in Figure 4-13 is the transforming region with titanium varying from 65 to 77 at.% and Cu varying from 0 to 4 at.%. Synchrotron x-ray analysis of the film with 68 at.% Ti and 3 at.% Cu verified the reversible transformation. The x-ray diffraction spectra of this spot are shown in Figure 4-12. In addition, the x-ray

patterns also showed large amounts of Ti_2Ni precipitates which is consistent with the

high concentration of Ti in the alloy. This is an exciting finding from an application's
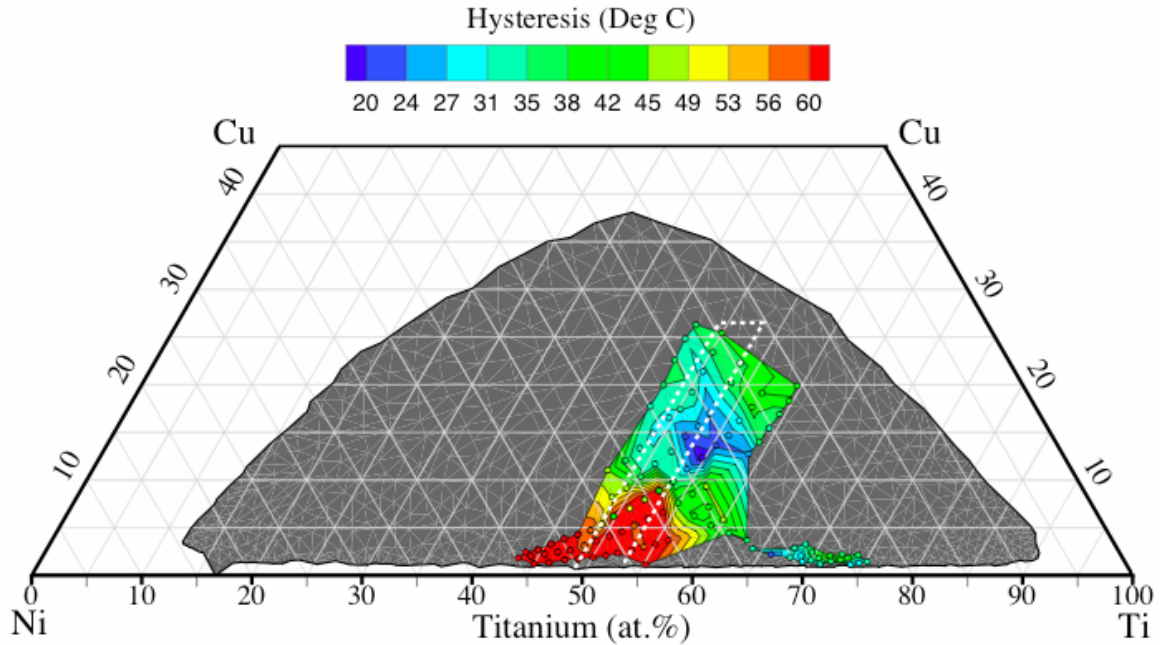
Figure 4-13: Transforming regions and thermal hysteresis in the Ni-Ti-Cu alloy system. The grey shaded region represents the overall composition region covered in the composition spread. The strip area enclosed by white dotted lines represents the compositions previously reported to exhibit the shape memory effect.

point of view because low concentration of Ni implies better biocompatibility, and the

large amount of precipitates promises more control over the shape memory properties

such as transformation temperatures and the level of the superelasticity plateau, which

can be by adjusting the heat treatment schedule. To verify this finding, four bulk samples

with compositions $Ni_{35.4}Ti_{62.9}Cu_{1.7}$, $Ni_{33.6}Ti_{65.2}Cu_{1.2}$, $Ni_{35}Ti_{65}$, and $Ni_{25}Ti_{75}$ were prepared

by arc melting. Differential scanning calorimetry indicated that all the alloys transformed

to the austenite near 50 °C, and to martensite near 75 °C, which are in good agreement

with the transformation behavior observed on the composition spread wafer. While these

alloys do not exhibit the low hysteresis we were looking for, their lower Ni content and more adjustable SMA properties compared to the well-known Ni-Ti SMA composition is highly attractive for medical applications. This finding is a good example of serendipitous discoveries made by the combinatorial approach.

Another interesting finding as seen in Figure 4-13 is the thermal hysteresis distribution. It shows that the composition with minimum hysteresis is located near Ti 55 at.% and Cu 12 at.%. From this spot, any variation of Ni, Ti or Cu concentrations results in large increase of hysteresis, especially toward the lower copper concentration where zero copper yields the largest hysteresis. If the concentration of titanium is focused to 47 to 52 at.% as most published research has been, the minimum hysteresis becomes higher, and the region with minimum hysteresis changes to Cu 12 to 20 at.%, which agrees with the published data [15, 16].

According to the geometric non-linear theory, the transformation hysteresis is directly related to how close the values of the det($\mathbf{U}$) and λ_2 are to 1. Figure 4-14, summarizes our findings. Each data point corresponds to one composition in the region mapped in Figure 4-13. We observe a clear relationship between the hysteresis and the value of λ_2 in agreement with the theory. As for the plot of det($\mathbf{U}$), the trend is less clear. From these results, it seems that the det($\mathbf{U}$) value is not as critical as λ_2 in determining the hysteresis behavior. This is indicative of the fact that the compatibility along the austenite/martensite interface plays a bigger role on the transformation hysteresis than the volume change of the material during the phase transformation. This is in accord with the notion that better compatibility along the interface signifies better ability to self-accommodate the transformation deformation, and as long as the transformation

deformation is easily digested by the material, the volume change caused by the transformation becomes less important. A simple way to look at this is that the geometric
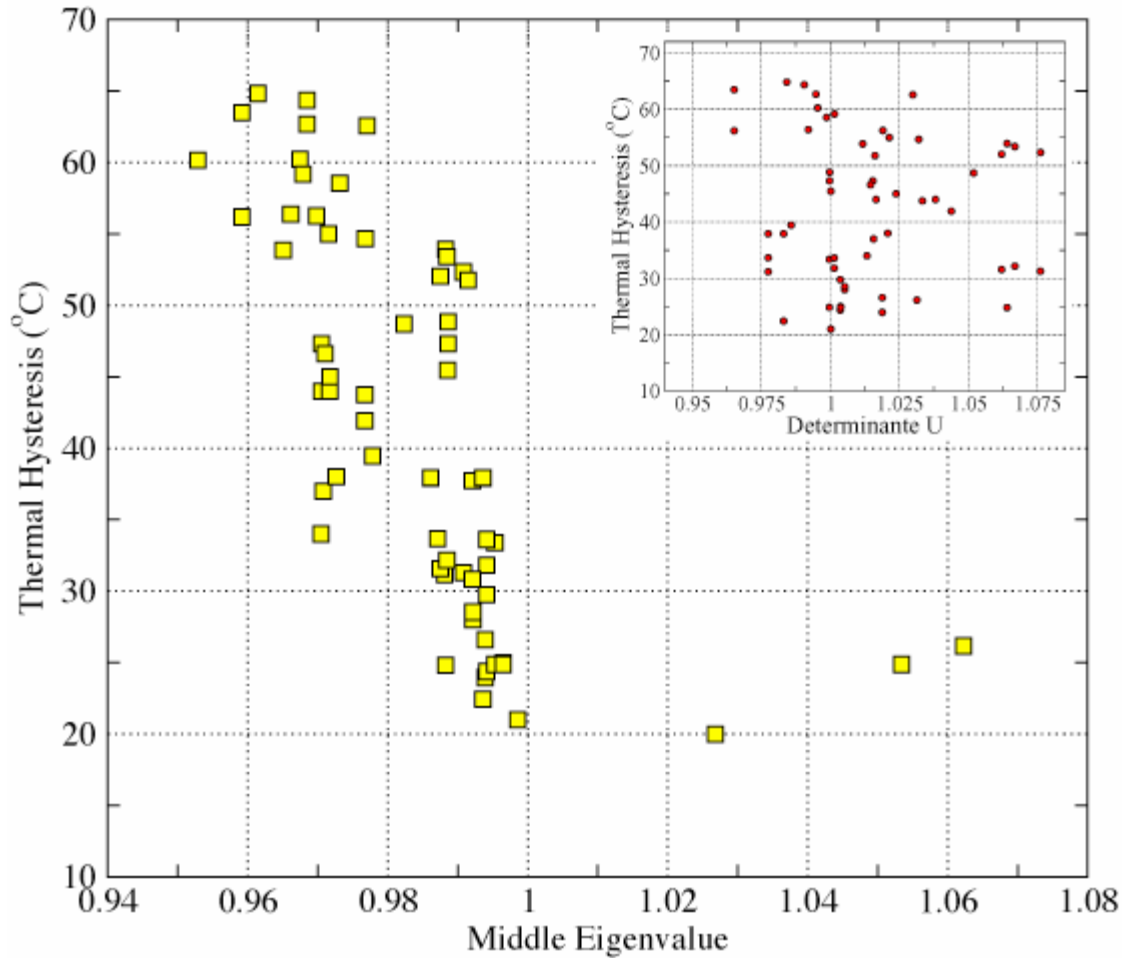
Figure 4-14: Transformation hysteresis versus the determinants and middle eigenvalues of the transformation stretch matrix.

compatibility describes the efficiency and the volume change describes the size of the work. As long as the efficiency is high, the size is less important. However, if the size is too big, then regardless of the efficiency, the energy cost will still be high. Using this argument, we can understand that for a martensitic phase transformation, the transformation hysteresis will be smaller if the parent and product phases are more

compatible and if their volume difference is not substantial. This is the first time that the geometric non-linear theory of structural transformation has been experimentally verified.

4.8 Conclusions

We have developed high-throughput techniques for mapping the structural transition behavior of shape memory alloy thin films using synchrotron x-ray microdiffraction and a 4-terminal resistance mapping probe. Complete lattice parameters and martensitic transition hysteresis were obtained for a selected region in the Ni-Ti-Cu system in order to test the geometric non-linear theory of structural transitions which is widely applicable to any transformation between crystal structures. A clear evidence of the validity of the theory was obtained for the first time. New shape memory alloys were identified in the Ti-rich region of the phase diagram.

This experiment underscores the effectiveness of the combinatorial approach in systematically validating phenomenological theories in general. Indeed, if one were to carry out such a study using the conventional one-by-one bulk synthesis and characterization techniques, it could take years just to cover one phase diagram. The present study represents an important step in our search for SMAs with minimal hysteresis. We can now use the middle eigenvalue constraint as the main guideline to delineate the search direction. Other ternary alloy systems are currently under investigation.

Chapter 5

Conclusions and Recommendations for Future Work

5.1 Conclusions

In this thesis, combinatorial synthesis has been used to systematically explore a variety of ternary FMSA and SMA alloy systems. We have developed a novel rapid characterization technique that allows us to qualitatively and quantitatively screen entire composition spreads in a single experiment for properties of interest.

In Chapter 3, using thin-film composition spreads, we have mapped the functional phase diagram of a number of ternary alloy systems in search of FSMA compositions. A characterization technique that allows detection of martensitic transitions by visual inspection was developed and combined with quantitative magnetization mapping using scanning SQUID microscopy for this purpose.

We found in both the Ni-Mn-Ga and Ni-Mn-Al systems that there are large, previously unexplored regions outside the Heusler composition which contain reversible martensites that are also ferromagnetic. A clear relationship between magnetization and the martensitic transition temperature was observed in the Ni-Mn-Ga system, revealing a strong thermodynamical coupling between magnetism and martensitic instability across a large fraction of the phase diagram.

We have also obtained room temperature remanent magnetization mapping for Co-Mn-Ga, Ni-Co-Ga, Ni-Fe-Al, Ni-Mn-In, and Gd-Ge-Si systems. We did not find reproducible evidence of martensites in many of these systems. This however does not

rule out the possibilities that there are reversible martensites in these systems. This is because we make our wafers in a "pseudo-equilibrium" manner and we can not detect many of the martensites which are known to be metastable phases formed via quenching. We could instead conclude that in these systems there are no stable martensitic phases which can be formed by equilibrium processes without quenching. One can perhaps argue that martensites which are stable at room temperatures and can be formed without quenching are more desirable for applications. Our composition spread detection technique is ideal for search of such martensites.

The result here reinforces the importance of systematically exploring structural transitions in looking for novel ferroic materials as well as understanding their physical origin. Guided by techniques such as the ones described in here, it would also be possible to make a systematic search and survey of functional correlations of other multiferroic materials.

In Chapter 4, we have developed high-throughput techniques for mapping the structural transition behavior of shape memory alloy thin films using synchrotron x-ray microdiffraction and a 4-terminal resistance mapping probe. Complete lattice parameters and martensitic transition hysteresis were obtained for a selected region in the Ni-Ti-Cu system in order to test the geometric non-linear theory of structural transitions which is widely applicable to any transformation between crystal structures. A clear evidence of the validity of the theory was obtained for the first time. New shape memory alloys were identified in the Ti-rich region of the phase diagram. This experiment underscores the effectiveness of the combinatorial approach in systematically validating phenomenological theories in general. Indeed, if one were to carry out such a study using

the conventional one-by-one bulk synthesis and characterization techniques, it could take years just to cover one phase diagram. The present study represents an important step in our search for SMAs with minimal hysteresis. We can now use the middle eigenvalue constraint as the main guideline to delineate the search direction. Other ternary alloy systems are currently under investigation.

5.2 Future work

There are a variety of other interesting multiferroic ternary and higher order alloy systems to which we can apply the combinatorial methodology. Here, we list some of the ongoing and future work in our group.

In this thesis we have demonstrated the validity of this research methodology in a few ternary systems. The number of possible combinations of elements to produce ternary systems is vast. Our methodology offers us the opportunity to accelerate the exploration of the composition-structure-property relationship in different ternary phase diagrams in general. We are currently exploring other ternary alloy systems for potential FSMAs. One system of immediate interest is Fe- Ga-Pd, which contains known FSMAs and giant magnetostrictive materials.

Artificially synthesized multiferroic materials that behave as FSMAs is a future idea. Once an understanding of the composition-structure-property relationship is developed, one could conceivably proceed to come up with an artificial design of a layered or composite FSMA materials consisting of separated SMA and ferromagnetic regions. Such 'hybrid' FSMAs could have tunable magnetically induced strains with varying magnitudes. This would have a number of applications especially in sensors and actuators.

As mentioned in Chapter 3, we believe that some of the systems that did not show FSMA behavior or was not reproducible may have been due to our inability to form metastable phases in the alloys. We have recently designed and built a quenching furnace for thin film samples. This will be used to explore the effect of quenching on

FSMA thin film composition spreads. If we can quench our samples, we can potentially stabilize the metastable phases as well as systematically study the effect of order/disorder in these compounds.

We can use our combinatorial cosputtering system for investigation of metallic alloys for other applications. We are currently using the composition spread technique to explore next-generation CMOS metal gate materials and hydrogen storage materials.

The direct product of any combinatorial synthesis experiment is a large amount of data that need to be organized and analyzed. Thus, the challenge is how to properly and accurately collect, visualize, analyze and store the data. The data generated can be in the gigabytes to terabyte range for one experimental measurement. We are currently using data analysis techniques such as principle components analysis (PCA) to analyze the large amount of data collected. We are also developing visualization techniques using the MATLAB software to easily process and convert the data into visual data. The goal here is to come up with effective methods to manage the data so that we can quickly extract pertinent information and generate materials databases for future use. Much of this type of research work is yet to be fully developed and demonstrated. As these "informatics" aspects of the experiments develop, we expect to be able to implement the combinatorial strategy with greater efficiency.

APPENDICES

Appendix A: Micromachining of silicon wafers

As mentioned in earlier chapters we have used micromachining techniques to pattern silicon wafers into either physical shadow mask patterns or actual cantilever arrays for different experimental purposes. Here I will discuss their fabrication process. The procedure for carrying out the micromachining and recipes for the wet etching solutions used in the process are outlined in the Takeuchi group standard operating procedures (SOP) notebook.

The SOP is specific to the wafer type and orientation. The specifications for our wafers are as follows:

Diameter: 3.00 Inches

Type-Dopant: P/Boron

Orientation: <100>

Surface: Polished/Etched (i.e. one side is polished and the other etched)

Oxide: 2 μm of Thermal Silicon Dioxide

Resistivity: 1.0 to 10 Ohm-cm

Thickness: 330-440 μm

Growth Method: Czochralski (CZ)

The wafers can be single or double sided polished. This depends on the feature size to be patterned on each side of the silicon wafer. A good rule of thumb is for feature sizes smaller than 100 μm the surface should be polished. This allows us to obtain very

sharp features. The silicon dioxide coating serves two purposes. First, it is used in the micromachining process as a masking to transfer the desired pattern. It is also used as a diffusion barrier layer between the silicon substrate and the deposited composition spread thin film.

One important factor in the micromachining process which is sometimes overlooked and can be the cause of a number of problems is the useful life of the chemical solutions used. For example, the buffered oxide etchant (BOE- See Note at end of this section!) solution used to etch the silicon dioxide layer after the PR has been exposed and developed has about 2 to 3 etchings before it needs to be replaced with a fresh batch. The etch rate of a good batch of BOE is roughly about 0.12 μm/min at room temperature. The effective etch rate decreases dramatically with each use and is affected by the solution temperature also. A good rule of thumb is to use the same solution to process no more than 2 wafers before replacing it with a fresh batch.

Similarly, the potassium hydroxide (KOH) solutions etch rate decreases over the period of usage. Here the chemical reaction that takes place during the etching process is a limiting reaction. Once the reactants are consumed, etching will stop or dramatically decrease. A typical 25-30% by weight solution of KOH would process about 20 to 25 wafers at 70 °C. The etch rate of the KOH solution is also affected by the temperature of the solution. At 70 °C the etch rate is about 1.0 to 1.2 μm/min. At these conditions a typical wafer with a thickness of 330-440 μm would take about 5 to 6 hours to etch through assuming one etches from one side only. When etching from both sides it should take about 3 hours. One could increase the temperature of the KOH to 90 °C and this would increase the etch rate and reduce the etching time to about 3 hours to etch

120

completely through a typical wafer. However, one loses the anisotropy in the process. This can be used for large feature sizes or instances where sharp edges and the dimensions are not so important. For our experiments, the 70 $^{\circ}$C etching temperature seemed to work best for etching.

Another factor that affects the etch rate of the KOH solution is contaminants in the solution. Any foreign bodies in the solution or other chemicals other than KOH reduces the effective etch rate of the solution. So it is important to keep contaminants out of the solution. It is also important to properly clean and rinse the wafers at each step before the final etch step in the KOH solution.

Micromachining Patterns

1. **Physical shadow mask for fabricating gridded composition spreads:** In order to perform SQUID measurements on our films, it was necessary to have addressable squares which corresponded to different samples that could then be measured using the scanning SQUID microscope. We first made the shadow mask out of a 1 mil thick, 3-in diameter stainless steel sheets which were used for room temperature deposition of composition spreads. This was due to the sharp difference in the thermal expansion coefficient of the stainless steel mask and the silicon wafer at high temperatures. Even during room temperature depositions, the stainless steel mask would lift off the center of the wafer due to localized heating during deposition from the energy of the sputtering plasma. In order to overcome this problem, we micromachined the shadow mask pattern out of ~350 micron thick, 3-in diameter silicon wafers. Figure A - 1 shows the pattern used

for this process. A front and back pattern is used so that the etching process is about 3 hours instead of 5 to 6 hours. This also ensures that the edges of the squares are sharp. To make sure that the front and back patterns are aligned we used the four cross hairs indicated around the outside of the patterns.

Opening
to be etched

Alignment
Cross-hairs

Front pattern   Back pattern
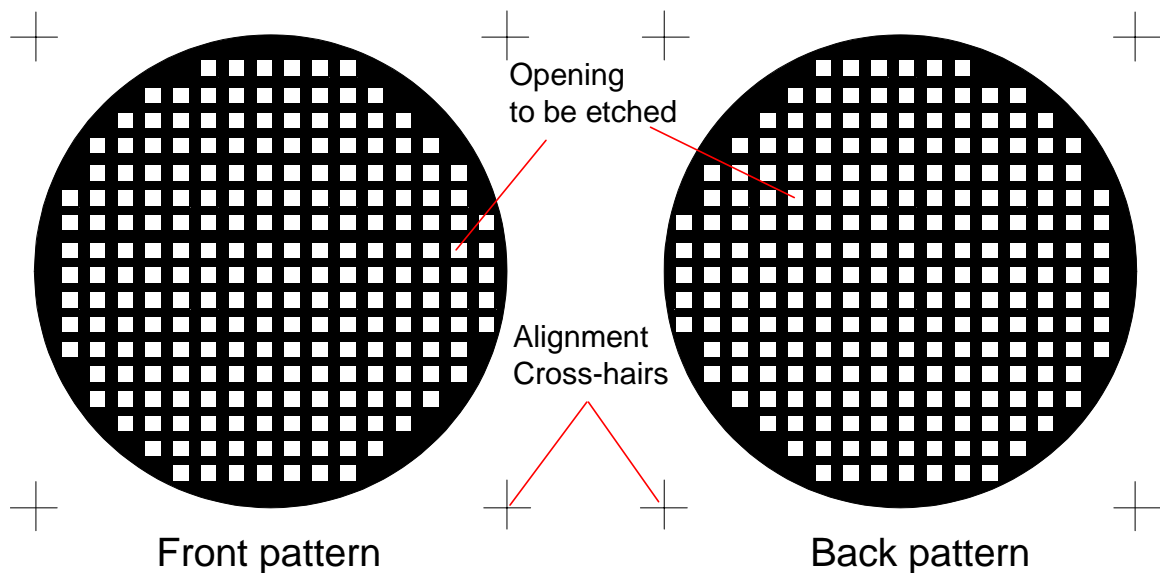
Figure A - 1: Pattern for lithography mask to make gridded silicon shadow mask for composition spread thin film deposition. Squares are 1.75 by 1.75 mm with 1 mm spacing between each square. A typical gridded shadow mask has 525 squares. The white areas are etched away in the etching process.

2. **Cantilever array library:** To characterize the SMA properties of composition spreads, we micromachined the cantilever array library into the silicon wafer and deposited our films on the array. The dimensions of the individual cantilevers in the array are ~ 8.5 mm in length, 1.5 mm in width, and ~70-100 μm thick. In these measurements and experiments the pattern used in the micromachining process is shown in Figure A - 2. A typical cantilever array library contains ~ 100

122

individual cantilevers.   Separation between individual cantilevers is ~ 0.5 mm.

Again, aligning the front and back patterns is important and the cross-hairs are

used to align the two patterns.

(a)   Front pattern   (a)   Back pattern
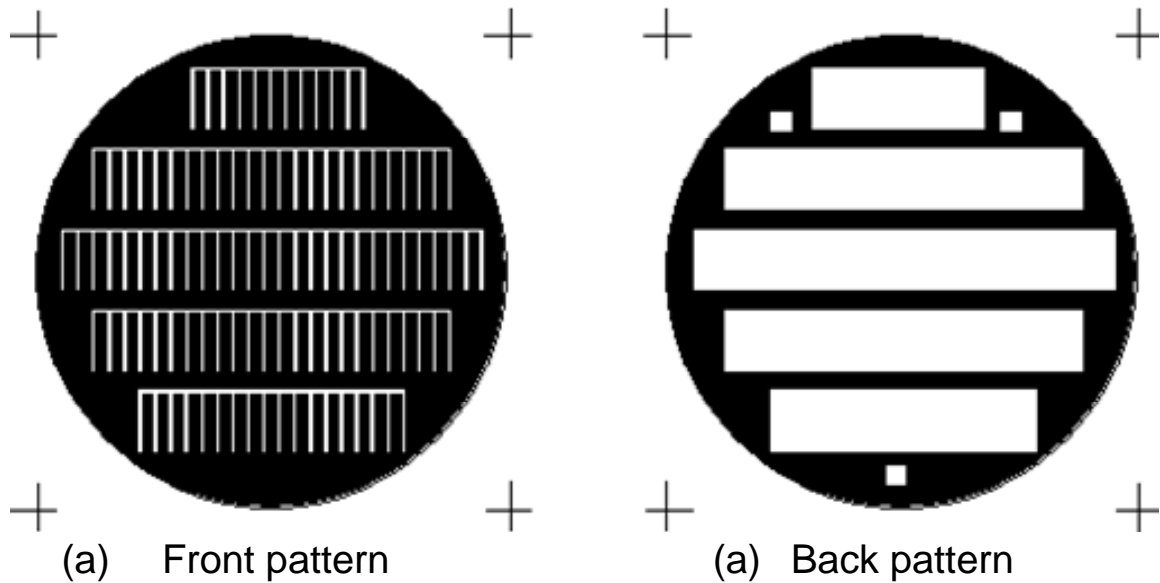
Figure A - 2: Pattern for lithography mask to fabricate the cantilever array library for the
visual observation of SMA properties of the composition spread thin film deposited on
the arrays. (a) Front (polished side when using single polished wafers) pattern and (b) is
the back pattern (etched side of a single polished wafer).   The white areas are etched
away in the etching process.

I would like to note that BOE is a very dangerous chemical. Extreme caution

must be exercised when it is used in the micromachining process.   Users are strongly

advised to read the MSDS sheets of all chemicals and use the necessary safety equipment

when handling the materials.

Alternative to BOE step in micromachining process

An alternative to the BOE step in the micromachining process which is less dangerous can is reactive plasma etching. The silicon dioxide coated wafers can be replaced with silicon nitride coated wafers for this. The remaining steps in the SOP remain the same, only the BOE etching step is replaced. The reactive plasma etching is better since this does not involve wet etching. It is a dry etching process that takes place in a reactive plasma etching chamber. Procedures for this alternative can be obtained via the internet.

Appendix B: Structure refinement and lattice parameter determination

We performed x-ray microdiffraction measurements using our in-house x-ray microdiffractometer and synchrotron x-ray source measurements on our composition spread thin films. The data gathered from both measurements were used to perform a structure refinement to determine the structure of the thin film materials and the lattice parameters used in the ideal SMA search experiments.

This process is labor intensive and requires some knowledge or a good guess of what the structure and lattice parameter of the films are. We used a program freely available on the internet that was developed by Brian Toby at NIST[1]. The program allows us to import our measured data into the program, and by inputting parameters that we know we can adjust the lattice constant values and compare the resulting spectrum to the measured data. This is performed until a good fit is obtained. Not only does one have to adjust the lattice constant but other factors also need to be adjusted such as the group space, what structure it could be and the wavelength of the x-ray source.

---

[1] http://www.ncnr.nist.gov/programs/crystallography/software/cmpr/cmprdoc.html

A major drawback of this process is that only one spectrum can be processed at a time. In our case we have hundreds of different spectra from different compositions on our spreads. The structure and phases of each material is not the same.

The process of refinement is outlined below. This is not meant to be a detailed user manual for the CMPR program, but it is a short tutorial that can get a user started and familiar with the steps involved. The program can be downloaded from the internet by performing a search for the CMPR refinement program or from the NIST website.

Once the program is started from either an icon in MS-Windows (or typing CMPR on a UNIX command line), the user runs CMPR. This brings up the following two screens:
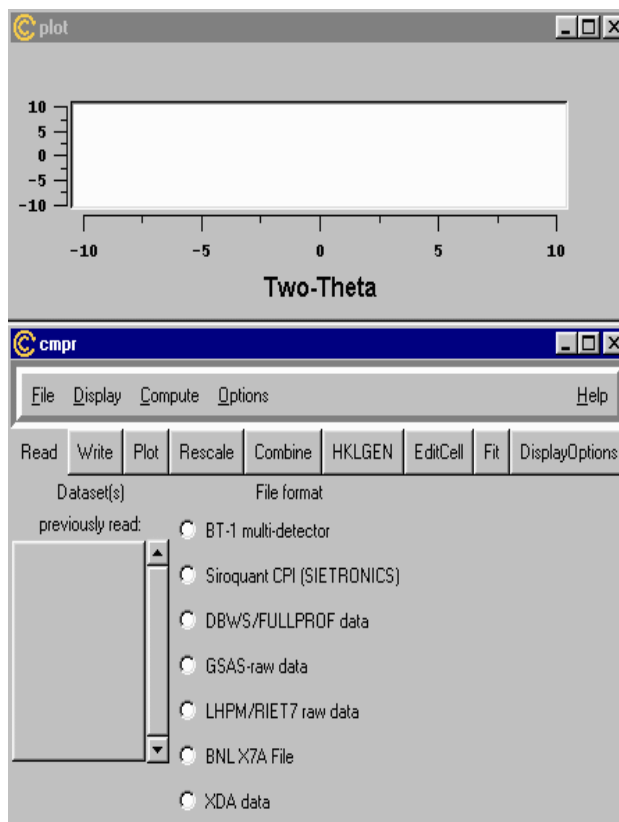
Figure B-1: CMPR program initial screen.

In this particular example, we will open a cubic flourite data file in the CPI format ("standard" dataset from the IUCr CPD Quantitative Analysis Round Robin). Depending on how the raw x-ray data is collected one can use a different format to open the file. The program also allows the user to label the hkls. It also shows what happens when a phase transformation occurs as in the case of a line splitting in going from cubic to tetragonal cells.

One clicks on the CPI format or any other format button to bring up a file menu, which allows one to browse the directory structure. In this case, we selected flourite.cpi.
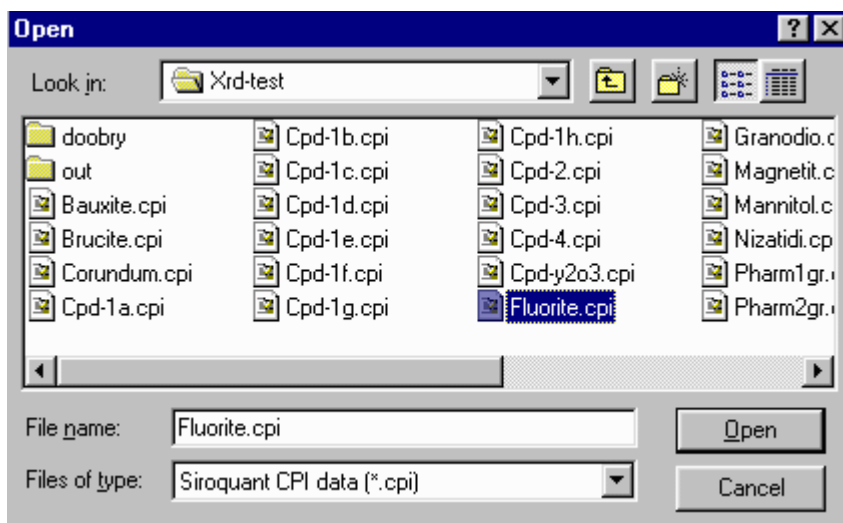
Figure B- 2: CMPR window for loading raw x-ray data files.

After pressing the Open button, a small window will pop up indicating that CMPR is loading the file, after which it will display the spectrun in the Plot Window (which is resizable).

127
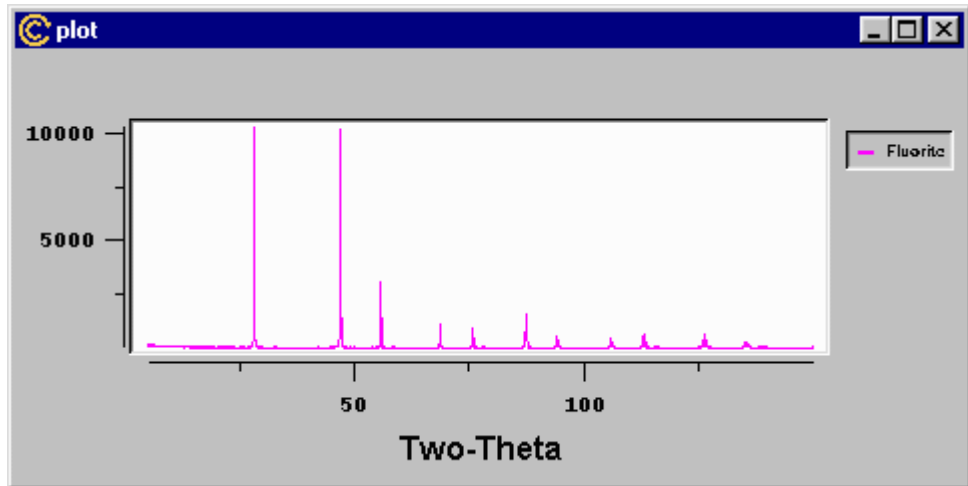
Figure B- 3: CMPR plot window displaying the x-ray spectrum of the imported raw data file.

The user can zoom in and out of the data in the plot windows by clicking and dragging with the mouse around the region to zoom.
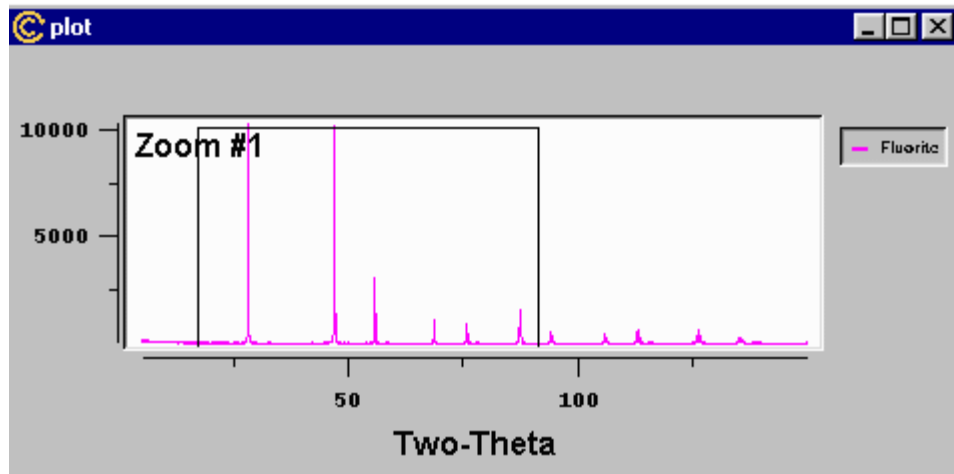
Figure B- 4: CMPR plot window with zoom box around region of spectrum to zoom.
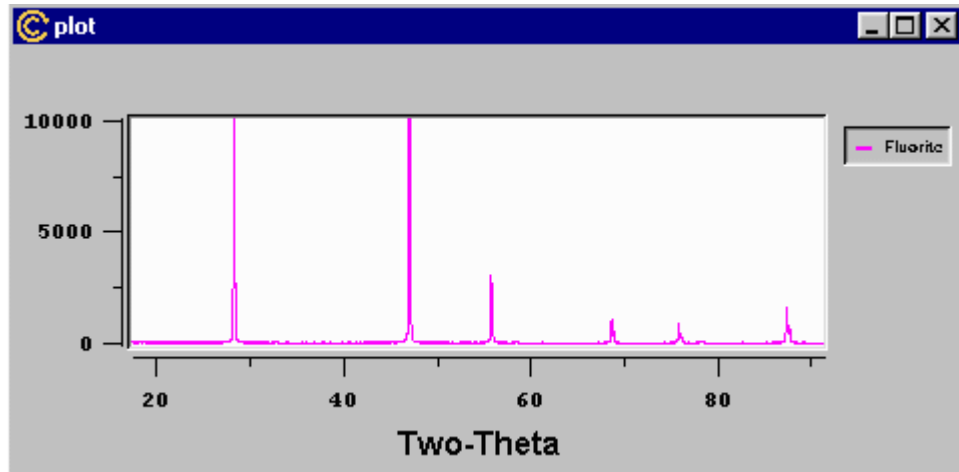
Figure B- 5: Zoomed region of x-ray spectrum in plot window.

To perform the manual indexing, one clicks the **Edit Cell** button to bring up the following window.
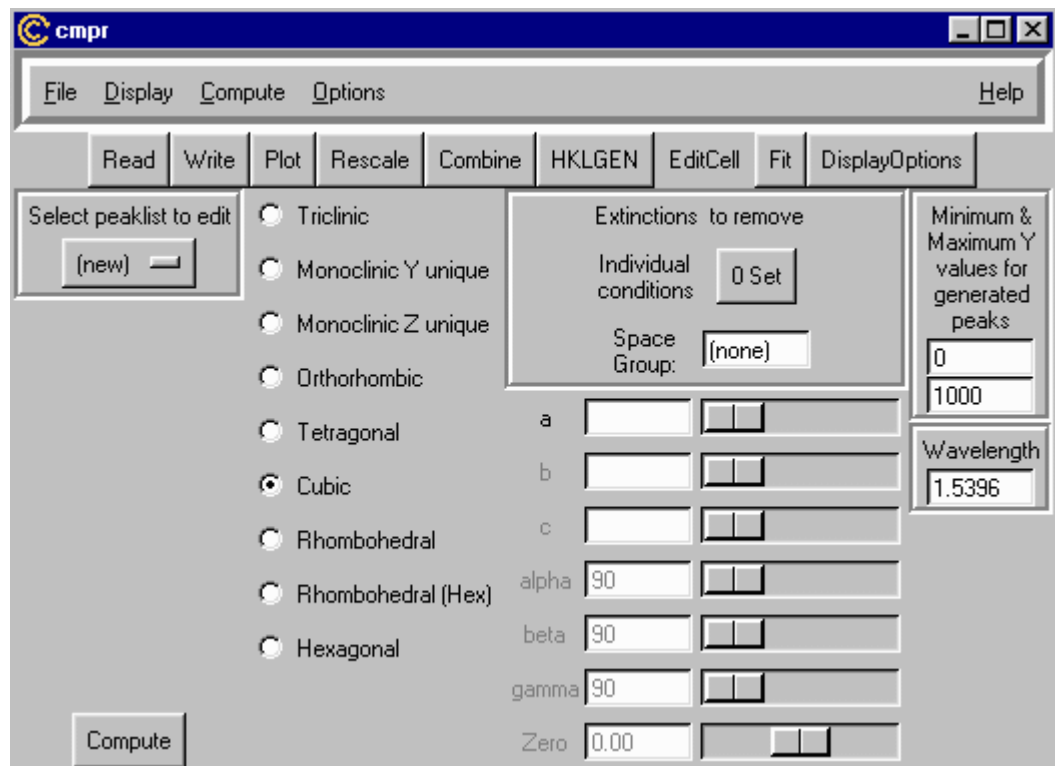
Figure B- 6: Edit Cell display of CMPR program.

The user can generate multiple cells to overlap with the raw x-ray data. For simplicity we will now do this for a cubic sample. The wavelength can be adjusted to the correct value (in this case 1.54056 A - Cu K alpha1); the height you would like the calculated peaks to overlap the data (in counts - in this case -1500 to 0 counts so that the lines are displayed under the raw data pattern.); select the cell type (in this case cubic); then enter a rough guess of the cell values (this value is usually obtained from the literature - they can be recalculated); **then press the Compute button**. The x-ray raw data pattern will disappear from the screen. Reselecting the dataset will bring this back with the calculated lines underneath. (The 2-θ range can be limited to your data range by going into the **HKLGEN** window and set the **2 theta max to an appropriate value**)
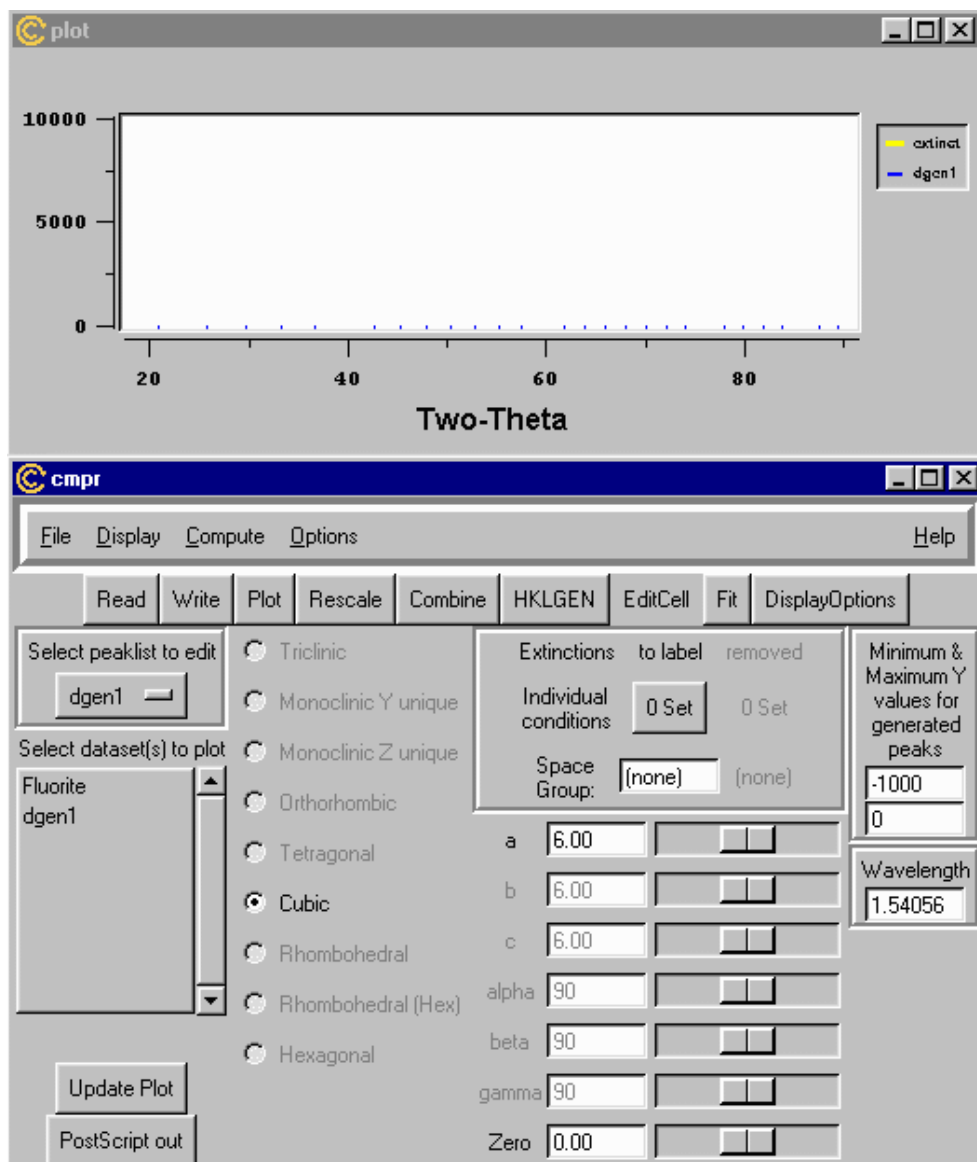
Figure B- 7: Edit cell window of CMPR showing the initial guess parameters and the corresponding spectrum peak locations in the plot window (the blue lines).

As implied above, doubling clicking using the mouse on "**Flourite**" in the "**Select dataset(s) to plot**" box will bring back with the calculated lines underneath. (you can also zoom to make this a bit clearer)
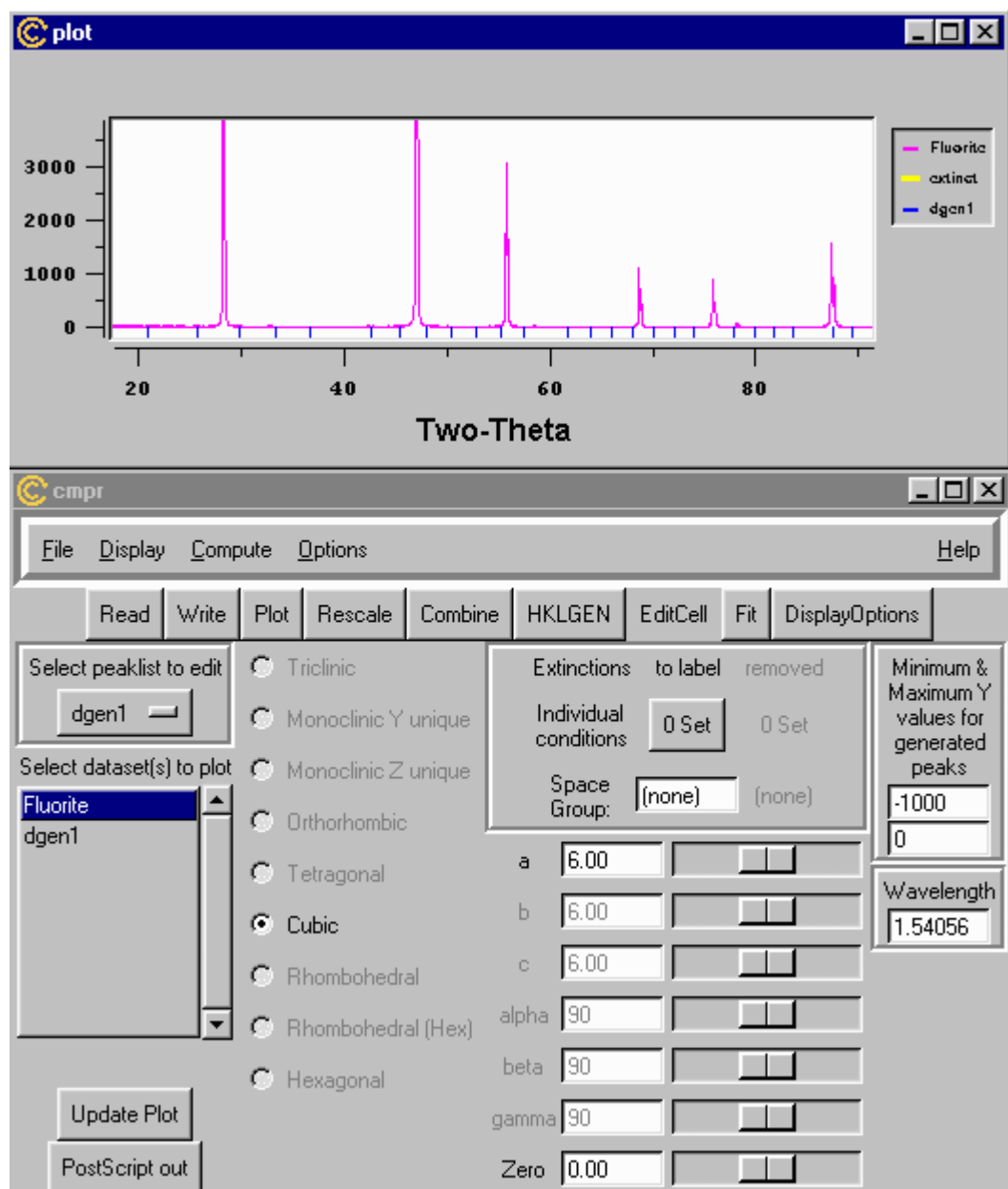
Figure B - 8: Edit cell window of CMPR showing the initial guess parameters and the corresponding spectrum peak locations in the plot window (the blue lines) and the imported raw data spectrum (the pink line).

As the user moves the a-axis scroll bar, the lines will move accordingly to keep pace with the changing value of the cell value as it changes.
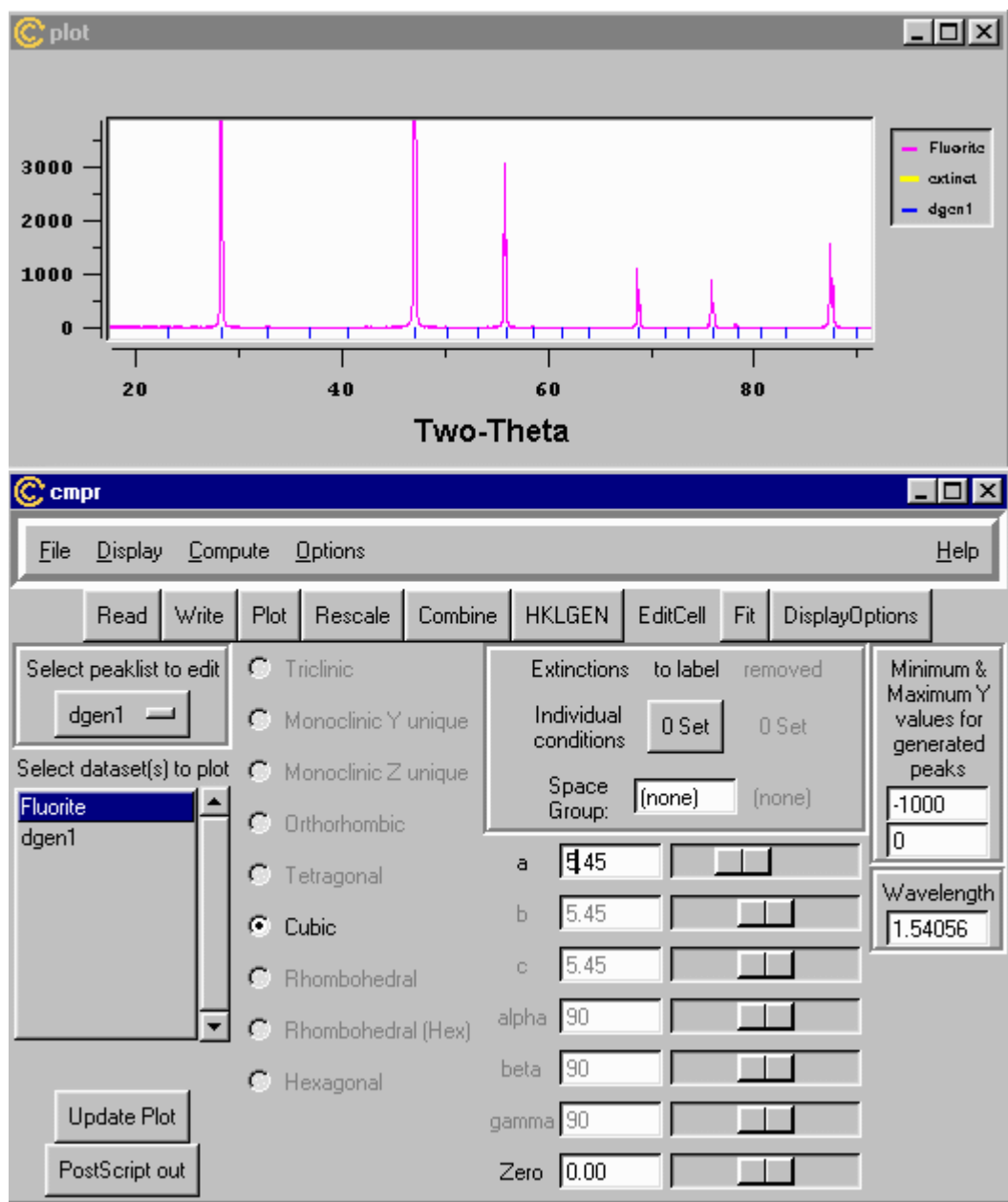
Figure B - 9: Raw data spectrum and adjusted guess lattice parameter peak locations that match the raw data peaks.

It is also possible to specify symmetry operators and check what extinctions (peaks that are not present) occur using the **Individual Conditions** option.

133
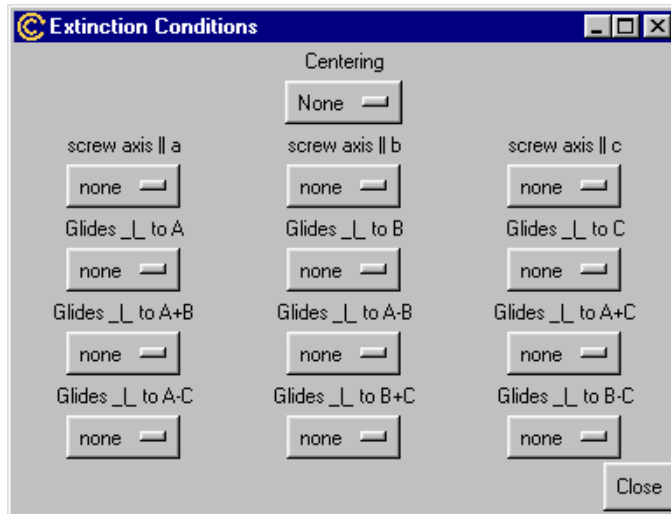
Figure B- 10: CMPR symmetry specification window for extinction peak conditions.

The user can also specify a space group - in this case F D 3 M, which generates a good set of extinctions that match this particular data set. In this case, the yellow lines indicate the extinct lines.
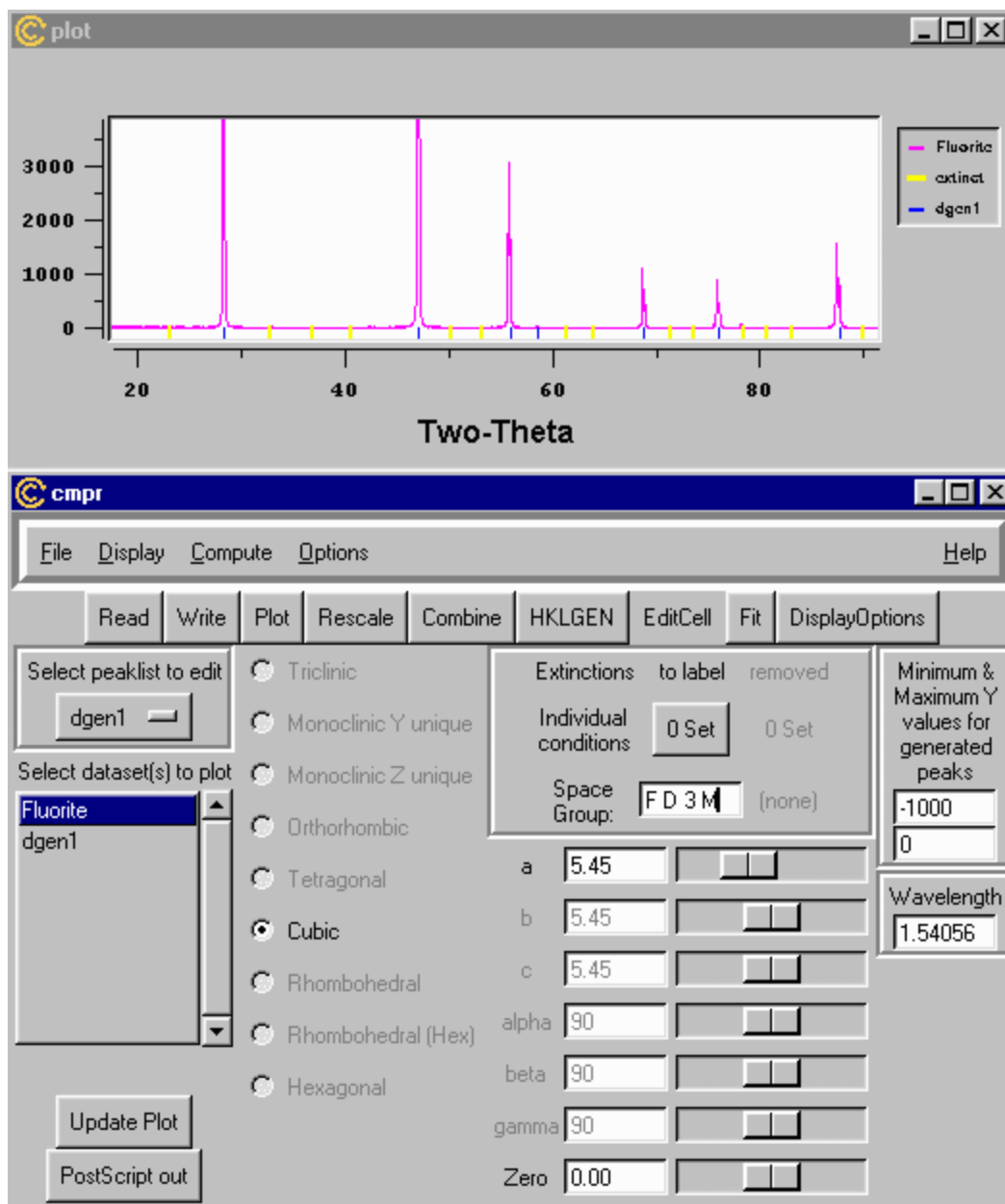
Figure B - 11: CMPR display window showing raw data spectrum, guessed lattice parameter (5.45 A), the extinction peaks (yellow lines), and the space group corresponding to the matched guess spectrum peak locations displayed in the plot window.

The user can also label hkls on individual reflections by clicking [SHIFT] left mouse button and adding the peak label manually.
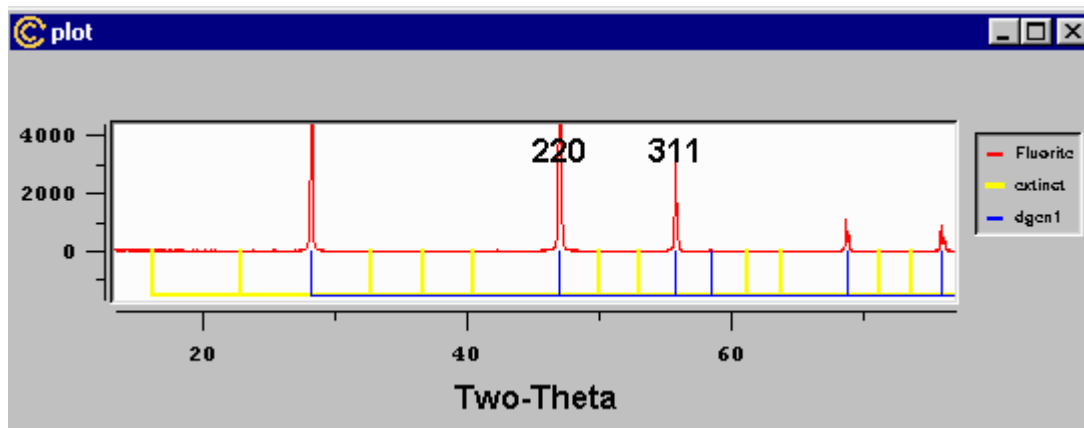
Figure B - 12: CMPR plot window showing result of manual peak labeling.

By selecting a new peak list to edit (create), the user can explor the effects of symmetry changes on peak splitting. In this example, we have the simple case of cubic to tetragonal transformation.
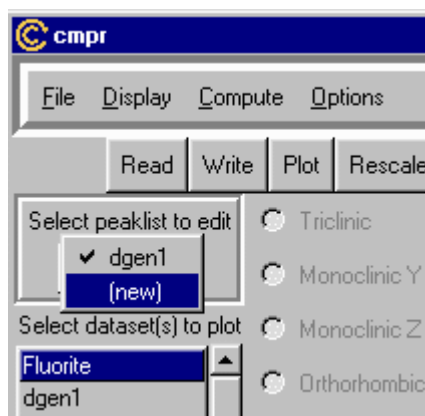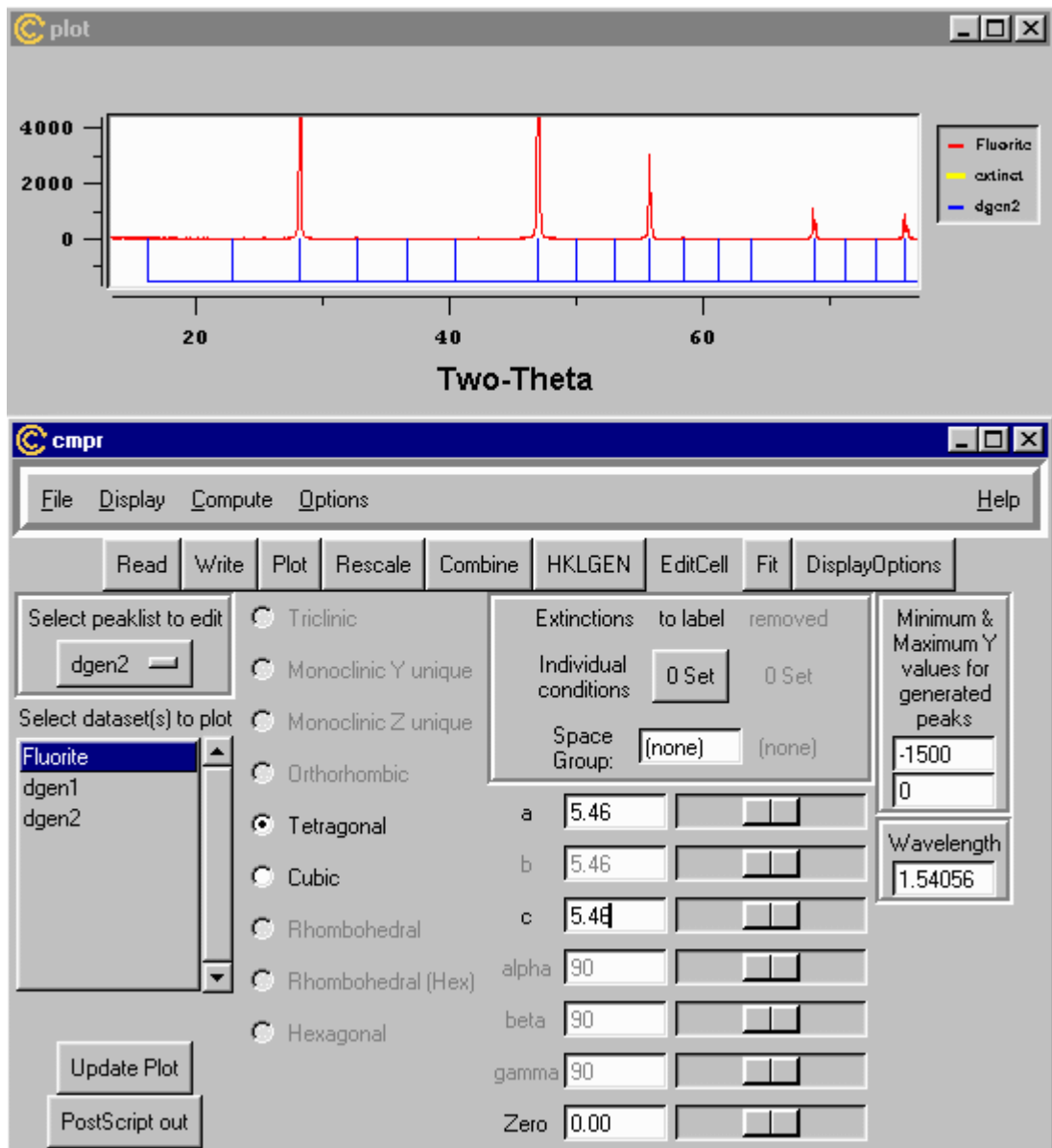
Figure B- 13: Spectrum indexing for a cubic to tetragonal transformation.

Scrolling the a-axis or c-axis control bar now lets the user see the effects of distorting the cell from cubic to tetragonal.
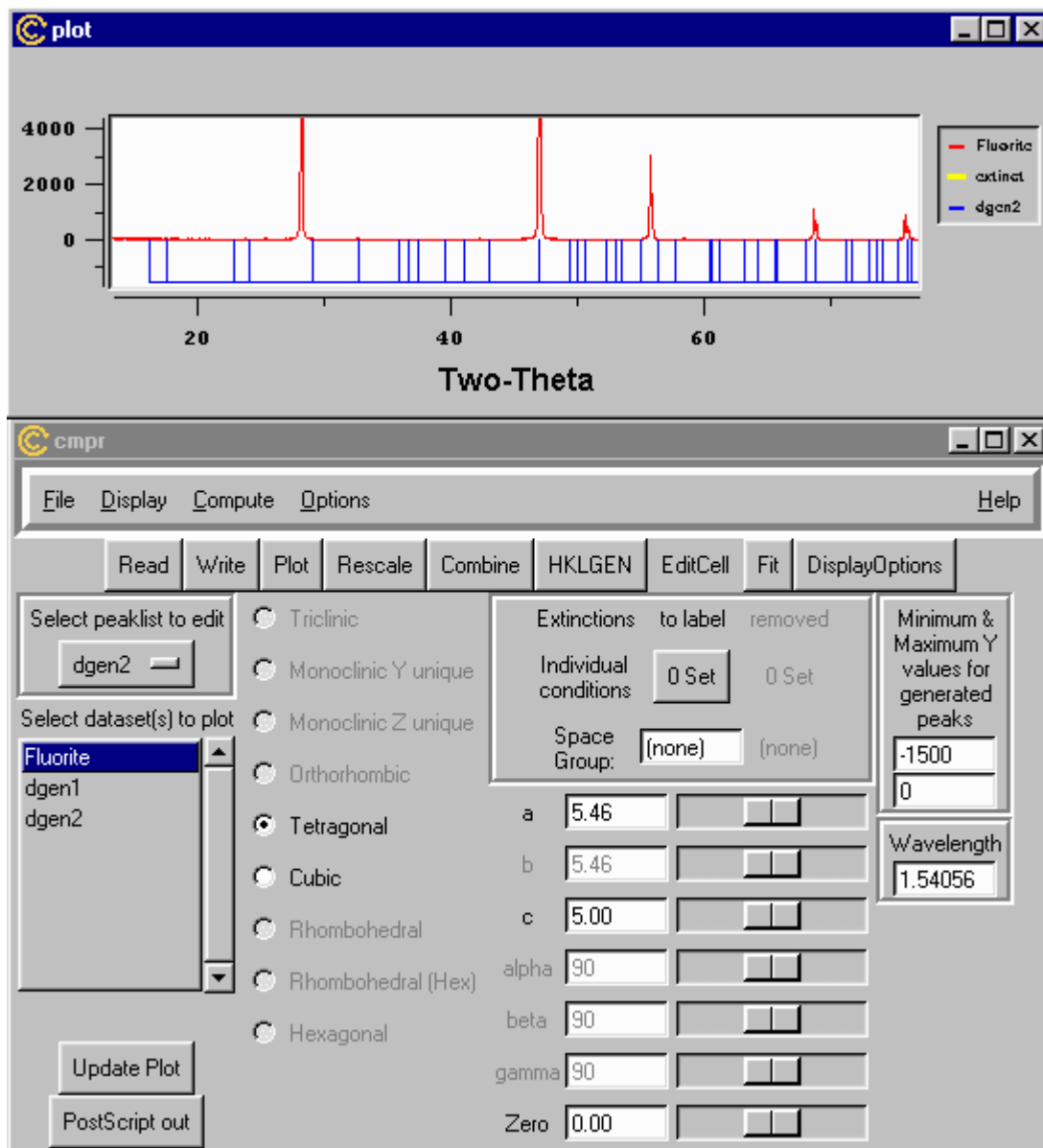
Figure B- 14: Effect of changing the lattice constant on the spectrum.

When the user matches or accounts for each peak in the spectrum the a-axis and c-axis are the refined lattice parameters for the composition spectrum. These numbers are then used in the calculations for the non-linear geometric theory for ideal SMAs in Chapter 4.

Since we are making hundreds of different compositions, there are compositions that have not been studied in the literature. Finding lattice parameters and structural information on these compositions is unlikely. We have resorted to using another program called Fullprof/Winplotr (peak find and Dicvol). For the compositions for which we have no literature data, we use this program to provide an initial lattice parameter and index number for the CMPR program. This program is also freely available on the internet. However, it is more complicated and requires some familiarity and training to use. There are short tutorials on the web that a user can use to become familiar with the workings of the program.

Appendix C: Wavelength Dispersive Spectroscopy (WDS) of combinatorial samples

In this thesis we have made extensive use of WDS to characterize the composition of the composition spread thin films we fabricated. Even though WDS is a well established characterization tool, there are a few things one must be aware in order to obtain accurate composition mappings. The WDS probe is very good at characterizing conductive materials very accurately. On the other hand, non-conducting or insulating materials are a problem.

With insulating materials, charging of the samples occurs and this leads to errors in the composition measurements at best, and erroneous results at worst. It is the case where slight charging is occurring in the samples that are not easily observed. Especially in our composition spreads one has to be careful and diligent in picking the elements to alloy and understand their mixing behavior. In some ternary alloys one could run into a situation where some compositions on the spread are conducting and certain compositions are non-conducting. When setting up the composition spread to be scanned it is important for the user to pay close attention to the SE image on the WDS analyzer. Conducting or semi-conducting materials will exhibit a liquid shiny flow pattern. Sometimes this pattern is intermittent, especially for semi-conducting materials. As the user scans across the sample, one must look for this liquid shiny property row by row. A solution to this problem is simple. In order to make sure all samples are conducting, the wafer can be coated with a very thin layer of graphite carbon.

Table C-1 shows representative statistical data on the accuracy of the measurements of compositions measured for individual elements in the Ni-Mn-Ga system. A similar table can be made for each system with similar results.

Element	Composition (Weight %)	Composition (Atomic %)	Standard Deviation (2 sigma %)	Detection Limit (Weight %)
Ni	33%	33%	0.33 %	0.0184%
	15%	15%	0.47%	0.0170%
Mn	32%	33%	0.50%	0.0144%
	14%	15%	1.09%	0.0197%
Ga	35%	33%	0.70%	0.0214%
	17%	15%	0.71%	0.0119%

Table C-1: Typical WDS data statistical information on accuracy of compositions measured for Ni-Mn-Ga system.

Appendix D: Curriculum Vitae

Olugbenga O. Famodu

U.S. Citizen

7523 Dover Lane ◊ Lanham, MD 20706 ◊ (301) 552-3861

famodu@umd.edu

OBJECTIVE:

To obtain a challenging position with increasing responsibility with a company that will use my professional experience, leadership, organizational and communication skills as well as my resourcefulness in a positive and productive way.

EDUCATION:

Ph. D. Materials Science & Engineering, May 2005	**B. S. Chemical Engineering,** May 1995
University of Maryland, College Park (GPA 3.739)	University of Maryland, College Park
M. S. Materials Science & Engineering, Dec. 2004	**A. S. Engineering,** February 1995
University of Maryland, College Park	Prince George's Community College, Largo

PH. D. CANDIDATE: Fall 2000–Aug.2005

- Research in the Combinatorial Exploration of Ferromagnetic Shape-Memory Alloys: Ni-Mn-Ga system.
- Author or co-authored six journal papers.
- GEM Ph.D. Fellow and Sloan Ph. D. Scholar.
- Synthesis and characterization of combinatorial libraries of ferromagnetic materials.
- Nanostructure thin film fabrication: magnetron co-sputtering and thermal evaporation.
- Micromachining: wet and dry etching, ion milling, and photolithography.
- Thin film characterization: scanning SQUID, scanning x-ray diffractometer, wavelength dispersive spectroscopy (WDS), vibrating-sample magnetometer (VSM), atomic force spectroscopy (AFM).

WORK EXPERIENCE:

PROFESSIONAL INTERN, DuPont Company (Flouroproducts® K-19 Group), Chambers Works, New Jersey   Summer 2000

- Supported management of pilot plant production of Hydrofluoric (HF) gas for use in microelectronic industry.
- Collected and analyzed production data.
- Compiled, updated and generated process reports.
- Guided the maintenance and optimization of product processes.
- Supervised 3-4 plant operators.

PROFESSIONAL INTERN, DuPont Company (Lycra®/Terathane® Group), Wilmington, Delaware   Jan. 1999–Aug. 1999

- Oversaw the installation and testing of a scale-down model of fluidized bed flow metal reactor.
- Collaborated with senior research engineers on the analysis and evaluation of a new catalyst for hydrogenation reaction kinetics study report.
- Designed and built a small-scale laboratory fluid bed reactor for study of catalyst.
- Analyzed and interpreted data and published reports on butane oxidation reaction kinetics.

PROFESSIONAL INTERN, DuPont Specialty Chemicals, East Chicago, Indiana   Jan. 1998–Aug. 1998

- Designed and oversaw the construction and installation of an automation process for the doping of LUDOX® a $50,000 project that was projected to increase production capabilities.
- Identified and purchased necessary parts and materials needed for automation installation.
- Managed and maintained project budget.
- Collected, tested and analyzed process data that was used to verify correlations used to automate doping process.
- Tested a new de-watering screen and recommended the purchase of an additional screen to increase product production ($20,000 project and potential increased production of $500,000 in sales).

- Planned and coordinated a 6-week summer program for incoming freshman science and engineering students.
- Managed a $300,000 National Science Foundation budget.
- Hired and collaborated with 3 instructors, 2 assistants and 2-3 student workers.
- Collected, analyzed and generated statistical data for annual grant reports.
- Administered weekly time-management workshops for 30 students annually.
- Advised students, prepared budgets and assisted in planning annual student recognition and alumni banquets.

LEADERSHIP EXPERIENCE:

M.L. CHERRY MEMORIAL SCHOLARSHIP COMMITTEE CHAIRPERSON, Black Engineers Society   2000-2004

- Managed and oversaw the selection and award of one-year scholarships.
- Solicited committee members and educated them on selection criteria and purpose of scholarship.
- Revised and updated memorandum of understanding for the scholarship.
- Planned and coordinated award of scholarship and award plaque.

REGION II PRE-COLLEGE INITIATIVE (PCI) CHAIRPERSON, National Society of Black Engineers   1995–1996, 1998–1999

- Planned and executed leadership workshop training session for 30 chapter PCI chairpersons.
- Evaluated chapter PCI chairperson reports bi-monthly.
- Chaired Regional PCI Committee.
- Planned and coordinated a summer camping conference for pre-college students.
- Managed a $24,000 budget.

PROFESSIONAL AFFILIATIONS:

National Society of Black Engineers (NSBE)	American Institute of Chemical Engineers (AIChE)
American Physical Society (APS)	Materials Research Society (MRS)

ACADEMIC HONORS:

NSBE BCA Scholar	Frederick Douglas Grant
GEM Ph. D. Fellow	Senatorial Scholarship
Sloan Scholar	Merit Award
M. L. King Jr. Comm. Service Award	Dean's List
Outstanding PCI Chairperson	Presidential Scholarship

PUBLICATIONS:

1. I. Takeuchi, C.J. Long, O. O. Famodu, M. Murakami, J. Hattrick-Simpers, and G. W. Rubloff; "Data management and visualization of x-ray diffraction spectra from thin film ternary composition spreads," *Rev. Sci. Instrum.*, **76,** 062223 (2005).
2. O. L. Warren, A. Dwivedi, T. J. Wyrobek, O. O. Famodu, and I. Takeuchi; "Investigation of machine compliance uniformity for nanoindentation screening of wafer-supported libraries," *Rev. Sci. Instrumen.*, **76,** 062209 (2005).
3. O. O. Famodu, J. Hattrick-Simpers, M. Aronova, K.-S. Chang, M. Murakami, M. Wuttig, T. Okazaki, Y. Furuya, L. A. Knauss, L. A. Bendersky, F. S. Biancaniello and I. Takeuchi; "Combinatorial investigation of ferromagnetic shape-memory alloys in the Ni-Mn-Al ternary system using a composition spread technique," *Materials Transactions*, **45**, no. 2, 173 (2004).
4. I. Takeuchi, O. O. Famodu, J. C. Read, M. A. Aronova, K.-S. Chang, C. Craciunescu, S. E. Lofland, M. Wuttig, F. C. Wellstood, L. Knauss and A. Orozco; "Identification of novel compositions of ferromagnetic shape-memory alloys using composition spreads," *Nature Materials*, **2,** issue 3, 180 (2003).
5. K.-S. Chang, M. Aronova, C.-L. Lin, M. Murakami, M.-H. Yu, J. Hattrick-Simpers, O. O. Famodu, S. Y. Lee, R. Ramesh, M. Wuttig, I. Takeuchi, C. Gao, and L. A. Bendersky; "Exploration of multiferroic thin film heterostructures using composition spreads," *Appl. Phys. Lett.* April 12 (2004).
6. K. S. Chang, M. Aronova, O. Famodu, I. Takeuchi, S. E. Lofland, J. Hattrick-Simpers, and H. Chang; "Multimode quantitative scanning microwave microscopy of in situ grown epitaxial Ba$_{[1 - x]}$ Sr$_{[x]}$ TiO$_3$ composition spreads," *Appl. Phys. Lett.* **79**, 4411 (2001).
7. S. I. Patil, Deng Tan, S. E. Lofland, S. M. Bhagat, I. Takeuchi, O. Famodu, J. C. Read, K.-S. Chang, C. Craciunescu, and M. Wuttig; "Ferromagnetic resonance in Ni-Mn-Ga films," *Appl. Phys. Lett.* **81**, 1279 (2002).

Appendix E: Published papers related to this dissertation

1. I. Takeuchi, C.J. Long, O. O. Famodu, M. Murakami, J. Hattrick-Simpers, and G. W. Rubloff; "Data management and visualization of x-ray diffraction spectra from thin film ternary composition spreads," *Rev. Sci. Instrum.*, **76,** 062223 (2005).

2. O. L. Warren, A. Dwivedi, T. J. Wyrobek, O. O. Famodu, and I. Takeuchi; "Investigation of machine compliance uniformity for nanoindentation screening of wafer-supported libraries," *Rev. Sci. Instrumen.*, **76,** 062209 (2005).

3. O. O. Famodu, J. Hattrick-Simpers, M. Aronova, K.-S. Chang, M. Murakami, M. Wuttig, T. Okazaki, Y. Furuya, L. A. Knauss, L. A. Bendersky, F. S. Biancaniello and I. Takeuchi; "Combinatorial investigation of ferromagnetic shape-memory alloys in the Ni-Mn-Al ternary system using a composition spread technique," *Materials Transactions*, **45**, no. 2, 173 (2004).

4. I. Takeuchi, O. O. Famodu, J. C. Read, M. A. Aronova, K.-S. Chang, C. Craciunescu, S. E. Lofland, M. Wuttig, F. C. Wellstood, L. Knauss and A. Orozco; "Identification of novel compositions of ferromagnetic shape-memory alloys using composition spreads," *Nature Materials*, **2,** issue 3, 180 (2003).

5. S. I. Patil, Deng Tan, S. E. Lofland, S. M. Bhagat, I. Takeuchi, O. Famodu, J. C. Read, K.-S. Chang, C. Craciunescu, and M. Wuttig; "Ferromagnetic resonance in Ni-Mn-Ga films," *Appl. Phys. Lett.* **81**, 1279 (2002).

Investigation of machine compliance uniformity for nanoindentation screening of wafer-supported libraries

Oden L. Warren,[a] Arpit Dwivedi, and Thomas J. Wyrobek
Hysitron, Inc., 10025 Valley View Road, Minneapolis, Minnesota 55344

Olugbenga O. Famodu and Ichiro Takeuchi
Department of Materials Science and Engineering, University of Maryland, College Park, Maryland 20742

The reliability of nanoindentation results can depend critically on an accurate assessment of the machine compliance term. The common practice is to determine the machine compliance from a small reference specimen, then apply its value to a much larger wafer-supported library. The present study investigates the validity of this approach by thoroughly testing bare 76.2 mm diameter, 410 μm thick Si(100) wafers mounted on two vacuum chucks of different design. We find that the small-sample value of the machine compliance is adequate for the majority of the wafer, including areas directly over vacuum rings and a circular center port of ordinary dimensions. However, vacuum chucks with a tweezer slot should be avoided in combinatorial materials science applications. But even in the absence of a tweezer slot, it may be necessary to generate an accurate machine compliance map for the wafer perimeter if the thin-film library extends beyond the outermost vacuum ring to the wafer edge. The Young's modulus and the hardness of silicon are found to be 169±3 GPa and 12.2±0.2 GPa, respectively, over well-mounted regions of the wafer; both values are in good agreement with the literature. © *2005 American Institute of Physics.* [DOI: 10.1063/1.1906089]

I. INTRODUCTION

Nanoindentation[1] is being exploited as a relatively high-throughput technique for screening wafer-supported, thin-film libraries with regard to their mechanical properties.[2] For example, a recent 8-month combinatorial investigation entailed 70 000+indentations to assess the elastic modulus and the hardness of 12 000+low-*k* dielectric films on silicon wafers.[3] The prevalent use of wafers as templates for material libraries raises a concern about the quality of the mounting condition between the wafer and the vacuum chuck holding the wafer. A classical nanoindentation test specimen has a mounting area only of the order of 1 cm^2, but a typical wafer-supported library (76.2 mm in diameter) covers 45.6 cm^2 of the chuck surface. It is easy to imagine a greater potential for nonuniform mounting conditions in the case of the much larger wafer.

Nanoindenters adhere to design principles that maximize knowledge of the combined deformation of the indenter and the sample; ideally, a measured change in displacement relative to the sample surface corresponds exactly to the change in combined deformation. In reality, other instrument components deform as well, so the measured change in displacement relative to the sample surface will be an overestimation of the true change in combined deformation. Introducing a machine compliance (or stiffness) term in the analysis of nanoindentation data is the standard way of accounting for the deformation of other instrument components.[1,4,5] This term can be largely ignored in the case of nanoindentation

into soft, compliant samples, but in the case of nanoindentation into hard, stiff samples, the contact stiffness easily can be within an order of magnitude of the machine stiffness. For example, a 10 mN indentation test on a hypothetical material characterized by 400 GPa elastic modulus, 0.25 Poisson ratio, and 30 GPa hardness results in a maximum-load contact stiffness of 2×10^5 N/m when diamond is the indenter material, which is only about an order of magnitude less than the machine stiffness of a typical nanoindenter.

In this study, we have examined the uniformity of machine compliance across bare Si(100) wafers mounted on vacuum chucks. The wafers are chosen to be free of films so that they represent model material libraries endowed with zero variation in mechanical properties. Consequently, any significant deviation in measured mechanical properties relative to the expected values is an indicator of a machine compliance issue. Ideally the machine compliance is dictated only by the instrument, but, in reality, sample mounting can affect this term considerably if not done properly.

II. EXPERIMENT

Nanoindentation force-displacement (*P-h*) curves were measured with a TriboIndenter® nanomechanical test instrument (Hysitron, Inc., Minneapolis, MN) equipped with a three-plate capacitive force-displacement transducer and a Berkovich diamond indenter. Two vacuum chucks of different design were mounted on the lateral translation staging of the instrument to establish their efficacy at supporting wafers. The Oliver-Pharr method of analysis[4] was used to determine the hardness *H* of the test specimen as well as the

---
[a]Electronic mail: owarren@hysitron.com

reduced modulus $E_r = [(1-\nu_i^2)/E_i + (1-\nu_s^2)/E_s]^{-1}$ of the contact, where E represents elastic or Young's modulus, ν indicates Poisson ratio, and subscripts i and s denote indenter and sample, respectively. Curves were corrected for residual zero-point errors and thermal drift prior to analysis. Fused quartz (from a calibration kit supplied with Hysitron instrumentation) served as the reference material for calibration of the indenter area function (projected contact area A_c vs. contact depth h_c), and for determination of the small-sample value of the machine compliance term C_m. The machine deformation is assumed to be the product of C_m and P. Further details on calibration, test, and analysis methods can be found elsewhere.[1,4,5]

Uniformity of C_m over a large sample area was investigated by carrying out series of indentation tests on the mirror-finished side of blank 76.2 mm diameter, 410 μm thick Si(100) wafers (International Wafer Service, Santa Clara, CA) mimicking wafer-supported libraries. All indentations on silicon were conducted using the following digital feedforward/feedback control algorithm:[6] (1) measure the drift rate at a wholly elastic preload of 1 μN, (2) lift the indenter by 10 nm, (3) reseek the surface under displacement control until reaching 1 μN for the purpose of providing data for zero-point correction, (4) load the sample at a constant loading rate of 500 μN/s until achieving a peak load P_{max} of 5000 μN, (5) hold the load constant for 5 s, and (6) unload the sample at a constant unloading rate of 500 μN/s.

III. RESULTS AND DISCUSSION

For noncontact techniques, and even for lightly contacting techniques such as atomic force microscopy, the basic requirement of a vacuum chuck is that it holds a wafer stationary. However, in the case of nanoindentation testing, common vacuum chuck features such as a circular center port, concentric vacuum rings, and a slot to permit tweezer access are causes for concern when considering the uniformity of machine compliance. Figure 1 displays two vacuum chucks of different design; the one shown at the top will be referred to as the "slotless chuck" and the one shown at the bottom will be referred to as the "slotted chuck," henceforth. For both chucks, the center port is 4.78 mm in diameter and the channel width of the vacuum rings is 2.26 mm, and for the slotted chuck, the tweezer slot is 19.05 mm wide in the short direction; these dimensions are not out of the ordinary for vacuum chucks. The combination of features found on these two chucks provides an opportunity for a practical assessment of the impact of chuck design on nanoindentation results.

The small-sample machine compliance was established as the value determined from the procedure of calibrating the indenter area function together with the machine compliance. The fused quartz reference specimen used for this procedure is 8.1×9.5 mm^2 in lateral dimensions, 1.5 mm in thickness, and is bonded by a thin layer of cyanoacrylate glue to a 15.24 mm diameter, 0.85 mm thick steel disk; the disk was held stationary by being placed over the center port of the vacuum chuck. A six-coefficient indenter area function and the machine compliance were optimized from
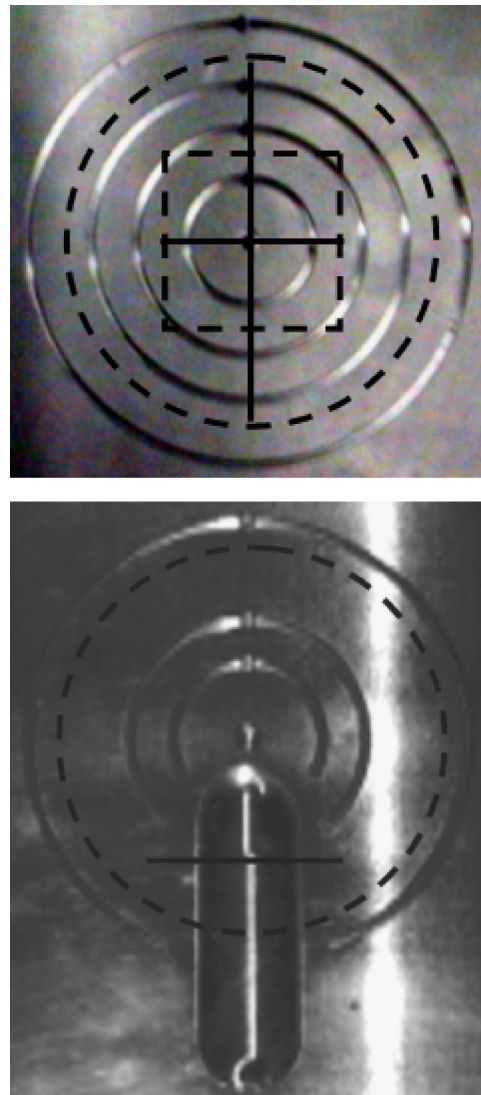
FIG. 1. Slotless (upper photograph) and slotted (lower photograph) vacuum chucks. Dashed circles represent silicon wafers. The dashed square indicates a 10×10 array of indents. Solid lines signify line profiles of indents. In the case of the slotless chuck, indents also were placed around the wafer perimeter at locations $\sim$1 mm from the wafer edge.

multiple-partial-unloading[7] indentation data obtained from the reference specimen to yield a constant reduced modulus of 69.6 GPa ($E=72$ GPa and $\nu=0.17$ for fused quartz; $E=1141$ GPa and $\nu=0.07$ for diamond) and a depth-independent H vs. h_c plot for contact depths ranging from 16.1 to 186.3 nm. Both the resulting hardness of 9.4 ± 0.1 GPa and the resulting small-sample machine compliance of 0.80 nm/mN are consistent with the historical average of the instrument employed in this investigation.

The appropriateness of transferring the small-sample machine compliance to a large-area specimen such as a wafer-supported library was tested initially by making an equally spaced 10×10 array of indents on a bare Si(100) wafer mounted on the slotless chuck (see Fig. 1 for a pictorial representation of the array size and location). All 100 force-displacement curves are displayed in Fig. 2 to provide a visual sense of the level of repeatability. Of note, three curves reveal a significant pop-out event during unloading;
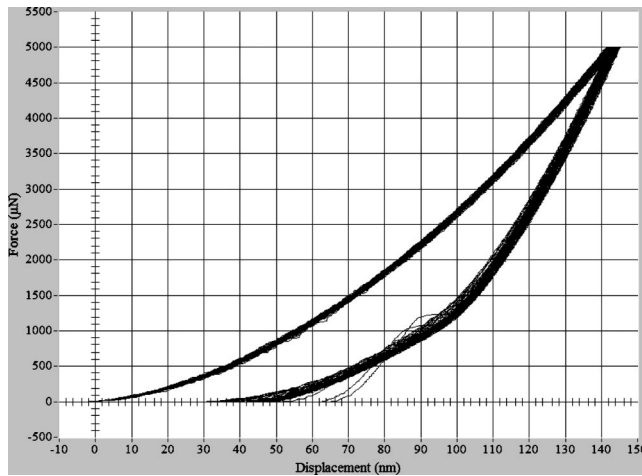
FIG. 2. Force-displacement curves for silicon from the 10×10 array of indents covering the dashed square drawn on the upper photograph of Fig. 1. Three curves reveal a significant pop-out event during unloading; the remaining curves exhibit a more subtle slope change at ~75% removal of load.

the remaining curves exhibit a more subtle slope change at ~75% removal of load. Silicon is known to undergo a pressure-induced phase transformation from the diamond structure to the metallic β-tin structure when the hydrostatic pressure under the indenter reaches ~11 GPa.[8] During unloading, the β-tin structure transforms to amorphous silicon or other crystalline structures, depending on the unloading rate.[8] Significant pop-out events are associated with the phase transition from the β-tin structure to other crystalline structures, a process that is favored by slow unloading.[8] Apparently, our chosen unloading rate is sufficiently fast to cause the β-tin structure to transform to amorphous silicon about 97% of the time (this percentage accurately reflects the entirety of this study).

To prevent the unloading phase transformation from affecting the determination of the initial unloading slope or maximum-load contact stiffness S, the power-law fitting procedure (steps of the Oliver-Pharr method of analysis) was restricted to the upper 60% of the unloading curve in terms of load. With the machine compliance kept at the small-sample value, the mean and the standard deviation of the reduced modulus, the hardness, and the maximum contact depth are 156 ± 2 GPa, 12.2 ± 0.2 GPa, and 110.3 ± 1.0 nm, respectively. Assuming a value of 0.25 for the Poisson ratio of silicon, the reduced modulus result corresponds to a Young's modulus result of 169 ± 3 GPa. The percent relative standard deviations ($\pm 1.8\%$ for Young's modulus, $\pm 1.6\%$ for hardness, and $\pm 0.91\%$ for maximum contact depth) are sufficiently low to proclaim this set of curves acceptably independent of indent location.

Grillo *et al.*[9] reported nanoindentation results of $E = 169 \pm 2$ GPa (corresponding to $E_r = 156 \pm 2$ GPa) and $H = 12.7 \pm 0.1$ GPa for Si(100) using a Berkovich indenter; the orientation of the indenter corners relative to the surface lattice vectors did not affect the values. Other examples of published nanoindentation results for single-crystal silicon (unspecified surface orientation) include $E = 169$ GPa and $H = 11.13$ GPa using a Berkovich indenter,[10] $E = 169$ GPa and

$H = 12.32$ GPa using a Vickers indenter,[10] and $E = 170$ GPa (corresponding to $E_r = 157$ GPa) and $H = 12.02$ GPa using an indenter of unspecified geometry.[11] Our result for Young's modulus (an intrinsic property) is in excellent agreement with the previously published values. There is greater variability in the previously published values for hardness (an extrinsic property); our result resides close to their mean. Anyhow, the level of agreement with literature is sufficiently good to accept the small-sample machine compliance as valid for the interior of the wafer.

To investigate machine compliance away from the wafer interior, 50 indents encircling the wafer were placed ~1 mm from the wafer edge, where erroneously reduced mechanical properties and increased data scatter resulted. Keeping the machine compliance at the small-sample value yields $E_r = 138 \pm 10$ GPa (corresponding to $E = 147 \pm 12$ GPa), $H = 11.9 \pm 0.3$ GPa, and $h_c = 112.0 \pm 1.6$ nm, consistent with a springboard effect at the wafer periphery. Interestingly, the reduced modulus decreased far more than the hardness (by 11.5% vs. by 2.5%, respectively) in comparison to the 10×10 array results. In fact, the hardness values from both stages of the study are in agreement when one takes into account their uncertainties. This differing dependency on machine compliance can be understood in the following way. Reduced modulus can be expressed as $E_r = \pi^{1/2} S / (2 A_c^{1/2})$, and hardness is defined as $H = P_{max} / A_c$, where the contact area A_c is that of maximum load. Machine compliance directly affects the initial unloading slope representing the maximum-load contact stiffness; therefore, it highly influences the reduced modulus. The peak load, on the other hand, is independent of machine compliance, so hardness depends only weakly on the integrity of sample mounting through the denominator of its mathematical expression. In actuality, any dependence whatsoever on machine compliance via apparent shifts in the maximum-load contact area is an artifact caused by the Oliver-Pharr method of analysis, since the physically realized contact area at maximum load does not depend at all on machine compliance.

To examine the radial extent of the springboard effect found at the wafer edge, 58 equally spaced indents were placed in a line nearly spanning the wafer diameter (see Fig. 1 for a pictorial representation of the line length and location). The results displayed in Fig. 3 demonstrate that only the two outermost indents (located at each end of the line profile) yield noticeably lower values for the reduced modulus (but neither yields an unusual hardness). The distance from the wafer edge to the second outermost indent (the first acceptable indent) is 2.35 mm. The distance from the wafer edge to the outermost vacuum ring residing under the wafer is 5.72 nm. The downward pull associated with this ring might be causing the wafer to bow upward at its edge. To maximize the surface area suitable for nanoindentation testing, the outermost vacuum ring residing under the wafer should be as close as possible to the wafer edge. Excluding the two outermost indents and keeping the machine compliance at the small-sample value, $E_r = 155 \pm 2$ GPa (corresponding to $E = 168 \pm 3$ GPa), $H = 12.3 \pm 0.2$ GPa, and $h_c = 109.8 \pm 0.9$ nm along the line profile. These values overlap with the 10×10 array results.
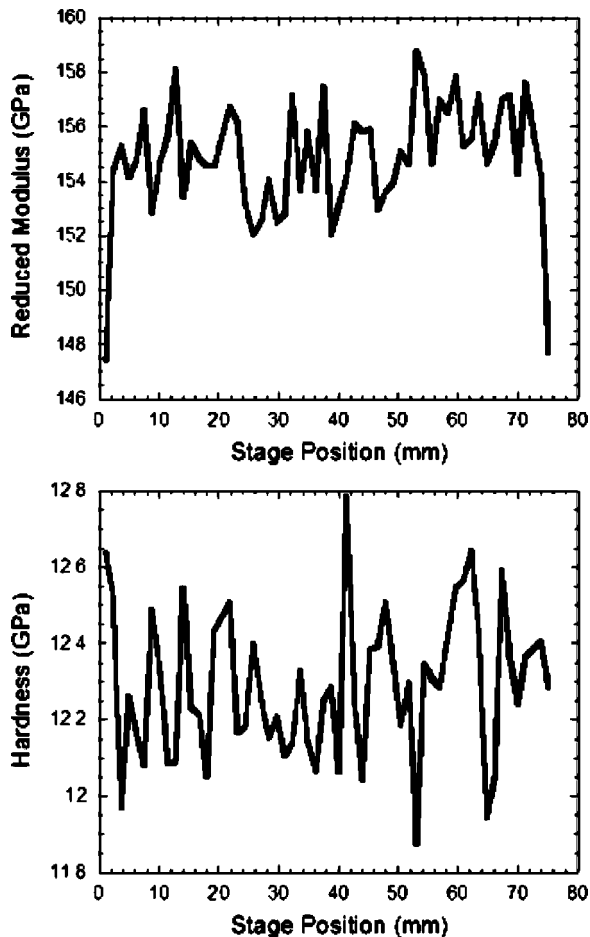
FIG. 3. Reduced modulus and hardness of silicon along the vertical solid line drawn on the upper photograph of Fig 1.

FIG. 4. Reduced modulus and hardness of silicon along the horizontal solid line drawn on the upper photograph of Fig. 1. Vertical dashed lines represent the borders of the circular center port.

Vacuum chuck features such as the circular center port of either chuck and the tweezer slot of the slotted chuck warrant closer attention. Figure 4 shows reduced modulus and hardness as a function of position for a line of 40 equally spaced indents passing over the midpoint of the center port of the slotless chuck (see Fig. 1 for a pictorial representation of the line length and location). Both in terms of level and scatter, the results over the center port are consistent with the results over the remainder of the line profile, indicating that the diameter of the center port is sufficiently small to prevent a noticeable increase in machine compliance. Keeping the machine compliance at the small-sample value yields $E_r = 157 \pm 2$ GPa (corresponding to $E = 171 \pm 3$ GPa), $H = 12.2 \pm 0.2$ GPa, and $h_c = 110.3 \pm 0.8$ nm along the line profile, again consistent with the 10×10 array results. The diameter of the center port is more than twice the channel width of the vacuum rings; therefore, except for the previously noted possibility of inducing upward bowing at the wafer perimeter, the vacuum rings should not be problematic.

Figure 5 shows reduced modulus and hardness as a function of position for a line of 27 equally spaced indents crossing the tweezer slot of the slotted vacuum chuck (see Fig. 1 for a pictorial representation of the line length and location, and the upper plot of Fig. 6 for a visual display of the corresponding force-displacement curves). The detrimental im-

pact of the tweezer slot is obvious; the reduced modulus results depend strongly on position, and, although far more weakly, the hardness results also clearly depend on position. Keeping the machine compliance at the small-sample value yields $E_r = 140 \pm 19$ GPa (corresponding to $E = 150 \pm 23$ GPa), $H = 12.3 \pm 0.4$ GPa, and $h_c = 109.9 \pm 2.1$ nm upon blind averaging of the results. The lower plot of Fig. 6 demonstrates that the widely spread curves shown in the upper plot of Fig. 6 can be made remarkably consistent by optimizing the machine compliance individually to produce a constant reduced modulus of 156 GPa or correspondingly a constant Young's modulus of 169 GPa (the 10×10 array value). This confirms that the assumption of a linear spring for machine compliance is adequate, and suggests that local fluctuations in machine compliance may be the dominant source of scatter in nanoindentation testing of smooth, highly homogeneous materials. The procedure of optimizing the machine compliance individually results in $H = 12.6 \pm 0.1$ GPa and $h_c = 108.5 \pm 0.6$ nm along the line profile. Surprisingly, both values fall just short of overlapping the 10×10 array results; the reason for this is unknown at this time. The hardness after machine compliance optimization does, however, match
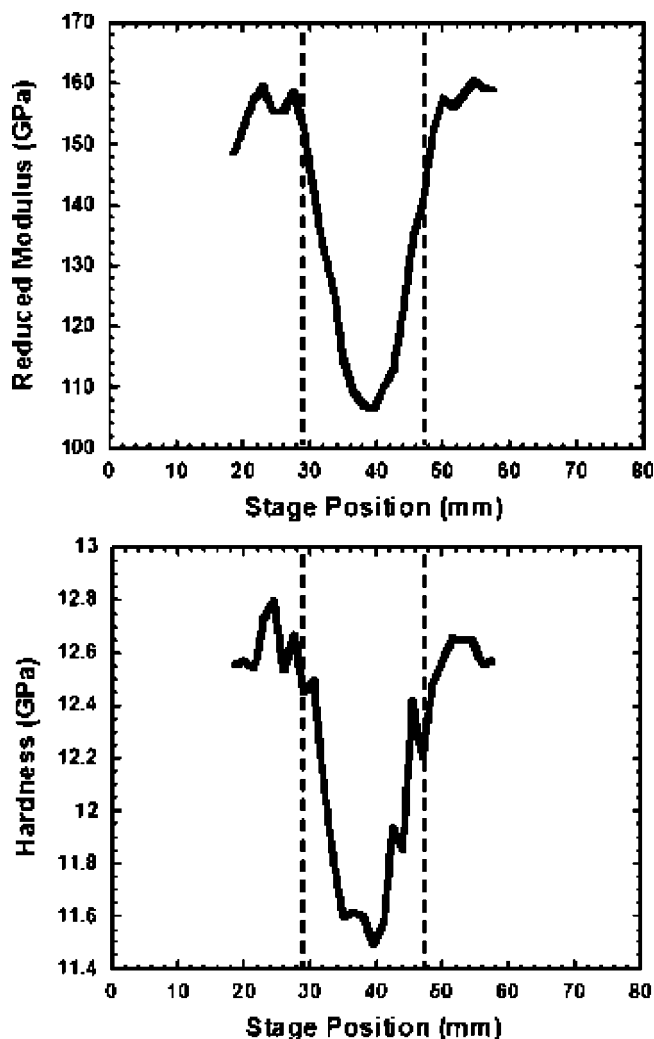
FIG. 5. Reduced modulus and hardness of silicon along the horizontal solid line drawn on the lower photograph of Fig. 1. Vertical dashed lines represent the borders of the tweezer slot.

FIG. 6. Force-displacement curves for silicon along the horizontal solid line drawn on the lower photograph of Fig. 1. Upper plot: the machine compliance is fixed at the small-sample value of 0.80 nm/mN. Lower plot: the machine compliance is permitted to vary to produce a constant reduced modulus of 156 GPa or correspondingly a constant Young's modulus of 169 GPa.

the published value of Grillo *et al.* extremely well. It is not apparent whether Grillo *et al.* examined Si(100) as an intact wafer or as a small piece off of a wafer.

The worst case machine compliance found along the executed line profile is 4.53 nm/mN at the midpoint of the slot. Compliances are additive, thus the maximum observed influence of the slot is the addition of 3.73 nm/mN to the small-sample value of 0.80 nm/mN. Beam and plate bending compliances scale inversely with thickness to the third power.[12] To suppress the additional 3.73 nm/mN in machine compliance to no more than 10% of the small-sample value, the thickness of the silicon wafer must increase from 410 μm to at least 1.48 mm $[t_2 = (t_1^3 C_1/C_2)^{1/3}$, where $t_1 = 410$ μm, $C_1 = 3.73$ nm/mN, and $C_2 = 0.1 \times 0.80$ nm/mN]. Increasing wafer thickness to the stated value would have reduced the maximum effect of uncorrected additional machine compliance along the executed line profile to 0.97% and 0.16% (determined using the analysis routines of the instrument software) in terms of reduced modulus and hardness of silicon, respectively; however, thick wafers tend to be costly and in short supply. Hence, it is more practical to eliminate the tweezer slot altogether; shutting down vacuum and slid-

ing off the wafer to break the vacuum seal are simple tasks to accomplish. Another option is to correct the data taken above the slot via a machine compliance map generated from a bare wafer nominally identical to the one supporting the library (the well-established Young's modulus of silicon also can be exploited to generate a machine compliance map of the wafer periphery if the thin-film library extends to the wafer edge and edge compliance remains a complication). The relative standard deviation in additional machine compliance is proportional to the relative standard deviation in wafer thickness. The thickness tolerance of the wafer batch used in this study is ± 5 μm; therefore, a bare wafer implemented as a machine compliance standard and a wafer-supported library possessing the same nominal wafer thickness should differ by no more than 2.4% in terms of additional machine compliance. In the case of silicon, an error of 2.4% in machine compliance impacts reduced modulus and hardness by only 0.23% and 0.04%, respectively. Yet another option for eliminating the influence of the tweezer slot is to rotate the wafer relative to the slot to finish the screening experiment, but this is not conducive to high-throughput combinatorial research. As a final note, a total of 304 indentations were

performed on silicon (a relatively hard material) during the course of the investigation without appreciably blunting the diamond indenter.

[1] A. C. Fischer-Cripps, *Nanoindentation* (Springer, New York, 2004).

[2] For a review article on the use of nanoindentation in combinatorial materials science, see O. L. Warren and T. J. Wyrobek, Meas. Sci. Technol. **16**, 100 (2005).

[3] K. Chondroudis, K. Cendak, E. Ramberg, and M. Devenney, "A combinatorial workflow for the rapid discovery and optimization of low dielectric constant materials," presented at 2003 MRS Spring Meeting, Session E8, 21–25 April 2003, San Francisco, CA (abstract available at http://www.mrs.org/meetings/spring2003/program/AbstractBookE.pdf).

[4] W. C. Oliver and G. M. Pharr, J. Mater. Res. **7**, 1564 (1992).

[5] ISO 14577-1:2002, ISO 14577-2:2002, and ISO 14577-3:2002 are ratified standards for instrumented indentation testing.

[6] O. L. Warren, S. A. Downs, and T. J. Wyrobek, Z. Metallkd. **95**, 287 (2004).

[7] K. I. Schiffman and R. L. A. Küster, Z. Metallkd. **95**, 311 (2004).

[8] For a recent paper describing many aspects of nanoindentation-induced phase transformations in silicon, see J. E. Bradby, J. S. Williams, and M. V. Swain, Mater. Res. Soc. Symp. Proc. **750**, Y8.24.1 (2003).

[9] S. E. Grillo, M. Ducarroir, M. Nadal, E. Tournié, and J.-P. Faurie, J. Phys. D **36**, L5 (2003).

[10] L. Riester, R. J. Bridge, and K. Breder, Mater. Res. Soc. Symp. Proc. **522**, 45 (1998).

[11] T. F. Page, G. M. Pharr, J. L. Hay, W. C. Oliver, B. N. Lucas, E. Herbert, and L. Riester, Mater. Res. Soc. Symp. Proc. **522**, 53 (1998).

[12] J. J. Tuma, *Handbook of Physical Calculations* (McGraw-Hill, New York, 1983).

Data management and visualization of x-ray diffraction spectra from thin film ternary composition spreads

I. Takeuchi,[a] C. J. Long, O. O. Famodu, M. Murakami,
J. Hattrick-Simpers, and G. W. Rubloff
Department of Materials Science and Engineering and Center for Superconducting Research,
University of Maryland, College Park, Maryland 20742

M. Stukowski and K. Rajan
Department of Materials Science and Engineering, Rensselaer Polytechnic Institute, Troy, New York 12180

We discuss techniques for managing and visualizing x-ray diffraction spectrum data for thin film composition spreads which map large fractions of ternary compositional phase diagrams. An in-house x-ray microdiffractometer is used to obtain spectra from over 500 different compositions on an individual spread. The MATLAB software is used to quickly organize the data and create various plots from which one can quickly grasp different information regarding structural and phase changes across the composition spreads. Such exercises are valuable in rapidly assessing the "overall" picture of the structural evolution across phase diagrams before focusing in on specific composition regions for detailed structural analysis. We have also shown that simple linear correlation analysis of the x-ray diffraction peak information (position, intensity and full width at half maximum) and physical properties such as magnetization can be used to obtain insight about the physical properties. © *2005 American Institute of Physics.* [DOI: 10.1063/1.1927079]

I. INTRODUCTION

The combinatorial approach to materials has proven to be effective in uncovering new materials phases with enhanced physical properties as well as rapidly mapping composition-structure-property relationships in complex materials systems.[1–3] In particular, composition spreads experiments are instrumental in mapping compositional phase diagrams of multicomponent systems.[4–7] Mapping phase diagrams is central in obtaining comprehensive pictures of materials systems, and mapping active physical properties such as magnetism and ferroelectricity as a function of composition is an integral part of understanding the underlying physical mechanism of the properties.[7–9] The diffusion-multiple approach has been developed to map phase diagrams using assembly of three or more bulk metal pieces.[10,11] In thin film composition spreads, large fractions of compositional phase diagrams can be mapped out with a high density of data points on an individual wafer. The large number of data points can truly bring out the strength of the spread technique because systematic mapping can reveal subtle composition dependence effects which are otherwise very difficult to discern from individual sample experiments with sparse sampling in composition space.[7] Thin film materials can often display properties with deviation from bulk samples, but it has been shown in many systems that one can indeed obtain compositional trends which closely resemble or mirror those of bulk counterparts.[7,12] There are also instances where the target application of a specific materials system is a thin film device. In such cases, using thin film spread samples for mapping composition dependence is well justified.[6]

There have been significant advances in the area of rapid characterization and screening techniques, and there are now a variety of physical properties that can be mapped for combinatorial libraries and composition spreads with relatively quick turn around.[1–3,13] One piece of information of paramount importance is the phase and crystal structure distribution. There are scanning x-ray microdiffraction techniques, which can be employed to obtain a large number of diffractograms from combinatorial samples.[5,14–18] Synchrotron x-ray microdiffraction is a natural technique for this task because the high intensity x-ray beam available can be used to quickly step through a large number of positions on a combinatorial library with minimal time to obtain a diffraction spectrum at each point.[14–17] In-house microdiffraction x-ray units require much longer time to take data per point, but their advantage is that one can perform the experiments locally.[5,7,18]

Obtaining and analyzing x-ray diffraction (XRD) spectra for phase and structure determination is a central part of any materials research exercise, and it should play a significant role in combinatorial materials research as well. Ideally, one would take and study x-ray spectra of all the positions on every sample in order to obtain complete mapping of phase and structural information across the combinatorial samples. However, despite the availability of the microdiffraction techniques, there are practical problems one immediately encounters in implementing such an exercise. First of all, one needs to come up with an efficient way to file and store a large number of x-ray spectra data. The sheer quantity of data produced by these processes presents a significant logis-

[a]Author to whom correspondence should be addressed; electronic mail: takeuchi@umd.edu

tical challenge. A common analysis method for a diffraction spectrum is to fit the peaks with reflections of known compounds using software such as JADE by Materials Data, Inc. and TOPAZ by Bruker. Although some software can be automated to fit a large number of x-ray spectra serially, it is a very cumbersome process and fitting does not necessarily produce the "correct answers." Because the very premise of the combinatorial experimentation is that there are potentially entirely new phases with previously unknown crystal structures in the library, any simple fitting procedure using reflections from known phases is not sufficient. The situation is further complicated by the fact that in any compositional phase diagram, there can be multi-phase regions.

Despite such difficulties, XRD analysis remains a most fundamental method in materials science, and one must find a way to effectively incorporate it into the overall combinatorial strategy. In this article, we discuss our methodology and procedures for data management and visualization of x-ray microdiffraction spectra of combinatorial samples. The ultimate goal of such an exercise is to obtain a comprehensive and accurate mapping of phase and structure distribution across composition spreads of rich and complex materials systems containing previously unknown materials phases. Although the techniques described here only represent a first step toward this goal, we demonstrate that even simple data visualization and analysis exercises can be effective in extracting important insight about the properties of materials systems under study.

II. EXPERIMENT

As a model system, we have looked at the Ni–Al–Mn ternary system. This system contains Heusler alloys that are ferromagnetic shape memory alloys.[19] We have previously used a scanning superconducting quantum interference device (SQUID) microscope and micromachined arrays of cantilevers to map composition regions which are ferromagnetic and reversible martensites in this system, respectively.[20] Despite a number of previous phase mapping studies including ours, much is still unknown about different regions of this phase diagram. The Heusler alloys are known to display significant variation in magnetism and martensite properties depending on the chemical order parameter which in turn strongly depends on the processing conditions. It is also well known that many compositions in this system display modulated structures giving rise to extra diffraction peaks.[21] The present work therefore is a part of an ongoing effort to better understand this ternary system.

Natural thin film composition spreads of the Ni–Mn–Al system were deposited using an ultrahigh-vacuum three gun magnetron co-sputtering system with a base pressure of 10^{-9} Torr (10^{-7} Pa) on 3 in. (76.2 mm) diameter (100) oriented Si wafers. The details of the synthesis procedure can be found in Refs. 7 and 20.

The composition spread wafers were deposited at room temperature followed by an *in situ* annealing for 2 h in high vacuum at temperatures in the range of 853–970 K. The total processing time (i.e., deposition and heat treatment of the composition spread) of a sample is roughly 5–6 h before
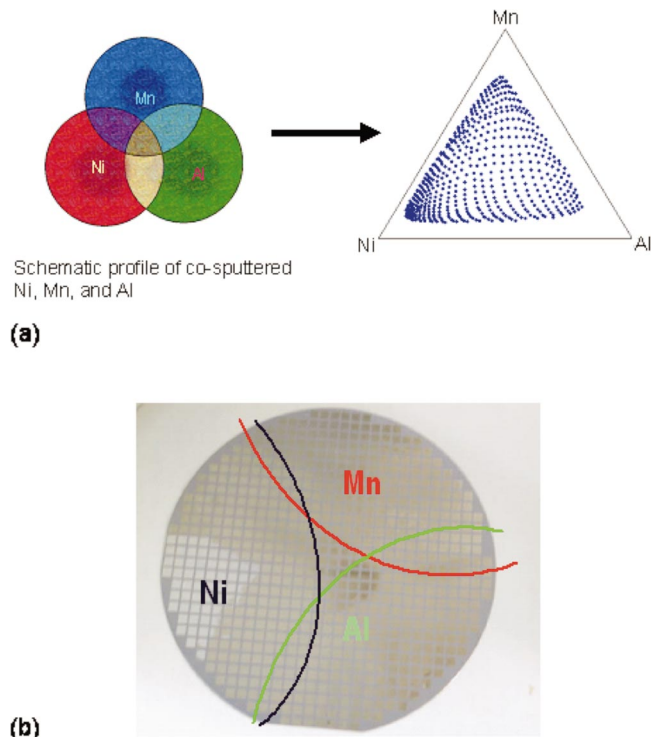
FIG. 1. (Color) Thin film natural composition spreads made using three-gun co-sputtering (a) shows the schematic of the deposition profile (left) and the composition region covered on a single experiment mapped on a ternary phase diagram. (b) A photograph of a 3 in. composition spread wafer. The spread is patterned into squares using a physical shadow mask placed over the wafer during the deposition. The lines are a guide to the eye of the approximate concentration profile.

it is ready for rapid characterization. After the deposition, the composition of the wafer spread is immediately determined via wavelength dispersive spectroscopy (WDS) in atomic percent. This measurement can determine the percent fraction of each atom contained at each point on the wafer accurately. The total scan time for this measurement is $\sim 12-14$ h for the entire wafer. Figure 1(a) shows a schematic procedure for the synthesis of a ternary composition spread which covers most of the phase diagram.

X-ray microdiffraction of the fabricated films was performed using the ω-scan mode of a D8 DISCOVER for combinatorial screening (Bruker-AXS). It is equipped with a GADDS two-dimensional (2D) detector which captures the data for a fixed range of 2θ and ω at once. Each composition spread wafer contained 535 individual 1.75 mm $\times$ 1.75 mm squares with continuously changing compositions [Fig. 1(b)]. In order to scan the 2θ range of interest (2θ from 25 to 75°), microdiffraction was performed in three frames for each square. We use an x-ray beam spot size of 500 μm in diameter. We have determined that to collect sufficient data, it takes at least 5 min for each square per frame. Even though scanning of the beam is automated, one still needs to preset the positions of all the squares manually. This process can take up to roughly 2 h for an entire wafer with 535 squares. Because we can only scan the entire library for the same frame before moving to the next frame, the entire spread library must be scanned three times to cover the 2θ range from 20 to 75°. For each x-ray microdiffraction frame,
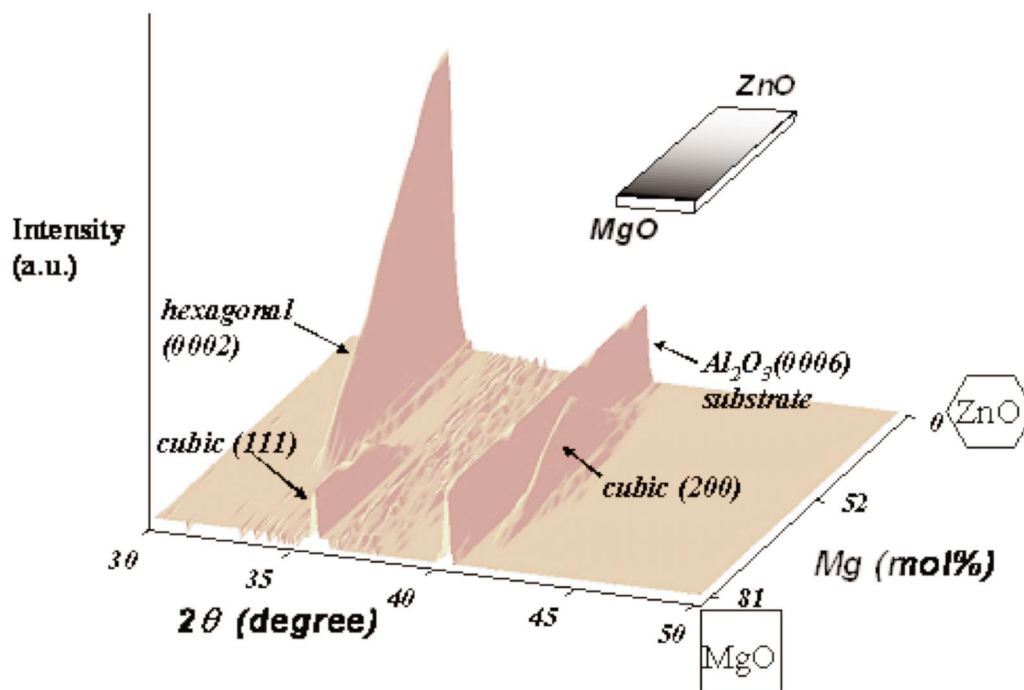
FIG. 2. (Color) Example of an x-ray microdiffraction of a binary composition spread. The composition continuously changes from ZnO to MgO. Compositions up to $Mg_{0.81}Zn_{0.19}O$ are plotted. The phase distribution and evolution are readily identified from such a plot. The inset is a schematic of the binary spread (Ref 5).

the scan takes ~45 h (~1.86 days). Therefore, to complete all three frames takes ~134 h (~5.57 days). Once this is accomplished, the microdiffraction data are in the form of 2D detector images. The size of data generated by this process is on the order of 4 gigabytes for a single spread wafer.

Once the actual scans are completed, the raw data are compiled and integrated to obtain the 2θ angles and peak intensities using the D8 GADDS program and a script to automate the process. At this stage, the data are converted to numeric two column text data in an ASCII format. In this format, data
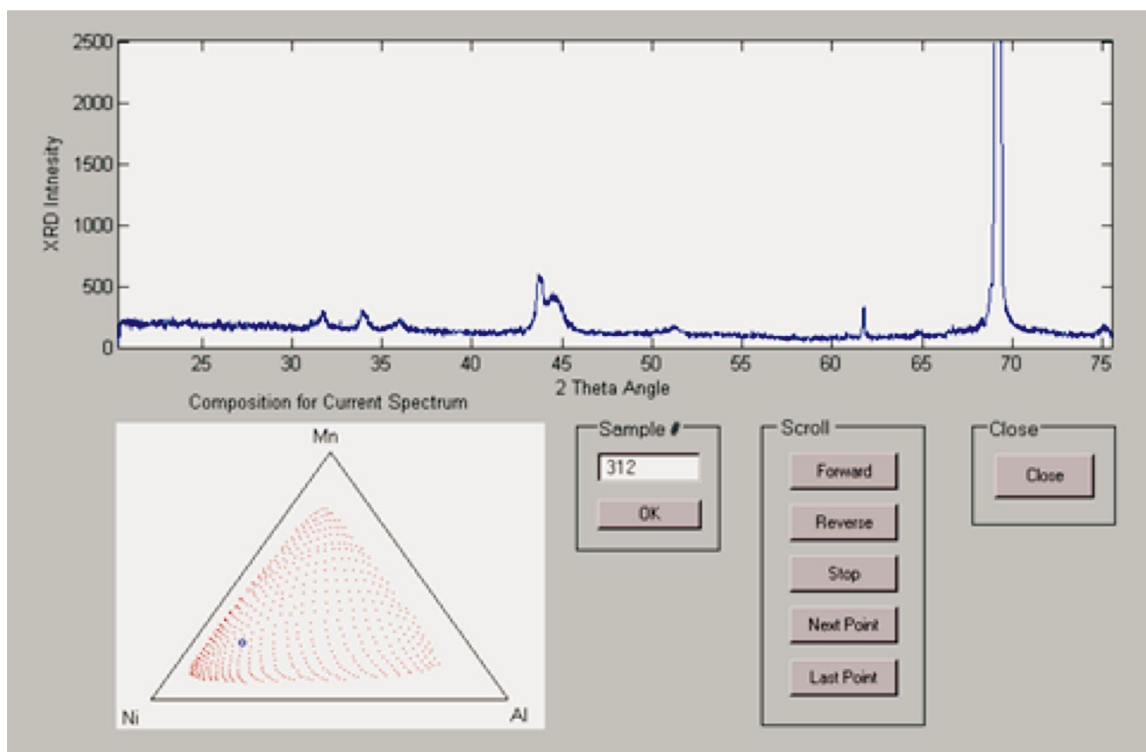
FIG. 3. (Color) The Spectrum Scroller visualization scheme. X-ray diffraction spectra from every single spot on the spread wafer are organized in such a way so that one can scroll through the compositional phase diagram viewing the spectra one by one or in a scrolling manner. [Animation is available as an EPAPS movie file (see Ref. 35). It is also available at www.combi.umd.edu].
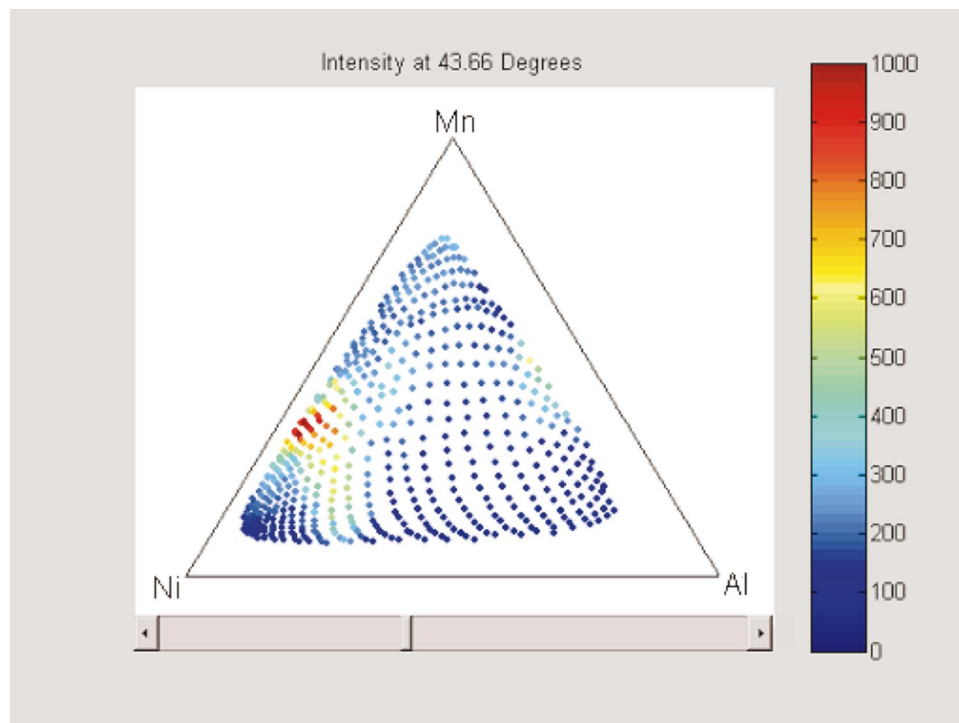
FIG. 4. (Color) The Angle Scroller visualization scheme. It gives an intensity plot of the x-ray signal for the entire spread. The 2θ angle can be changed or scrolled to monitor the composition region where a peak exists. [Animation is available as an EPAPS movie file (Ref. 35). It is also available at www.combi.umd.edu].

for each square on the composition spread takes up about 45 kbytes, and the total data volume is ~30 MB. This step takes ~7 h. Then the data for each of the three frames for each composition square are merged using a MATLAB script.

III. DATA VISUALIZATION

We have chosen MATLAB as the primary program for the organization, storage and analysis of this large quantity of data because it has the capacity to import data from a variety of sources, store the data in arbitrarily large data structures, manipulate that data using a large base of both built-in and user defined functions, and because it has a powerful set of graphical rendering tools.

It takes about 1 h to import and consolidate all of the relevant data into MATLAB using scripts developed specifically for this purpose. One script consolidates the XRD data from about 1500 ASCII files (three frames for each of 535 compositions) into numerical matrices within a MATLAB workspace. Other scripts are used to import composition data obtained using WDS and quantitative values of other physical properties measured using various rapid characterization techniques. There properties may include resistivity, saturation magnetization, and coercive field. Once the data are imported into MATLAB, one can perform numerical operations and create graphical representations.

Visual inspection of x-ray spectra is a crucial part of the materials analysis process. It is often the case that one gets so accustomed to looking at x-ray spectra of a particular materials system under study that after a while, just a quick glance at a spectrum can suffice to provide most of the essential information about the structural properties of the material. Thus, it is imperative that we are able to view together all of the spectra we take. In composition spread experiments where the composition continuously changes from a known

composition region with a known structure to a new region of interest, visual inspection and simple comparison of the spectra can be used to quickly determine evolution in the composition-structure relationship. This has been well illustrated in the binary composition spreads where the composition changes continuously from one to another.[5,22] In binary systems, three axes are sufficient to render all of the data; one axis describes the composition, one describes the diffraction angle and a third describes the diffraction intensity. The data are then rendered as a surface in that parameter space. Figure 2 shows XRD data from a $Mg_xZn_{1-x}O$ composition spread where the composition changes continuously from pure ZnO to MgO. Its synthesis procedure is described in Ref. 5. From such a plot, one can readily discern all the major features. Careful scrutiny of this plot was instrumental in identifying a new epitaxial relationship between coexisting cubic and hexagonal phases of $Mg_xZn_{1-x}O$.[5]

In ternary systems, an additional axis is needed to describe all of the possible compositions. One immediate solution is to reduce the amount of information. For instance, one can create a plot describing the intensity, angular position, or the full width at half maximum of a limited number of peaks, each representing a different phase.[23,24] This may suffice for materials systems where there is minimal change in the structure across the spread and where one can track the structural change in terms of the shift in one or two main diffraction peaks. However, this is not the case for complicated systems such as Ni–Mn–Al. In addition to the main reflections, there may be satellite peaks arising from the chemical ordering as well as modulation in the structure. Thus, it is desirable to be able to visualize the entire spectrum for the entire composition spread.

One way to represent this data is as a scalar volumetric array. In this case, two axes (X and Y) are used for the composition, one (Z) is used for the diffraction angle, and the
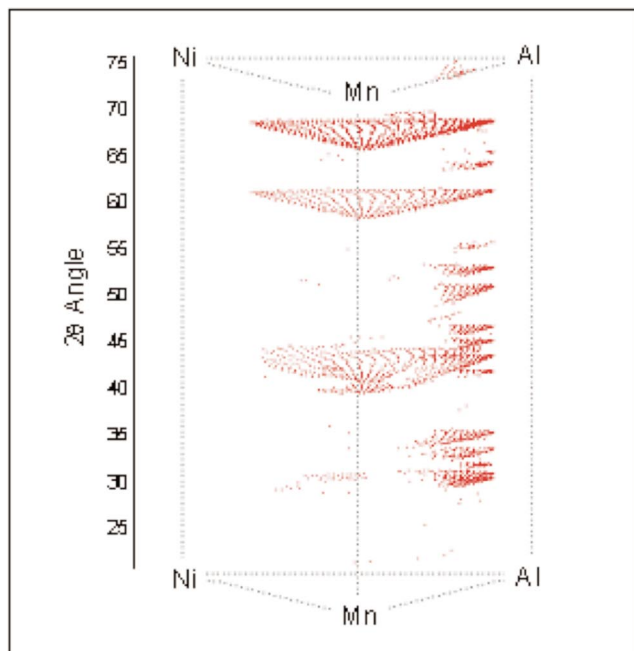
(a)
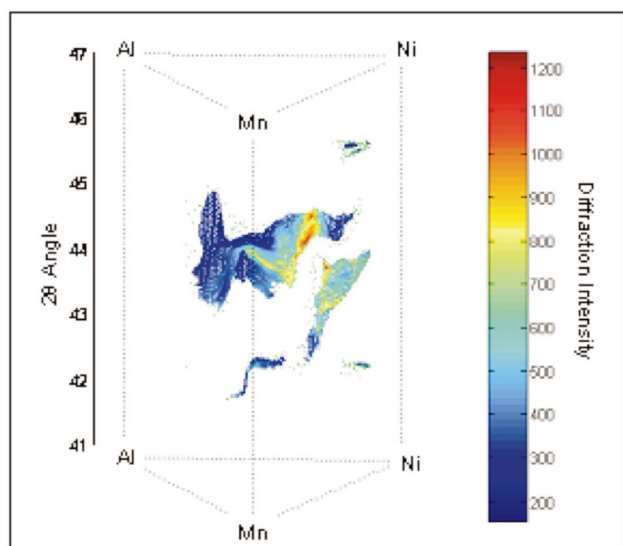
(b)

FIG. 5. (Color) The Peak Plotter visualization scheme. This scheme displays the positions of all the diffraction peaks for every point on the composition spread in a 3D space (a). The intensity information can be added in the form of color (b). [Perspective rotation greatly facilitates the visualization: animation is available as an EPAPS movie file (see Ref. 35). It is also available at www.combi.umd.edu].

intensity is represented as a scalar at all points in the parameter space. Volumetric scalar arrays of data are common in many other fields, including computed tomography (CT), magnetic resonance imaging, and computer modeling using finite element analysis[25–27] and much work has been done on the visualization of these arrays.[28–34] However, due to the nature of the information contained within an XRD spec-

trum, not all of the techniques which have been developed are useful for our purposes. To date, there are basically three different techniques used to visualize volumetric data: (1) looking at planar cross sections of the data, (2) the rendering of binary surfaces at some threshold value (isosurfacing) and (3) treating the data as a solid object with varying transparency and/or color values at each voxel, then casting parallel "rays" through it onto some observation plane. The first technique is useful and will be discussed below. The second technique is less useful because it does not present all (or even most) of the important information that is contained in an XRD spectrum. The information that is valuable about an XRD peak is its intensity, diffraction angle and full width at half maximum. Rendering an isosurface at some intensity value throws away all of the information about how the intensity changes as a function of diffraction angle and composition (except that it is higher on one side of the surface than the other). This means that it disregards information about the maximum intensity of XRD peaks and the full width at half maximum of these peaks. The third technique may be useful, and may be pursued in the future. In the following paragraphs, we will discuss our adaptations of these techniques to the rendering of volumetric XRD data

The first scheme, the Spectrum Scroller, allows a user to rapidly view hundreds of XRD spectra and the corresponding compositions in a matter of minutes. The ordering of the spectrums is such that the composition changes only slightly from spectrum to spectrum. This allows the user to see trends in the change of the spectrum as a function of composition. The user interface for this technique is shown in Fig. 3. The graph at the top shows the XRD spectrum. The graph at bottom left shows where the composition for this spectrum is located on the ternary composition diagram. All of the points for which spectra have been obtained are shown in red and the composition for the displayed spectrum is circled in blue. The program can be operated to "scroll" through all of the compositions in a predetermined order. As the program scrolls, the spectrum continuously changes to reflect the structure of the compositon indicated by the graph on the bottom left. (A movie animation illustrating the utility of this scheme is available as supplementary information. It is also available at www.combi.umd.edu.) Because the Spectrum Scroller allows one to look at individual spectra in the standard format, it is helpful when one needs to quickly grasp an idea about the distribution of peak patterns across the phase diagram. The act of scrolling enables one to track the evolution in the spectrum as a function of composition. For instance, from this exercise, we were able to quickly identify the regions in the phase diagram where the (220) peak of the austenite phase near 44° splits into the peaks of the lower symmetry martensite phase due to the martensitic transition of the shape memory alloy.

The second visualization technique, the Angle Scroller, allows a user to look at the intensity data for all of the spectra simultaneously, but it looks at only one angle at a time. The angles are scrolled through in time to get a full picture of the data. The user interface for this technique is shown in Fig. 4. This technique is useful for two main features: (1) it allows one to see in a single image the composition range
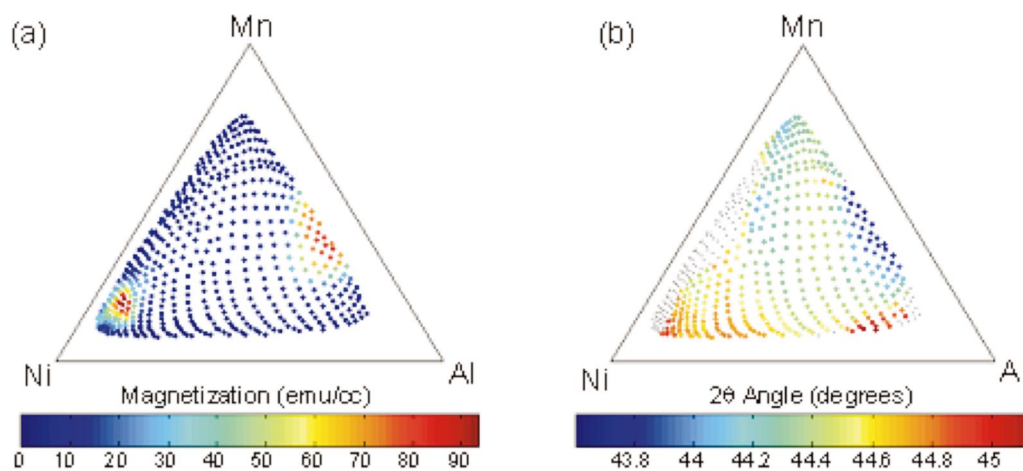
FIG. 6. (Color) (a) Mapping of remanent magnetization value calculated from scanning SQUID microscopy data. (b) Mapping of the shift in the x-ray peak position near ~45°. With respect to the strongly magnetic region in the Al-rich region, the two plots have strong anti-correlation.

over which a particular peak "exists" at a particular angle and (2) it allows the user to track the shift in the position of the peak (as a function of angle) in the composition space. The utility of this visualization scheme is illustrated in an animation where the composition region with high diffraction intensity is seen to change continuously as a function of angle (through time). (The animation is available as supplementary information. It is also available at www.combi.umd.edu). We found this scheme to be useful in rapidly assessing the size of the composition region with the same structure as well as for closely monitoring how a particular peak shifts its position in angle as the composition changes. It is worth noting that this method is identical to that of viewing planar cross sections of CT data. In CT, it is often useful to look at cross sections in other planar directions. However, when looking at XRD data of ternary compositions, we are mostly interested in how the diffraction intensity changes with respect to composition. The only planes in which the variation of the data is due to changing composition are those that are either at a constant diffraction angle, or those which are parallel to the diffraction angle axis. In this model, we have chosen to use the planes describing a single angle (and all compositions) because it allows us to look at the variation of data over the entire composition region. If a plane parallel to the diffraction angle axis were to be chosen, then that data would represent a binary (two composition) spread and could best be visualized using the binary visualization technique already discussed.

Both of the preceding schemes have required the use of time as an extra dimension in the visualization of ternary XRD data. The next scheme makes use of three-dimensional (3D) rendering in order to show all the XRD peaks for all compositions simultaneously. This is the Peak Plotter, and it is shown in Fig. 5. In order to create this plot, it is necessary to separately record the positions and the intensity of all the peaks for each composition.

Two techniques have been developed to perform this task. In the first technique, we use a peak search program (written in Igor), which takes a spectrum and creates a list of peaks with their positions and the intensity. This process can be automated and applied to an arbitrary large number of

spectra to create a table containing all the peaks. The problem with this technique is that the automated peak search often fails to find small peaks, properly separate adjacent peaks, and/or correctly index the same peak appearing in different spectra as the same peak. It is particularly difficult to handle a situation where a peak evolves into twin peaks as the composition is changed. Since part of our inquiry is to find reversible structural transitions, the problem of not being able to discern divergent peaks is particularly problematic.

As an alternative to the automated peak search approach, a more reliable, semiautomated/semimanual method has been developed. In this approach, a person sifts through all the spectra to record the positions and the intensity of each XRD peak maximum. If done entirely by hand, this would require a significant amount of work. For example, in the Ni–Mn–Al system, there may be as many as 18 peaks in the 2θ range of 25–75° for each composition sampled. Generally, from the 535 spectra, the positions and the intensity of about 3500 peaks are recorded. To reduce the difficulty of the recording task, a program similar to the Spectrum Scroller described above is used. By using this program, the recording and organization of the position and the intensity of the peaks are reduced to a point and click process, instead of being carried out entirely by hand. The task of going through 535 spectra and picking out the 3500 peaks takes about 3 h. Once that is complete, it is possible to make a plot such as shown in Fig. 5. However, if a plot of, say, only the angular position of the peak corresponding to the main phase is desired, then another sorting step is required. The peaks for each spectrum must be indexed such that "the same" peak can be picked out in all of the spectra where it exists. This is accomplished by fitting a surface (usually a plane) between each group of points in Fig. 5. Peaks are then sorted and indexed by assigning a peak number according to which planes they fall between.

In the Peak Plotter scheme, the presence of a peak at a particular 2θ angle and at a particular composition is signified by a point in the 3D space [Fig. 5(a)]. The color of the point can be chosen to represent either the intensity or the full width at half maximum. However, given the fact that there are potentially a large number of peaks which are yet to

be identified reflections from yet to be identified phases, comparing absolute intensity or full width at half maximum is not necessarily useful. In fact, we have found that just marking the peak position is effective in conveying the breadth of structural variation across the phase diagram. Once one decides to zoom into a particular 2θ range, the intensity information can be added [Fig. 5(b)]. In such a plot, shifts in the position and the intensity of selected peaks can be mapped across the entire spread. Since this is plotted in a 3D environment, it is best to see it from multiple perspectives. An animation of a rotating perspective is available as supplementary information. It is also available at www.combi.umd.edu.

The shifts in the peak position and the intensity are often directly correlated with change in the physical properties. Thus, one can use the information in the table of all the peak positions and intensity compiled for this scheme to look for correlation between the structural change and physical properties. One way to find these correlations is to calculate the correlation coefficients between all the columns in the table together with added columns for the values of some physical properties. Correlation coefficients which are near 1 indicate high linear correlation and those near −1 indicate that two parameters are linearly anti-correlated. Linear anti-correlation means that when one parameter has high values relative to its average, the other parameter has low values relative to its average.

Figure 6(a) shows the in-plane remanent magnetization mapping of the Ni–Mn–Al system. There is a large ferromagnetic region near the Ni deficient Mn–Al region of the phase diagram which had not been previously reported. Mn–Al and some Mn–Al–Ni are known as ferromagnets, but to the best of our knowledge, there have not been reports of ferromagnetism in the composition region with such high Al concentration. We have calculated the correlation coefficients between the remanent magnetization and all of the XRD peak information and found that there is a strong anti-correlation between the magnetization and the angular position of the peak which is centered at around 44.5°. This peak is the (220) or similar reflections of the main phase present throughout the phase diagram. The shift in this peak position is mapped in Fig. 6(b). The comparison of the figures indicates that magnetization increases when the lattice parameter increases (the peak shifts toward a lower angle). Mn has a magnetic exchange integral which changes its sign from negative (antiferromagnetic) to positive (ferromagnetic) ordering as the distance between the atoms is increased. From the correlation, therefore, we conclude that even in such an Al-rich region, it is the Mn atoms in the crystal that are giving rise to the ferromagnetism. Thus, we have demonstrated the utility of the XRD analysis for the entire composition spread in obtaining an important insight about the physical property of the material system. Note that this was carried out *without* in-depth structural analysis involving fitting of the spectra and figuring out the exact crystal structure. In the future, full width at half maximum information for all the XRD peaks can also be included for such analyses.

It is possible to investigate the structure property relation in a broader context. Correlation between structure information and a variety of physical properties can be investigated using the visualization techniques discussed here. Some of the properties of interest which we can map in a high throughput manner include band gap, conductivity, dielectric constant, martensitic transformation temperature, saturation magnetization and coercive field. All of this information is then mapped out to produce a complete phase diagram.

[1] H. Koinuma and I. Takeuchi, Nat. Mater. **3**, 429 (2004).
[2] *Combinatorial Materials Syntheses*, edited by Ichiro Takeuchi and Xiao-Dong Xiang (Dekker, New York, 2003) (ISBN: 0-8247-4119-6).
[3] I. Takeuchi, R. B. van Dover, and H. Koinuma, MRS Bull. **27**, 301 (2002).
[4] T. Fukumura, M. Ohtani, M. Kawasaki, Y. Okimoto, T. Kageyama, T. Koida, T. Hasegawa, Y. Tokura, and H. Koninuma, Appl. Phys. Lett. **77**, 3426 (2000).
[5] I. Takeuchi, W. Yang, K.-S. Chang, M. Aronova, R. D. Vispute, T. Venkatesan, and L. A. Bendersky, J. Appl. Phys. **94**, 7336 (2003).
[6] R. B. van Dover, L. F. Schneemeyer, and R. M. Fleming, Nature (London) **392**, 162 (1998).
[7] I. Takeuchi *et al.*, Nat. Mater. **2**, 180 (2003).
[8] S.-W. Cheong and H. Y. Hwang, *Ferromagnetism vs. Charge/Orbital Ordering in Mixed-Valent Manganites: Colossal Magneto-Resistive Oxides*, edited by Y. Tokura (Gordon and Breach, Amsterdam, 2000), p. 237.
[9] A. Damascelli, Z. Hussain, and Z.-X. Shen, Rev. Mod. Phys. **75**, 473 (2003).
[10] J. C. Zhang, Adv. Eng. Mater. **3**, 143 (2001).
[11] J. C. Zhang, J. Mater. Res. **16**, 1565 (2001).
[12] M. J. Turchinskaya, L. A. Bendersky, A. J. Shapiro, K. S. Chang, I. Takeuchi, and A. L. Roytburd, J. Mater. Res. **19**, 2546 (2004).
[13] Special issue of Meas. Sci. Technol. on Combinatorial Materials Science, **16** (2005).
[14] E. D. Issacs, M. Marcus, G. Aeppli, X.-D. Xiang, X.-D. Sun, P. G. Schultz, H.-K. Kao, G. S. Cargill, and R. Haushalter, Appl. Phys. Lett. **73**, 1820 (1998).
[15] Y. K. Yoo, T. Ohnishi, G. Wang, F. W. Duewer, X.-D. Xiang, Y.-S. Chu, D. D. Mancini, Y.-Q. Li, and R. C. O'Handley, Intermetallics **9**, 541 (2001).
[16] Y. S. Chu, A. Tkachuk, S. Vogt, P. Illinski, D. A. Walko, D. C. Mancini, E. M. Dufresne, L. He, and F. Tsui, Appl. Surf. Sci. **223**, 175 (2004).
[17] E. D. Specht, A. Rah, G. M. Pharr, E. P. George, P. Zschack, H. Hong, and J. Ilavsky, J. Mater. Res. **18**, 2522 (2003).
[18] M. Ohtani *et al.*, Appl. Phys. Lett. **79**, 3594 (2001).
[19] R. Kaimuna, H. Nakano, and K. Ishida, Metall. Mater. Trans. A **27A**, 4153 (1996).
[20] O. O. Famodu, J. Hattrick-Simpers, M. Aronova, K.-S. Chang, M. Murakami, M. Wuttig, T. Okazaki, Y. Furuya, and I. Takeuchi, Mater. Trans., JIM **45**, 173 (2004).
[21] M. Kohl, V. A. Chernenko, M. Ohtsuka, H. Reuter, and T. Takagi, Proceedings of the MRS Fall 2005 Symposia, Boston, MA, 29 November - 3 December 2004.
[22] K. S. Chang, M. Aronova, O. Famodu, I. Takeuchi, S. E. Lofland, J. Hattrick-Simpers, and H. Chang, Appl. Phys. Lett. **79**, 4411 (2001).
[23] X.-D. Xiang, Appl. Surf. Sci. **223**, 54 (2003).
[24] K. Hasegawa, P. Ahmet, N. Okazaki, T. Hasegawa, K. Fujimoto, M. Watanabe, T. Chikyow, and H. Koinuma, Appl. Surf. Sci. **223**, 229 (2003).
[25] B. Cabral, N. Cam, and J. Foran, Proceedings of the 1994 Symposium on Volume Visualization, Tysons Corner, VA, 17-18 October 1994, pp. 91–98.
[26] H. Fuchs, M. Levoy, and S. M. Pizer, Computer **22**, 46 (1989).
[27] R. S. Gallagher, Proceedings of the Second Conference on Visualization, San Diego, CA, 22-25 October 1991, pp. 68-75.
[28] T. T. Elvins, ACM SIGGRAPH Comput. Graph. **26**, 194 (1992).
[29] G. T. Herman and H. K. Liu, Comput. Graph. Image Process. **9**, 1 (1979).

[30] M. Levoy, IEEE Comput. Graphics Appl. **8**, 29 (1988).

[31] R. A. Drebin, L. Carpenter, and P. Hanrahan, ACM SIGGRAPH Comput. Graph. **22**, 65 (1988).

[32] W. E. Lorensen and H. E. Cline, ACM SIGGRAPH Comput. Graph., **21**, 163 (1987).

[33] L. Westover, ACM SIGGRAPH Comput. Graph. **24**, 367 (1990).

[34] H. Fuchs, Z. M. Kedem, and S. P. Uselton, Commun. ACM **20**, 693 (1977).

[35] See EPAPS Document No. ERSINAK-76-257506 for animation of the figures as movie files. This document can be reached through a direct link in the online article's HTML reference section or via the EPAPS homepage (http://www.aip.org/pubservs/epaps.html).

Combinatorial Investigation of Ferromagnetic Shape-Memory Alloys in the Ni-Mn-Al Ternary System Using a Composition Spread Technique

Olugbenga O. Famodu[1], Jason Hattrick-Simpers[1], Maria Aronova[2], Kao-Shuo Chang[1], Makoto Murakami[1], Manfred Wuttig[1], Teiko Okazaki[3], Yasubumi Furuya[3], Lee A. Knauss[4], Leonid A. Bendersky[5], Frank. S. Biancaniello[5] and Ichiro Takeuchi[1,2]*

[1] *Small Smart Systems Center, Department of Materials Science and Engineering, University of Maryland, College Park, MD 20742, USA*
[2] *Center for Superconductivity Research, Department of Physics, University of Maryland, College Park, MD 20742, USA*
[3] *Faculty of Science and Technology, Hirosaki University, Hirosaki, Japan*
[4] *Neocera, Inc., 10000 Virginia Manor Road, Beltsville, MD 20705, USA*
[5] *Materials Science and Engineering Laboratory, National Institute of Standards and Technology (NIST), 100 Bureau Drive, Gaithersburg, MD 20899-8555, USA*

Using a thin-film composition spread technique, we have mapped the phase diagram of the Ni-Mn-Al ternary system in search of ferromagnetic shape-memory alloys (FMSA). A characterization technique that allows detection of martensitic transitions by visual inspection using micromachined cantilever arrays was combined with quantitative magnetization mapping using scanning superconducting quantum interference device (SQUID) microscopy. A large compositional region in the Al deficient part of the phase diagram was found to be ferromagnetic and reversibly martensitic at room temperature. In addition, in the Al rich region, a new compositional range that displays marked ferromagnetism was found.

1. Introduction

Ferromagnetic shape-memory alloys (FMSAs) are an important class of materials that can be used for applications in magnetomechanical devices and sensors.[1] Research in this field has been largely focused on Fe-Pd and Ni_2MnGa due to the large strains induced in these systems by an external magnetic field.[2–4] Other alloy systems such as Co_2NiGa and Co_2NiAl have also been found to be FMSAs.[5,6] Previously, we have demonstrated functional mapping of the Ni-Mn-Ga ternary system and found a large previously unexplored region of the ternary phase diagram that is ferromagnetic and reversibly martensitic.[7] Partly due to the brittleness of these known materials, there is a continuing interest in finding other FMSAs.[8,9] The Ni-Mn-Al alloy system is considered to be a good candidate because it does not contain Ga and the alloys are less brittle than Ni-Mn-Ga.[6,9–11,31,32] In this work, we have mapped the physical properties of the Ni-Mn-Al ternary system with respect to ferromagnetism and martensitic transitions using the composition spread technique.

2. Experimental Techniques

We have developed thin-film based high-throughput fabrication and detection techniques for exploring FSMAs.[7,27] The screening technique employs micromachined arrays of mechanical cantilever libraries to detect structural transformation in thin-film composition spreads, combined with room-temperature quantitative remnant magnetization mapping using a scanning SQUID microscope. In

addition, a scanning x-ray microdiffractometer is used to map the structure.[7]

Natural composition spreads of the Ni-Mn-Al system were deposited using an ultra high-vacuum magnetron co-sputtering system (with a base pressure in the range of 10^{-7} Pa) on 76.2 mm (three-inch) diameter (100) Si wafers. Three 38.1 mm (1.5-inch) diameter guns are placed parallel and adjacent to each other in a triangular configuration. Figure 1 illustrates our composition spread deposition scheme. Each gun is housed in a 50.8 mm (2-inch) long chimney which
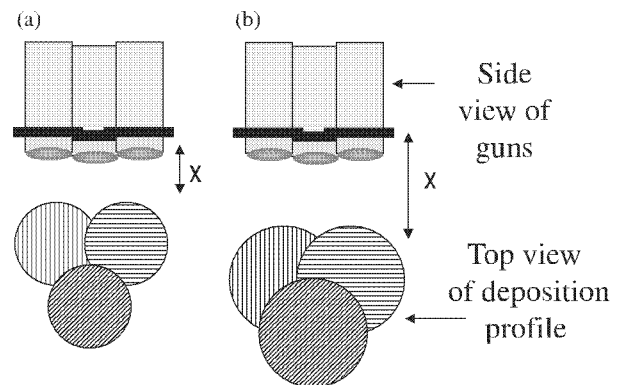
Fig. 1 Schematic of co-sputtering of natural ternary composition spread using parallel gun geometry. Three 38.1 mm (1.5-inch)-diameter guns are placed parallel and adjacent to each other in a triangular configuration. By adjusting the distance (x), between the substrate and parallel guns we can control the compositional region of the phase diagram covered on the substrate. (a) shows a schematic of deposition pattern for a short distance between the substrate and guns. (b) shows the schematic of deposition pattern at a further distance.

*Corresponding author, E-mail: takeuchi@squid.umd.edu

helps to minimize the cross contamination of the guns. The three targets used in the present experiment were Ni, Mn and Al, and both DC and RF sputtering were used. The typical gun power was 50~150 watts, and spread films with thicknesses in the range of 250 nm to 0.5 μm were deposited in 1~2 h. By adjusting the power applied to each gun and the distance between the guns and the substrate (typically 12 cm), different regions of the ternary phase diagram can be mapped. The composition spread wafers were deposited at room temperature followed by an *in-situ* annealing in vacuum at temperatures in the range of 853–970 K for 2 h. X-ray microdiffraction of the fabricated films was performed using the ω-scan mode of a D8 DISCOVER (Bruker-AXS for combinatorial screening). Wavelength dispersive spectroscopy (WDS) was used to accurately map the composition spread of every wafer.

For rapid characterization of magnetic properties, we used a room temperature scanning SQUID microscope,[12] which provides mapping of local magnetic field emanating from samples at room temperature. Prior to the scan, the spread wafer is magnetized in an in-plane direction. Figure 2(a) is a magnetic field image of a Ni-Mn-Al spread wafer. This spread was annealed at 973 K for 2 h. Variation in the strength of the magnetic field, as a function of composition is evident. In this ternary system, we have consistently observed two distinct compositional regions, which showed ferromagnetism at room temperature. We have used a numerical algorithm to directly convert the field distribution information into quantitative remanent magnetization.[13] The values of remanent magnetization extracted here are consistent with those obtained by a vibrating sample magnetometer (VSM) on separate individual composition samples measured at room temperature. The result of this calculation was then combined with the composition mapping to obtain a room-temperature magnetic phase diagram (Fig. 2(b)).

In order to map the regions of shape memory alloys and their transition temperatures for the entire spread, we have micromachined arrays of cantilevers and deposited the composition spreads directly on the array wafers (Fig. 3(a)). In order to study the thermally induced actuation of the entire cantilever array simultaneously by visual inspection, we developed a method that works on the simple principle that individual cantilevers with metallic films deposited on them behave as concave mirrors. During a transition, stress-induced actuation on a cantilever results in a sudden change in the radius of the "mirror", and an image reflected off of the cantilevers responds very sensitively as the concavity of the mirrors change. By monitoring the change in the image as a function of temperature, composition regions undergoing a transition can be readily discerned.[7]

Figure 3(a) is a photograph of a spread deposited on a cantilever array, which is reflecting an image of a series of colored lines. The measurement consists of recording the image projected on cantilever arrays as the temperature is varied. From the cantilevers displaying transitions, another phase diagram is constructed (Fig. 3(b)) which shows the composition regions that undergo martensitic transitions, and the corresponding transition temperatures. Because of the finite size of individual cantilevers, there is compositional
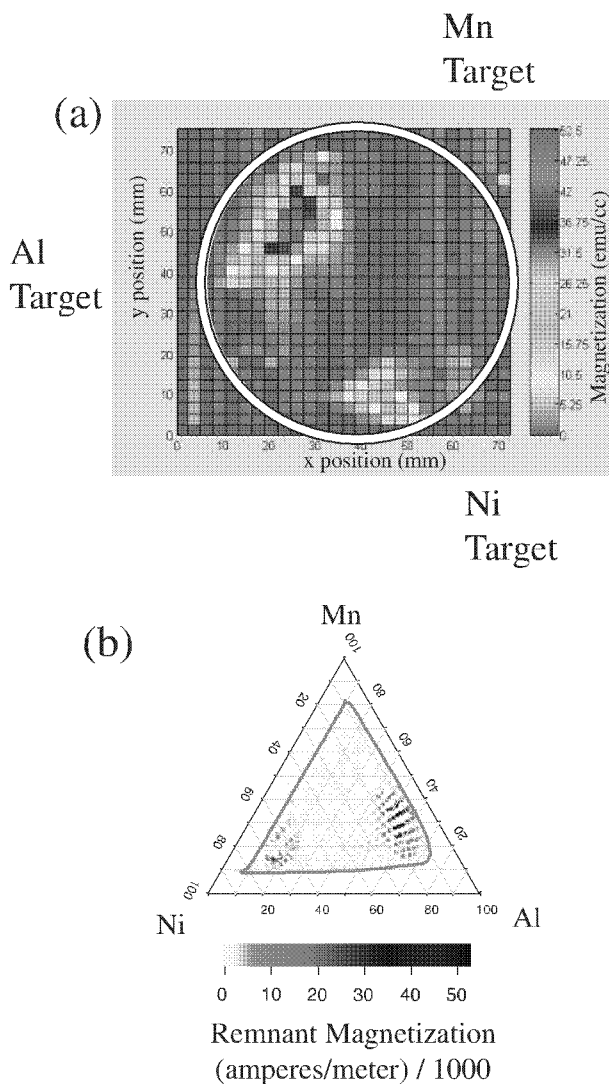
Fig. 2 Scanning SQUID microscope mapping of magnetic properties at room temperature. (a) Scanning SQUID image of a N-Mn-Al spread wafer. The spread is patterned into arrays of 1.75 mm × 1.75 mm square grids so that the microscope can detect variation of magnetization in the in-plane magnetized samples. The SQUID microscope is sensitive to magnetic poles. The separation between the SQUID and the sample is about 0.3 mm, which defines the spatial resolution of the measurement. The circle is the outline of the wafer. This wafer was annealed at 973 K. (b) Room-temperature magnetic phase diagram of Ni-Mn-Al deduced from (a). The region inside the curve is the compositional region mapped on the spread wafer.

variation on each cantilever. A typical thermal hysteresis width of a martensitic transition observed here is about 50 K, and this is partly attributed to the compositional variation within each cantilever. WDS was performed at three positions along the length of each cantilever. Since it is difficult to distinguish the martensitic transformations of different regions on a single cantilever, for the purpose of mapping, we have labeled three compositions with one transition temperature observed for the cantilever. In Fig. 3(b), we plot results from one composition spread wafer. This spread was annealed at 853 K for 2 h. A clear trend emerges, and the general region that undergoes martensitic transitions

(a)

(b)

Martensite Start Transition, T/K
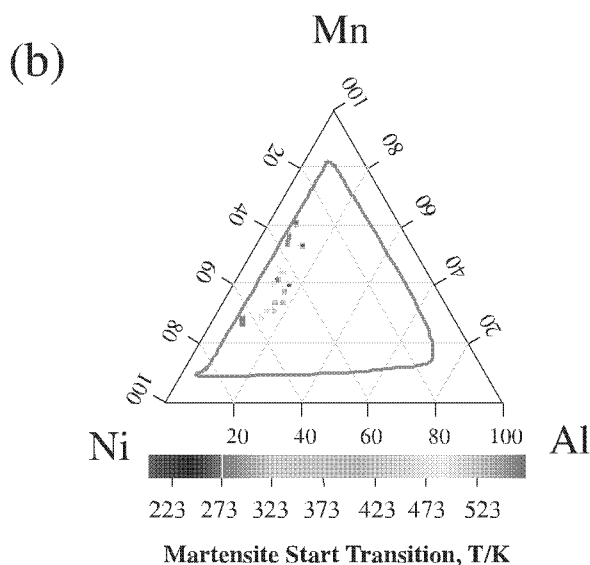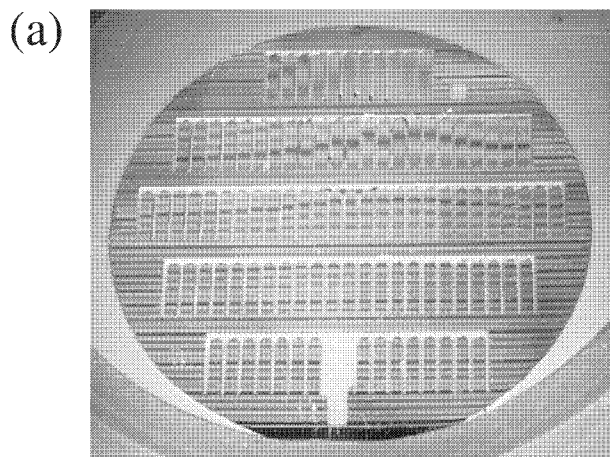
Fig. 3 Micromachined cantilever arrays used for detection of shape-memory alloys. (a) A photograph of a spread deposited on a cantilever library during the temperature-dependent measurement. A typical cantilever has an area of 2 mm by 8.5 mm and thickness of 60 μm. The lines are a reflection of an image with colored lines held at an incident angle over the wafer. The shift in the line positions of the reflected image as a function of temperature is used to detect small changes in the local curvature of the cantilever. (b) Mapping of the compositional regions on the phase diagram that displayed martensitic transformation on one wafer, which was annealed at 853 K. Martensite start temperature is plotted. The region inside the curve is the compositional region mapped on the spread wafer.

Fig. 4 Trends observed in spread pictured in Fig. 2(b) and the cantilever library in Fig. 3(b) are summarized. Ferromagnetism was observed in two regions. Martensites are observed in a compositional region similar to the region in the Ni-Mn-Ga system.

3. Discussion

There have been a number of reports on the investigation of properties of different regions of the Ni-Mn-Al ternary system over the years. Most of the work has been on bulk alloy samples. Recently, there have also been reports on Ni-Mn-Al thin films.[2,17] There are some discrepancies in the reported magnetic properties of Ni-Mn-Al alloys. This appears to originate from the sensitivity of the properties on thermal treatment, which varies among different studies.[18] Different thermal treatments naturally affect the degree of crystallization as well as the degree of disorder in samples.

Figure 4 summarizes our findings in the present experiment. There are two compositional regions that display ferromagnetism in this ternary system as can be seen in Fig. 2(b). In Region A, the composition range encompasses Ni (50–90 at%), Mn (10–40 at%), and Al (8–23 at%) and in Region B the composition range covers Ni (9–25 at%), Mn (15–50 at%), and Al (40–70 at%). In Region A, the magnitude of remnant magnetization becomes stronger as one goes towards higher Ni contents. The maximum remanent magnetization found here in Region A was in the range of $\sim$40000 A/m per meter ($\sim$40 emu/cc) for a nominal composition of $Ni_{76}Mn_{17}Al_7$.

It is well-known that order-disorder plays an important role in determining ferromagnetic and antiferromagnetic (AFM) properties of materials as has been reported in previous work.[7,19,28,30] It is known that the nominal Ni_2MnAl composition can display ferromagnetism or antiferromagnetism depending on processing conditions, and in turn on the degree of order/disorder.[17,19,33] We believe that this is the main reason for the discrepancy between our findings in Region A and other reports.

In principle, different phases and crystal structures exist across our spreads, thus the atomic order parameter after a specific heat treatment is different for various regions. Previously, we have found that our heat treatment results predominantly in equilibrium phases. Thus, we believe that the phases present in our spreads have a relatively high degree of ordering. We are currently investigating the details of the effect of order/disorder by fabricating spreads with

can be easily seen from the phase diagram. The exact martensitic transition temperatures are known to depend on many factors such as atomic ordering, microstructure and the residual stress in the film.[14–16] Reported values of the martensitic transition temperatures of Ni-Mn-Al samples in the literature also vary widely, depending on the composition and processing conditions. For this reason, we focus on the trend of the martensitic transition temperature as a function of compositional variation, rather than on the exact transition temperatures.

different cooling procedures so that different degrees of order/disorder will occur in our films.

We find that the compositional trend of martensites here appears to be very similar to what we found in the Ni-Mn-Ga system.[7] This region stretches from the Heusler composition of Ni_2MnAl to the Al-deficient region (Fig. 4). As one moves towards the more Al-deficient region, the martensite transition temperature increases (Fig. 3(b)). This region appears to correspond exactly with the region where the β/B2 parent phase has been reported.[9,10,18,20,29,30] An X-ray microbeam diffraction scan of the entire spread library indicates that most of the regions have diffractions consistent with the $L2_1$ or the B2 phase. This is in agreement with other published work.[8-10,17,20-24] Previously, Kainuma, *et al.*[9,20] also mapped the martensites in this region and reported a similar trend.

The finding here seems to indicate the presence of FMSAs in the Al-deficient Ni-rich region of the phase diagram where there is an overlap of compositions displaying martensites and remanent magnetization.

In order to confirm our findings from composition spreads, a bulk sample was made with a nominal composition of $Ni_{52.5}Mn_{30.9}Al_{16.5}$, which is in the ferromagnetic and martensitic region. An ingot o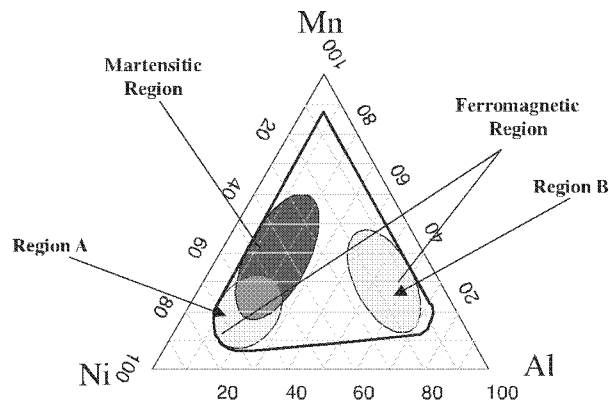f the $Ni_{52.5}Mn_{30.9}Al_{16.6}$ alloy was prepared from manganese, nickel and aluminum by using an arc-melting method in an argon atmosphere. A composition of the alloy was determined by electron microprobe. The bulk sample was annealed for 1 h at 773 K and then quenched in water. Figure 5 shows the room temperature X-ray diffraction of the bulk sample. After the anneal, the (220) peak has split into two peaks indicating that the alloy is indeed a martensite. This sample was however found to be mostly paramagnetic down to 4 K. We again attribute the difference in magnetic properties to different degrees of disorder in the bulk sample and our thin film spread. Analysis of the XRD result for the bulk sample also showed that the sample was polycrystalline and orthorhombic. An optical microscope study of a bulk sample has revealed plate like features consistent with presence of martensites.

We have found a large, previously unknown, area of the ternary phase diagram (Region B) that displays marked ferromagnetism. This region contains compositions with remnant magnetizations up to 50000 A/m (50 emu/cc). A qualitative remnant maximum of magnetization 53000 A/m (53 emu/cc) is reached at $Ni_{14}Mn_{32}Al_{54}$ on the spread. This

was confirmed by measuring a single square sample of the thin film cut from the spread with a VSM.

Near Region B, MnAl is known to have a metastable bct τ-phase, which displays hard ferromagnetic properties. There have been reports of synthesis of this phase in bulk as well as in thin film samples.[24-26] In sputtered films, it was found that upon substituting Ni ions into MnAl, the lattice forms a more stable cubic κ-phase, which has a CsCl type structure.[26] It has been reported that the magnetic properties of the κ-phase varies as the Ni concentration is increased.

We have discovered a much larger area which displays ferromagnetism that was previously unexplored. The qualitative trend of magnetization we observe for iso-aluminum samples in our spreads, which include the region in which the κ-phase was reported, is very similar to the reported trend, and there is a rather broad maximum of remnant magnetization being observed for intermediate dopings of Ni. The values of magnetization we observe in this region are of the same order as those in the previous reports.[25,26]

XRD data of our spread wafers show that in this compositional region the value of the lattice constant is higher than in any other region of the ternary phase diagram. This may explain the occurrence of ferromagnetism: it is consistent with the picture that as the distance between Mn ions is increased, exchange interaction shifts from anti-ferromagnetic to ferromagnetic.[19]

4. Summary

Using composition spreads, we have found that there are regions where both ferromagnetic and shape-memory properties coexist in the ternary Ni-Mn-Al alloy system. In addition, we observed a large Al-rich region of the phase diagram that shows remanent magnetism. We attribute the discrepancies in magnetic properties between our observations and other reports on different degrees of disorder in the samples. We confirmed that the martensitic composition found in our phase diagram indeed shows XRD consistent with a martensite in a bulk sample. More detailed investigation of individual compositions selected from the regions of interest is currently underway. In addition, further work on XRD phase mapping of the crystal structure is planned.

Acknowledgements

$$Ni_{52.5}Mn_{31}Al_{16.5}$$

(220)
(202)

Annealed at 773K for 3.6ks

20 30 40 50 60 70 80 90 100

Diffraction Angle, 2θ

Fig. 5 X-Ray diffraction taken at room temperature of a bulk sample after it is annealed at 773 K for 1 h.

REFERENCES

1) R. C. O'Handley, S. J. Murray, M. Marioni, H. Nembach and S. M. Allen: J. Appl. Phys. **87** (2000) 4712–4717.
2) R. D. James and M. Wuttig: Philos. Mag. A **77** (1998) 1273–1299.
3) K. Ullakko, J. K. Huang, C. Kantner, R. C. O'Handley and V. V. Kokorin: Appl. Phys. Lett. **69** (1996) 1966–1968.
4) A. Fujita, K. Fukamichi, F. Gejima, R. Kainuma and K. Ishida: Appl. Phys. Lett. **77** (2000) 3054–3056.
5) K. Oikawa, T. Ota, F. Gejima, T. Ohmori, R. Kainuma and K. Ishida: Mater. Trans. **42** (2001) 2472–2475.

6) C. Craciunescu, Y. Kishi, T. A. Lograsso and M. Wuttig: Scri. Mater. **47** (2002) 258–288.

7) I. Takeuchi, O. O. Famodu, J. C. Read, M. A. Aronova, K.-S. Chang, C. Craciunescu, S. E. Lofland, M. Wuttig, F. C. Wellstood, L. Knauss and A. Orozco: Nature Materials **2** (2003) 180–184.

8) L. Manosa, A. Planes, M. Acet, E. Duman and E. F. Wassermann: J. Appl. Phys. **93** (2003) 8498–8500.

9) R. Kainuma, H. Nakano and K. Ishida: Metall. Mater. Trans. A **27A** (1996) 4153–4162.

10) S. Morito, T. Kakeshita, K. Hirata, and K. Otsuka: Acta Mater. **46** (1998) 5377–5384.

11) Y. Sutou, I. Ohnuma, R. Kainuma, and K. Ishida: Metall. Mater. Trans. A **29A** (1998) 2225–2227.

12) E. F. Fleet, S. Chatraphorn, F. C. Wellstood, L. A. Knauss and S. M. Green: Rev. Sci. Inst. **72** (2001) 3281–3290.

13) Fleet, E. F. Ph.D. thesis, University of Maryland, 2000.

14) M. Ahlers: Journal de Physique IV, Colloque C8, supplement au Journal de Physique III **5** (1995) C8-71-C8-80.

15) S. Miyazaki and A. Ishida: Mater. Sci. Eng. A**273** (1999) 106–133.

16) C. M. Craciunescu, J. Li and M. Wuttig: Scri. Mater. **48** (2003) 65–70.

17) X. Y. Dong, J. W. Dong, J. Q. Xie, T. C. Shih, S. McKernan, C. Leighton and C. J. Palmstrom: J. Crys. Growth **254** (2003) 384–389.

18) Ll. Manosa, A. Plans, Ch. Somsen, Ch. Fell and M. Acet: J. Phys. IV France **11** (2001) Pr8-245-249.

19) M. Acet, E. Duman, E. F. Wasserman, Ll. Manosa and A. Planes: J. Appl. Phys. **92** (2002) 3867–3871.

20) R. Kainuma, F. Gejima, Y. Sutou, I. Ohnuma and K. Ishida: Mater. Trans., JIM **41** (2000) 943–949.

21) [21] P. L. Potapov, N. A. Polyakova, V. A. Udovenko and E. L. Svistunova: Z. Metallkd. **87** (1996) 33–39.

22) R. C. Taylor and C. C. Tsuei: Solid State Communi. **41** (1982) 503–506.

23) Y. Tan, T. Shinoda, Y. Mishima, and T. Suzuki: Mater. Trans. **42** (2001) 464–470.

24) D. P. Hoydick, E. J. Palmiere, and W. A. Soffa: Scr. Mater. **36** (1997) 151–156.

25) J. P. Harbison, T. Sands, R. Ramesh, L. T. Florez, B. J. Wilkens, and V. G. Keramidas: J. Cryst. Growth **111** (1991) 978–983.

26) A. Morisako, N. Koshiro, M. Matsumoto and M. Naoe: J. Appl. Phys. **67** (1990) 5655–5657.

27) J. Soltys: Physica Status Solidi (A) **66** (1981) 485–491.

28) R. M. Bozorth: IEEE Press, New Jersey. Ferromagnetism (1993) 317.

29) T. Shinoda, Y. Mishima and T. Suzuki: Mat. Res. Soc. Symp. Proc. **364** (1995) 573–577.

30) S. Morito and K. Otsuka: Mater. Sci. Engr. A**208** (1996) 47–55.

31) T. Kanomata, K. Shirakawa and T. Kaneko: J. Mag. Mag. Mater. **65** (1987) 76–82.

32) W. Deng, R. S. Brussa, G. P. Karwasz and A. Zecca: Mater. Sci. Forum **363–365** (2001) 198-200.

33) K. K. Jee, P. L. Potapov, S. Y. Song and M. C. Shin: Scr. Mater. **36** (1997) 207-212.

ARTICLES

Identification of novel compositions of ferromagnetic shape-memory alloys using composition spreads

I. TAKEUCHI*[1–3], O. O. FAMODU[1], J. C. READ[2], M. A. ARONOVA[2], K.-S. CHANG[1], C. CRACIUNESCU[1], S. E. LOFLAND[4], M. WUTTIG[1], F. C. WELLSTOOD[2], L. KNAUSS[5] AND A. OROZCO[5]

[1]Department of Materials Science and Engineering, University of Maryland, College Park, Maryland 20742, USA
[2]Center for Superconductivity Research, Department of Physics, University of Maryland, College Park, Maryland 20742, USA
[3]Small Smart Systems Center, University of Maryland, College Park, Maryland 20742, USA
[4]Department of Chemistry and Physics, Rowan University, Glassboro, New Jersey 08028, USA
[5]Neocera, Inc., 10000 Virginia Manor Road, Beltsville, Maryland 20705, USA
*e-mail: takeuchi@squid.umd.edu

Exploration of new ferroic (ferroelectric, ferromagnetic or ferroelastic) materials continues to be a central theme in condensed matter physics and to drive advances in key areas of technology. Here, using thin-film composition spreads, we have mapped the functional phase diagram of the Ni–Mn–Ga system whose Heusler composition Ni_2MnGa is a well known ferromagnetic shape-memory alloy. A characterization technique that allows detection of martensitic transitions by visual inspection was combined with quantitative magnetization mapping using scanning SQUID (superconducting quantum interference device) microscopy. We find that a large, previously unexplored region outside the Heusler composition contains reversible martensites that are also ferromagnetic. A clear relationship between magnetization and the martensitic transition temperature is observed, revealing a strong thermodynamical coupling between magnetism and martensitic instability across a large fraction of the phase diagram.

An underlying characteristic shared by most ferroic properties is that they are associated with structural transitions. As temperature or compositional variation is swept through the phase transition, ferroic materials display an onset and/or a peak in the respective ferroic functionality. Thus, one clear strategy for exploring novel ferroic materials is to search for compositions that are near structural phase transitions. In multiferroic materials, there is a complex interplay between ferroelectric, magnetic and elastic properties, and in some biferroics, such as natural magnetic ferroelectrics, the exact nature of coexistence of functionalities and their correlation are yet to be understood[1]. In multiferroic materials, the relative locations of the phase transitions of individual functionalities in phase space and temperature are important in determining their transducing behaviour, as well as an indicator of their functional correlation[2]. We have developed high-throughput fabrication and detection techniques, based on thin films, for exploring one class of multiferroics, ferromagnetic shape-memory alloys (FSMAs). These are ferromagnetic materials that undergo reversible martensitic transformation. Strong magnetoelastic coupling in FSMAs results in enormous magnetic-field-induced strain (9.5% at about 1 T)[3].

The new screening technique uses micromachined arrays of mechanical cantilever libraries to detect structural transformation on thin-film composition spreads combined with room-temperature quantitative magnetization mapping using a scanning SQUID (superconducting quantum interference device) microscope. In addition, a scanning X-ray microdiffractometer is used to map the structure and confirm the phase transitions. Previous combinatorial investigations and composition-spread studies have been largely limited to screening for physical properties that were immediately relevant for applications, or to mapping of well known systems[4–7]. Here, we demonstrate mapping of a mechanical property of thin-film materials for the first time, and by extracting an underlying relationship between composition, structure and property across the phase diagram, gain new insight into the physics of complex functionalities of the material system.
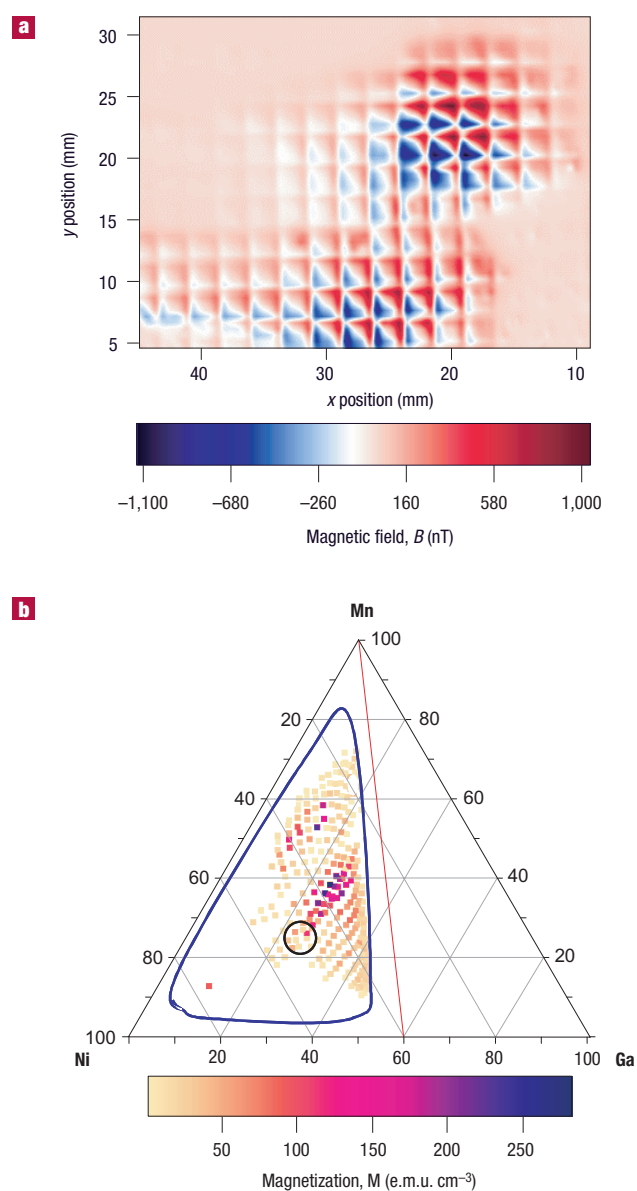
Figure 1 Mapping of magnetic properties using a room-temperature scanning SQUID microscope. a, Scanning SQUID image of part of a Ni–Mn–Ni$_2$Ga$_3$ spread wafer. The microscope is sensitive to magnetic poles. The spread is patterned into arrays of 2 mm × 2 mm square grids so that variation of magnetization in in-plane magnetized samples can be detected. The separation between the SQUID and the sample is about 0.3 mm, which defines the spatial resolution of the measurement. **b**, Room-temperature magnetic phase diagram of Ni–Mn–Ga. The region inside the blue curve is the compositional region mapped on the spread wafer. The composition where the red line meets the Ni–Ga line is Ni$_2$Ga$_3$ which is one of the three target compositions used here. The circle marks the compositions near the Ni$_2$MnGa Heusler composition.

We have mapped the bifunctional phase diagram of the Ni–Mn–Ga system in search of ferromagnetic shape-memory alloys. We observe a clear systematic relation between the Curie temperature and the martensitic transition temperature in a wide range of compositions across the ternary phase diagram. On the basis of our finding, the origin of the martensite in the Ni–Mn–Ga system is attributed to the Ga-induced structural instability in the ferromagnetic/antiferromagnetic transition region in Ni$_{1-x}$Mn$_x$.

Composition spreads—created by natural mixing due to co-deposition—were deposited in an ultra-high-vacuum magnetron co-sputtering system (with a base pressure in the range of 10^{-9} torr) on 3-inch-diameter (100) Si wafers. Three 1.5-inch-diameter guns were placed parallel and adjacent to each other in a triangular configuration. Each gun is housed in a 2-inch-long chimney, which helps to minimize the cross-contamination of the guns. The three targets used in the present experiment were Ni, Mn and Ni$_2$Ga$_3$, and both direct-current and radiofrequency sputtering were used. We used two deposition conditions that produced similar results. In the first, we deposited the spread at room temperature followed by annealing the wafer *in situ* at 550 °C for 2 hours in vacuum, and in the second, we directly deposited it on a wafer heated to 500 °C. The typical gun power was 50–100 watts, and spread films with thicknesses in the range of 500 nm to 1 μm were deposited in 1–2 hours. X-ray diffraction of the fabricated films revealed that they were fibre-textured with predominantly (110) orientation normal to the substrate. Wavelength-dispersive spectroscopy was used to accurately map the composition spread of every wafer. We have confirmed that, by adjusting the power applied to each gun and the distance between the guns and the substrate (typically 12 cm), different regions of the ternary phase diagram can be mapped out.

FSMAs occur in materials that are simultaneously ferromagnets and reversible martensites, which are shape-memory alloys. This defines one strategy for high-throughput screening: search for compositions that show both properties. For rapid characterization of magnetic properties, we used a scanning SQUID microscope[8], which provides mapping of local magnetic field emanating from samples at room temperature. Figure 1a shows a typical magnetic field image of a region from a spread wafer. Variation in the strength of the magnetic field as a function of composition is evident. We used a numerical algorithm to convert directly the field distribution information into quantitative magnetization[9]. The result of this calculation was then combined with the composition mapping to obtain a room-temperature magnetic phase diagram (Fig. 1b). In this figure, inside the blue curve is the compositional region mapped on this particular wafer. It is clear that the most strongly magnetic region stretches from near the middle of the phase diagram towards slightly Ni-rich composition. The black circle indicates the region surrounding the Heusler composition, Ni$_2$MnGa, which has been extensively studied[10–13], and which lies near one end of this highly magnetic region. As one moves away from this region, the magnetization gets smaller. Nickel is strongly magnetic, but its moment decreases rapidly as it is diluted with other elements, and in the Ni-rich region covered in this spread, it is already only weakly magnetic. Manganese is antiferromagnetic, and this is not detectable by SQUID.

The peak in magnetization is observed near the centre of the phase diagram around the half-Heusler composition, NiMnGa. Several spread wafers fabricated under slightly different conditions (that is, annealing temperatures) were all found to result in a similar phase diagram pattern. The values of magnetization extracted here are consistent with those of saturation magnetization obtained by a vibrating sample magnetometer on separate individual composition samples at room temperature. Ferromagnetic resonance measurements of the individual samples showed a very narrow linewidth (as low as 70 Oe) as well as well-defined spin resonance waves, indicating that the films are generally of very high quality and magnetically very homogeneous[14].

Properties of thin-film shape-memory alloys can be studied by depositing them on micromachined Si cantilevers[15]. By monitoring the reversible thermally induced actuation of such SMA film/Si cantilever bimorphs, martensitic transformation temperatures can be detected[15]. For individual cantilevers, actuation is typically measured using a capacitance formed between the end of the cantilever and a separate electrode. To map the regions of SMAs and their transition temperatures for the entire spread, we have micromachined arrays of
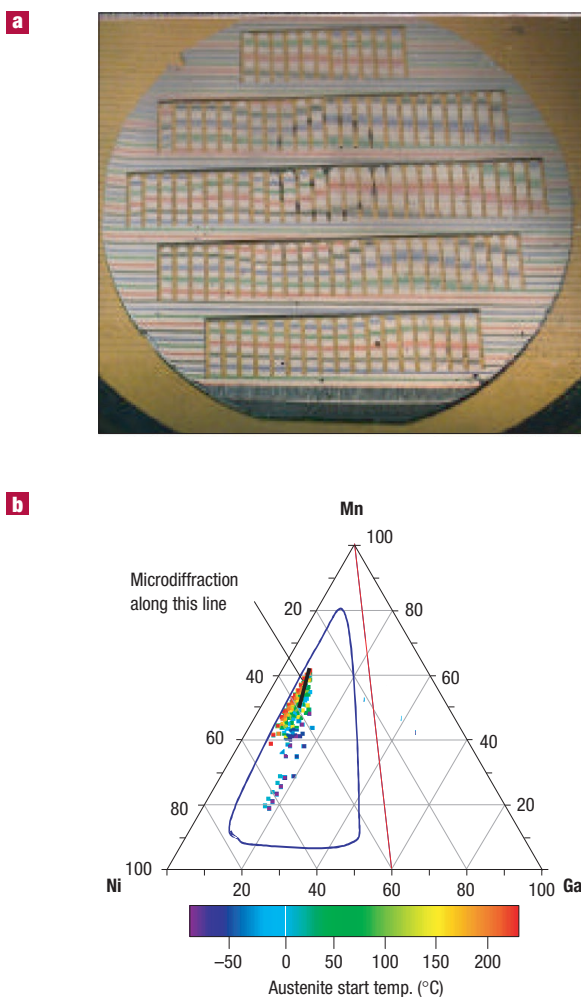
Figure 3 Scanning X-ray microdiffractogram taken at room temperature along a compositional region marked by the solid black line in Fig. 2b. The three peaks correspond to two from a martensite and the middle one from an austenite.

Figure 2 For detection of shape-memory alloys, Si wafers with micromachined cantilever arrays are used. **a**, A photograph of Ni–Mn–Ni$_2$Ga$_3$ spread deposited on a cantilever library taken during the temperature-dependent measurement. A typical cantilever has an area of 2 mm by 1 cm and thickness of 60 μm. The lines are a reflection of an image with coloured lines held over the wafer. The shifts in the positions of the lines as a function of temperature are used to detect small changes in the local curvature of the cantilever. See Supplementary Information for a video showing the structural transitions as detected by visual inspection. **b**, Mapping of compositional regions on the phase diagram that displayed martensitic transformation. Austenite start temperature is plotted. The composition where the red line meets the Ni–Ga line is Ni$_2$Ga$_3$.

cantilevers and deposited the composition spreads directly on the array wafers (Fig. 2a). To study thermally induced actuation of the entire cantilever array simultaneously by visual inspection, we have developed a method that works on the simple principle that individual cantilevers with metallic films deposited on them behave as concave mirrors. During a transition, stress-induced actuation of a cantilever results in a sudden change in the radius of curvature of the 'mirror', and an image reflected off the cantilevers responds very sensitively as the concavity of the mirrors change. By monitoring the change in the image as a function of temperature, we can readily discern composition regions undergoing a transition. In this manner, a cantilever array serves as a 'self-reporting' combinatorial library for detection of structural phase transitions. Figure 2a is a photograph of a spread deposited on a cantilever array that is reflecting an image (a series of coloured lines). The measurement

consists of recording the image projected on cantilever arrays as the temperature is varied. All transitions observed here were found to be reversible. From the cantilevers displaying transitions, another phase diagram is constructed (Fig. 2b), which shows the composition regions that undergo a martensitic transition and the corresponding transition temperature. (Because of the finite size of individual cantilevers, there is compositional variation on each cantilever. A typical thermal hysteresis width is about 50 K, and this is partly attributed to the compositional variation within each cantilever. Wavelength-dispersive spectroscopy was done at three positions along the length of each cantilever. For the purpose of mapping, we have labelled these three compositions with one transition temperature observed for the cantilever.)

Because of the layout of the cantilever libraries, there are regions of the spread not covered by active areas on cantilevers. We therefore compiled data from several spread wafers deposited at slightly different relative orientation of the sputtering guns with respect to the cantilever wafers. A clear trend emerges, and the general region that undergoes martensitic transitions can be easily seen from the phase diagram. The exact martensitic transition temperatures are known to depend on many factors such as atomic ordering, microstructure and the residual stress[16–18]. Reported values of the martensitic transition temperature of nominally Ni$_2$MnGa samples vary widely, and in one study[12] it was found to range from 113 K to 298 K. Naturally, we expect to have regions that undergo transitions at temperatures out of the range of our measurements (150–570 K), and we believe this is the reason we do not see Ni$_2$MnGa transforming in our measurement range in this particular experiment.

Rather than focusing on the exact transition temperature, we discuss the trend as a function of compositional variation. There are reversible martensites in large compositional regions previously not reported. This region stretches from near Ni$_2$MnGa to Ga-deficient, Mn-rich regions. The transition temperature increases as the molecular percentage of Ga is decreased. A typical composition here is Ni$_{43}$Mn$_{47}$Ga$_{10}$, whose martensite start temperature was found to be 400 K. In much of the newly discovered region the martensitic transformation temperature is near room temperature or above, which is desirable for practical applications.

Figure 4 Coexistence of ferromagnetism and reversible martensites in the Ni–Mn–Ga system. a, Functional phase diagram deduced from the present experiment. The hatched region has compositions with average electron/atom ratio 7.3–7.8. The dotted line surrounds the region of reversible martensites. In the ferromagnetic region, the red area has the highest magnetization. **b**, Martensitic start temperature against room-temperature saturation magnetization for data points mapped in Fig. 2b. For this magnetization, cantilevers were measured individually using a vibrating sample magnetometer. The line is a linear fit to the data.

The scanning X-ray microbeam diffraction (performed using a D8 DISCOVER with GADDS for combinatorial screening by Bruker-AXS) of the spread indicates that most of the regions have the diffraction pattern consistent with the L2$_1$ str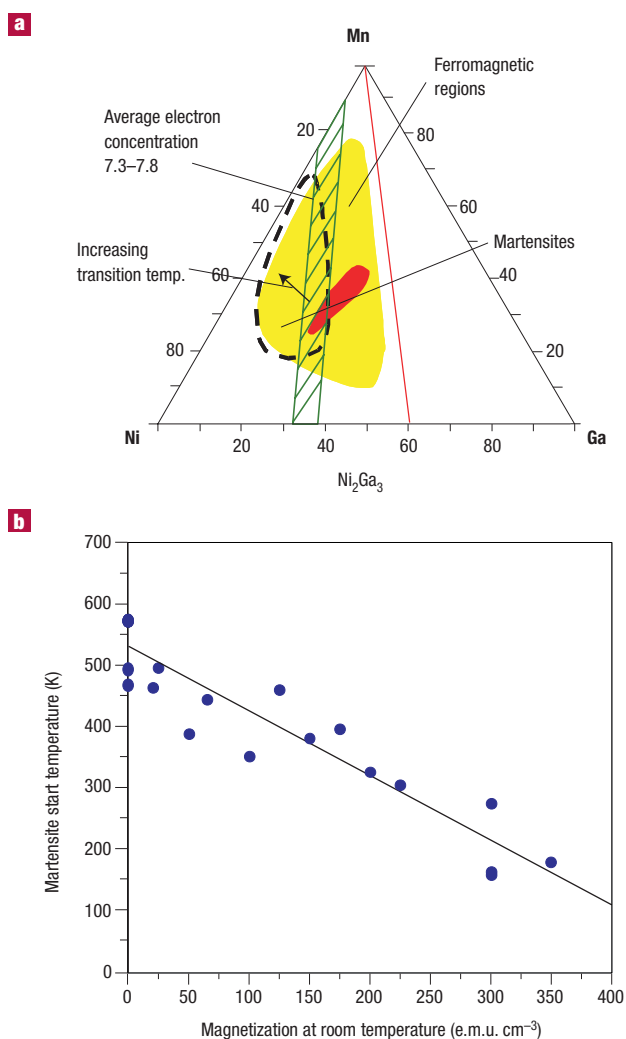ucture of the Heusler composition or a tetragonally distorted L2$_1$ structure (for the martensite). Figure 3 shows a scanning diffractogram taken at room temperature along the black line in Fig. 2b. In this region, the composition goes from the mixed phase displaying three peaks (two from the martensite and one from the austenite) to a region where it is mostly austenite.

Figure 4a summarizes the magnetic and the martensite phase diagrams deduced from the obtained data. It is evident that there is a large region well outside the near-Heusler composition that contains ferromagnetic, reversible martensites. It has been shown[19,20] that this class of material displays martensitic instability for stoichiometries

where the average number of electrons per atom is ~7.4. This behaviour is similar to that shown by vibrationally stabilized Hume–Rothery phases such as binary b.c.c. (body-centred cubic) Cu-based alloys which transform martensitically near a critical s-electron/atom ratio. The green hatched area in Fig. 4a covers the region where the average number of electrons per atom is 7.3–7.8. There is a large overlap between this region and the observed reversible martensite region. Because the electron/atom ratio rule is expected to apply strictly in the L2$_1$ structure, the overlap is perhaps an indication that the structure in the region is indeed L2$_1$ or one close to it.

The closer the composition is to the Ni$_{1-x}$Mn$_x$ line of the phase diagram, the lower the magnetization becomes. A separately prepared Ni$_{1-x}$Mn$_x$ spread did not show any indication of reversible martensites. Ni$_{1-x}$Mn$_x$ is known to be ferromagnetic for $x < 0.25$–0.4 and antiferromagnetic for greater x, and the actual value of x where the transition takes place is dependent on atomic ordering[21,22]. Martensitic instabilities are often associated with magnetic transitions[23]. We speculate that it is the ferromagnetic–antiferromagnetic transition or competition in Ni$_{1-x}$Mn$_x$ that is serving as the precursor to the martensites in the Ni–Mn–Ga system. The martensitic instability is perhaps set off by introduction of a small Ga concentration. The robustness of the martensite associated with the L2$_1$ phase may be reflecting the large solid-solution region in the Ni$_{1-x}$Mn$_x$ phase diagram near the Ni end.

The room-temperature magnetization against the martensitic start temperature is plotted in Fig. 4b for the compositions studied here. There is a clear relationship between the two parameters: the higher the magnetization, the lower the transformation temperature. We have confirmed that, for different samples, the magnetization at room temperature is proportional to the Curie temperature. The plot points to a strong thermodynamic magneto-structural coupling in this system. Such a coupling has previously been observed in a limited range of composition near Ni$_2$MnGa (inside the circle in Fig. 1b)[13], and a Ginzburg–Landau model has been used to explain the influence of the magnetic order on the martensitic transition[13,24]. Our experiment shows that the same coupling behaviour holds for a much wider compositional range. A phenomenological interpretation of this is that magnetism tends to stabilize the structure of the alloy, and this necessarily lowers the structural transformation temperature, as was first pointed out by Zener in reference to b.c.c. iron[25]. It is interesting that a first-principles calculation has suggested[26] that a cubic to tetragonal change would actually result in a slight increase in the total magnetic moment in Ni$_2$MnGa. The seeming discrepancy may indicate the importance of a magneto-elastic coupling term in the free energy which gives rise to the observed trend.

For applications, the goal when searching for new FSMAs is to find compositions with (1) high Curie temperature, and thus increased room-temperature magnetization, which in turn results in increased magnetostatic energy necessary for rotating the magneto-elastic domains, and (2) high martensitic transition temperatures. Our results clearly indicate an intrinsic trade-off between the two in a given system. Also, within a given ternary system, the Heusler composition does not necessarily provide the optimized functionality. This may also be the case for other properties such as complete spin polarization, which has been predicted in some Heusler compounds but not yet unambiguously established[27]. Perhaps exploration is warranted outside the Heusler composition in the ternary phase diagram.

Our work reinforces the importance of systematically exploring structural transitions in looking for novel ferroic materials as well as understanding their physical origin. Guided by techniques such as the ones described here, it would also be possible to make a systematic search and survey of functional correlations of other multiferroic materials.

ARTICLES

References

1. Hill, N. A. & Filippetto, A. Why are there any magnetic ferroelectrics? *J. Magn. Magn. Mater.* **242**, 976–979 (2002).
2. James, R. D. & Wuttig, M. Magnetostriction of martensite. *Phil. Mag. A* **77**, 1273–1299 (1998).
3. Sozinov, A., Likhachev, A. A., Lanska, N. & Ullakko, K. Giant magnetic-field-induced strain in NiMnGa seven-layered martensitic phase. *Appl. Phys. Lett.* **80**, 1746–1748 (2002).
4. Xiang, X. D. *et al.* A combinatorial approach to materials discovery. *Science* **268**, 1738–1740 (1995).
5. Wang, J. *et al.* Identification of a blue photoluminescent composite material from a combinatorial library. *Science* **279**, 1712–1714 (1998).
6. van Dover, R. B., Schneemeyer, L. F. & Fleming, R. M. Discovery of a useful thin-film dielectric using a composition-spread approach. *Nature* **392**, 162–164 (1998).
7. Yoo, Y. K. *et al.* Continuous mapping of structure-property relations in $Fe_{1-x}Ni_x$ metallic alloys fabricated by combinatorial synthesis. *Intermetallics* **9**, 541–545 (2001).
8. Fleet, E. F., Chatraphorn, S., Wellstood, F. C., Knauss, L. A. & Green, S. M. Closed-cycle refrigerator-cooled scanning SQUID microscope for room-temperature samples. *Rev. Sci. Instrum.* **72**, 3281–3290 (2001).
9. Fleet, E. F. *Design and Applications of a Cryo-cooled Scanning SQUID Microscope.* Thesis, Univ. Maryland (2000).
10. Murray, S. J. *et al.* Large field induced strain in single crystalline Ni–Mn–Ga ferromagnetic shape memory alloy. *J. Appl. Phys.* **87**, 5774–5776 (2000).
11. Murray, S. J., Marioni, M., Tello, P. G., Allen, S. M. & O'Handley, R. C. Giant magnetic-field-induced strain in Ni–Mn–Ga crystals: experimental results and modeling. *J. Magn. Magn. Mater.* **242**, 945–947 (2001).
12. Chernenko, V. A., Cesari, E., Kokorin, V. V. & Vitenko, I. N. The development of new ferromagnetic shape memory alloys in Ni–Mn–Ga system. *Scripta Metall. Mater.* **33**, 1239–1244 (1995).
13. Vasil'ev, A. N. *et al.* Structural and magnetic phase transition in shape-memory alloys $Ni_{2+x}Mn_{1-x}Ga$. *Phys. Rev. B* **59**, 1113–1120 (1999).
14. Patil, S. I. *et al.* Ferromagnetic resonance in Ni–Mn–Ga films. *Appl. Phys. Lett.* **81**, 1279–1281 (2002).
15. Wuttig, M., Craciunescu, C. & Li, J. Phase transformations in ferromagnetic NiMnGa shape memory films. *Mater. Trans. JIM* **41**, 933–937 (2000).
16. Ahlers, M. Phase stability of martensitic structures. *J.Phys. IV* **5**, 71–80 (1995).
17. Miyazaki, S. & Ishida, A. Martensitic transformation and shape memory behavior in sputter-deposited TiNi-base thin films. *Mater. Sci. Eng. A* **273**, 106–133 (1999).
18. Craciunescu, C. M., Li, J & Wuttig, M. Thermoelastic stress-induced thin film martensites. *Scripta Mater.* **48**, 65–70 (2003).
19. Wuttig, M., Liu, L., Tsuchiya, K. & James, R. D. Occurrence of ferromagnetic shape memory alloys. *J. Appl. Phys.* **87**, 4707–4711 (2000).
20. Chernenko, V. A. Compositional instability of β-phase in Ni–Mn–Ga alloys. *Scripta Mater.* **40**, 523–527 (1999).
21. Bozorth, R. M. *Ferromagnetism* 317 (IEEE Press, New Jersey, 1993).
22. Wijn, H. P. J. (ed.) *Data in Science and Technology* 54 (Springer, Berlin-Heidelberg, 1991).
23. Wassermann, E. F., Kastner, J., Acet, M. & Entel, P. Electronic origin of the martensitic transitions in Fe-based systems and Hume–Rothery systems: a comparison. *Proc. Int. Conf. Solid-State Phase Transitions '99 (JIMIC-3)* 807–814 (1999).
24. Zayak, A. T., Buchelnikov, V. D. & Entel, P. A Ginzburg–Landau theory for Ni–Mn–Ga. *Phase Transit.* **75**, 243–256 (2002).
25. Zener, C. in *Elasticity and Anelasticity of Metals* 37 (Univ. Chicago Press, Chicago, 1948).
26. Godlevsky, V. V. & Rabe, K. M. Soft tetragonal distortions in ferromagnetic Ni_2MnGa and related materials from first principles. *Phys. Rev. B* **63**, 134407–1–5 (2001).
27. Pickett, W. E. & Moodera, J. S. Half metallic magnets. *Phys. Today* **54**, 39–44 (2001).

Competing financial interests

The authors declare that they have no competing financial interests.

Ferromagnetic resonance in Ni–Mn–Ga films

S. I. Patil,[a)] Deng Tan,[b)] S. E. Lofland,[c)] and S. M. Bhagat
*Ferromagnetic Resonance Group, Department of Physics, University of Maryland,
College Park, Maryland 20742*

I. Takeuchi,[d)] O. Famodu, J. C. Read, K.-S. Chang, C. Craciunescu, and M. Wuttig
Department of Materials Science and Engineering, University of Maryland, College Park, Maryland 20742

Textured thin films of nominal composition $Ni_{0.50}(MnGa)_{0.50}$ were sputter deposited on Si substrates and studied by x-ray diffraction, micromechanical displacement, dc magnetization, and ferromagnetic resonance (FMR). We report the observation of spin wave resonances in this alloy, yielding a spin wave stiffness of $D = 200$ meV Å^2 at 300 K. A marked thermal hysteresis is observed in the temperature-dependent FMR data arising from the reversible martensitic transition. © *2002 American Institute of Physics.* [DOI: 10.1063/1.1501161]

Ni_2MnGa and related alloys are magnetic shape memory alloys (MSMAs) which exhibit extremely large magnetic-field induced strains.[1] Ferromagnetic domains in these materials are identical with the tetragonal variants in the martensitic state, and the field-induced twin boundary motion in the martensite can give rise to strains as large as 6% in applied fields of ~5 kOe.[1] One important direction of research in MSMAs is the fabrication of thin films, which hold potential for sensor and actuator devices with applications in microelectromechanical systems. In general, these thin films display properties which are rather different from those of bulk because their mechanical properties are greatly affected by their geometry, microstructure, and the constraint from the substrate.[2] There is a subtle interplay between the magnetic and structural properties that dictates their overall mechanical behavior, and understanding these relationships is of paramount importance in realizing the potential of these materials.

Ferromagnetic resonance (FMR) is one of the most powerful methods for probing the magnetic quality of thin films. In particular, narrow FMR lines and the observation of well resolved spin wave resonances (SWR) imply a high degree of magnetic homogeneity. In this letter, we present a FMR study of Ni–Mn–Ga alloy films grown by magnetron sputtering on Si substrates. In the perpendicular geometry (magnetic field $H \perp$ film plane), we have observed FMR linewidths (full width at half maximum) as narrow as 70 Oe, about an order of magnitude smaller than those reported for bulk polycrystalline samples of Ni–Mn–Ga.[3] In addition, in the films with thickness ≈ 200 nm, we have observed up to eight SWR modes and made the first determination of the temperature dependence of the spin wave stiffness. In thicker films (>500 nm), the temperature dependent FMR displays pronounced thermal hysteresis associated with the reversible martensitic transition.

Ni–Mn–Ga films were deposited by rf magnetron sputtering on Si (100) substrates in a high-vacuum chamber with a base pressure of $\sim 5 \times 10^{-9}$ Torr.[4] During the deposition, Ar gas at $\sim 5 \times 10^{-3}$ Torr was introduced in the chamber and controlled via throttling. The nominal starting composition of the target was Ni_2MnGa. Stoichiometric deviation from the target composition is expected in the deposited films, and wavelength dispersive spectroscopy was performed on individual films to obtain the exact composition. Measured chemical compositions are given in Table I. The films were either deposited at elevated temperature up to 500 °C or they were deposited at room temperature followed by an *in situ* annealing in the chamber at temperatures up to 500 °C. The film thickness ranged from ~150 to ~1000 nm. We also deposited relatively thick films (~1 μm) on micromachined Si cantilevers for detection of martensitic transitions. X-ray diffraction of the films at room temperature indicated that the films were textured with the peak from the (110) orientation of the austenite phase being the predominant feature.[4] The ferromagnetic transition temperature was determined to be near 370 K for all the films; which is the Curie temperature for bulk Ni_2MnGa.[3]

FMR was measured using a conventional homodyne spectrometer operating at 9.87 GHz, in the temperature range of 77–400 K. The applied field H was rotated in the plane perpendicular to the film.

We first discuss the room temperature data. Referring to Table I, films A and B are comparatively thin, <200 nm, and

[a)]Also at: Dept. of Physics, University of Pune 411007, India; electronic mail: patil@glue.umd.edu
[b)]Intern from: Eleanor Roosevelt High School, Greenbelt, MD 20770.
[c)]Also at: Center for Materials Research and Education, Dept. of Chemistry and Physics, Rowan University, Glassboro, NJ 08028.
[d)]Also at: Center for Superconductivity Research, University of Maryland, College Park, MD 20742; electronic mail: takeuchi@squid.umd.edu

TABLE I. Room temperature characteristics of thin films ($g = 2$), Eqs. (1) and (2).

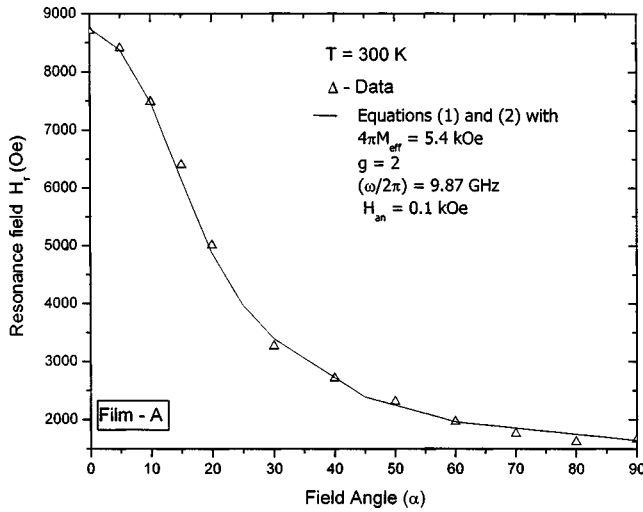| Sample ID	$H_{\parallel}$ (kOe)	$H_{\perp}$ (kOe)	H_{an} (kOe)	$4\pi M_{eff}$ (kOe)	$\Delta H_{\perp}$ (Oe)	Composition
A	1.64	8.70	0.10	5.40	100	—
B	1.28	9.58	0.27	6.35	70	$Ni_{0.50}Mn_{0.33}Ga_{0.17}$
C	1.68	7.04	0.40	3.90	600	$Ni_{0.54}Mn_{0.31}Ga_{0.15}$
D	1.85	7.17	0.20	3.90	300	$Ni_{0.50}Mn_{0.30}Ga_{0.20}$
E	1.27	9.82	0.24	6.60	300	$Ni_{0.49}Mn_{0.36}Ga_{0.15}$

FIG. 1. Angular dependence of resonance field at $T = 300$ K in film A. The full line was obtained using Eqs. (1) and (2) with the parameter values given in Table I.

FIG. 2. Spin wave resonance fields for film B at $T = 300$ K vs n^2. The inset shows the SWR pattern for the same film.

show a narrow FMR line with $\Delta H_\perp < 100$ Oe in the perpendicular geometry ($H \perp$ film plane). The other three films are ~ 1 μm thick and $\Delta H_\perp \sim 300$–600 Oe. All the films studied were found to show significantly wider resonance lines (>700 Oe) for $H\parallel$ to the film plane. Next, the angular dependence of the resonance field (H_r) was used to establish that the magnetization was uniform and that the strain-induced anisotropy field had a symmetry axis along the film normal. Namely, H_r is given by the equation

$$\left(\frac{\omega}{\gamma}\right)^2 = (H_r \cos\alpha - 4\pi M_{\text{eff}} \cos\theta)^2 + H_r \sin\alpha (H_r \sin\alpha + 4\pi M_{\text{eff}} \sin\theta) \quad (1)$$

combined with the equilibrium condition

$$\frac{\sin(\theta - \alpha)}{\sin\theta \cos\theta} = \frac{4\pi M_{\text{eff}}}{H_r}, \quad (2)$$

where $\omega = 2\pi f$, f is the frequency, γ is the gyromagnetic ratio, and θ (α) measures the angle between the $\mathbf{M}$ ($\mathbf{H}_r$) and the film normal.

In order to understand the data for all the films using a single value of g (2.00), it was necessary to introduce a small anisotropy field H_{an} to augment H_r. As before,[5] this is a field-induced anisotropy with the easy axis aligned parallel to H. As seen in Fig. 1, Eqs. (1) and (2) provide an excellent fit to the data, showing that the film is a fairly homogeneous ferromagnet. The room temperature parameter values for different films are listed in Table I, and it is notable that the lines are among the narrowest observed in Ni$_2$MnGa, again attesting to the high "magnetic quality" of the film. While vibrating sample magnetometer measurements yield $4\pi M(300\text{ K}) \cong 8 \pm 0.5$ kOe, the values for $4\pi M_{\text{eff}} = 4\pi M + 2K_u/M$ are significantly lower, thereby indicating that the strain-induced anisotropy field $2K_u/M$ is negative and 1–2 kOe in magnitude, i.e., the "easy" axis is out of plane.

Note that H_{an} is necessary to keep $g = 2$ for every film. Otherwise, the calculated g values show unphysically large
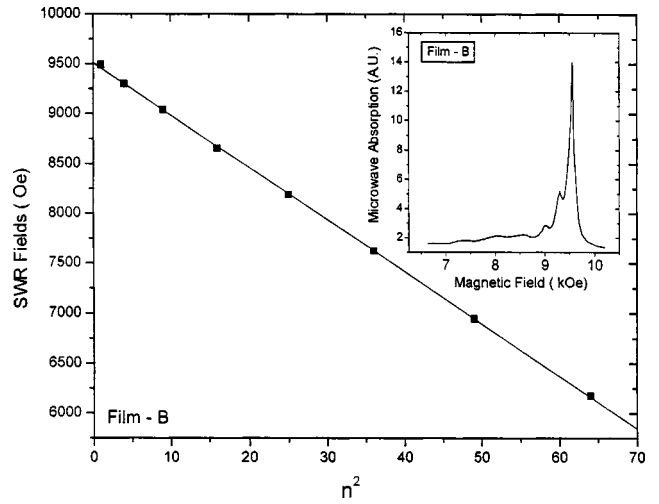
changes from film to film. As usual, $2K_u/M$ is needed to account for the difference between $4\pi M_{\text{eff}}$ and the dc magnetization ($4\pi M$).

In the thinner films (films A and B), several spin wave resonances were observed (inset of Fig. 2). The resonance fields follow the n^2 dependence expected for Kittel modes (albeit with both even and odd n) in a homogeneous ferromagnetic film, namely

$$\frac{\omega}{\gamma} = H + \frac{D}{\gamma\hbar}\left(\frac{n\pi}{L}\right)^2 - 4\pi M_{\text{eff}} + H_{\text{an}}, \quad (3)$$

yielding a spin wave stiffness of $D(300\text{ K}) = 200$ meV Å^2 (full line in Fig. 2) for $L = 1800$ Å. Although the temperature interval is rather narrow (250–350 K) it is notable that the temperature dependence of D follows $D = D_0 (1 - CT^{5/2})$, with $D_0 = 300$ meV Å^2 and $C = 3 \times 10^{-7}$ K$^{-5/2}$, as shown in Fig. 3. Thus we have demonstrated that the low-lying excited states are spin waves and that the stiffness renormalizes with temperature in accord with the simple spin wave theory. There are no neutron scattering data available for the present alloys. In the Heusler alloys D_0 values of 100–200 meV Å^2 have been reported and the temperature dependence follows
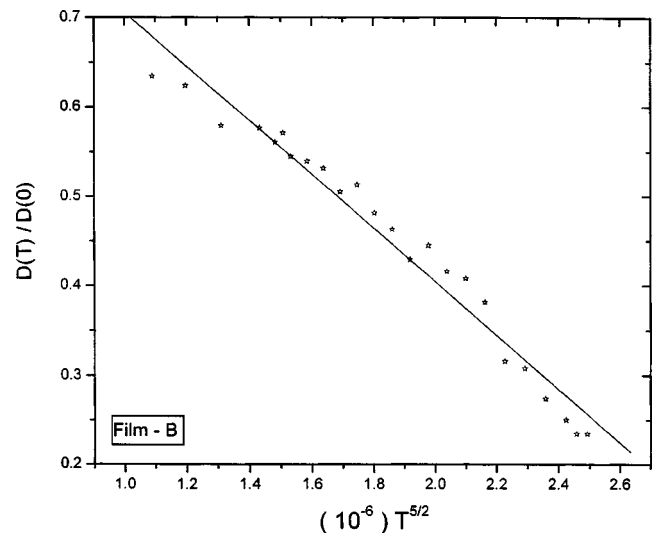

FIG. 3. Normalized spin wave stiffness constant as a function of $T^{5/2}$.
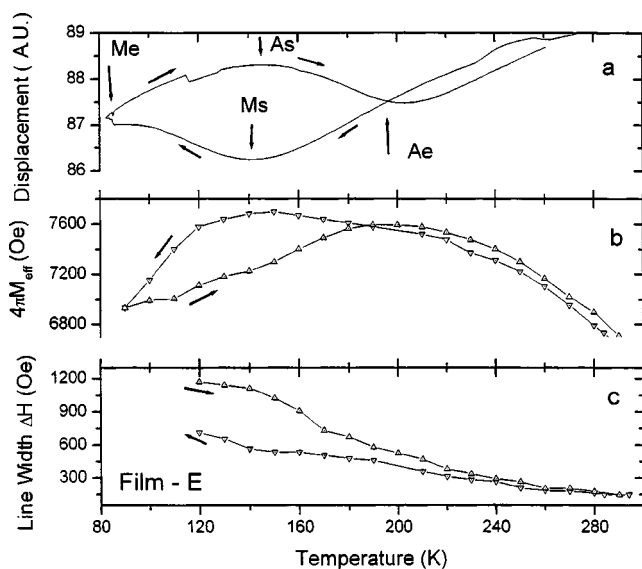
FIG. 4. The dependence of (a) micromechanical displacement, (b) effective magnetization, and (c) FMR linewidth on temperature for film E.

the spin wave theory.[6] However, the present D values are exceptionally large for a material with $T_C \sim 370$ K.

Figures 4(a)–4(c) show the temperature dependence of the micromechanical displacement and the FMR characteristics. Figure 4(a) represents the result of a thermomechanical measurement of a ~ 1 μm film (film E) deposited on a micromachined Si cantilever. Thermally activated displacement of the cantilever is monitored using a capacitance formed between the cantilever and a separate electrode.[7] A clear thermal hysteresis loop is observed indicating the occurrence of a reversible martensitic transformation in the film. Martensite start and end and austenite start and end temperatures are marked in the figure as M_s, M_e, A_s, and A_e, respectively. The observed transition behavior is very similar to that of previously reported Ni–Mn–Ga films.[8] Figures 4(b) and 4(c)

show the temperature dependence of the resonance parameters $4\pi M_{\mathrm{eff}}$ (derived from $H_\perp$ using $g=2$) and $\Delta H_\perp$ for the same sample. The hysteresis is also very apparent in the FMR data, and the hysteresis end points agree with the points of the multiphase region [M_e and A_e in Fig. 4(a)] quite well. In addition, when the martensite phase is dominant, the linewidth is much larger; as would be expected from a state with many martensitic variants. Indeed, for $T < 130$ K the FMR line becomes severely distorted [hence, the arrows in Fig. 4(c)]. Also, during warming, $4\pi M_{\mathrm{eff}}$ is significantly lower, indicating that the (negative) strain-induced field ($2K_u/M$) is enhanced by several hundred oersted. However, the onsets at A_s, M_s are not too obvious in the FMR data except that, on cooling, $4\pi M_{\mathrm{eff}}$ begins to drop rapidly for $T \lesssim M_s$.

To conclude, using FMR we have demonstrated that one can grow thin films of $Ni_{1-x-y}Mn_xGa_y$ that are magnetically very homogeneous. We have determined the spin wave stiffness ($D_0 = 300$ meV Å^2) and shown that it renormalizes as $T^{5/2}$. The martensite transition is well delineated by the resonance data in agreement with micromechanical experiments.

[1] S. J. Murray, M. Marioni, S. M. Allen, and R. C. O'Handley, Appl. Phys. Lett. **77**, 886 (2000).
[2] A. Ishida and V. Martynov, MRS Bull. **27**, 111 (2002).
[3] B. D. Shanina, A. A. Konchits, S. P. Kolesnik, V. G. Gavriljuk, I. N. Glavatskij, O. Soderberg, V. K. Lindroos, and J. Foct, J. Magn. Magn. Mater. **237**, 309 (2001).
[4] I. Takeuchi, O. Famodu, and J. C. Read (unpublished).
[5] D. J. Webb, and S. M. Bhagat, J. Magn. Magn. Mater. **42**, 109 (1984).
[6] U. Stuhr, P. Vorderwisch, and V. V. Kokorin, Physica B **234**, 135 (1997).
[7] M. Wuttig, C. Craciunescu, and J. Li, Mater. Trans., JIM **41**, 933 (2000).
[8] C. Craciunescu, Y. Kishi, L. Saraf, R. Ramesh and M. Wuttig (unpublished).

REFERENCES

Chapter 2

1. M. Lebl, J. Comb. Chem, **1**, 3-24 (1999).

2. X.-D. Xiang, X. Sun, G. Briceno, Y. Lou, K.-A. Wang, H. Chang, W. G. Wallace Freedman, S.-W. Chen, and P. G. Schultz, Science **268**, 1738 (1995).

3. H. Chang, I. Takeuchi, and X.-D. Xiang, Applied Physics Letters **74**, 1165 (1999).

4. I. Takeuchi, H. Chang, C. Gao, P. G. Schultz, X.-D. Xiang, R. P. Sharma, M. J. Downes, and T. Venkatesan, Applied Physics Letters **73,** 894 (1998).

5. J. Wang, Y. Yoo, C. Gao, I. Takeuchi, X. Sun, H. Chang, X.-D. Xiang, and P. G. Schultz, Science **279**, 1712 (1998).

6. H. Chang, C. Gao, I. Takeuchi, Y. Yoo, J. Wang, P. G. Schultz, X.-D. Xiang, R. P. Sharma, M. Downes, and T. Venkatesan, Applied Physics Letters **72**, 2185 (1998).

7. I. Takeuchi, O. O. Famodu, J. C. Read, M. A. Aronova, K.-S. Chang, C. Craciunescu, S. E. Lofland, M. Wuttig, F. C. Wellstood, L. Knauss, and A. Orozco, Nature Materials **2**, 180 (2003).

8. D. A. R. Barkhouse, A. Bonakdarpour, M. Fleischauer, T. D. Hatchard, and J. R. Dahn, Journal of Magnetism and Magnetic Materials **261**, 399 (2003).

9. T. Fukumura, M. Ohtani, M. Kawasaki, Y. Okimoto, T. Kageyama, T. Koida, T. Hasegawa, Y. Tokura, and H. Koinuma, Applied Physics Letters **77**, 3426 (2000).

10. G. Briceno, H. Chang, X. Sun, P. G. Schultz, and X.-D. Xiang, Science **270**, 273 (1995).

11. I. Takeuchi, D. Fukuma, and J. Matsui, Analytical Chemistry **71**, 285 (1999).

12. M. Gross, D. C. Muller, H. C. Nothofer, U. Sherf, D. Neher, C. Brauchle, and K. Meerholz, Nature **405**, 661 (2000).

13. C. H. Reynolds, Journal of Combinatorial Chemistry **1**, 297 (1999).

14. S. Sakahara, K. Yajima, R. Belosludoy, S. Takami, M. Kubo, and A. Miyamoto, Applied Surface Science **189**, 253 (2002).

15   J. D. Hewes, and L. A. Bendersky, Applied Surface Science **189**, 196 (2002).

16. J. C. Phillips, Physics of High-T_c Superconductors (Academic Press, New York, 1989).

17. M. A. Aronova, K. S. Chang, I. Takeuchi, H. Jabs, D. Westerheim, A. Gonzalez-Martin, J. Kim, and B. Lewis, Applied Physics Letters **83**, 1255 (2003).

18. H. Y. Hwang and S.-W. Cheong, Science **28**, 1607 (1997).

19. Y.-K. Yoo, F. Duewer, H. Yang, Y. Dong, J.-W. Li, and X.-D. Xiang, Nature **406**, 704 (2000).

20. M. J. Turchinskaya, L. A. Bendersky, A. J. Shapiro, K. S. Chang, I. Takeuchi, A. L. Roytburd, Journal of Materials Research, **19** (2004).

21. A. Stein, S. W. Keller, T. E. Mallouk, **259** 1558 (1993).

22. I. Takeuchi, R. B. van Dover, H. Koinuma, MRS Bulletin **27**,301 (2002).

23. K. Wasa, M. Kitabatake, and H. Adachi, Thin Film Materials Technology: Sputtering of Compound Materials, 49 William Andrew Publishing, NY (2004)

24. K. Wasa, T. Tohda, Y. Kasahara, and S. Hayakawa, Rev. Sci. Instr., **50**, 1086 (1979).

25. B. Jagannathan, W. A. Anderson, and J. Coleman, Solar Energy Materials and Solar Cells, **46**, 289 (1997).

26. E. D. McClanahan, and N. Laegreid, Sputtering by Particle Bombardment III, Springer-Verlag, Berlin, (1991)

27. F. M. Penning, U.S. Patent 2,146,025 (Feb. 1935).

28. K. Wasa and S. Hayakawa, Rev. Sci. Instr., **38**, 1693 (1987).

29. A. Rar, et al., Meas. Sci. Technology, **16**, 46-53 (2005).

30. N. C. Miller, G. A. Schirn, Appl. Phys. Letters. **10**, 86 (1967).

31. G. C. Schwartz, R. E. Jones, L. E. Maissel, J. Vac. Sci. Technol. **6**, 359 (1969).

32. J. J. Hanak, J. Materials Sci., **5**, 964-971 (1970).

33. J. J. Hanak, J. I. Gittleman, Iron-nickel-silica ferromagnetic cermets. AIP Conf. Proc., **10**, 961-965 (1973).

34. J. J. Hanak, Japan J. Appl. Phys., (Suppl. 2, Part1), 809-812 (1974)

35. J. J. Hanak, J. Non-Crystalline Solids, **3536**, 755-759 (1980)

36. J. J. Hanak, Solar Energy, **23**, 145-147 (1979)

37. J. J. Hanak and J. I. Gittleman, AIP Conference Proceedings, Part 2(10), 961-965 (1973).

38. R. B. van Dover, L. F. Schneemeyer, and R. M. Fleming, Nature, **392**, 162 (1998).

39. E. S. Ramakrishnan, K. D. Cornett, G. H. Shapiro, and H-Y. Howng, J. Electrochem. Soc., **145**, 358 (1998).

40. O. Nakagawara, et. al., J. Appl. Phys., **80**, 388 (1996).

41. S. Semancik, & R. E. Cavicchi, Acc. Chem. Res. **31**, 279–287 (1998).

42. S. Semancik, Combinatorial Materials Synthesis (eds X.-D. Xiang & I. Takeuchi), Dekker, New York (2003).

Chapter 3

1. R. E. Newnham, MRS Bulletin **22**, No 5 (1997).

2. A. Sozinov, A. A. Likhachev, N. Lanska, and K. Ullakko, Applied Physics Letters, **80**, 1746 (2002).

3. K. Otsuka and T. Kakeshita, MRS Bulletin, **27**, p. 91 (2002).

4. J. D. Harrison, D. E. Hodgson, Shape memory effects in alloys, New York, p. 517 (1975).

5. H. Ohkata, H. Tamura, Materials Research Society Symposium Proceedings **459** p. 345 (1997).

6. H. Kakamoto, K. Uematsu, M. Momota, S. Tanable, T. Suzuki, T. Endo, U.S. Patent No. 4,925,445 (1990).

7. J. K. Nichilson, R. F. Gatturna, U.S. Patent No. 4,616,656 (1986).

8. M. Wuttig, L. Liu, K. Tsuchiya, R. D. James, Journ. Appl. Phys. **87,** 4707 (2000).

9. M. Wuttig, C. Craciunescu, J. Li, Materials Transactions JIM **41**, 933–937 (2000).

10. S. Miyazaki, Ishida, Mater. Sci. Eng.A **273**, 106–133 (1999).

11. M. A. Aronova, Ph.D. Thesis, University of Maryland (2004)

12. O. L. Warren, et. al., Rev. Sci. Instrum., **76**, 062209 (2005).

13. O. L. Warren and T. J. Wyrobek, Measurement Science and Technology, **16**, 100-110 (2005).

14. A.C. Fischer-Cripps, Nanoindentation , Springer-Verlag, New York (2004)

15. W.C. Oliver and G.M. Pharr, Journal of Materials Research, **7**, n. 6, 1564-1582 (1992).

16. S. J. Murray, M. A. Marioni, A. M. Kukla, J. Robinson, R. C. O'Handley, S. M. Allen, Journal of Applied Physics **87**, 5774–5776 (2000).

17. S. J. Murray, M. A. Marioni, P. G. Tello, S. M. Allen, R. C. O'Handley, Journal of Magnetic Materials **242**, 945–947 (2001).

18. V. A. Chernenko, E. Cesari, V. V. Kokorin, I. N. Vitenko, Scripta Metall. Materials **33**, 1239–1244 (1995).

19. A. N. Vasil'ev, A. D. Bozhko, and V. V. Khovailo, I. E. Dikshtein and V. G. Shavrov V. D. Buchelnikov , M. Matsumoto, S. Suzuki, T. Takagi, and J. Tani, Physical Review B **59**, 1113 –1120 (1999).

20. S. I. Patil, Deng Tan, S. E. Lofland, and S. M. Bhagat, I. Takeuchi, O. Famodu, J. C. Read, K.-S. Chang, C. Craciunescu, and M. Wuttig, Applied Physics Letters **81**, 1279–1281 (2002).

21. M. Ahlers, J.Phys. IV **5**, 71–80 (1995).

22. C. M. Craciunescu, J. Li, M. Wuttig, Scripta Mater. **48**, 65–70 (2003).

23. http://cst-www.nrl.navy.mil/lattice/struk/l2_1.html

24. M. Wuttig, L. Liu, K. Tsuchiya, and R. D. James, Journal of Applied Physics, **87**, 4707–4711 (2000).

25. V. A.Chernenko, Scripta Mater., **40**, 523–527 (1999).

26. R. M. Bozorth, Ferromagnetism **317** (IEEE Press,New Jersey, 1993).

27. H. P. J. Wijn, (ed.) Data in Science and Technology **54** (Springer, Berlin-Heidelberg, 1991).

28. E. F. Wassermann, J. Kastner, M. Acet, P. Entel, Proc. Int. Conf. Solid-State Phase Transitions '99 (JIMIC-3) 807–814 (1999).

29. A. T. Zayak, , V. D. Buchelnikov, P.A. Entel, Phase Transit. **75**, 243–256 (2002).

30. V. V. Godlevsky, K. M. Rabe, Phys. Rev. B **63**, 134407–1–5 (2001).

31. W. E. Pickett, J. S.Moodera, Physics Today **54**, 39–44 (2001).

32. C. Wedel and K. Itagaki, Journal of Phase Equilibria **22**, 324 (2001)

33. R. D. James and M. Wuttig: Philos. Mag. A **77**, 1273–1299 (1998).

34. K. Ullakko, J. K. Huang, C. Kantner, R. C. O'Handley and V.V. Kokorin: Appl. Phys. Lett., **69**, 1966-1968 (1996).

35. A. Fujita, K. Fukamichi, F. Gejima, R. Kainuma and K. Ishida: Appl. Phys. Lett., **77**, 3054-3056 (2000).

36. K. Oikawa, T. Ota, F. Gejima, T. Ohmori, R. Kainuma and K. Ishida: Materials Transactions JIM, 2472-2475 (2001).

37. C. Craciunescu, Y. Kishi, T. A. Lograsso and M. Wuttig: Scripta Materialia **47**, 258-288 (2002).

38. L. Manosa, A. Planes, M. Acet, E. Duman and E. F. Wassermann: J. Appl. Phys. **93**, 8498-8500 (2003).

39. R. Kainuma, H. Nakano and K. Ishida: Metall. Mater. Trans. A, **27A**, 4153-4162 (1996).

40. S. Morito, T. Kakeshita, K. Hirata, and K. Otsuka: Acta Mater., **46**, 5377-5384 (1998).

41. Y. Sutou, I. Ohnuma, R. Kainuma, and K. Ishida: Metall. Mater. Trans. A, **29A**, 2225-2227 (1998).

42. X. Y. Dong, J.W. Dong, J.Q. Xie, T.C. Shih, S. McKernan, C. Leighton and C. J. Palmstrom: Journal of Crystal Growth, **254**, 384-389 (2003).

43. L1. Manosa, A. Plans, Ch. Somsen, Ch. Fell and M. Acet: J. Phys. IV France, **11**, Pr8-245-249 (2001).

44. I. Takeuchi, O. O. Famodu, J. C. Read, M. A. Aronova, K.-S. Chang, C. Craciunescu, S. E. Lofland, M. Wuttig, F.C. Wellstood, L. Knauss and A. Orozco: Nature Materials, 2, 180-184 (2003).

45. M. Acet, E. Duman, E. F. Wasserman, Ll. Manosa and A. Planes: J. Appl. Phys., **92**, 3867-3871 (2002).

46. S. Morito and K. Otsuka: Mater. Sci. & Engr., **A208**, 47-55 (1996).

47. K. K. Jee, P. L. Potapov, S. Y. Song, and M. C. Shin: Scripta Materialia, **36**, 207-212 (1997).

48. R. Kainuma, F. Gejima, Y. Sutou, I. Ohnuma and K. Ishida: Mater. Trans., JIM, **41**, 943-949 (2000).

49. P. L. Potapov, N. A. Polyakova, V. A. Udovenko and E. L. Svistunova: Z. Metallkd., **87**, 33-39 (1996).

50. Y. Tan, T. Shinoda, Y. Mishima, and T. Suzuki: Mater. Trans., **42**, 464-470 (2001).

51. D.P. Hoydick, E.J. Palmiere, and W.A. Soffa: Scripta Materialia, **36**, 151-156 (1997).

52. O. L. Warren and T. J. Wyrobek, Meas. Sci. Technol., (accepted for publication)

53. J.P. Harbison, T. Sands, R. Ramesh, L.T. Florez, B.J. Wilkens, and V.G. Keramidas: Journal of Crystal Growth, **111**, 978-983 (1991).

54. A. Morisako, N. Koshiro, M. Matsumoto and M. Naoe: J. Appl. Phys., **67**, 5655-5657 (1990).

55. G. Carmen, Private communication.

Chapter 4

1. K. Bhattacharya, S. Conti, G. Zanaotto, and J. Zimmer, Nature, **428** 55(2004) .

2. K. Bhattacharya, R. D. James, The material is the machine, Science, **307** 53 (2005).

3. J. M. Ball, R. D. James, Phil. Trans. Royal Soc. London **A338** 389 (1992).

4. K. Otsuka and T. Kakeshita, MRS Bulletin, **27**, p. 91 (2002).

5. C. Chu, Hysteresis and microstructures: A study of biaxial loading on compound twins of copper aluminum nickel single crystals, Ph.D. thesis, University of Minnesota (Aug. 1993).

6.   P. Sittner, D. Vokoun, G. D. and R. Stalmans, Materials Science and Engineering **A286**, 298 (2000).

7.   S. Miyazaki, K. Mizukoshi, T. Ueki, T. Sakuma, Y. Liu, Materials Science and Engineering **A273-275**, 658 (1999).

8. A. Ishida, A. Takei, S. Miyazaki, Thin Solid Films, **228**, (12) 210–14 (1993).

9. A. Ishida, M. Sato, A. Takei, S. Miyazaki, Materials Transactions, JIM, **36** (11) 1349–55 (1995).

10. A. Gyobu,Y. Kawamura, H.Horikawa, T. Saburi, Materials Transactions, JIM, **37** (4) 697 – 702 (1996).

11. C. L. Shih, B. K. Lai, H. Kahn, S. M. Phillips, A. H. Heuer, IEEE J. of MicroElectroMechanical Systems, **10** (1) 69–79 (2001).

12. I. Takeuchi, O. O. Famodu, J. C. Read, M. A. Aronova, K. S. Chang, C. Craciunescu, S. E. Lofland, M. Wuttig, F. C. Wellstood, L. Knauss, A. Orozco, Nature Materials, **2** (3) 180–4 (2003).

13. M. G. Faulkner, J. J. Amalra j, A. Bhattacharyya, Experimental determination of thermal and electrical properties of niti shape memory wires, Smart Mater. Struct., **9**, 632–9 (2000).

14. http://www.ncnr.nist.gov/programs/crystallography/software/cmpr/cmprdoc.html

15. P. Sittner, D. Vokoun, G. D. and R. Stalmans, Mater. Sci. and Engr., **A286**, 298 (2000).

16. S. Miyazaki, K. Mizukoshi, T. Ueki, T. Sakuma, and Y. Liu, Mater. Sci. and Engr., **A273-275**, 658 (1999).